Real-time control of wall-bounded turbulence

Dacome, G.

DOI
10.4233/uuid:07c484e9-0bb8-48d8-898f-9ec5f55d18eb

Publication date
2025

Document Version
Final published version

Citation (APA)
Dacome, G. (2025). *Real-time control of wall-bounded turbulence*. [Dissertation (TU Delft), Delft University of Technology]. https://doi.org/10.4233/uuid:07c484e9-0bb8-48d8-898f-9ec5f55d18eb

Real-time control of wall-bounded turbulence

Giulio Dacome

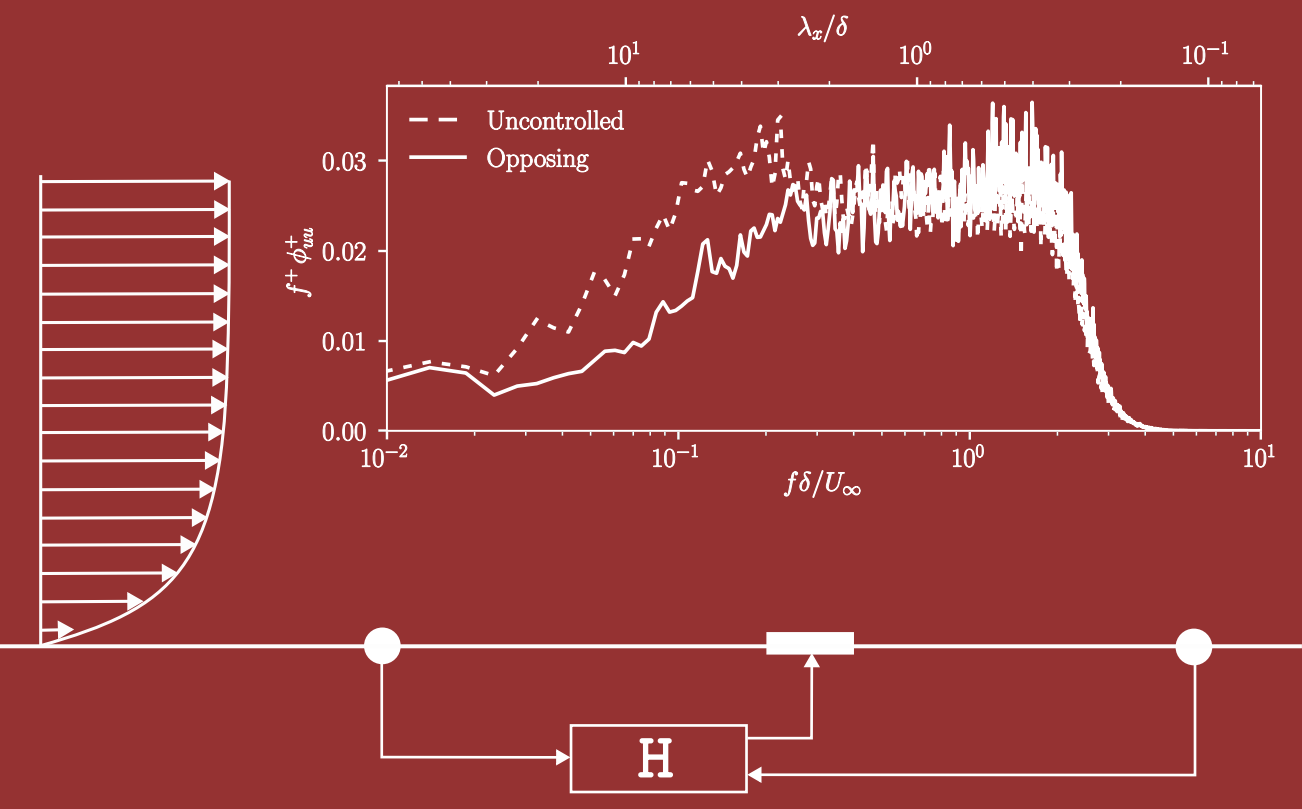

REAL-TIME CONTROL OF WALL-BOUNDED TURBULENCE

REAL-TIME CONTROL OF WALL-BOUNDED TURBULENCE

Dissertation

for the purpose of obtaining the degree of doctor
at Delft University of Technology
by the authority of the Rector Magnificus, prof. dr. ir. T.H.J.J. van der Hagen,
chair of the Board for Doctorates
to be defended publicly on
Thursday 23rd October 2025 at 10:00

by

Giulio DACOME

Master of Science in Aerospace Engineering,
Delft University of Technology, Delft, The Netherlands
born in Ravenna, Italy

This dissertation has been approved by the promotors.

Composition of the doctoral committee:

Rector Magnificus,	chairperson
Prof. dr. M. Kotsonis,	Delft University of Technology, *promotor*
Dr. ir. W.J. Baars,	Delft University of Technology, *copromotor*
Independent members:	
Prof. dr. L.L.M. Veldhuis	Delft University of Technology
Prof. dr. S. Discetti	Universidad Carlos III de Madrid, Spain
Prof. dr. S. Ghaemi	University of Alberta, Canada
Prof. dr. B. Frohnapfel,	Karlsruhe Institute of Technology, Germany
Prof. dr. F. Scarano,	Delft University of Technology, *reserve member*
Other members:	
dr. G. Bellani,	University of Bologna, Italy

Keywords: Wall-bounded Turbulence, Turbulent Boundary Layer, Real-Time Control, Skin-Friction Drag Reduction, Wall-Pressure, Wall-Shear Stress, Skin-Friction Control

Printed by: Uitgeverij U2pi - Den Haag, The Netherlands

Cover by: Artistic representation of a generic schematic of the control system implemented in this dissertation.

ISBN 978-94-6384-859-6

An electronic copy of this dissertation is available at
https://repository.tudelft.nl/.

Men will never fly, because flying is the privilege of angels.

Milton Wright - father of the Wright brothers

Ai miei nonni.

CONTENTS

SUMMARY

The work presented in this dissertation focuses on the developed and implementation of real-time control techniques for turbulent wall-bounded flows, with the aim of achieving skin-friction drag reduction. After an initial control system was developed that utilized instantaneous wall-shear stress fluctuations, wall-pressure fluctuations were subsequently used as the input quantity to the real-time flow control systems considered in this dissertation. Furthermore, the control algorithm complexity was escalated from a relatively simple feedforward opposition control logic to an adaptive control strategy.

The research presented in this dissertation is fully experimental in nature. Experimental activities were conducted in two main facilities. The bulk of testing was performed in the W-Tunnel at Delft University of Technology: an open-return wind tunnel, where a modular test section was integrated to perform experiments on zero-pressure–gradient turbulent boundary layer flows. A subset of measurements were conducted at the Center for International Cooperation in Long-Pipe Experiments (CICLoPE) at Bologna University, in Italy. Here, simultaneous measurements were conducted of velocity fluctuations in the logarithmic region and wall-pressure.

A stochastic spectral correlation analysis between wall-pressure fluctuations and velocity fluctuations in the logarithmic of a turbulent pipe flow reveal Reynolds-number–independence of the wall-pressure linear coherence spectrum. This is a first-of-its-kind result, hinting at the feasibility of scaling an input sensing strategy based on wall-pressure fluctuations from a low-Reynolds-number environment to operational engineering conditions.

An initial controller based on wall-shear stress fluctuations was developed to target drag-producing large-scale structures in the logarithmic region. The flow response was measured in terms of both the statistical (and spectral) response of the TBL flow to real-time control and in terms of the effect the control has not only on the friction coefficient, but also on the integral measures. This analysis revealed three main findings: (1) an attenuation of energy at streamwise wavelengths characteristic of large-scale motions, (2) a decrease in skin-friction and (3) an attenuation of the statistical integral measures of skin-friction (*i.e.* bulk production and FIK terms).

A similar control architecture was also implemented that employed wall-pressure (and wall-pressure–squared) as the input quantity. It was found that the wall-pressure–squared term improves the accuracy of an estimator enabling the prediction of off-the-wall velocity fluctuations from a wall-based position. Furthermore, its inclusion is essential, given that the linear term does not retain sufficient coherence over the relatively large streamwise extent separating input and actuation locations.

The final controller that was developed in the context of this dissertation is an adaptive one, relying on the Filtered-X Least Means Squares (Fx-LMS) algorithm. This strategy does not rely on *a-priori* system identification, as was the case for the previous two

control strategies mentioned above. Instead, it automatically identifies the coefficients of the transfer functions relating input to output in the controller. For this study, this algorithm was deployed both to a flow case that was strongly modulated by cylinder vortex shedding and to a fully broadband turbulent boundary layer flow. In the former case, the controller readily identified the shedding frequency as the control target. For the latter, the controller converges to a situation where the large-scales were targeted and their intensity successfully attenuated.

ACKNOWLEDGEMENTS

To all those who think a Ph.D. is boring and lonely, to all those who think a Ph.D. is too big of a commitment and to all those who think a Ph.D. is too much... I must say, you are right... to a point. You are right if you just want the big bucks, you are right if you just want "Dr." or ", Ph.D." on your business card and you are right if you can't rely on your peers for support and guidance. A Ph.D. is a long journey, with plenty of very low lows and (hopefully) a greater than or equal number of very high highs. This journey would not be (and would not have been for me) a great adventure should it not have been shared with the people I have had the honor to meet and collaborate.

First and foremost, a massive thank you to my co-promotor and daily supervisor, Woutijn. I am 100% sure when I say that this Ph.D. would not have been the same without your help, guidance and motivation. From insightful scientific discussion to tremendously-valuable feedback and to casual pizzas in Forlì, I will take with me an extremely fond memory of our collaboration in Delft. Thank you!

A massive thank you also to my promotor, Marios. Your insight into turbulence, experimental activities and, in general, the Ph.D. process has been invaluable through the years. Your input always came at the right moment and always brought a more "external" view to my project, which always helped me to get unstuck.

The Marios & Woutijn supervisor package is definitely the best the market has to offer! With you both I understood what it means to work in Academia and how to make the best time out of it. Thank you again for being such great mentors and colleagues!

I owe a big thank you also to the great collaborators for the University of Bologna, without whom a part of this dissertation would not have happened. Grazie mille Lorenzo, Gabriele and Alessandro for hosting us in "the mountain", with special grazie mille to Lorenzo for the several calls we had following up from the experiment. It was also a pleasure to have you with us in Delft for some time and I wish you all the best as the *Warden of CICLoPE*.

Dankjulliewel to all the technical and support staff across the AE Faculty, FPT Department and Aerodynamics section. Special thank you to Colette for being always on top the section's smooth operations and for all of your timely help in dealing with urgent matters. Thank you to the great technical staff in both the HSL and LSL, including Peter, Dennis, Frits, Emiel, Stefan, Martijn, Adam, Floris and Gert-Jan (who I hope is not afraid of me anymore because "I am tall").

People say that a Ph.D. programme is usually a lonely job. Yet, although each Ph.D. candidate works on their own project with their own supervisory team, sharing the past four years with the rest of the Ph.D. colleagues has been a tremendous privilege and one the greatest honors in my career. Thank you very much to all those people with whom I had the chance to cross paths, both in HSL for the first two years and in then in the LSL.

Having started my Ph.D. at the end of the pandemic, the first people I met in the office

were the highlight of that period, and these great people are Alessandro, Giulia, Edoardo, Jane, Gabriel, Varun, Christoph, Kushal, Beto, Alessandro, Sven, Kaisheng, Jordi, Lluis, Haris, Constantin and Ilda. As fundamental part of the now *Old Guard* also come in Ata, Thomas, Wencan, Babak, Tyler, Adrian, Mengjie, Renzhi and Luuk. Great thanks to all those colleagues whom I did not have the chance to get to know better, given my move to the LSL, including Brian, Sajad, Kevin, Joel, Marco, Sara, Suyash, Andrea and Aneek. An enourmous thank you also goes to those colleagues with whom I shared the second half of my Ph.D., in the Low Speed Lab. To Abdoo, Max, Parisa, Babak, Marina, Yifu, Suzanna, Pierre, Marco, Nick, Antonis, Srinivas, Martín, Martino, Erica and Hendrik... thank you, grazie, merci, gracias, $\epsilon\nu\chi\alpha\rho\iota\sigma\tau\omega$!

During my Ph.D. I also had the privilege to be involved in the supervision of some amazing master thesis students, who I hope had a good ride with us in the lab and to whom I renew my greetings and express my gratitude! I definitely learned a lot from you guys, and hope I was able to do the same for you. Renko, Pratyush, Robin and Gonzalo, thank you! Also, many thanks to the many more master students in whose project I was not involved in, but had the privilege to meet and help: Toma, Martina, Alessandro, Gabriele, Edoardo and Elias.

Life outside the office would not have been the same without the unwavering support from my dear friends, both from the lab and not. *Muchas gracias* José for our the trust you have in me and for the great friendship we built across two continents. *Grazie mille* Matteo for truly always being there in times of need and *grazie mille* Federico for being a constant source of wisdom and irony! Also *grazie mille* to all my dear friends back home: Federico, Giovanni and Camilla for always being there for me and for the several meetings filled with fun we often arranged when I come by! *Dankjewel* Stijn and Johannes for being such great travel companions and people I can confidently rely on! *Grazie mille* Giulia for being a (harsh) and great card game companion! Thank you Parisa for all the casual great chats and the great literature/poetry/music recommendations! Thank you Ata for our great music and surfing sessions and for being such a great friend! Thank you Alessandro, Thomas, Abdoo, Antonis and Max for being more than just colleagues, but also some of the most amazing people I've come across!

This acknowledgments' section would not be complete without including the people who most supported during these past four years: my family! Grazie mille to my great parents, who showed unwavering support for my decisions and efforts and on whom I can confidently rely no matter what! Grazie zia Carolina, zia Lucia, Joseph, Marco and my great cousins Lorenzo and Leonardo for always believing in me.

Esta tesis no se puede cerrar sin agradecer a mi maravillosa novia, Jazmin, que siempre ha estado a mi lado. Hemos vivido juntos incontables momentos llenos de risas, alegría y complicidad. Gracias por tu apoyo, tu cariño y por llenar cada etapa de este camino de entusiasmo y felicidad.

E grazie mille ai miei fantastici nonni, che mi hanno sempre incoraggiato a fare ciò che mi piace, che mi hanno sempre detto di non badare a ciò che pensano gli altri e di seguire sempre le mie passioni. Questa tesi è dedicata a voi. Alla nonna Enrica, al nonno Angelo, alla nonna Almea e al nonno Alberto.

Thank you all! Fly high everyone!

Giulio

P.S. And finally, a special thank you to those who doubted me. To those who said I wouldn't make it, who rolled their eyes at my ambition, who thought I was too soft, too calm, too nice — thank you. To those who assumed I'd never finish on time, that I lacked the fire or that I could not handle it — thank you. To those who claimed I only got this position because I studied here before — thank you. To the ones who took from me without giving back, who drained my time, leaned on my work, asked for help and forgot my name — thank you. To those who mistook my kindness for weakness and my availability for exploitability — thank you. To the ones who demanded my time and offered me silence — thank you. To those who disrespected the way I think — clear, calm, disciplined — thank you. That same fire you thought I lacked now burns harder than ever. That blaze, I will carry with me today and forever. To each of you: I bow — not out of respect, but out of triumph.

Because I won.

I

PREAMBLE

1

INTRODUCTION

The greatest enemy of progress is the illusion of knowledge.

John Young (STS-9)

This initial chapter presents the context, motivation and scientific background to the research work that will be elaborated upon in this dissertation. An overview of the state-of-the-art in experimental active flow control development is presented that forms the basis of this work. Additionally, relevant literature describing the complex dynamics of a turbulent boundary layer flow is introduced as the theoretical background to the work.

1

1.1. MOTIVATION

Air transport is a pillar of modern society, enabling high-speed, cost-efficient movement of people and goods both regionally and globally. Infrastructure investments, advancing aircraft technology and low air fares are constantly driving the number of yearly air passengers up. According to a June 2024 report by the International Air Transport Authority, in fact, total air passenger numbers are forecast to increase by more than 30% in 2027, compared to 2023 numbers [IATA, 2024]. Such high demand not only poses a concern in terms of current infrastructure capacity, air traffic congestion and long-term accessibility to economically sustainable air travel, but also on how its scale affects global carbon emissions and fuel consumption. Ritchie [2024] illustrates how, in 2021 (just before the COVID-19 pandemic), the contribution of aviation emission was almost 2.5% of the global emissions of CO_2. With the expected increase in global passenger numbers, the percentage contribution is only set to considerably increase, especially as other industrial efforts gradually commit to de-carbonization.

The combustion of kerosene for powering aircraft engines is the main culprit for intense carbon emission in the aviation industry. With the fuel consumption being directly correlated to the aerodynamic drag that needs to be overcome in flight, it is of utmost important to understand the flow mechanisms that correlate to drag production. For flight in the transonic regime, as is the norm for commercial jetliners, drag can be decomposed in form, wave and friction components. The first two result from the pressure distribution around the vehicle [and do not fall within the scope of this work], whereas the latter results from the entire flow-exposed (*i.e.* wetted) surface area of the vehicle being "encapsulated" in a viscous layer (the boundary layer) in order to abide by the no-slip condition. While initially laminar and generating relatively low friction, a boundary layer quickly transitions to a turbulent state, whereby its friction coefficient drastically increases. Throughout most of an aircraft's wetted surface area, the boundary layer is actually turbulent.

Friction (or *viscous*) drag alone contributes to, approximately, 50% of the total drag of a commercial jet transport aircraft in cruise flight [Ricco et al., 2021].

Research into turbulent wall-bounded flows has been the focus of many scientific research groups around the globe for several decades. Most of the initial studies focusing on turbulent boundary layers (TBLs) focus on the dynamics of the so-called *coherent structures* forming within it, that can be considered as regions of fluid that display either temporal or spatial coherence in a quantity of interest [Jiménez, 2018]. The dynamical interplay between such structures at the vast range of scales that characterizes a TBL at a sufficiently high friction Reynolds number needs to be untangled to analyze the underlying drag-producing mechanisms. This understanding has the potential to generate a profound impact on the (1) design of flow-exposed surfaces and (2) the definition of control systems targeting wall-bounded turbulence for skin-friction drag reduction. While the former aspect is not within the scope of this dissertation [entails the definition of passive control methods], the latter forms the *fil rouge* that binds this work together.

The control of wall-bounded turbulence and, more specifically, TBL flows has been explored both in its passive and active forms. With passive techniques promising low complexity, minimal added cost and high effectiveness, active control strategies have the potential to achieve much higher performance compared to their passive counterpart, at the cost of non-zero input-power. While the question of whether or not net energy savings can be achieved is one that still needs an answer [which will not be provided in dissertation], it is critical to explore the feasibility of implementing active flow control techniques. In particular, the focus of this work is to investigate and implement reactive (real-time) control strategies targeting a reduction in skin-friction drag. Real-time control techniques also have an added benefit in being *selective*: the controller is designed to only act upon specific features in the flow (in a pre-determined manner, in some cases) as the target for control; *e.g.* coherent structures of a certain scale. A great array of control algorithms can be employed to optimize the controller's performance and efficiency. In essence, real-time (or re-active) control can be designed to only target the features of the wall-bounded flow that are, in fact, drag-producing, while otherwise being inoperative.

Active flow control is sparking interest in the aviation industry, but has not yet seen widespread deployment (nor consideration) when compared to passive solutions. The latter, for instance, include passive surface modifications, such as riblets and small-scale surface protrusions. Riblets are currently considered the most promising passive drag reduction technology. They consisted of shallow elongated ridges that extend in the streamwise direction and allow the near-wall turbulence production cycle to stabilize. They, in particular, have seen entry into service embedded in an adhesive film for retrofitting of operational aircraft fleets (see Fig. 1.1a or the work of MicroTau[1]). Airlines, for instance, have retrofitted aircraft with the technology[2], and do report promising fuel savings.

The aviation industry, in general, is rather keen on adopting passive flow control techniques, mainly due to their operating costs (*i.e.* maintenance). However, passive techniques for skin-friction drag reduction are rather novel and their technologies readiness level is low (apart from riblets). Still, passive flow control technologies targeting different aerodynamic phenomena (*e.g.* flow separation or mixing) have seen extensive deployment in the aviation industry, such as fixed leading edge vortex generators (see Fig. 1.1b) for stall mitigation and swirling flaps for enhancing mixing in the combustion chambers of aeronautical engines.

The potential of active flow control techniques for achieving considerably higher control authority compared to passive techniques is undeniable. Not only for skin-friction, but also for separation control, for instance. In fact, the industry commissioned several studies, run both by private industrial entities, as well as by government-funded research centers, whose aim is to investigate the feasibility of integrating active flow control into full-scale aircraft. The DARPA consortium, for instance, was tasked with initiating a study into the replacement of the traditional hinged control surfaces with active flow control techniques for modifying the flow around regions of a wing where, conventionally, an actuator would be located. This would therefore generate a control moment that induces a rotation of the aircraft about a given axis. The programme took

[1] MicroTau - microtau.com.au
[2] Lufthansa Technik - lufthansa-technik.com/en/aeroshark

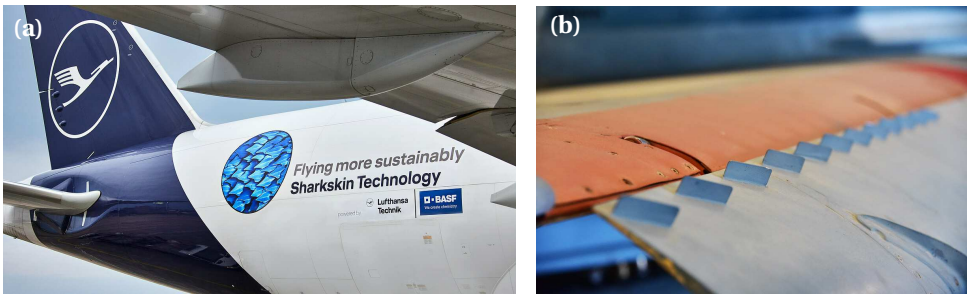

Figure 1.1.: (a) Photograph of the aft section of a Lufthansa aircraft retrofitted with a riblet skin. Courtesy of Lufthansa Technik GmbH. (b) Photograph of the array of leading-edge vortex generators on the wing of a military trainer aircraft (TA-4J Phantom). Copyright free.

shape under the designation X-65 CRANE, which is still in the early development stages (a wind tunnel model used in this programme is illustrated in Fig. 1.2a). Furthermore, NASA and Boeing collaborated in the ecoDemonstrator programme to retrofit an existing operational jetliner (photograph in Fig. 1.2b) to incorporate sweeping jets into the vertical stabilizer, to reduce its aerodynamic drag.

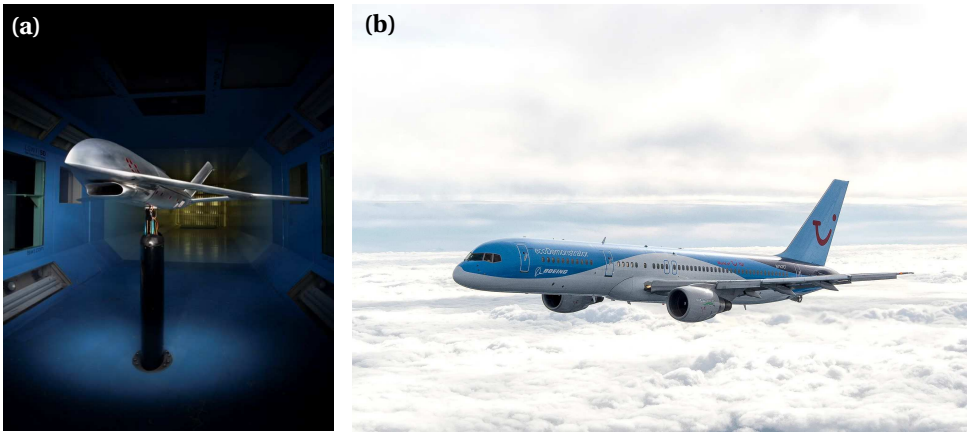

Figure 1.2.: (a) Photograph of the wind tunnel model employed for testing in the preliminary phases of the CRANE program, run by DARPA. Courtesy of Aurora Flight Sciences. (b) Photograph of the Boeing 757 ecoDemonstrator, incorporating active flow control solutions to mitigate the drag of the vertical stabilizer. Courtesy of Boeing.

The reader might notice, however, how the efforts that have characterized the implementation of active flow control in full-scale aircraft were not actually targeting drag reduction. Both in the case of the X-65 and the ecoDemonstrator, the goal is to enhance

the performance of control surfaces by means of active flow control techniques, but not to reduce skin-friction drag. One can find other examples in the open literature and publicly available news that similar attempts have been performed in fields other than the aerospace one, such as high-speed rail transport (where, anyway, skin-friction drag is not critical).

This work sets out to explore the applicability and implementation of real-time active flow control techniques to a zero-pressure-gradient turbulent boundary layer flow for skin-friction drag reduction in an experimental setting. As for any real-time control system, one first needs to clarify three main aspects:

1. what the controller should target;
2. what input it should be based on;
3. how the controller should actuate upon its target.

These three points form the core of this dissertation and will be discussed in the remaining of this section and in subsequent chapters.

1.2. TURBULENT BOUNDARY LAYER CONTROL

Up until this point in this dissertation, several flow phenomena have been mentioned whose control with active means improves aircraft performance. From this section onward, the focus of this work is going to exclusively pivot towards the analysis of turbulent wall-bounded flows and their control with the aim of skin-friction drag reduction.

Several studies can be found in the literature that implement active control strategies for the reduction of skin-friction drag in a zero-pressure-gradient turbulent boundary layer (ZPG-TBL), among which the publications of Abbassi et al. [2017], Cheng et al. [2021a] and Yu et al. [2021] are some examples. A rather wide range of control configurations can be evinced from the literature, with differences lying in the control target, the type of actuators, the choice of algorithm, *etc.* In the foregoing, a review of the main publications available in the open literature that inspired this work is going to be presented. Additionally, the main pitfalls and challenges are going to be illustrated that still prevent active flow control strategies from attaining a commercially-viable technology readiness level. In particular, the three main requirements for the successful implementation of a control strategy are listed below.

1. **Maximum net power saving.** Being the *"Holy Grail"* of any flow control technique, this requirement translates not only to the employment of low-power hardware and low-overhead control algorithms, but also to the design of both sensors and actuator that are minimally-intrusive in the TBL flow. For instance, a configuration relying on active surfaces protruding into the flow would obviously not be suited to meet this requirement, because of the additional parasitic drag induced by the system itself. Therefore, as will emerge from the following sections of this dissertation, the work presented here will rely on wall-embedded hardware only. Furthermore, exploiting the (by-design) selectivity of the controller, by tuning it to only target certain structures in the flow and being inactive for the rest of the time, increases the control system's efficiency.

2. **Low complexity.** Considerations of complexity (and cost) are essential for the widespread adoption of a control system in an industrial setting. Therefore, a control configuration making use of a relatively low number of sensors and actuators should be employed. This results in the need of both effective actuators, as well as the identification of a control target with a relatively long spatio-temporal lifespan and slow dynamics. This removes the need for constant and finely-spaced (spatially) control stations.

3. **Reynolds-number scaling.** Engineering systems operate at Reynolds-numbers that are orders of magnitude larger than laboratory experiments. Therefore, careful consideration must be posed on the scalability of a chosen control method. For real-time control, requirements for parameters such as loop frequency and hardware miniaturization scale rather unfavorably with an increase in Reynolds number.

All three requirements call for complex design choices and careful analysis of the chosen control parameters, which are closely interlinked with the dynamics of the turbulent boundary layer flow.

Strategies for friction control of wall-bounded turbulence rely on the fundamental understanding of boundary layer flows and their friction-generating mechanisms. Research has revealed how different coherent structures exist, and how the structures' characteristics vary as a function of wall-normal distance, particularly when considering their sizing and spatio-temporal dynamics [Kline et al., 1967, Falco, 1977, Kim and Adrian, 1999, Lee and Sung, 2011, Jiménez, 2018]. In the inner region, structures scale with the viscous length scale ν/U_τ, and time scale ν/U_τ^2, with ν being the kinematic viscosity and $U_\tau \equiv \sqrt{\tau_w/\rho}$ being the friction velocity (τ_w is the wall-shear stress and ρ is the fluid density). Variables that are normalized following inner-scaling will be presented with a superscript "+". In the outer region, instead, structures scale with the boundary layer thickness δ as the characteristic length scale and δ/U_∞ as time scale, with U_∞ now being the free-stream velocity. The ratio of outer-to-inner length scales is provided by the friction Reynolds number, which is defined as $Re_\tau \equiv \delta U_\tau/\nu$.

1.2.1. NEAR-WALL CYCLE CONTROL

When focusing on control, a large number of studies aim at manipulating the near-wall cycle (NWC) dynamics (for instance, Rathnasingham and Breuer [1997], Tardu [1998], Rathnasingham and Breuer [2003], Bai et al. [2014], Qiao et al. [2017], among others) and this generally leads to a disruption of the turbulence production cycle in the inner region [Orlandi and Jiménez, 1994, Hamilton et al., 1995, Jimenez and Pinelli, 1999]. For engineering systems of practical relevance, friction Reynolds numbers are in the order of $\mathcal{O}\left(10^3\right)$ to $\mathcal{O}\left(10^6\right)$, depending on the application. Inner-layer structures that are mainly responsible for fueling near-wall cycle dynamics decrease in size with increasing Re_τ, and their characteristic frequency increases. The work of Kasagi et al. [2009] presents a clear schematic (reported hereby in Fig. 1.3), illustrating how the characteristic size and frequency changes depending on the application in consideration. By inspection of Fig. 1.3, one can immediately appreciate how, although near-wall cycle structures might

be a suitable control target for low-Reynolds-number application, such as pipelines or automotive, high-speed transportation systems require a degree of control complexity (*i.e.*, speed and miniaturization) that renders the usage of conventional control hardware unfeasible. For this reason, work in the literature has been carried out to explore the usage of micro-electromechanical systems (MEMS, Sheplak et al. [2004]) that can comply with the implementation of a control strategy relying on the employment of MEMS is the inherent need for a fine spatial distribution of sensors and actuators. That is due to the small-scale structures, that characterize the near-wall cycle dynamics, having a spatio-temporal lifespan that is rather short.

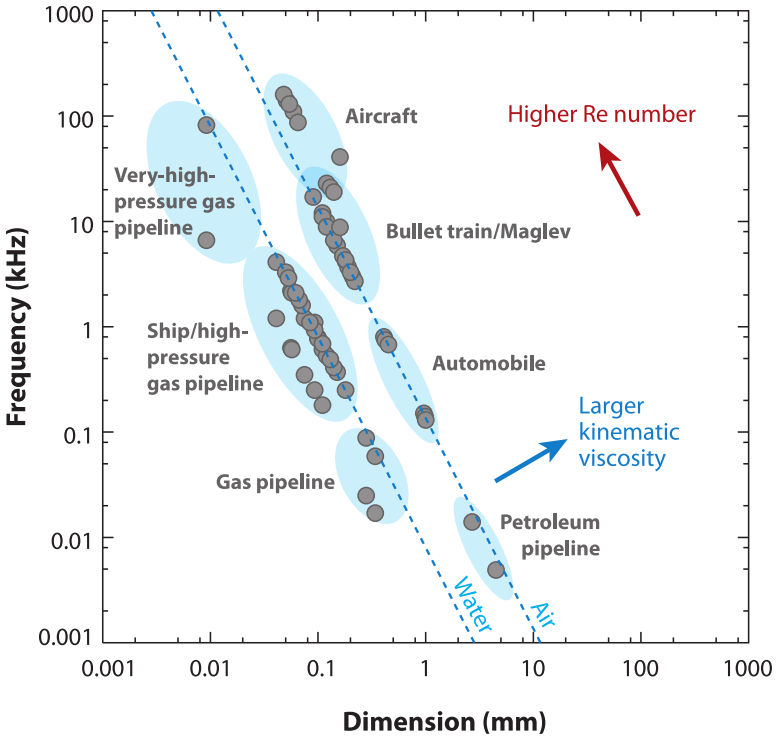

Figure 1.3.: Spatiotemporal scales of coherent structures in the near-wall cycle in engineering applications. Closed circles correspond to a 30 wall-unit length and 0.01 wall-unit frequency in different applications. Taken from Kasagi et al. [2009].

In fact, one can inspect the linear coherence spectrum between near-wall quantities (*e.g.*, streamwise velocity fluctuations) at two distinct streamwise locations. Linear coherence, in this context, can be explained as the frequency-dependent degree of predictability of the flow at the downstream location, given the upstream measurement. Samie et al. [2020], amongst others, perform such an analysis for a turbulent channel flow (TCF) at $Re_\tau \approx 590$. Given the characteristic streamwise wavelength of near-wall structures of $\lambda_x^+ = U_c^+ / f^+ \approx 1000$ (with U_c being the convection velocity and f the fre-

quency), they observed how coherence at this wavelength drops from a value of $\gamma^2_{uu} \to 1$ for streamwise separations of $\Delta x^+ < 100$, to $\gamma^2_{uu} < 0.5$ for $\Delta x^+ = 870$ (with Δx^+ being the inner-scaled streamwise separation between the upstream and downstream measurements stations). This means that, for control to be streamwise persistent, a high amount of streamwise input-output stations would need to be integrated into an aerodynamic surface. In fact, even with a separation of $\Delta x^+ \approx 1000$, the spacing in physical units would be mere tens of millimeters, requiring hundreds, if not thousands of control stations to be installed on, *e.g.*, an aircraft fuselage.

From the available literature, it is apparent that a strategy based on the identification and control of near-wall structures does not scale favorably with Reynolds number, thus leading to the question of what can be a good candidate for control for drag reduction of a ZPG-TBL.

1.2.2. LARGE-SCALE MOTIONS CONTROL

As mentioned above, near-wall scales in a TBL are characterized by a relatively small size and relatively high passage frequency. These structures mostly convect within the inner layer of a TBL, encompassing the near-wall and buffer regions, up to $y/\delta \approx 0.2$. At higher wall-normal locations, more elongated structures start to appear and dominate the spectral energy distribution of the fluctuating velocity signals. These structures are known as *large-scale*, or very-large scale (depending on their size) motions (LSMs and VLSMs, respectively). With longer characteristic time and length scales, they present themselves as a more appealing target for real-time control, compared to near-wall scales.

First evidence of these large-scale structures was first uncovered by Kim and Adrian [1999], who found evidence of uniform momentum zones with a characteristic streamwise wavelength of 12-14 times the radius of the pipe in which they were conducting experiments. They propose a physical model that illustrates how these extended structures result from the concatenation of several hairpin packets, with a characteristic time scale of, roughly, 400 viscous units. In later study, Hutchins and Marusic [2007] studied the development of LSMs in a TBL experiment and show how their length can commonly exceed 20δ and exhibit distinctive spanwise coherence (see Fig. 1.4a). Additionally, these structures exhibit a spanwise-meandering behavior, whereby these structures display a spanwise spatial oscillation with a sinusoidal shape (see Figs. 1.4b,c). In general, LSMs refer to regions of lower velocity induced between the legs of hairpin packets, and regions of higher velocity outside of said packets. Due to the streamwise momentum difference between high- and low-speed zones, large-scale rollers are formed with a downwash and upwash in the zones with a momentum surplus and deficit, respectively [Hutchins and Marusic, 2007].

Although these uniform momentum zones form in the logarithmic region and, in general, LSMs are mostly energetic in said region of the TBL, a modulation effects exists, whereby these structures modulate inner-region dynamics. In other words, beneficially for real-time control purposes, LSMs present a large degree of wall-coherence [Baars et al., 2017], *i.e.*, a measurable imprint on the wall in the form of a low-frequency component. In particular, modulation is a type of scale interaction, whereby the amplitude of the small-scale (in this case, near-wall) fluctuations is continuously proportional to the near-wall footprint of the large-scale velocity fluctuations. In addition to modula-

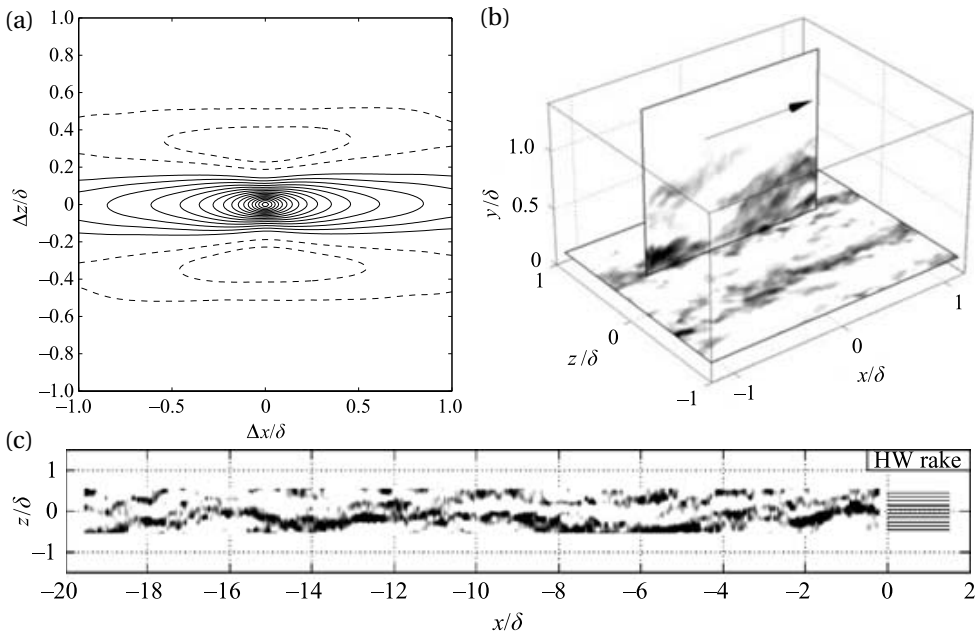

Figure 1.4.: Experimental data visualizing evidence of (V)LSMs in turbulent boundary layers, taken from the work of Hutchins and Marusic [2007]. (a) Two-point correlations of the streamwise velocity fluctuations on a horizontal (xz)-plane calculated at $y/\delta = 0.087$ at $Re_\tau \approx 1100$. (b) Instantaneous PIV snapshot on a visualization combining a horizontal and a vertical plane at $Re_\tau \approx 1100$. (c) Example of a wire-rake signal at $y/\delta = 0.15$ for $Re_\tau \approx 14380$. The x-axis is reconstructed using Taylor's hypothesis and a convection velocity based on the local mean, $U = 15.9\,\mathrm{m/s}$.

tion, which is a non-linear phenomenon, superposition consists of a linear imprint of large-scale fluctuation onto near-wall, inherently small-scale, fluctuations. This results in a large-scale "footprint" being measurable at the wall, which enables the identification of kernels (or *transfer functions*) that can be used to estimate the flow state in the logarithmic region, based on near-wall input quantities [Sasaki et al., 2019]. A controller can therefore be designed to detect (and actuate upon) LSMs with marginal intrusiveness, thanks to the detectable footprint these impart on the near-wall flow.

The energy carried by LSMs increases with Reynolds number, and these structures not only carry the bulk of the turbulence kinetic energy (TKE) in a TBL (up to 45% of it, according to Lee and Sung [2011]), but are also responsible for most of the kinetic energy production mechanisms at high-Re_τ conditions [Smits et al., 2011a]. For TBL flows at $Re_\tau \gtrsim 2000$, they are responsible for the appearance of a secondary peak in the energy spectrogram of stramwise velocity fluctuations, evidence of which has been extensively documented by the turbulence community [Hutchins and Marusic, 2007, Deck et al., 2014, Baars and Marusic, 2019, among others]. For an increasing friction Reynolds number,

Marusic et al. [2021] illustrate how the spectral signature of the near-wall flow sees a increasing contribution by large-scale (*i.e.* low-frequency) structures (see Fig. 1.5). This benefits potential net power savings. This conclusion, however, is in contrast with the results from the work of Gatti and Quadrio [2016] and Gatti et al. [2024], who instead show a decrease in the effectiveness of large-scale control with increasing Reynolds number. Nonetheless, it is interesting to investigate the potential of controlling large-scale motions in real-time by means of local, discrete forcing, instead of by applying a spanwise wall-forcing. In fact, large-scale fluctuations in turbulence quantities induced by the passage of LSMs correlate to skin-friction drag production mechanisms since, as illustrated by Renard and Deck [2016], LSMs carry a major part of the Reynolds shear stress, $\overline{u'v'}$.

From the brief review that was presented above, one can find a large body of literature studying the dynamics of large-scale motions in a ZPG-TBL flow and its relation to skin-friction drag. In general, the two main conclusions are that, at high Reynolds numbers:

1. the flow displays a vast range of scales, and that large-scale motions are increasingly responsible for turbulence kinetic energy (TKE) production as the Reynolds number increases;

2. a large degree of wall-coherence is measurable between the large-scales, mostly inhabiting the logarithmic region, and the near-wall flow. This can be leveraged to build a controller that can interact with large-scale motions, but employing wall-based input quantities only.

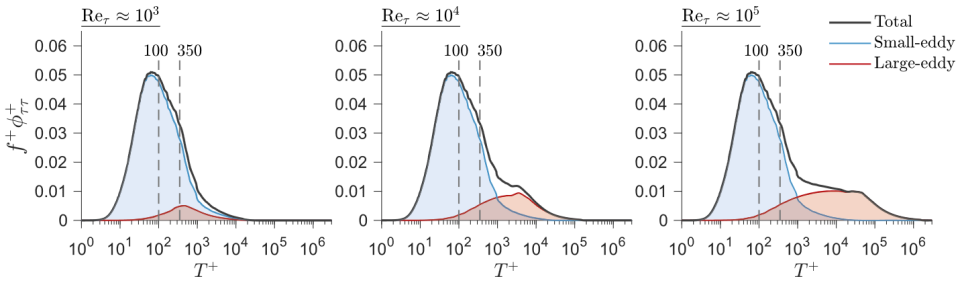

Figure 1.5.: Pre-multiplied spectra of wall-shear stress fluctuations at three values of Re_τ, displaying the contribution of both small and large scales. Taken from Marusic et al. [2021].

From a control perspective, and especially from a perspective of a feasible implementation of real-time control strategy at application-level conditions, large-scale motions form the ideal target for real-time flow manipulation. Their larger length and time scales make them more accessible to conventional control hardware, while their growing contribution to TKE production and near-wall superposition at high-Re_τ makes them a strategically relevant target for control. Various experimental activities are presented in this dissertation that explore various real-time control system architectures. All of these will consider large-scale motions as the prime target for control.

1.3. THE CHALLENGE OF CHOOSING AN INPUT QUANTITY

Up to this point in this dissertation, a general overview has been presented of the requirements underlying the design of a real-time control system and the necessity to identify a control target that is accessible using conventional control hardware (*i.e.* not MEMS). From this point onwards, the focus of this dissertation is going to pivot towards analyzing a control system targeting coherent structures convecting in a TBL flow.

A generic schematic of a (two-dimensional) flow control system is displayed in Fig. 1.6. Here, a TBL flows from left to right in the diagram, grazing over several points of interest on the wall for the definition of a control law. Point $\mathscr{I}$ represents the location of a hypothetical input sensor while, at a downstream distance (s_1), an actuator produces a control output (point $\mathscr{A}$). Point $\mathscr{E}$, located at a further distance (s_2) downstream of the actuator, acts as an error sensor for advanced control laws that will be discussed in a later chapter of this dissertation (Ch. 7). The information relayed from points $\mathscr{I}$ and $\mathscr{E}$ are elaborated in real-time by the controller, which is based on a transfer function ($\mathscr{H}$) that models the physical dynamics of the TBL by (1) estimating the state of the flow at the streamwise location of point $\mathscr{A}$ and (2) incorporating the measurements of point $\mathscr{E}$ for optimization of the control law.

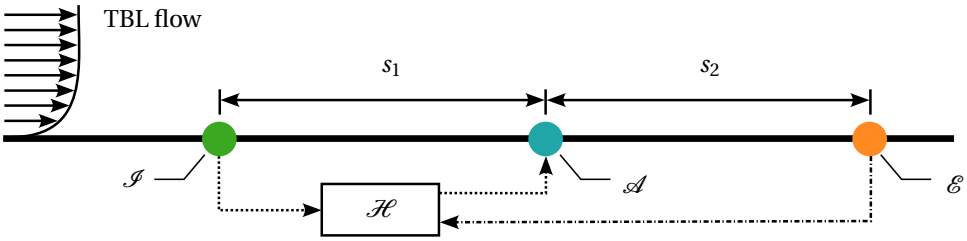

Figure 1.6.: Schematic displaying a generic control system for a TBL flow, whereby targeted features travel with the incoming flow (from left to right).

However, as a first and fundamental step in the definition of a real-time control system, one needs to consider which quantity is going to be considered as the input to the real-time controller (measured at point $\mathscr{I}$ in Fig. 1.6). The remainder of this section is going to be dedicated to reviewing preliminary concepts, requirements and literature enabling the selection of a suitable input quantity.

The main issue relating to the selection of such input quantity is the problem of *observability*. Critical to the design of any control system, this concept was first introduced in the work of Kalman [1963]. In essence, considering a linear *state-space* representation of a dynamic system, such system is said to be observable if, for every possible evolution of the state and control vectors, the current state can be estimated from output information only (*i.e.* the information measured by physical sensors). Although a linear representation might be challenging to define for a dynamic system characterized by strong non-linearity such as a TBL, the concept of observability is one that needs to be carefully considered. In fact, the need for a control system with a low degree of complexity translates, by design, to a sparse input sensor layout, with which limited information can be inferred of the TBL flow, which raises issues in regards to observability. Literature showing

implementation of real-time control strategies in wall-bounded flows shows how maximum observability of off-the-wall velocity fluctuations can be attained by placing the input sensing plane not at the wall ($y = 0$), but rather at an off-the-wall location (*e.g.* Guseva and Jiménez [2022]). However, it must be noted that full three-dimensional and temporal access to the fluid domain is available in a numerical simulation, as is the case for the work of Guseva and Jiménez [2022], as well as most other studies found in the literature on this topic. Instead, in a laboratory context, not only it is practically unfeasible to implement such an input configuration, but it would also be detrimental to the overall drag performance of the system, as sensors located off-the-wall would produce additional drag.

To understand which wall-based quantities best correlate to the passage of LSMs, there are two main factors to consider:

1. **Wall-coherence.** The degree with which an off-the-wall state can be predicted from a wall-based position.

2. **Sensing complexity.** The number and cost of necessary sensors and the ease of integrating the acquisition (and the potentially needed filtering) of the signal in real-time by the controller.

1.3.1. NEAR-WALL FLOW FLUCTUATIONS

Instantaneous fluctuations in wall-shear stress possess a strong correlation with streamwise velocity fluctuations at off-the-wall locations. Given the superposition effect that was mentioned in the above, by which the near-wall flow retains the “footprint" of larger structures convecting at higher wall-normal locations, this wall-based quantity retains a strong correlation with velocity fluctuations induced by LSMs. Thus, this makes it an ideal candidate for the estimation of a large-scale velocity state.

In the literature, considerable work has been conducted on the study of the large-scale superposition of the near-wall flow. For instance, Mathis et al. [2009] illustrate how the structures inhabiting the logarithmic region (*i.e.* LSMs) cause a significant superposition of the scales found in the buffer layer of a TBL flow. They also report how this superposition signature becomes increasingly intense as the Reynolds number increases logarithmically with Re_τ. Based on this strong correlation, Baars et al. [2016] propose a stochastic strategy to couple the near-wall flow to higher wall-normal locations, given the self-similarity that exists between wall-attached eddies of all scales [Baars et al., 2017]. In particular, a universal self-similar scaling of wall-attached eddies exists, comprising eddies having a characteristic size bounded by an inner scale of $\lambda_x/y \approx 14$ and by an outer one of $\lambda_x/\delta \approx 10$. This is in accordance with the Attached Eddy Hypothesis (AEH), a comprehensive review of which can be found in the work of Marusic and Monty [2019]. This is evidence of a self-similar hierarchy of scales across the boundary layer.

1.3.2. WALL-PRESSURE FLUCTUATIONS

Another input quantity that sparks significant interest in being employed as an input quantity for real-time control is wall-pressure fluctuations. In fact, juxtaposed to wall-shear stress measurements, whereby complex sensors are required to accurately mea-

sure it, wall-pressure sensors are characterized by low complexity and low cost, which renders them ideal for widespread deployment.

Studies on wall-pressure fluctuations of turbulent wall-bounded flows have focused on, amidst other aspects, the scaling of the pressure intensity and spectral signature. Scaling trends are a function of the friction Reynolds number, Re_τ. In particular, the works of Farabee and Casarella [1991], Tsuji et al. [2007] and Klewicki et al. [2008] revealed a characteristic inner-spectral peak in the wall-pressure spectra at a frequency of $f_p^+ \approx 0.04$. The amplitude of said peak increases in magnitude with an increase in Re_τ, as does the large-scale energy content. Efforts with direct numerical simulation (DNS) have confirmed these trends [*e.g.*, Jiménez and Hoyas, 2008, Panton et al., 2017, Yu et al., 2022] and illustrated how, when considering spatial spectra, the inner-spectral peak resides at $\lambda_{x,p}^+ \approx 250$ (thus f_p^+ and $\lambda_{x,p}^+$ are related at the peak-scale through a streamwise convection velocity of $U_c^+ \approx 10$).

Relations between velocity structures and wall-pressure events have also been investigated. For instance, Thomas and Bull [1983] revealed characteristic wall-pressure signatures associated with burst-sweep events in a turbulent boundary layer (TBL) flow, which are exclusively confined to the near-wall region. Gibeau and Ghaemi [2021] reported a low but significant scale-dependent linear coherence between wall-pressure (see Fig. 1.7), and streamwise (u) and wall-normal (v) velocity fluctuations in a TBL flow, at low frequencies (in the remainder of our manuscript lower-case quantities denote the fluctuations, while upper case ones signify time-averaged quantities). They ascribed this stochastic coupling to the passage of large-scale motions (LSMs). Recently, the work of Deshpande et al. [2024] assessed the growth of broadband energy in the wall-pressure spectrum by considering how the energy in velocity fluctuations, associated with active (producing turbulence kinetic energy) and inactive motions, scales with Re_τ and how this energy contributes to the energization of the intermediate and large pressure scales. Linking the wall-pressure field to the turbulence dynamics of LSMs is highly relevant for real-time flow control, because LSMs are a feasible target for an experimental implementation of control, as mentioned in § 1.2. Moreover, a larger fraction of the turbulent velocity scales becomes strongly correlated across the wall-normal direction, and leaves a distinct imprint on the dynamics of near-wall turbulence and wall-pressure fluctuations [*e.g.*, Marusic et al., 2010, Tsuji et al., 2015].

1.4. CONTROL LAW DEFINITION

Large-scale control was first pioneered for the control of wall-bounded turbulent flows in the legacy work by Schoppa and Hussain [1998] and did not consider a real-time strategy. They showed that large-scale spanwise velocity forcing could lead to a 50 % reduction in friction drag. However, the relatively low Reynolds number of $Re_\tau \approx 180$ implied that: (1) control was effectively targeting a weak instability as turbulence was only marginally sustained [Canton et al., 2016b,a], and (2) large-scale control at those low values of Re_τ was matching the NWC dynamics 'equally-well'. That is, in the context of practical applications, a large-scale control strategy requires a high-enough Reynolds number for sufficient scale separation to appear. This is conveniently achieved through experimental studies. Recently, predetermined control with large-scale forcing was proven effective at

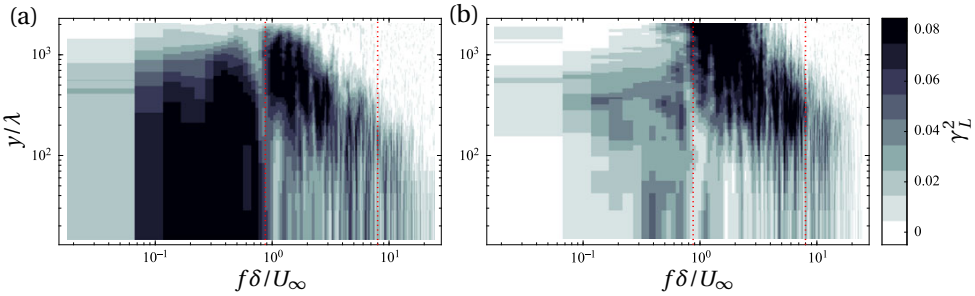

Figure 1.7.: Contour plot showing the variation of the linear coherence between wall-pressure and (a) streamwise and (b) wall-normal velocity fluctuations, as a function of dimensionless frequency, obtained from time-resolved particle image velocimetry data. Taken from Gibeau and Ghaemi [2021].

high Re_τ [Marusic et al., 2021, Deshpande et al., 2022] and the inherent lower-frequency nature of outer scales also renders LSMs a more approachable target than inner scales, when considering real-time implementations. Many more contributions can be found in the literature that implement a control strategy whereby large-scale structures in a TBL are targeted, but only following a pre-determined (*i.e.* open-loop) action. Cheng et al. [2021a], for instance, demonstrate how a considerable friction-drag reduction can be obtained by the periodic blowing action of jet actuators at frequencies characteristic of the passage of LSMs. A similar control configuration was adopted by Yu et al. [2021], whereby the optimal pulsing and relative output phase of each jet in an array was identified by means of genetic optimization.

In general, blowing jets have also been demonstrated to be effective for the active (albeit open-loop control) control of turbulent boundary layers even in a distributed configuration. Distributed microblowing occupies a particular place in the evolution of turbulent boundary-layer control strategies. As reviewed by Kornilov [2015], finely perforated surfaces with uniform microblowing have been shown to consistently reduce skin-friction drag, in some cases by up to 90%, and to delay separation under adverse pressure gradients. The principle lies in weakening near-wall turbulent structures by injecting low-momentum fluid, which reduces shear stresses and alters Reynolds stress distributions. Early works, such as Hwang [2004] and Tillman and Hwang [1999], demonstrated drag reduction in both subsonic and supersonic applications using distributed microblowing, while later experiments [Kornilov and Boiko, 2012, 2014] extended this to flat plates and non-uniform blowing configurations. However, as Kornilov [2015] emphasizes, effectiveness depends critically on geometric parameters such as porosity, orifice arrangement, and uniformity of injection. While distributed microblowing remains a relatively simple and reliable passive/active hybrid method, its limitations—energy cost, sensitivity to uniformity, and scale-dependence—highlight the need for algorithmic approaches that can adaptively optimize control inputs in real time. Thus, in the context of this dissertation, microblowing serves as a motivating case for the development of real-time control algorithms capable of addressing the unsteady, nonlinear dynamics of turbulent boundary layers.

Cheng et al. [2021b] also propose a control strategy based on the utilization of plasma actuators to induce streamwise vortices, which stabilize the motion of large-scale quasi-streamwise vortices induced by large-scale features in the flow. Although some control output do cause skin-friction drag by themselves, such as wall-normal blowing, it is important to be able to decouple the effects the actuator has on the flow from the effects of the control logic. In this regard, it is necessary to compare the response of the TBL to real-time (*i.e.* targeted) actuation to a case where the flow was subjected to fully random control.

In fact, the work presented in this dissertation revolves around the development and implementation of control strategies where the control output is determined in a reactive fashion. In this regard, when choosing a control law for a problem at hand, one needs to consider several factors, relating to the dynamical system at hand, the available hardware for sensing and actuation and the degree of physical modeling embedded within the control law. This last factor, in particular, is of crucial importance when considering real-time overhead management by the controller. In fact, the computational cost for a real-time controller is a function of the degree of physical modeling performed in real-time. For instance, if the modeling were based on a full representation and time-marching of the Navier-Stokes equations (*i.e.* an ultra-white box model, see Fig. 1.8), it would be extremely costly and, realistically, not manageable by conventional real-time processors. Decreasing cost, model predictors can incorporate hybrid analytical-empirical relations, with an increasing dependence on input-output data. A model whose dependence on physical laws decreases, while increasingly being a function of empirical input-output data (black-box), lacks interpretability, with the benefits corresponding to low-overhead computations and (usually) low-memory requirements.

For the present dissertation, one needs to consider that all real-time control efforts have been implemented experimentally in a laboratory setting. Thus, the option of running expensive high-order models was not feasible. Therefore, this work employs techniques pertaining to the categories of grey-box, black-box and model free controller design.

1.4.1. FEEDFORWARD OPPOSITION CONTROL

The array of available control algorithms for control of nonlinear systems is rather long, as can be evinced from the comprehensive review by Brunton and Noack [2015]. However, most require the availability of dense spatio-temporal information, which are usually not accessible when implementing control in an experimental setting in a wind tunnel facility. Even less complex system representation, such as a linear state-space system, would lack the requirement information on local gradients and flow derivatives to fully describe the TBL dynamics. Thus, relatively “simple" control laws need to be defined that can take input-output data into account.

Opposition control is a type of *stabilizing control* [Brunton and Noack, 2015] that was initially applied to turbulent flows in the context of computational investigations. This technique proved rather effective in suppressing turbulent fluctuations and even reducing skin-friction drag [Choi et al., 1994, Guseva and Jiménez, 2022]. This type of control was pioneered experimentally in the works of Rebbeck and Choi [Rebbeck and Choi, 2001, 2006] for the control of NWC dynamics with great success. Their control con-

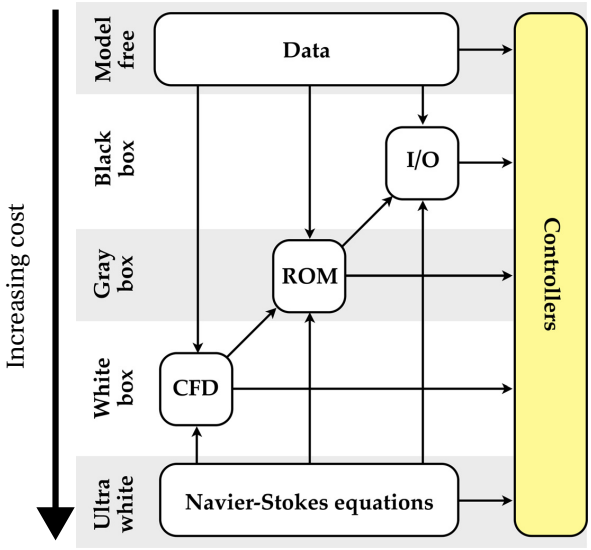

Figure 1.8.: Diagram showing hierarchical model dependence on governing equations, adapted from Brunton and Noack [2015].

figuration was based on measuring inner-region turbulence fluctuations by employing a wall-wire and piston-driven jet as the actuator (see Fig. 1.9). With a hot-wire probe mounted downstream, they could monitor the performance of the control system and verify whether the intensity of near-wall sweeps was actually attenuated.

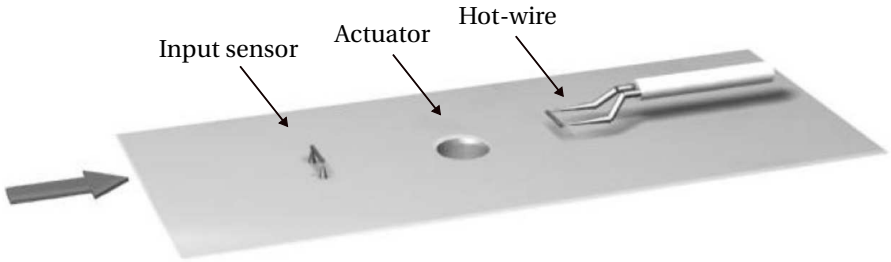

Figure 1.9.: Diagram showing the control architecture for performing opposition control of the near-wall cycle sweeps in a low-Reynolds-number TBL. Adapted from the work of Rebbeck and Choi [2001].

A few years later, Abbassi et al. [2017] demonstrated a selective opposition control system to target LSMs carrying higher streamwise momentum than average, in an attempt to reduce the skin-friction drag induced by large-scale events in a TBL at $Re_\tau \approx 14000$. A spanwise array of jet actuators, together with hot-film input sensors located upstream, counteracted the naturally-occurring drag-producing LSMs. This yielded a reduction of

the intensity of the velocity fluctuations in the logarithmic region, as well as a ~ 3 % reduction in the mean wall-shear stress.

The present work builds upon the approach taken by Abbassi et al. [2017]: the momentum surplus that characterizes high-speed zones is to be counteracted by lower-streamwise-momentum fluid, generated by a wall-normal blowing jet actuator. To minimize the parasitic drag associated with the control system, wall-embedded flush-mounted hardware is required. This constraint leads to an estimation problem of the flow state at a point away from the input sensor when aiming at the manipulation of large-scale structures at their wall-normal location of maximum intensity (*e.g.*, in the geometric center of the logarithmic region). Still, the question remains as to how accurate estimations of the flow state at a location above the actuator can be performed. Abbassi et al. [2017] took Gaussian kernels as transfer functions and convolved those with the input signals. In the present work, we employ a data-driven approach to obtain the input-output relation, namely to relate changes in wall-shear fluctuations to velocity fluctuations in the logarithmic region. Using spectral Linear Stochastic Estimation (LSE) [Tinney et al., 2006, Baars et al., 2016], it was possible to generate such a physics-informed kernel.

1.4.2. CLOSED-LOOP ADAPTIVE CONTROL

Traditional opposition control relies on the prior identification of a transfer function to estimate the flow state that needs to be controlled. Generally, as will emerge from following chapters in this dissertation, such transfer function is identified in a prior step to the deployment of the controller to the plant in consideration. However, the design and deployment of a real-time controller for commercial engineering flow control applications would benefit from adaptability to the performance envelope of the dynamic plant it is applied to (*e.g.* cruise conditions for an airliner). Adaptive control algorithms can be employed, in this context, to (1) automatically identify the system dynamics, and (2) adapt to slowly-varying conditions in the fluid dynamic system. The Filtered-x Least Mean Squares (Fx-LMS) algorithm is one that has proven itself as being applicable to achieve control adaptability, as shown in the literature for both acoustic noise attenuation [Hansen, 2001] and control of convective harmonic flow disturbances [Kotsonis et al., 2013].

A comprehensive review of the Fx-LMS can be found in Hansen [2001], of which a brief summary is provided here. In particular, the Fx-LMS algorithm is an adaptive control strategy that was initially developed for active noise control (*e.g.* noise-cancelling devices [Hansen, 2001]). This algorithm (whose block diagram is presented in Fig. 1.10) essentially operates as a gradient-descent–based optimizer that works towards the minimization of an error signal. Whereas in the case of acoustic noise attenuation the goal would be to minimize the noise in a certain environment, in this work it coincides with the attenuation (or *opposition*) of the turbulence-induced fluctuations at the location of the downstream array of error sensors, located at point $\mathscr{E}$ in Fig. 1.6. This is accomplished with the aid of the real-time identification of two finite impulse response (FIR) kernels: the cancellation path (FIR 2) and the control (FIR 1) kernels. The former is identified in an initial phase of the deployment of the Fx-LMS and models the conditional response of the error signal as a function of the actuator output (plotted in Fig. 2.1c). The latter, instead, is deployed as the primary control kernel, when convolved in real-time with the

input signal (plotted in Fig. 2.1d). A more elaborate description of the algorithm can be found in Hansen [2001]; essentially, the controller identifies the most energetic fluctuations in the flow and actuates upon those.

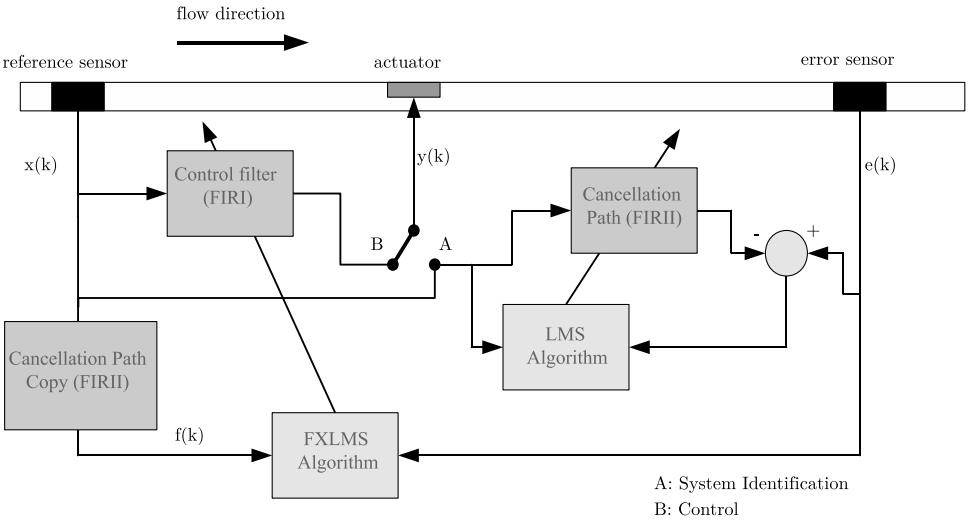

Figure 1.10.: Block diagram of the Fx-LMS algorithm, applied to a flow control problem targeting harmonic convective flow instabilities in a transitional boundary layer [Kotsonis et al., 2013].

1.5. OBJECTIVES OF THIS WORK

The research presented in this dissertation focuses on the experimental investigation of real-time control techniques for skin-friction drag reduction in a ZPG-TBL. Particular focus is devoted to the analysis of the response of the TBL to the action of the controller, both in terms of temporal and spatial statistics. Additionally, a secondary strong focus point of this work is the definition and identification of transfer functions that can accurately represent the state of the boundary layer flow at off-the-wall position from a purely wall-based measurement. For the first time, a control implementation is presented that relies on wall-pressure fluctuations as an input to the real-time controller, after careful considerations of coherence between wall-pressure and off-the-wall velocity fluctuations in a TBL flow.

This thesis is divided into two main parts, the first of which focuses on the physical relation between wall-pressure and off-the-wall velocity fluctuations in a turbulent wall-bounded flow. The objectives of this part are the following:

- to present a reliable methodology to disambiguate between hydrodynamic and acoustics-driven fluctuations in a temporal signal acquired experimentally;
- to analyze the spectral coupling between wall-pressure and off-the-wall velocity fluctuations and its scaling across a wide range of Reynolds numbers.

The second part of the work deals with the design and the development of a real-time control strategy targeting large-scale structures in the TBL to quench low-frequency drag-producing mechanisms. In particular, the objectives were:

- to describe the implementation of a feedfoward real-time controller using instantaneous wall-shear stress fluctuations as the input quantity and to quantify the response of the flow to it in terms of both mean skin-friction drag and integral metrics of wall-shear stress decomposition;
- to report on the deployment of a pioneering real-time control system using wall-pressure, instead of wall-shear, as the input quantity.

Finally, the last part of this thesis focuses on the implementation of an adaptive controller to the problem of the TBL flow. Due to the increased complexity in controller design compared to the feedforward opposition controller, a two step approach is taken for its design.

- First, the controller is deployed to a flow characterized by highly-harmonic disturbances. This step is meant to provide a proof-of-concept for the implementation of the adaptive controller as well as to test its applicability to convective flow disturbances in a turbulent wall-bounded flow.
- Second, once this preliminary testing was completed, the adaptive control law was then deployed to the fully broadband TBL case.

This dissertation is divided into several chapters. Chapter 2 contains the description of the wind tunnel facilities used for carrying out the experimental work contained in this dissertation as well as the measurement techniques. Chapter 3, consequently, first describe the intricacies behind the choice and filtering of the input quantity for real-time control, with Ch. 4 describing the statistical correlation that exists between wall-pressure and off-the-wall velocity fluctuations and the latter analyzing methods to filter noise-contaminated wall-pressure signals. Chapter 5 presents a first implementation of a feedforward controller, based on wall-shear stress as the input quantity, before switching to the use of wall-pressure in the implementation of a similar controller in Ch. 6. Finally, Ch. 7 reports on the implementation of an adaptive control strategy to the TBL flow problem, before concluding this dissertation in Chapter 8.

2

EXPERIMENTAL METHODOLOGY

Science is fun. Science is curiosity. We all have natural curiosity. Science is a process of investigating. It's posing questions and coming up with a method. It's delving in.

Sally Ride (STS-41-G)

The work presented in this dissertation is mostly based on data acquired experimentally. This section contains the presentation of the wind tunnel facilities employed for testing and data collection. In particular, the bulk of the experimental campaigns were conducted at the Delft University of Technology, in the W-Tunnel open-return wind tunnel facility. Additionally, part of this dissertation is based on data collected at the center for International Cooperation for Long-Pipe Experiments (CICLoPE) at the University of Bologna, in Italy. Furthermore, this section contains the presentation of the measurement techniques employed for the characterization and analysis of the flow.

2.1. TURBULENT BOUNDARY LAYER FACILITY

With wall-bounded turbulence flow control receiving growing attention in recent years and it being the exclusive focus of this dissertation, it is necessary to develop the capability to study such flows in the most complete way possible. It can be challenging and costly to recreate application-level conditions in an accurate computational simulation [*e.g.* direct numerical simulations (DNS)], given the enormous volume of resources required. Even experimental approaches are cursed with scaling to high friction Reynolds numbers and Mach numbers matching real flight conditions at altitude. For the present study, the goal was to design an experimental testing facility enabling the study of a ZPG-TBL flow at low-to-moderate values of Re_τ (that can also be reached by DNS simulations).

For a non-cryogenic and non-pressurized facility, there are two options available for generating a TBL at a given friction Reynolds number: (1) having a high freestream velocity and short development length and, vice-versa, (2) having a long development length and a relatively low freestream velocity. The latter is usually the preferred option, as it allows for the flow to have measurable scales, while still attaining the desired friction Reynolds numbers. The low velocity, in fact, generates a relatively thick boundary layer, resulting in the structures within it being relatively easily accessible with standard experimental techniques (*e.g.* particle image velocimetry). Conversely, the latter approach creates a thin boundary layer, rendering experimental data acquisition more challenging, given the higher requirement for spatial resolution of the measurement sensors. For this reason, in this study, a test section is designed with a relatively long streamwise development length, but having a relatively low freestream velocity, following the "long and slow" approach.

This section describes the design and the final layout of the experimental facility, as well as the characterization of the TBL flow generated within it.

2.1.1. FACILITY LAYOUT

Experiments were conducted in the W-tunnel at Delft University of Technology. This facility is an open-loop wind tunnel driven by a centrifugal fan which can attain a maximum velocity of 17 m/s. The flow is accelerated through a contraction having an exit area of 60×60 cm^2 and a contraction ratio of 2.78. A TBL test section was designed and built in September 2021 that consists of two twin segments with a length of 1.8 m each, which are placed downstream of the contraction exit plane. To avoid the propagation of vibrations through the test sections, they are free-standing in isolation, approximately 5 mm downstream of the lips of the contraction. The facility features modular floor plating to allow for insertion of control hardware and instrumentation. The leading edge of both the lower wall has a hyper-elliptical shape, while the upper wall has a knife-edge-shaped leading edge [Narasimha and Prasad, 1994], allowing the top and bottom inflow boundary layers to bleed off. P40 sandpaper is used as a tripping element on all four walls at the inlet of the upstream test section. A Venturi channel was created below the lip of the wind tunnel's contraction to alleviate blockage and prevent separation at the leading edge. Figure 2.1a shows a schematic of the test setup in use, with Figs. 2.1b and 2.1c displaying photographs of the facility in use for testing.

The tunnel's ceiling was made adjustable in height over the full length of the test section in order to modify the streamwise pressure gradient, $\partial p/\partial x$. The ceiling consists of a 4 mm thick polycarbonate plate with a smooth curvature. Through an iterative process, the ceiling was configured for a ZPG and the final ceiling height is displayed in Fig. 2.2a. The ZPG was characterized using two streamwise rows of static pressure taps in the floor (at $z' = \pm 0.20$ m), from which the local pressure coefficient could be inferred as $C_p = 2(P - P_\infty)/(\rho U_\infty^2)$ (with P_∞ being the freestream static pressure and P the mean static pressure at the streamwise station considered; plotted in Fig. 2.2b). For the nominal free-stream velocity of the current study ($U_\infty \approx 15$ m/s), the acceleration parameter $K \equiv (\nu/U_e^2)(\mathrm{d}U_e/\mathrm{d}x)$ [Schultz and Flack, 2007] remained in an acceptable range for a ZPG condition, since $K < 1.6 \cdot 10^{-7}$ (see Fig. 2.2c) for the entire length of the test section. In the definition of K, the velocity at the edge of the boundary layer, U_e, equals U_∞ for this study; its value was inferred from the measured static pressure at the floor by assuming $\partial p/\partial y \approx 0$. Finally, the free-stream turbulence intensity was found to be $\sqrt{\overline{u^2}}/U_\infty \approx 0.15\,\%$ at the primary measurement region (this was inferred using hot-wire anemometry, described later).

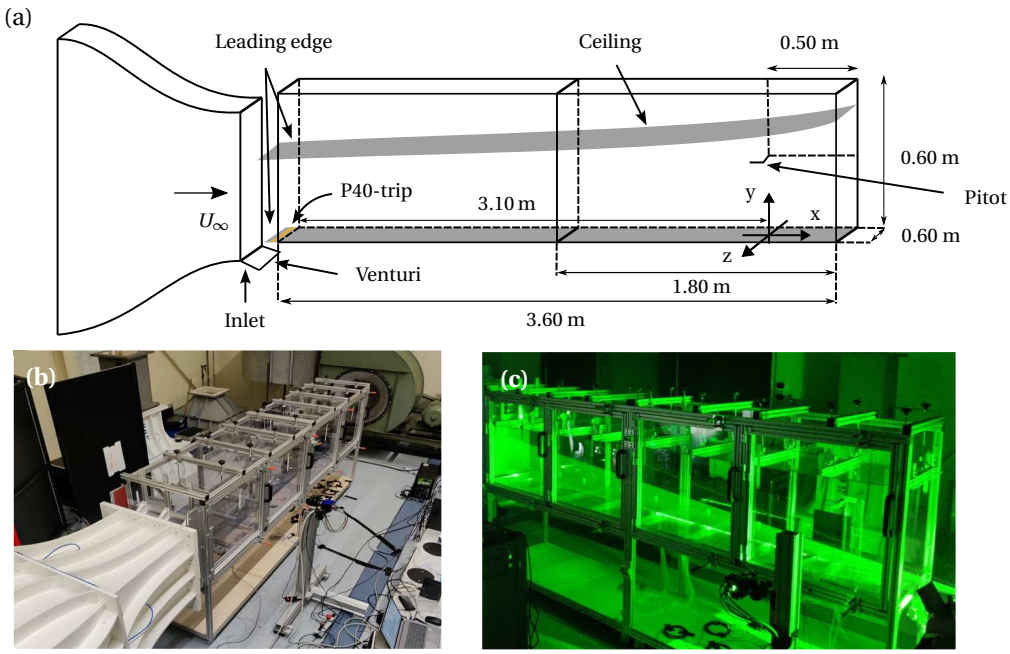

Figure 2.1.: (a) Schematic of the modular TBL test section installed in the W-Tunnel at Delft University of Technology. (b) Photograph of the TBL test section in November 2024. (c) Photograph of the TBL in use during a particle image velocimetry acquisition in May 2022.

A Pitot-static probe is installed on one of the vertical walls of the downstream section, 2.9 m downstream of the trip. The probe allows to infer the freestream velocity at that

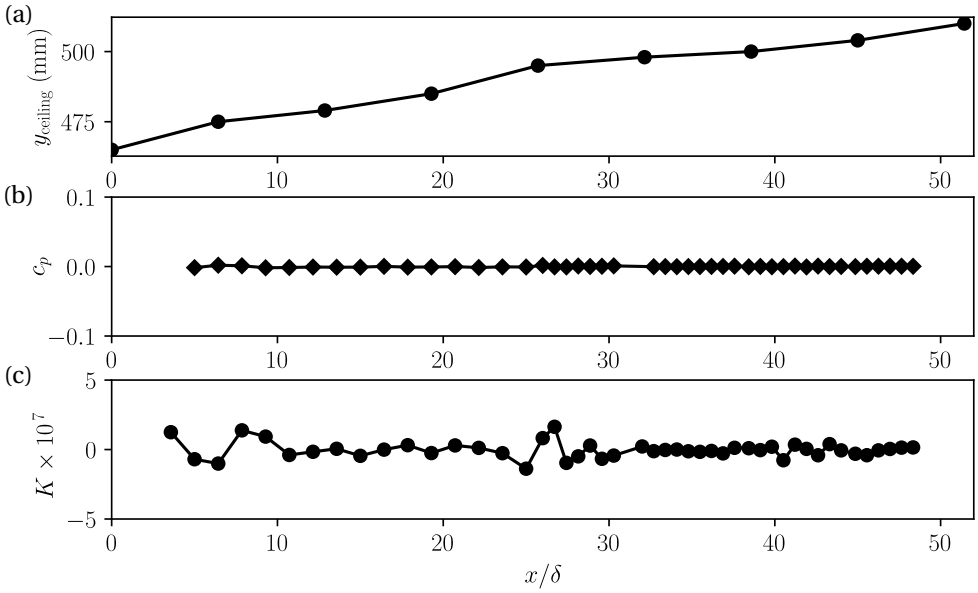

Figure 2.2.: Plots of (a) the ceiling height, (b) the pressure coefficient and (c) the acceleration parameter as a function of downstream distance from the sandpaper trip throughout the TBL test section.

location, which will be used for reference and normalization for all measurements. Additionally, a microphone is mounted at the same streamwise location as the Pitot probe, to measure the freestream acoustic signature of the wind tunnel facility. This consists of a single GRAS 46BE 1/4-in. CCP free-field microphone, with its standard grid-cap replaced by a GRAS RA0020 nosecone. This is intended to reduce stagnation-driven turbulence pressure fluctuations on the otherwise flow-exposed diaphragm.

In the foregoing, data will be presented following the definition of a Cartesian (x, y, z) right-handed coordinate system, also displayed in Fig. 2.1a. Its origin is located on the wall at $x' = 3.10$ m downstream of the sandpaper trip and in the spanwise center of the test section. The x-axis is aligned with the freestream velocity and positive in the downstream direction. The y-axis indicates the wall-normal direction and is positive when pointing away from the wall. Finally, the z-axis completes the right-handed system and indicates the spanwise coordinate.

2.1.2. TURBULENT BOUNDARY LAYER CHARACTERISTICS

A characterization of the uncontrolled TBL flow at the primary measurement location of $x = 0$ is here reported, based on first- and second-order statistics computed from hot-wire data. The freestream velocity for all measurement conducted in this experimental facility was set at $U_\infty = 15$ m/s. Figure 2.3a presents profiles of both the streamwise mean velocity and turbulence kinetic energy (TKE). A set of canonical boundary layer parameters was inferred through a composite fit procedure on the mean velocity pro-

file [Chauhan et al., 2009], with logarithmic layer constants of $\kappa = 0.38$ and $B = 4.7$. Parameters are reported in Table 2.1, where characterization data is included for two more freestream velocity values, namely $U_\infty = 5\,\mathrm{m/s}$ and $U_\infty = 10\,\mathrm{m/s}$. Here, θ is the momentum thickness and the viscous length scale is denoted with the symbol $l^* \equiv \nu/U_\tau$.

U_∞ (m/s)	δ (mm)	θ (mm)	Re_θ	U_τ (m/s)	Re_τ	l^* (µm)	t^* (µs)
5	72.6	6.89	2 248	0.204	988	72.35	346.67
10	71.3	6.86	4 572	0.377	1 783	39.37	102.65
15	69.9	6.83	6 930	0.480	2 227	30.54	61.79

Table 2.1.: Experimental parameters of the baseline TBL flow in the W-Tunnel facility at $x = 0$, for $U_\infty = 15\,\mathrm{m/s}$.

Since the measured streamwise TKE is subject to a well-known attenuation of small-scale energy, associated with the the finite resolution of hot-wire sensing length ($l^+ \approx 41$) [Hutchins et al., 2009], the missing energy can be accounted for as seen from the corrected measurement profile [following Smits et al., 2011b]. For both the mean velocity and corrected streamwise TKE profiles, the measurement data compare well to those of a DNS of channel flow [Lee and Moser, 2015] in the inner region and at a comparable value of Re_τ. This provides reassurance of a representative baseline flow.

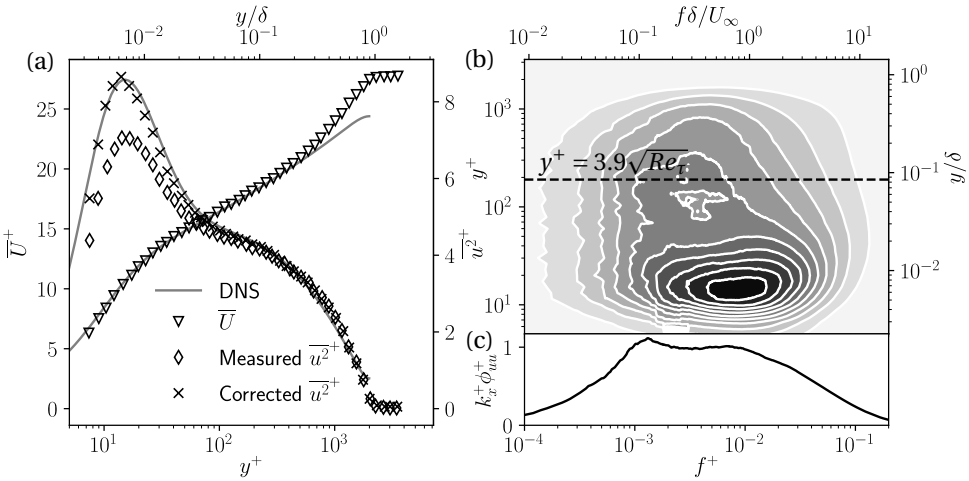

Figure 2.3.: (a) Wall-normal profiles of the mean streamwise velocity and streamwise TKE, based on hot-wire data and compared to DNS data of channel flow at $Re_\tau = 2000$ [Lee and Moser, 2015]. TKE corrected for attenuation due to sensor resolution [Smits et al., 2011b]. (b) Premultiplied energy spectrogram of the streamwise velocity; filled iso-contours correspond to magnitudes of 0.2:0.2:2.2. (c) Energy spectrum of the streamwise velocity fluctuations in the geometric center of the logarithmic region, $y_L^+ = 3.9\sqrt{Re_\tau}$.

For spectral analyses of the velocity $u(y,t)$, the one-sided spectrum is considered here

as $\phi_{uu}(y;f) = 2\langle U(y;f)U^*(y;f)\rangle$, where $U(y;f) = \mathscr{F}\left[u(y,t)\right]$ is the temporal fast Fourier Transform (FFT). Here, the angular brackets $\langle\cdot\rangle$ denote ensemble-averaging and the superscript "$*$" indicates the complex conjugate. Ensembles of $N = 2^{17}$ samples were subject to a Hanning windowing procedure, and resulted in a spectral resolution of $\mathrm{d}f = 0.39$ Hz. In addition, a 50 % overlap was implemented to yield a total of 120 ensembles for averaging. Energy spectra throughout the TBL flow are premultiplied, and are presented as an inner-scaled spectrogram, $f^+\phi^+_{uu}(y;f)$, in Fig. 2.3b. Being the primary location of interest for studying LSMs within the logarithmic region, Fig. 2.3c presents the broadband spectrum of streamwise velocity fluctuations in the geometric center of the logarithmic region, at $y^+ = 3.9\sqrt{Re_\tau} = 190$. The Reynolds number being relatively low does not yet allow for a noticeable outer-spectral peak to appear, but the inner-spectral peak is apparent at $(y^+;f^+) \approx (15;0.01)$. Moreover, a significant scale separation is present between energetic motions in the outer layer (say at $f^+ \lesssim 10^{-3}$) and the NWC peak at $f^+ \approx 10^{-2}$. The uncontrolled TBL conditions reported in Table 2.1 and Fig. 2.3 represent the baseline (uncontrolled) case, to which the controlled flow will be compared in subsequent chapters.

2.2. CICLoPE LONG-PIPE FACILITY

The results presented in Ch. 3 and Ch. 4 was carried outside of Delft University of Technology. Measurements were also performed in the long-pipe facility at the center for International Cooperation in Long-Pipe Experiments. The facility is managed by the CIRI Aerospace Institute of the University of Bologna and is located in a former military and industrial bunker built in the 1930s in Predappio, Italy. The underground location is ideal for minimizing external acoustic noise sources, but requires constant climate control to keep humidity and temperature at relatively low and acceptable values. This, however, ensures stable environmental conditions for testing.

The long-pipe facility itself consists of a closed-loop wind tunnel (see Fig. 2.4a): a 111.15 m-long circular pipe (Fig. 2.4b) with a radius of $R = D/2 = 0.4505$ m. The pipe is divided into 22 independent segments, originally intended for ease of assembly and transportation, which culminate into the test section (Fig. 2.4c), located at the downstream end of the facility. Each segment is 5.05 m long and realized in carbon fiber. The facility is equipped with a heat exchanger to ensure the temperature set for testing does not oscillate more than $1°C$. The flow is driven by two coaxial fans, spinning in opposite directions, through turning vanes and a contraction, which ensures laminar flow is present at the upstream end of the long pipe. The flow is not tripped, ensuring transition only occurs "naturally". The flow in the test section (nominally at 105.9 m = 117.5D downstream of the pipe inlet) can be considered fully developed. The high friction Reynolds number that can attained in the facility (up to $Re_\tau \approx 50\,000$) allows the study of a turbulent wall-bounded flow, although by design not ZPG, at Reynolds numbers nearing application-level orders of magnitude. Its design allows the for the full range of scales to be measurable with standard flow measurement equipment (*e.g.* off-the-shelf miniature hot-wire probes) at the test section location. Further details relating to the design and the characterization of the turbulent flow in the facility are described in the literature [Bellani and Talamelli, 2016, Örlü et al., 2017a].

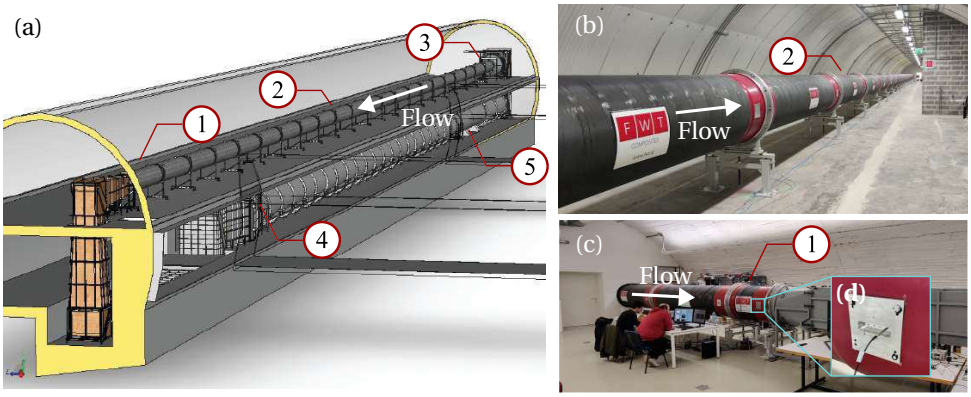

Figure 2.4.: (a) Schematic of the CICLoPE laboratory in Predappio, Italy. Courtesy of Fiorini [2017]. Labels refer to (1) the test section, (2) the carbon fiber pipe, (3) the contraction, (4) the heat exchanger and (5) the fan. (b) Photograph of the upper segment of the long-pipe facility. (c) Photograph of the test section of the long-pipe facility, with (d) showing one of the four modular plugs allowing access to the flow on the final segment of the long-pipe.

At each of the 22 carbon fiber segments, the pipe flow can be accessed at four locations by means of modular wall plugs, equally distributed in the azimuthal directions (Fig. 2.4d). For the experiments reported in this work, friction Reynolds numbers were in the range $4\,794 \lesssim Re_\tau \lesssim 47\,015$ (with corresponding center-line velocities of $3.837\,\mathrm{m/s} \leq U_{CL} \leq 44.60\,\mathrm{m/s}$).

2.3. MEASUREMENT TECHNIQUES

Throughout this work, several different measurement techniques are employed to measure specific properties and patterns of the turbulent flows in consideration. The foregoing contains a brief review of the main flow measurement techniques and their integration into the experimental facilities, although a more elaborate description of those can be found in the literature.

2.3.1. WALL-PRESSURE MEASUREMENTS

In this work, measurements of wall-pressure were carried out for two main objectives. The first was to study and understand the scaling of the statistical coupling between streamwise velocity and wall-pressure fluctuations, which is mainly treated in Ch. 3 and Ch. 4. The second one, building on top of the knowledge acquired with the first, was to employ wall-pressure fluctuation as the quantity for real-time control of a TBL for skin-friction drag reduction (Ch. 5 and Ch. 6). While the bulk of the data acquired to tend to the first objective was collected in the CICLoPE facility, real-time control experiments were only performed at Delft University of Technology. However, the integration

of the pressure sensors for measuring instantaneous fluctuations of hydrodynamic wall-pressure was equal for both cases.

Regarding the measurement of instantaneous pressure fluctuations in turbulent flows, some of the literature investigates the statistics of pressure fluctuations at off-the-wall stations (*e.g.* the work of Tsuji et al. [2007], among others), using Preston-tube-like probes to traverse the boundary layer and generate statistics along the wall-normal direction. This technique, however, is intrusive for application in real-time flow control, as (1) the sting holding the probe acts as an additional source of drag and alters the flow around it and (2) limits the accessibility of flow diagnostic techniques assessing the performance of the control system. Thus, measurements of fluctuating wall-pressure need to be collected at the wall.

THE CHALLENGES OF MEASURING WALL-PRESSURE FLUCTUATIONS

Carrying out unsteady wall-pressure measurement is a challenging feat for a plethora of reasons, which will be discussed in the foregoing. These range from spatial resolution issues to contamination of the signals by non-hydrodynamic sources, which all undermine the reliability of wall-pressure measurements.

For the selection of an appropriate sensor, one needs to keep in mind that the intensity of wall-pressure fluctuations is comparable to the intensity of typical acoustic emissions in a wind tunnel facility. In particular, Farabee and Casarella [1991] and Klewicki et al. [2008] report semi-empirical relations that relate the intensity of wall-pressure fluctuations to mean wall-shear stress, whereby $\mathcal{O}(p'_w) = \mathcal{O}(p'_{\text{acoustic}})$. Furthermore, given the requirement of time-resolved wall-pressure measurements and the pressure intensity (p') that characterizes wall-pressure fluctuations, microphones were selected as the sensors of choice. This, however, results in the need to discriminate, in post-processing, hydrodynamic from acoustics-driven pressure-information, to only retain the former. Filtering techniques were applied to accomplish this that are going to be presented in Ch. 3.

Also, for spatially-resolved hydrodynamic wall-pressure measurements, the requirement is that the sensing "length" of the sensor to be relatively small (in viscous units). Namely, the work of Gravante et al. [1998a] proves that full spatial resolution in wall-pressure measurements can only be achieved if the sensing diameter (d_p) is such that $d_p^+ < 27$. A larger sensing diameter would result in the microphone effectively acting as a hardware-induced spatial filter. In fact, any commercially available off-the-shelf pressure microphone features a sensing diaphragm whose size is considerably larger than the requirement set by Gravante. In order to artificially increase the spatial resolution of the microphone, therefore, it is necessary to integrate the device into a wall-embedded cavity. The cavity communicates with the grazing turbulent flow by means of a circular pinhole orifice (see Fig. 2.5a). Technically, the required of increased spatial resolution is not fundamental for the control experiments presented in this work. In fact, LSMs exhibit a characteristic size that does not necessarily require the microphone to be embedded in a pinhole cavity. However, the setup mentioned above was developed also for the acquisition of fully-resolved spectra.

Given the integration in a pinhole cavity, the geometry of the cavity itself results in it

acting as a Helmholtz resonator, with a resonance frequency f_r at:

$$f_r = \frac{a_0}{2\pi}\sqrt{\frac{S}{V_c(t_p + t^*) + P}}. \tag{2.1}$$

Here, a_0 is the speed of sound, $S = \pi d_p^2/4$ is the area of the pinhole orifice, $V_c = \pi D_c^2 L/4$ is the volume of the cavity and t_p is the thickness of the neck (see Fig. 2.5a and Tab. 2.2 for details). Finally, t^* and P are end-corrections that account for the added mass that needs to be displaced as a result of fluid oscillating not only within the neck, but also in the vicinity of the orifice. Different definitions for end corrections can be found in the work of, *e.g.*, Chanaud [1994]. For wall-pressure measurements, the cavity needs to be designed such that resonance occurs at a frequency that is considerably higher than the frequency-band of interest.

Parameter	d_p	D_c	t_p	L	f_r
W-Tunnel	0.4 mm	6.0 mm	1.0 mm	2.0 mm	2 725 Hz
CICLoPE	0.3 mm	4.6 mm	1.1 mm	0.2 mm	4 350 Hz

Table 2.2.: Table reporting the geometric parameters defining the pinhole cavities integrated in the W-Tunnel and in CICLoPE, as well as the corresponding resonance frequency.

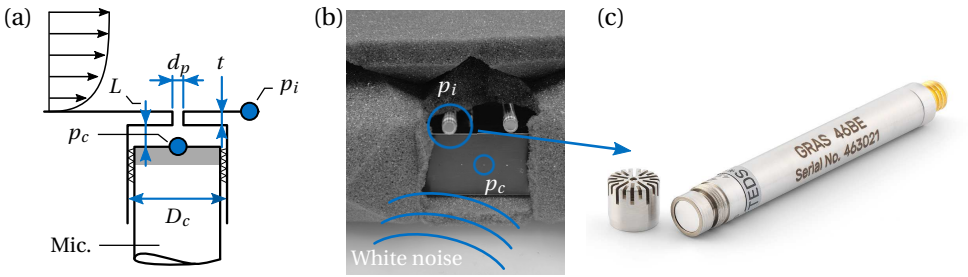

Figure 2.5.: (a) Schematic of the pinhole cavity for wall-pressure measurements. (b) Photograph of the characterization experiment of the pinhole cavity resonance frequency in the anechoic facility at Delft University of Technology. (c) Photograph of the GRAS 46BE microphone, employed for wall-pressure measurements. Courtesy of GRAS.

Correcting for the Helmholtz resonance is straightforward once the pinhole cavity has been characterized. Whereas Eq. 2.1 provides a design frequency f_r, it does not consider how the amplitude and phase of the measured pressure in the cavity relates to the inlet pressure. This can be modelled through a single input/output impulse transfer function, $H_r(f)$, by considering the mass-spring-damper system-equivalent of the resonator. Its

gain and phase are formulated as

$$|H_r(f)| = \left[\left(1-\left(\frac{f}{f_r}\right)^2\right)^2 + \left(\frac{2\xi f}{f_r}\right)^2\right]^{-0.5}, \text{ and } \varphi\left[H_r(f)\right] = -\tan^{-1}\left[\frac{2\xi\left(f/f_r\right)}{1-\left(f/f_r\right)^2}\right]. \quad (2.2)$$

Here, ξ is a damping constant and f_r is the resonance frequency. Both ξ and f_r require empirical characterization through a calibration experiment, using acoustic pressure excitation. This experiment was conducted in a facility that is anechoic at frequencies above 200 Hz [Merino-Martínez et al., 2020]. White noise was produced with a Bose® speaker and was recorded simultaneously by a reference microphone (measuring the excitation pressure at the inlet, p_i) and the cavity microphone (p_c), see Fig. 2.5b. Signals were acquired for a length of $T_a = 150$ s at a sample rate of $f_s = 51.2$ kHz. With the signal recordings, the experimental characterization of the Helmholtz resonator can be obtained by dividing the input-output cross-spectrum by the input spectrum:

$$H_r^{\text{exp}} = \frac{\langle P_c(f) P_i(f)\rangle}{\langle P_i(f) P_i^*(f)\rangle}. \quad (2.3)$$

The Bode plot of an exemplary kernel (obtained for the pinhole used for testing in the W-Tunnel at Delft University of Technology) is displayed in Figs. 2.6a and 2.6b. The former plot illustrates the gain of the resonator's transfer function, showing a clear peak around the resonance frequency. In parallel, the latter plot shows the spectral phase variation, indicating a reversal at the location of the resonance frequency. The highlighted area in both graphs illustrates the region where the resonance phenomenon impacts wall-pressure statistics in spectral space.

Finally, the correction of wall-pressure spectra for cavity resonance assumes the form of a simple division, in the frequency domain, of the raw spectrum by the square of the gain of the transfer kernel, as $\phi_{pp} = \phi_{pp,\text{r}}/|H_L|^2$ (here, ϕ_{pp} and $\phi_{pp,\text{r}}$ are the corrected and the raw wall-pressure spectra, respectively).

UNSTEADY WALL-PRESSURE SENSORS CHARACTERISTICS

The sensors consist of GRAS 46BE 1/4-in. free-field CCP microphones (see Fig. 2.5c), having a nominal sensitivity of 3.6 mV/Pa. These have an adequate dynamic range to capture the pressure fluctuations of interest (35 to 160 dB, with a reference pressure of $p_{\text{ref}} = 20\,\mu$Pa) with an accuracy of ±1 dB within the range of 10 Hz to 40 kHz. These microphones have an adequate dynamic range to capture the full range of wall-pressure fluctuations [Tsuji et al., 2007, Klewicki et al., 2008].

2.3.2. HOT-WIRE ANEMOMETRY

Hot-wire anemometry (HWA) is a minimally-intrusive measurement technique that allows for time-resolved measurements of velocity fluctuations. In the present work, HWA is used extensively not only as a flow diagnostic technique for assessing the performance of the control system downstream of the actuator location, but also for embodying the role of error sensor in the context of an adaptive control strategy (see Ch. 7).

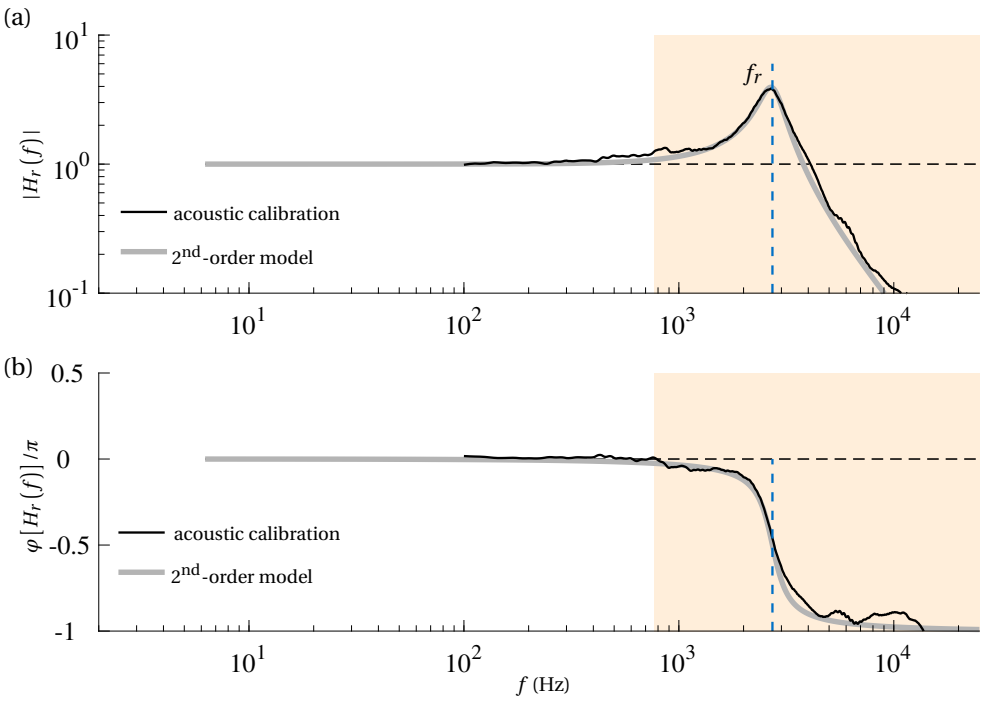

Figure 2.6.: (a) Gain and (b) phase of the pinhole cavity's transfer kernel. A comparison is made between the kernel obtained from the acoustic calibration, and a model kernel fitted to these empirical results. The filled area indicates the frequency range at which the resonance phenomenon starts to impact the statistics of wall-pressure.

The relatively small hot-wire probe sensing size allows for collecting data at precise spatial locations, if coupled with an accurate traversing system. Given the small wire diameter, the thermal inertia of the sensor is minimized while, at the same, maximizing spatial resolution. In fact, the wire can measure velocity fluctuations whose intensity is only a small fraction of the freestream velocity thanks to its fast frequency response. In this project, the hot-wire probe was operated in conjunction with a constant temperature anemometer (CTA). This type of velocity sensors relies on a Wheatstone bridge for operations, whereby one of the four resistances composing the bridge is now replaced by the hot-wire probe. A comprehensive review of this technique can be found in the work of Lomas [1985].

Calibration of the hot-wire probe is required to relate the output-voltage signal to a velocity measurement, namely $U = f(E)$, where E is the voltage. The calibration function f takes the form of King's Law, relating known velocity measurements to known voltages measured by the CTA bridge. Given the sensitivity of the hot-wire probe to temperature variations in the wind tunnel facility, constant monitoring of this quantity is

required. In the W-Tunnel, temperature drifts exist, although marginal over the course of a standard acquisition run. In the CICLoPE laboratory, temperature is constantly controlled by means of a heat exchanger, as explained in §2.2. On top of this, measurement time-series were corrected for temperature drift following the procedure outlined by Hultmark and Smits [2010].

HOT-WIRE CONFIGURATION

For the bulk of the experimental campaigns conducted at Delft University of Technology, a TSI IFA-300 CTA bridge was used, which features automatic overheat ratio adjustment. The hot-wire probe itself was a standard Dantec 55P15 boundary layer probe (see Fig. 2.7c), with a nominal wire diameter of $d_{HW} = 5\mu m$ and length of $l_{HW} = 1.25\,mm$, yielding a wire aspect ratio of $l_{HW}/d_{HW} = 250$. Data were sampled at a rate of $f_s = 51.2\,kHz$ using a 24-bit A/D conversion. The hot-wire was calibrated in-situ by fitting King's Law to 17 points of increasing velocity. The velocity probe was sting-mounted (see Fig. 2.7a) onto a Zaber X-LRQ-E traversing system, comprising two stages, allowing for traversing in two directions: the streamwise and wall-normal ones. With a step accuracy of 10 µm (smaller than 0.3 viscous units for the TBL flow in consideration), the precision of traversing is enough to capture both the outer, as well as the inner, flow dynamics, where the wall-normal gradient of the streamwise velocity component is the strongest.

For measurements in CICLoPE facility, the same type of boundary layer probe was operated in conjunction with a Dantec 90C10 CTA bridge. On top of single-probe HWA measurements, employed to measure time-series of the streamwise velocity component, dual-wire (or x-wire) probe probe measurements were carried out as well. This allowed for the accurate measurement of the wall-normal velocity fluctuations. The length and diameter of both wires in the x-wire probe (Dantec 55P61, see Fig. 2.7d) are equal to the ones of the single boundary layer probe's. In CICLoPE, hot-wire probes were calibrated *ex-situ* by employing a planar calibration jet. The single-wire probe was calibrated by fitting a 5^{th}-order polynomial function to 11 points of increasing velocity to obtain the calibration curve $U = f(E)$. For the calibration of the x-wire, instead, seven velocity settings and thirteen angular positions were set to generate a two-dimensional look-up table [Burattini and Antonia, 2004]. This relates the two velocity components to the voltage measured by each of the two wires: $(U_1, U_2) = f(E_1, E_2)$. Both the single and x-wire probes were sting-mounted into the pipe flow facility at a fixed wall-normal position (within the logarithmic region of the flow, see Ch. 4 and Fig. 2.7b for additional details).

UNCERTAINTY QUANTIFICATION

The uncertainty in the hot-wire measurements was computed following the procedure of Smith et al. [2018], whereby the uncertainty of the measurement is not defined by the raw number of samples acquired, but rather by the number of uncorrelated (or *effective*) samples in the dataset. In case of time-varying data, such as time-series data, two samples are said to be uncorrelated if they occur over a time interval that is greater than the integral time scale (T_i). In particular, T_i can be defined as:

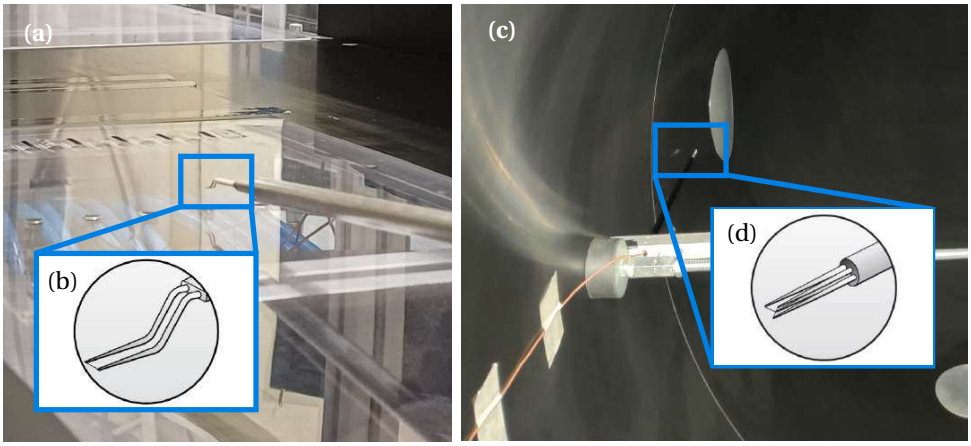

Figure 2.7.: (a) Photograph of the single-wire Dantec 55P15 [schematic shown in (c)] sting-mounted in the W-Tunnel facility. (b) Photograph of the x-wire Dantec 55P61 [schematic shown in (d)], mounted in the CICLoPE long-pipe facility at a fixed wall-normal location.

$$T_i = \int_0^\infty R(\tau)\mathrm{d}\tau\,, \tag{2.4}$$

with $R(\tau)$ being the autocorrelation function of the time series. Once the integral scale is known, one can divide the total length of the signal by T_i, to find the number of effective samples in the time series. Given the extremely broadband nature of a turbulent signal, the effective number of samples (N_s) required for statistical convergence has a lower bound in the number of required turnovers of the lowest frequency of interest. Once that is established, then the uncertainty for first and second-order statistics can be computed following Eqs. 2.5 and 2.6, respectively:

$$\varepsilon_{\overline{u}} = \frac{\sigma_u}{\sqrt{N_s}}\,, \tag{2.5}$$

$$\varepsilon_{\sigma_u} = \frac{\sigma_u}{\sqrt{2(N_s-1)}}\,, \tag{2.6}$$

with $\sigma_u = \overline{u'}$ being the standard deviation of the velocity time-series.

The application of this procedure for data collected in the W-Tunnel results in uncertainties in the estimation of the average velocity and standard deviation (at $y^+ \approx 15$, where turbulence fluctuations are the most intense) of 0.26 % and 1.02 %, respectively.

2.3.3. PARTICLE IMAGE VELOCIMETRY

Particle image velocimetry (PIV) is a non-intrusive optical technique that allows for the measurement of two and three-dimensional velocity fields. Although a much more extensive review of the technique can be found in the work of Raffel et al. [2018], this sec-

tion introduces some of the main concepts and configurations that will be exploited in this work. For the work presented in this dissertation, PIV acquisitions were only performed in the W-Tunnel at Delft University of Technology.

This technique is based on the tracking of particle clusters across the field of view of the imaging sensor between two frames in one image pair, separated by a small time interval, Δt. Particles (here having a diameter of $\approx 1\,\mu$m and being generated from the atomization of a water-glycol mixture by a SAFEX 2010+ for machine) need to be illuminated by an intense light source, such that the light scattered by the particles can be captured by the sensor on the camera. For planar two-dimensional two-component (2D2C) acquisitions typical of this work, the light source takes the form of a Quantel Evergreen 200 Nd:YAG double-pulse laser. The collimated laser light is expanded into a sheet with a thickness of $\delta z \approx 1\,$mm. The camera-mounted optics required for imaging need to account for both the diffraction of the scattered light and the required depth of field to ensure that that all particles within the laser sheet and the field of view are in focus. Given the low-speed acquisition setup, the acquisition frequency is set to $f_{\text{PIV}} = 15\,$Hz, resulting in consecutive image pairs being statistically uncorrelated. Imaging equipment in this work consisted of up to three LaVision sCMOS cameras. These are low-speed, 16-bit, double-shutter cameras, with a sensor size of $2\,560 \times 2\,160\,\text{px}^2$ and pixel pitch of $6.5\,\mu$m. Cameras were fitted with fixed-focal-length Nikkor lenses, whose focal lengths and f-stop values varied depending on the corresponding acquisition (see Chs. 5, 6 and 7).

For statistical convergence, a suitable number of images has to be determined, as a function of the maximum requirement for uncertainty set by the measurements. Equations 2.5 and 2.6 can be employed for this matter, with the only difference in that the effective number of samples (N_s) is now directly the number of image pairs to acquire, given the null statistical correlation between consecutive pairs. Given the highest standard deviation of streamwise velocity can be found at the inner-peak location of $y^+ \approx 15$ and that it equals $\overline{u^2}^+ = 8.1 \therefore \sigma_u = 1.38\,$m/s, 3000 image pairs are required to bring the uncertainty for both first and second-order statistics below our acceptable threshold of $\approx 3\%$. Calibration of the acquisition equipment was performed *in-situ* by fitting a polynomial model to a grid of equally-spaced points on a two-dimensional calibration target.

In this work, two main imaging planes were selected for PIV acquisitions. In particular, data were collected on wall-normal (xy), as well as on wall-parallel (xz) planes. The former allows for precise measurements of both the full dynamics of the boundary layer (referred to as "wide-field measurements" in the foregoing) in the wall-normal direction (from the wall up to the far wake) and accurate measurements of the near-wall flow (the "near-wall" measurements), also allowing for direct computation of the wall-shear stress (τ_w). Processing was performed with the aid of LaVision DaVis 10.2, which is a commercial software package allowing for multi-pass processing operations. In particular, for wide-field wall-normal and wall-parallel acquisitions, an initial pass with an interrogation window having size of $48 \times 48\,\text{px}^2$ was performed, followed by a final pass with a window having size of $24 \times 24\,\text{px}^2$. The overlap length was set to 50% of the window size, resulting in a final vector pitch of one vector every 12 pixels. Instead, for near-wall measurements, a Langrangian particle tracking method was preferred (see § 5.7.1). The vector pitch in physical units is, of course, dependent on the spatial arrangement of the

cameras and, thus, it will be reported for each analysis in the corresponding chapter of this dissertation.

MEASUREMENT CONFIGURATION

Hereby we introduce the measurement setup (in terms of hardware placement) for the planar PIV acquisitions. Figure 2.8 displays the hardware configuration for the two types of acquisitions that have been performed in the context of this work in Delft University of Technology: on the xy and xz-planes (streamwise–wall-normal and streamwise–wall-parallel planes, respectively). For both types of acquisitions, the laser sheet was introduced in the test section from the downstream end of the facility. The laser sheet was aligned with either plane of interest by rotating the cylinder lenses in the sheet-forming optics by 90 degrees.

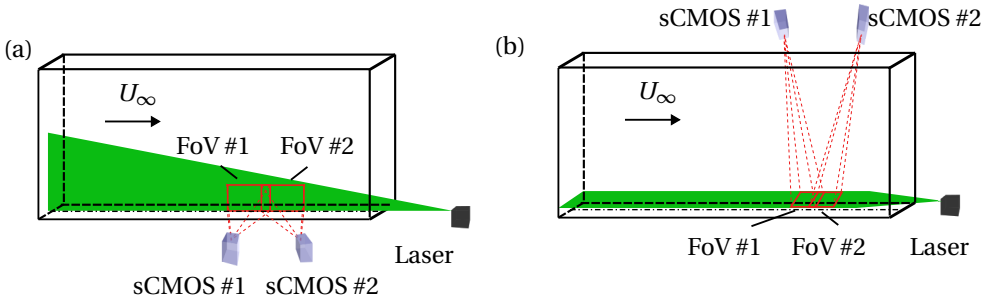

Figure 2.8.: (a) Schematic of the hardware configuration for planar 2D2C PIV acquisition in the W-Tunnel in Delft University of Technology on the xy-plane (wall-normal), featuring two sCMOS cameras. (b) Schematic of the hardware configuration for planar 2D2C PIV acquisition in the W-Tunnel in Delft University of Technology on the xz-plane (wall-parallel), featuring two sCMOS cameras.

Usually, PIV acquisitions have been performed with two sCMOS cameras in order to extend the field of view of the acquisition and enhance the statistics in the streamwise direction (apart for the results presented in Ch. 7, where three cameras were used). The fields of view (FOVs) of each camera overlap over a short extent to ensure continuity in the statistics and for ease of calibration and post-processing. For acquisitions on the xy-plane, the two cameras were mounted on a tripod structure on the side of the wind tunnel facility (Fig. 2.8a), while for wall-parallel PIV measurements they were mounted on the ceiling of the facility while pointing downwards to the wall (Fig. 2.8b).

UNCERTAINTY QUANTIFICATION

For PIV measurements, uncertainty on the computed velocity vector can be calculated locally. The work of Sciacchitano [2019] provides a comprehensive review of the several error sources that can affect PIV measurements and, consequently, methods for computing the uncertainty of said acquisitions. The statistical uncertainty related to the number

of frames (which can be computed using the same equations presented above for the uncertainty in HWA measurements) was computed to be 1.2% for the mean and 0.7% for the standard devtion of streamwise velocity at the location of the inner-spectral peak. Additionally, PIV acquisitions suffer from uncertainty caused by asymmetries in the correlation between interrogation windows. For this work, said uncertainty was computed to be at most 1%.

2.3.4. OIL FILM INTERFEROMETRY

Oil film interferometry (OFI) is a precise and localized measurement technique, allowing for the direct measurement of wall-shear stress. The working principle of OFI (summarized in the schametic in Fig. 2.9a) is the stretching of a thin layer of fluid of known viscosity under the influence of wall-shear stress. The fluid is deposited on a light-reflecting wall in the form of a drop. As the flow stretches the drop into a thin film, the light emitted from a source at a known wavelength (λ_{light}) is reflected on the surface of the drop and on the reflective wall underneath it. The resulting interference between these two wave fronts results in a pattern consisting of alternating bright and dark fringes on the surface of the drop (see Fig. 2.9c). The mean wall-shear stretches the drop in the streamwise direction, and the wavelength of bright-dark pattern developed under the influence of shear gradually increases with time (see Fig. 2.9b), and the rate of increase of said wavelength can be related to the skin-friction.

A more comprehensive review of this experimental technique can be found in the publications of Squire [1961] and Tanner and Blows [1976]. For this work, the local nature of OFI enables the measurement of shear stress at specific locations along the wall, providing crucial insights into localized flow dynamics of the TBL flow under the influence of control, enhancing the accuracy of turbulence characterization. In fact, OFI is particularly useful in complex experimental setups where precise measurement of wall shear stress is critical, while being too complex to obtain from other experimental techniques.

OFI CONFIGURATION

The bulk of the OFI measurements in this work were conducted in the context of Ch. 6. Here, OFI measurements were performed at 30 locations on the wall downstream of the actuator array and at three streamwise stations: $x/\delta = \{2,3,4\}$. Droplets were positioned at spanwise stations lying both directly downstream of a jet actuator as well as in between them. Xiamter PMX-200 silicone fluid with a viscosity of $\mu_{\text{oil}} = 100\,\text{cSt}$ was employed. Given the need to accurately monitor the viscosity of the oil and to correct for temperature (and, thus, viscosity) drifts in post-processing, four type-K thermocouples were used for monitoring the temperature in the freestream flow, on the underside of the wall-plate and on the side walls of the test section. A Nikkon D7500 camera with a Nikkor 135 mm lens was employed in time-lapse mode to capture 100 images of the oil droplets developing on the wall under the influence of the wall-shear at intervals of 10 s (Fig. 2.1c displays the evolution of the drop at three time instants). This camera has a sensor size of $5\,595 \times 3\,738\,\text{px}^2$, with a pixel pitch of $4.2\,\mu\text{m}$. The camera was mounted onto a fixed tripod structure and tilted to achieve a $\approx 45°$ viewing angle onto the oil droplet. Illumination was provided by a sodium-based light, with a characteristic

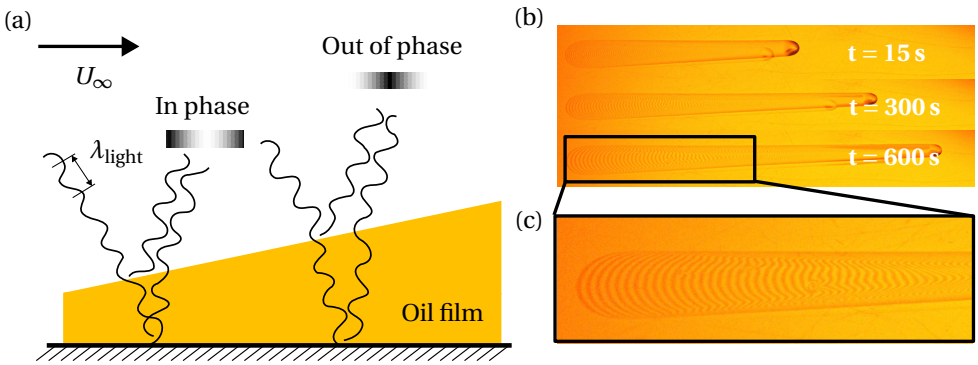

Figure 2.9.: (a) Schematic of the working principle of the OFI measurement technique, showing the incoming and reflected light waves. (b) Photographs displaying the development of a single oil droplet at three different time instants, during a measurement in the W-Tunnel in Delft University of Technology. (c) Detail of the of the pattern forming on the thin oil sheet consisting of bright-dark fringes.

wavelength of $\lambda_{light} = 589$ nm. Image processing was performed by computing a linear fit to the increasing fringe separation as a function of time [Gluzman et al., 2022].

UNCERTAINTY QUANTIFICATION

Uncertainties in oil film measurements stem from several different factors, most of which are attributable to the physical measurement setup. The variation of oil viscosity with temperature needs to be carefully characterized in order to avoid significant error propagation in post-processing. Additionally, the viewing angle of the camera also needs to be carefully measured. Rezaeiravesh et al. [2018] characterizes the several error sources that can affect OFI measurements. Error propagation was performed in this work, and the uncertainty was measured to be 2.5%.

II

WALL-PRESSURE SENSING AND FILTERING

3

WALL-PRESSURE FILTERING

Focus on the journey, not on arriving at a certain destination.

Chris Hadfield (ISS Expedition 35)

Measuring hydrodynamic pressure fluctuations in a turbulent flow experimentally is a challenging task as the signal is often contaminated by other interfering sources; most importantly by acoustic noise. This chapter analyses three different noise-removal techniques: proper orthogonal decomposition (POD), harmonic POD (hPOD), and conditional spectral analysis (CSA). The reported techniques are presented with decreasing degree of required user-input. The aim of applying these techniques is to isolate hydrodynamic wall-pressure fluctuations, which co-exist with acoustic-induced pressure fluctuations within the raw pressure time series. The effectiveness of the filtering approach is presented first by considering a set of synthetic signal designed considering a sparse array of five different microphones capturing wall-pressure fluctuations of a turbulent pipe flow.

Parts of this chapter are published in:

- L. Lazzarini, G. Dacome, G. Bellani, W. J. Baars, A. Talamelli (2025) Wall pressure filtering using spectral and modal analysis. **In preparation**.

3.1. INTRODUCTION

The scaling of turbulent wall-pressure fluctuations is a topic of significant interest, both for advancing the fundamental understanding of turbulent wall-bounded flows and for various engineering applications, such as flow control. This is most significant at spectral bands where hydrodynamic near-wall pressure fluctuations and acoustic-driven phenomena are active.

The main problem with utilizing wall-pressure as the input quantity to a real-time flow control system in an experimental setting is the contamination caused by external noise sources. In fact, the intensity of hydrodynamic turbulence-induced wall-pressure fluctuations is of a similar order of magnitude as the pressure fluctuations induced by acoustic waves generated by the operation of a wind tunnel facility [Farabee and Casarella, 1991, Tsuji et al., 2007, Klewicki et al., 2008]. This calls for the development, both for real-time operations and for post-processing requirements, of techniques that allows for disambiguation of acoustic-driven from turbulence-driven fluctuations. In particular, noise-filtering relies on the identification of spatio-temporal modes that correlate to the characteristic signature of the acoustic-driven pressure fluctuations. This procedure can either be accomplished via modal decomposition of spatio-temporal wall-pressure signals, or by following conditional spectral filtering, as will be reviewed in the foregoing.

POD-based methods are highly versatile and have been proven to be highly effective in identifying coherent structure in experimental datasets. There are two commonly known formulations of POD: “Lumley’s POD", also known as conventional POD [Lumley, 1967], and “Harmonic POD" (hPOD) [Payne and Lumley, 1967, Leib et al., 1984]. The former has been introduced to the turbulence community in the 1960s, with seminal reviews of this technique provided by Tutkun and George [2017] and Podvin and Fraigneau [2017]. The conventional approach is preferred when temporal resolution overcomes the spatial one; such a condition is typically met while performing experiments where time-resolved acquisitions are employed. However, combining harmonic analysis with classical POD is certainly not a new idea [Payne and Lumley, 1967, Leib et al., 1984]. Due to its efficiency and straightforward implementation, the discrete Fourier transform is the preferred approach to perform harmonic analysis on homogeneous, stationary, or periodic signals. The literature [Aubry et al., 1988, Baars and Tinney, 2014, Towne et al., 2018, Tinney et al., 2019] contains numerous examples of the POD technique being applied to both spatial and time-resolved data in turbulent flows. However, care must be taken while interpreting POD modes with regard to physical structures. Inevitably, modal decomposition requires the user to select the proper POD modes for reconstructing a turbulence signal. In POD, the modes are ranked by energy content, with the first few modes typically capturing the largest scales or most energetic features of the flow. However, high-energy modes do not always coincide with specific flow structures, especially in a broadband turbulent flow. They often represent coherent features that can span multiple physical phenomena. Consequently, interpreting these modes as physical structures requires caution, especially when dealing with complex flows or interactions, such as in wall-bounded turbulence or flows dominated by large coherent structures, such as (V)LSMs.

In addition to modal techniques, which rely on the user selecting the modes of interest, various noise-removal methods have been developed to enhance the quality of data ob-

tained from turbulent flows, without the need to 'interfere' with the filtering operation. Among these, spectral subtraction methods [Lauchle and Daniels, 1987, Horne, 1989] have been employed to remove both acoustic and vibration contamination from unsteady surface pressure measurements of turbulent pipe flow. Conditional spectral analysis, used by Bonness and Jenkins Jr [2012] was generalized by Richardson et al. [2023] for an arbitrary number of contaminant-input and contaminated output signals.

In this chapter, the effects of applying the described filtering techniques to extract physical information are explored. Such quantities are practically a robust input for a real-time control system aimed at modifying wall-bounded turbulence [Baars et al., 2024]. The goal of the present study is to demonstrate an application of the filtering techniques mentioned above to a dataset mimicking an acquisition where hydrodynamic wall-pressure fluctuations were measured with sparsely distributed sensors. These will be correlated with velocity to build a unique data set coming from wall-bounded turbulent flows at high Reynolds number at the CICLoPE laboratory (see Ch. 4).

3.2. METHODOLOGY

Here, the fundamentals are presented of the conventional POD, the hPOD and spectral decomposition techniques, that offers a complementary framework for analyzing complex systems by decomposing the data into principal components. To validate the effectiveness of these filtering procedures, a synthetic signal was generated comprising multiple sinusoidal components with added Gaussian noise, simulating the 5 different microphones that were employed during wind tunnel testing (see Ch. 4). The signal composition allows for an analysis of each method's ability to extract the underlying sinusoidal components and perform noise removal. Conventional and harmonic POD will be applied following the terminology of Tinney et al. [2020], whereas the spectral subtraction methodology is based on the work of Richardson et al. [2023].

3.2.1. SPARSE SENSOR AND DEFINITIONS

A generic configuration of sparsely located sensors is presented in Fig.3.1. In wind tunnel testing, time-resolved sensor acquisition focuses on capturing dynamic data with high temporal resolution, often from sensors (such as pressure transducers or microphones) that record unsteady phenomena. These sensors $(S_1 \dots S_n)$ are often sparsely placed at locations $(x_1, y_1) \dots (x_n, y_n)$ to balance data resolution, cost and physical restrictions of the facility. Sparse sensor placement is particularly important in large wind tunnels, where covering the entire test section with sensors is usually impractical. Instead, key regions of interest are usually equipped with sensors to ensure meaningful and high-quality data acquisition. The ability to combine and process the signals from these sparsely located, time-resolved sensors is crucial to obtain clean, usable data (P_i). Using techniques like POD, hPOD or spectral analysis allows researchers to differentiate between real aerodynamic effects and the noise (ξ_i) introduced by the wind tunnel environment.

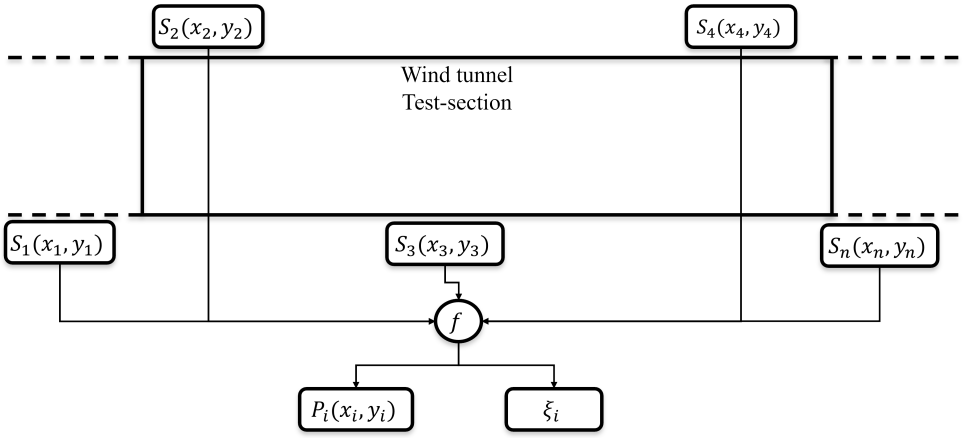

Figure 3.1.: Generic sparse sensors configuration in wind tunnels, $S_1 \dots S_n$ represents the sensors, $x_1 \dots x_n$ and $y_1 \dots y_n$ are perspectively the coordinate of each sensor location, f correspond to the filter applied, P_i represents the filtered signal, ξ_i represents the noise isolated by the filtering operation.

3.2.2. TESTING ON A SYNTHETIC SIGNAL

A synthetic signal generator was implemented to create artificial signals that can be employed to test the filtering procedures before their applications on the actual sparse measurements of wall-pressure fluctuations from a wind tunnel facility (CICLoPE, see Ch. 4). In wind tunnel experiments, the greatest contaminant is acoustic noise produced by the operation of the facility itself. In particular, four unsteady wall-pressure sensors were employed whose signal contains both the quantity of interest as well as the contaminant. Additionally, a fifth sensor was considered, that only measured the contaminant signal. In case of pressure measurements, facility acoustic noise, caused by the operation of the fan and mechanical vibrations of the tunnel, propagates at the speed of sound, while maintaining high coherence at the locations of all five sensors employed. Turbulence-induced hydrodynamic wall-pressure fluctuations, instead, given the length scales of typical wall-pressure structures, retain very low correlation when convecting with the mean fluid velocity.

Given these characteristics, the synthetic signal simulates the acoustic noise by incorporating two arbitrary high-amplitude tones (at $f = 90$ Hz and at $f = 190$ Hz). Turbulence, instead, is modeled as broadband white noise in the band $10\,\text{Hz} < f < 2\,500\,\text{Hz}$ (see Fig.3.2). The four wall-pressure sensors are fed a signal resulting from the linear superposition of the two components (acoustic and turbulence-induced), with the amplitude of the acoustic tones being ≈ 50 times higher than the background turbulence-induced noise. The centerline microphone, instead, by design, does not measure wall-pressure fluctuations, but only records acoustic noise.

By simulating such conditions, one can evaluate the effectiveness of the filtering techniques, such as POD, harmonic POD, or spectral analysis, to ensure that the final processed signal is free of undesired noise sources. Successfully filtering out these com-

ponents allows for an accurate representation of the desired flow information, ensuring more reliable data.

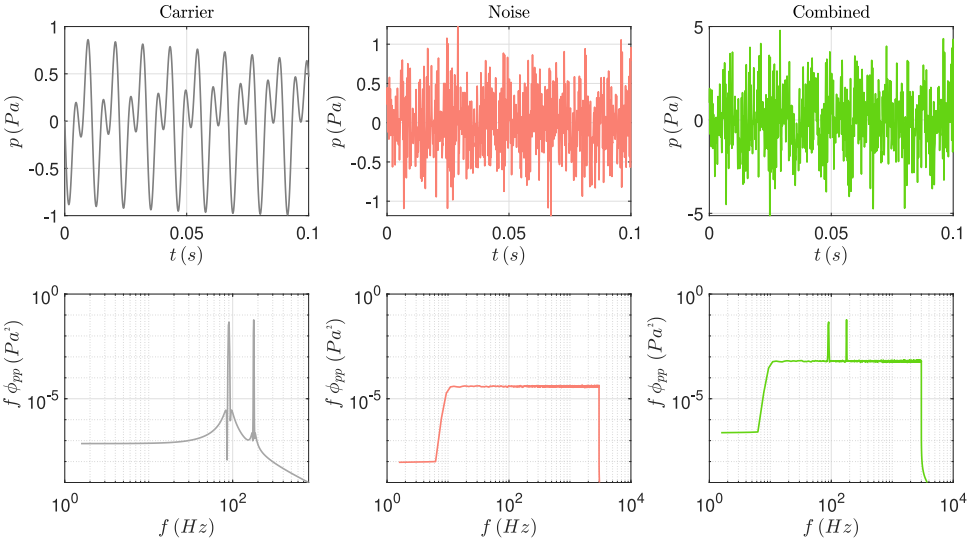

Figure 3.2.: Synthetic signal generator, the six plot shows the time-series along with the power spectral density of the signal at each steps: The carrier, Noise and the combination of the two are presented from left to right.

3.3. FILTERING WITH CLASSICAL PROPER ORTHOGONAL DECOMPOSITION

POD calls for the definition of a kernel constructed by Hilbert-Schmidt's theory of integral equations with symmetric kernels. The general form for this kernel (R) is written as follows:

$$R(\mathbf{x},\mathbf{x}') = \langle p(\mathbf{x},t)\, p^*(\mathbf{x}',t)\rangle\,, \tag{3.1}$$

where t is time and p is the unknown sought-after signal. Here, brackets $\langle\rangle$ denote ensemble averaging, $\mathbf{x}$ is a three-dimensional spatial vector, and $*$ denote the complex conjugate. As the classical POD decomposition does not capture inherent phase-shifts in the data, a preliminary step in the filtering must be performed. In particular, all signals must be temporally aligned, such that their relative phase is null. Whether the choice is made to apply scalar or vector form of the technique will have a deep effect on both the size of the kernel and the number of component it is constructed. The integral eigenvalue problem thus becomes:

$$\int_0^L R(\mathbf{x},\mathbf{x}')\phi^{(n)}(\mathbf{x}')d\mathbf{x}' = \lambda^{(n)}\phi^{(n)}(\mathbf{x}'), \tag{3.2}$$

from which eigenvalues (λ) and eigenfunctions (ϕ) are obtained (L is the extent of the physical domain). It is clear from the formulation above that there is a unique kernel

for each solution, thus implying that there is a unique (ϕ) for each mode. To generate a reduced order model, one must create the expansion coefficients by projecting the raw data onto the 'eigen modes':

$$a^{(n)}(t) = \int_0^L p(\mathbf{x}, t)\phi^{(n)}(\mathbf{x})\, d\mathbf{x}. \tag{3.3}$$

Modes are both orthogonal and time varying. Once decomposition is performed, data can be reconstructed as (denoted as p_f for a lower-order reconstruction):

$$p_f(\mathbf{x}, t) = \sum_{n=\{1\ldots5\}} a^{(n)}(t)\phi^{(n)}(\mathbf{x}). \tag{3.4}$$

The sum is performed over selected POD modes. If all modes are to be retained in the reconstruction of the reduced-order model, the original signal will be obtained.

An application of classical spatial POD will be presented here using a synthetic signals to prove the effectiveness of the algorithm. POD eigenmodes as function of mode number and sensor are depicted in Fig. 3.3, where modes 2, 3, 4 and 5 contain significant information related to the signal, while mode 1 seem to be constant and inactive at every sensor. Figure 3.5a depicts the pre-multiplied power spectral densities of the denoised (blue) and original (green) signals. Upon inspection of the plots, one can immediately perceive how the tonal peaks of the synthetic signal are attenuated almost completely with respect to the original signal, while the broadband noise appears unaltered.

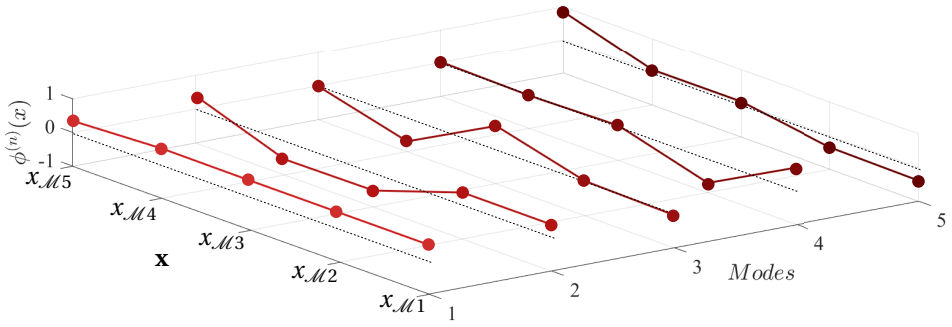

Figure 3.3.: Spatial modes $\phi^{(n)}(x)$ plotted as a function of mode number, n, and considered sensors.

3.4. FILTERING WITH HARMONIC PROPER ORTHOGONAL DECOMPOSITION

Applying a spectral-based kernel to tackle the POD eigenvalue problem resembles solving Eq.(3.2). In each scenario, the formulations condense any stationary, periodic, or homogeneous field direction (in space or time) into a collection of harmonic modes. The new kernel ($\check{R}$) will then be defined as follows:

$$\check{R}(\mathbf{x},\mathbf{x}';f) = \frac{1}{2\pi}\int_{-\infty}^{+\infty} \langle p(\mathbf{x},t)p^*(\mathbf{x}',t+\tau)\rangle e^{-i2\pi f\tau}\,d\tau\,, \tag{3.5}$$

with τ being the temporal variable and f the frequency. Such kernel can be used to solve the eigenvalue problem:

$$\int_0^L \check{R}(\mathbf{x},\mathbf{x}';f)\check{\phi}^{(n)}(\mathbf{x}';f)\,d\mathbf{x}' = \lambda^{(n)}(f)\check{\phi}^{(n)}(\mathbf{x};f). \tag{3.6}$$

The random orthogonal expansion coefficients are then obtained as follows:

$$\check{A}^{(n)}(f) = \int_0^L \widetilde{P}(\mathbf{x};f)\check{\phi}^{(n)*}(\mathbf{x};f)\,d\mathbf{x}. \tag{3.7}$$

The dataset is then reconstructed on a per-frequency basis, following the same procedure as for classical POD. Here, of course, one does not reconstruct the original time series, but its complex Fourier transform:

$$\widetilde{P}_f(\mathbf{x};f) = \sum_{n=\{1\ldots5\}} \check{A}^{(n)}(f)\check{\phi}^{(n)}(\mathbf{x};f). \tag{3.8}$$

The application of hPOD to a set of five synthetic signals demonstrated effective signal decomposition and filtering. An analysis was performed by examining the dominant mode as a function of sensor position and frequency, revealing key insights into the behavior of the signals. To further validate the effectiveness of hPOD, pre-multiplied power spectral densities were compared between the original synthetic signals and the hPOD-filtered output (see Fig. 3.5b). This comparison highlighted a successful attenuation of two significant tonal peaks by 98.1% and 94.9%, respectively, indicating a reduction in unwanted frequency components. Notably, only the first mode, which is highlighted in the figure 3.4, was discarded during the reconstruction process to achieve a noise-free signal, highlighting the precision of hPOD in targeting specific frequency contributions while preserving the integrity of the signal.

3.5. FILTERING WITH CONDITIONAL SPECTRAL ANALYSIS

Conditional spectra analysis is helpful when dealing with several noise sources and sensors. Richardson et al. [2023] proposed such a technique to remove facility noise adopting a multiple-input, multiple-output approach. Here, the same methodology is implemented, only considering four contaminant signals.

Assume a linear relationship between a complex column vector of s measured partially coherent input contamination signal $\widetilde{C} = \mathscr{F}(c)$, where $\mathscr{F}$ is defined as the Fourier transform of the contamination signals (c) expressed as time series, and a corrupted column vector of q output signals $\widetilde{D} = \mathscr{F}(d)$. The input contamination signals are individually filtered using an unknown complex matrix $H \in \mathbb{C}^{q\times s}$ (with $q = 1$ being the number of output signals and $s = 5$ the number of spatially-coherent input signals) and superimposed with the desired, yet unknown, considered signals $\widetilde{P} = \mathscr{F}(p)$. The values of H are assumed not to be correlated with C and produce contaminated pressure signals D. The model is given by:

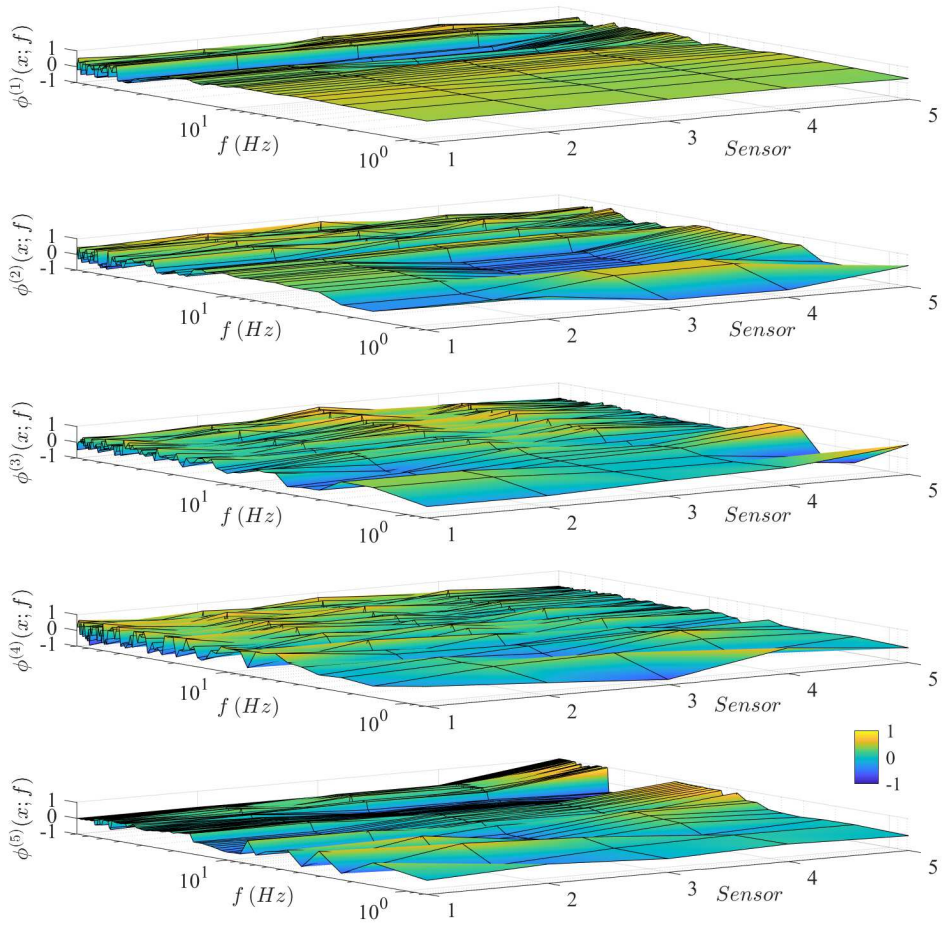

Figure 3.4.: Real part of spatial modes $\phi^{(n)}(\mathbf{x};f)$, $n = 1:5$, plotted as a function of frequency and sensors considered.

$$\underset{q\times 1}{D} = \underset{q\times s}{H}\,\underset{s\times 1}{C} + \underset{q\times 1}{P}, \tag{3.9}$$

which illustrates how the total (measured) signal is actually the linear combination between the unknown quantity of interest and some contaminant inputs. Multiplying by the complex conjugate transpose C^*, computing the spectral densities and considering that C and P are uncorrelated:

$$\underset{q\times s}{G_{cd}} = \underset{q\times s}{H}\,\underset{s\times s}{G_{c_k c_l}}. \tag{3.10}$$

The matrices G_{cd} and $G_{c_k c_l}$ represent, respectively, the cross-spectral densities be-

tween inputs and outputs and the auto-spectral densities of the inputs. The previous equation can be solved by matrix inversion provided that $G_{c_k c_l}$ is not singular:

$$H = G_{cd} G_{c_k c_l}^{-1}. \tag{3.11}$$

The final goal is to obtain the cross-spectral densities of the raw pressure signals, so P can be isolated:

$$\underset{q\times s}{P} = \underset{q\times 1}{D} - \underset{q\times s}{H}\,\underset{s\times 1}{C} \tag{3.12}$$

$$G_{p_k p_l} = G_{d_k d_l} - G_{cd} H^* - H G_{dc} + G_{cd} G_{c_k c_l}^{-1} G_{c_k c_l} H^* \tag{3.13}$$

$$= G_{d_k d_l} - H G_{dc} \tag{3.14}$$

$$= G_{d_k d_l} - G_{cd} G_{c_k c_l}^{-1} G_{dc}. \tag{3.15}$$

The diagonal and off-diagonal terms of $G_{p_k p_l}$ provide the denoised auto-spectral densities and cross-spectral densities, respectively. Figure 3.5c demonstrates the impact of the CSA filter on five synthetic signals. One served as the unknown pressure signal, while the other four acted as contamination sources. The pre-multiplied power spectral densities of the raw (green line) and de-noised (orange line) signals are displayed. The two peaks are clearly identified and attenuated: the second peak is fully filtered, while the first peak remains with an almost negligible intensity, as highlighted in the inset.

The application of three different filtering techniques: POD, hPOD, and CSA, to retain hydrodynamic fluctuations in synthetic signals with tonal peaks at 90 Hz and 190 Hz demonstrated that all techniques effectively detected and filtered out the tonal peaks. However, CSA partially retained the low-frequency peak (2.2%), while hPOD retained only 1.9% and 6.1% of the two tonal peaks, respectively. The effectiveness of the filtering methods was evaluated by the capacity to reconstruct the original signal, with reconstruction quality quantified through the integral of the pre-multiplied power spectra. All techniques achieved high-quality results, with reconstruction levels exceeding 90% of the original noise-free signal.

Figure 3.5d illustrates the differences between the pre-multiplied power spectral densities of the original synthetic signal (SS) and three filtering techniques, with each curve offset by two units to improve clarity. Instead of evaluating the overall reconstruction accuracy using integral differences between the SS and filtered signals, the focus here is on the normalized results, emphasizing the frequency content of the filtered signal. This approach allows us to identify local deviations or imperfections in the filtering process. The figure shows that both POD and hPOD effectively capture the original behavior of the synthetic signal, whereas CSA struggles to match the SS values, likely due to the low SNR of the synthetic data. Although POD and hPOD deliver more accurate reconstructions, they require careful mode selection to achieve optimal results. In contrast, CSA, despite its lower reconstruction accuracy—potentially due to the sparse configuration used—offers a simpler approach, as it does not require detailed consideration of mode shapes during processing.

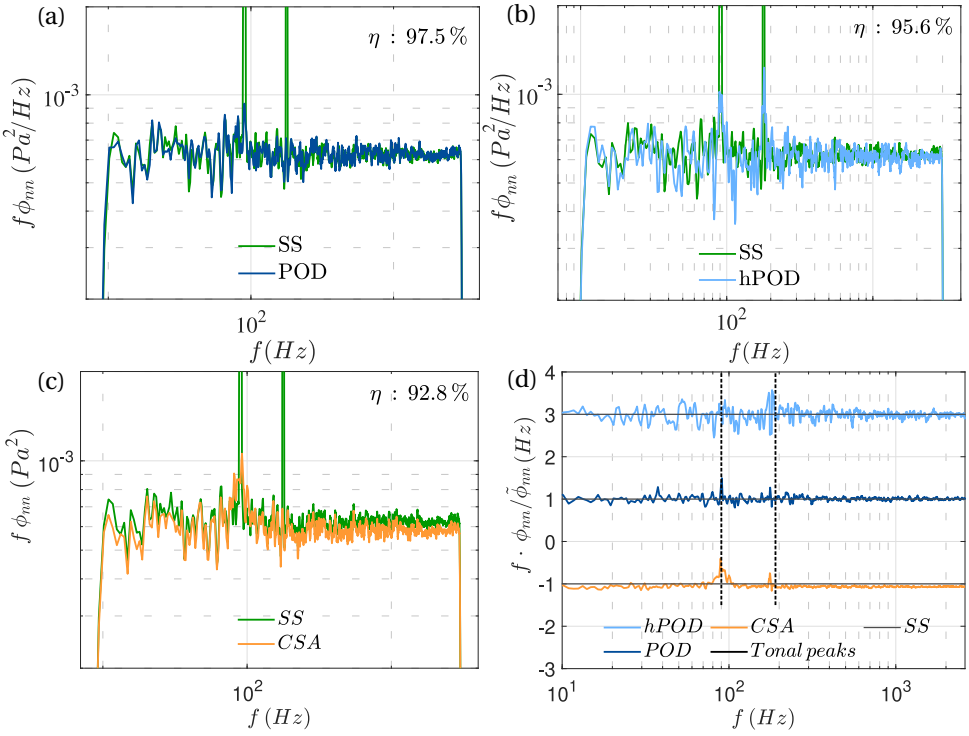

Figure 3.5.: (a) Pre-multiplied power spectral density of the original synthetic signal (green) and the reconstructed synthetic signal using only POD modes 2, 3, 4, and 5 (blue line). (b) Pre-multiplied power spectral densities of the raw synthetic data (highlighted in green) and reconstructed data using the harmonic POD technique (light blue), retaining only modes 2, 3, 4, and 5. (c) Pre-multiplied power spectral density of the unfiltered synthetic signal (green) and the filtered signal using CSA (orange). (d) Ratio of pre-multiplied power spectral densities of the filtered signal and original, noise-free, signal ($\widetilde{\phi}_{nn}$). Light blue line refers to hPOD results, dark blue line highlight POD data while orange line depicts CSA filtering operation. The results are offset by 2 unit to enhance the readability of the figure. Black dashed line reports the location of the two tonal peaks respectively at 90 Hz and 190 Hz. The three solid black lines presents the reference of the synthetic signal.

4

CORRELATION BETWEEN WALL-PRESSURE AND VELOCITY AT HIGH Re_τ

We are infinite beings with infinite possibilities.

Bernard A. Harris Jr. (STS-63)

An experimental study was conducted in the CICLoPE long-pipe facility to investigate the correlation between wall-pressure and turbulent velocity fluctuations in the logarithmic region, at high friction Reynolds numbers ($4\,794 \lesssim Re_\tau \lesssim 47\,015$). Hereby, the scalability is explored of employing wall-pressure to effectively estimate off-the-wall velocity states. Coherence spectra for wall-pressure and streamwise (or wall-normal) velocity fluctuations collapse when plotted against λ_x/y and thus reveals a Reynolds-number-independent scaling with distance-from-the-wall. When the squared wall-pressure fluctuations are considered instead of the linear wall-pressure term, the coherence spectra for the wall-pressure–squared and velocity are higher in amplitude at wavelengths corresponding to large-scale streamwise velocity fluctuations. This higher coherence typifies a modulation effect, because low-frequency content is introduced when squaring the wall-pressure time series. Finally, quadratic stochastic estimation is employed to estimate turbulent velocity fluctuations from the wall-pressure time series only. Results suggest that wall-pressure sensing can be employed for meaningful estimation of off-the-wall velocity fluctuations, and thus for real-time control of energetic turbulent velocity fluctuations at high Re_τ applications.

Parts of this chapter are published in:

- G. Dacome, L. Lazzarini, A. Talamelli, G. Bellani, W. J. Baars (2025) Scaling of wall-pressure–velocity correlations in high Reynolds number turbulent pipe flow. J. Fluid Mech. **1013**, A48.

4.1. INTRODUCTION

The design of a feasible real-time control system calls for the definition of robust input sensing strategies that can be scaled from an experimental (laboratory) setup to typical conditions of engineering systems. Given the relative simplicity and low cost that characterize unsteady wall-pressure sensors (*e.g.* microphones), the question arises as to whether pressure fluctuations at the wall of a turbulent flow can be employed to accurately estimate the state of the flow at off-the-wall positions. The work of Baars et al. [2024] investigates the spectral coherence between wall-pressure and streamwise velocity fluctuations in the logarithmic region in the case of turbulent wall-bounded flows at low values of Re_τ. In this chapter, the aim is to extend the findings of the literature to a considerably larger range of friction Reynolds number, and to analyze the estimation accuracy of velocity fluctuations from wall-pressure data. This sets the foundation of using wall-pressure as a reliable input quantity for real-time flow control of a turbulent wall-bounded flow.

4.2. EXPERIMENTAL METHODOLOGY

4.2.1. EXPERIMENTAL FACILITY

An experimental campaign was carried out in the Center for International Cooperation in Long-Pipe Experiments (CICLoPE, see Figs. 4.1a,b). The laboratory is realised inside a mountain to keep stable environmental conditions and to minimise background noise, while sound-absorbing material ensures minimal acoustic interference in the test section. The closed-loop facility comprises a 111.15 m-long circular pipe with a radius of $R = D/2 = 0.4505$ m. The primary streamwise location for measurements (where the flow is fully developed) is at $x' = 110.1\,\text{m} = 244.4R$ downstream of the pipe inlet. For the experiments reported, the pipe flow was operated at seven center-line velocities, with a maximum of $U_{CL} = 44.60$ m/s (corresponding to $Re_\tau \equiv U_\tau R/\nu = 47\,015$). Test conditions are elaborated upon in § 4.2.3. For presenting results, a Cartesian coordinate system is adopted with its origin at the primary streamwise location for measurements (at the center of sensor $\mathcal{M}_1$, indicated in Fig. 4.1c). Here the x-axis denotes the streamwise direction (positive in the downstream direction) and the y-axis denotes the wall-normal direction ($y = 0$ at the wall, and positive towards the center-line of the pipe). A comprehensive description of all design details of the facility can be found in § 2.2 of this dissertation and in the literature [Talamelli et al., 2009, Bellani and Talamelli, 2016].

4.2.2. MEASUREMENT INSTRUMENTATION

Time-resolved pressure sensors were integrated in the wall of the pipe, each within its own cavity communicating with the flow through a pinhole orifice. Figure 4.1e provides a schematic of the axisymmetric geometry of the pinhole and its corresponding sub-surface cavity, comprising a pinhole orifice diameter of $d_p = 0.3$ mm, a pinhole depth of $t_p = 1.1$ mm, an effective cavity diameter of $D = 4.6$ mm and a cavity length of $L = 0.2$ mm. The size of the pinhole orifice ensures a sufficient spatial measurement resolution for the purpose of the coherence analysis (§ 4.2.3). However, because of the sub-surface-cavity geometry, a Kelvin-Helmholtz resonance occurs. This resonance phe-

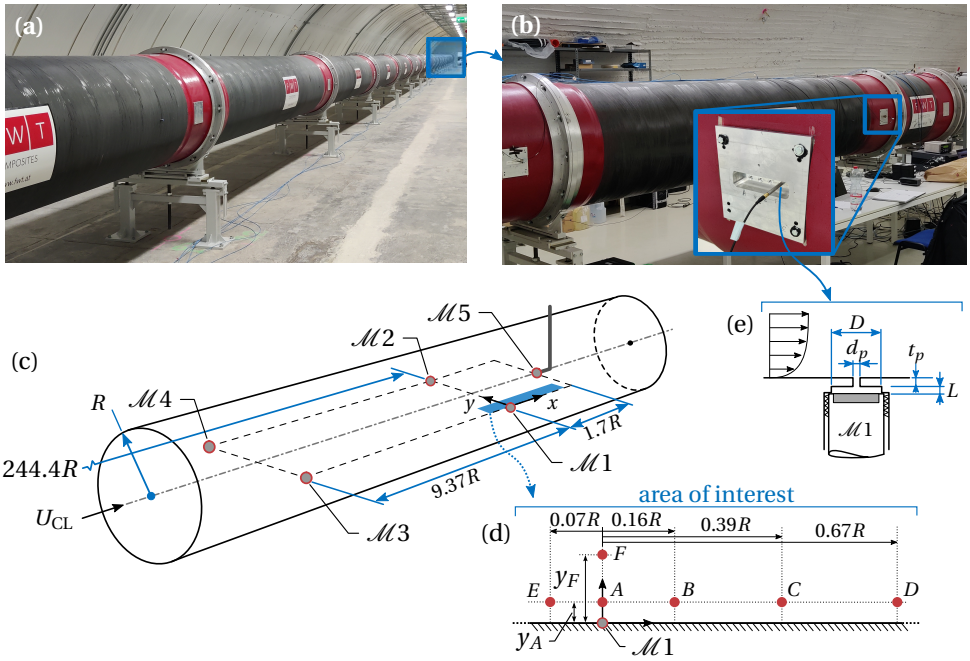

Figure 4.1.: (a,b) Photographs of the CICLoPE laboratory, with in (b) the test section at the downstream end of the long-pipe facility. (c) Schematic of the microphone sensor placement ($\mathcal{M}1$ to $\mathcal{M}4$ were mounted in the pipe wall, and $\mathcal{M}5$ was mounted along the pipe center-line). (d) Illustration of the points in the area of interest where acquisitions with single-wire and x-wire probes were performed. (e) Schematic of the pinhole–sub-surface-cavity, used to mount the microphones in the pipe wall.

nomenon was quantified by means of an acoustic characterization experiment, following an identical procedure (in the exact same facility) as the one described by Baars et al. [2024, pp. 30-32]. Similar procedures can be found in other works [*e.g.*, Gravante et al., 1998b, Tsuji et al., 2007, Gibeau and Ghaemi, 2021]. In short, pressures at the orifice inlet (p_i) and within the cavity (p_c) were measured simultaneously, in quiescent flow conditions, under a broadband acoustic excitation in an anechoic facility. A linear transfer kernel was constructed, relating cavity to inlet pressure in the frequency domain: $H_r^{\text{exp}}(f) = \langle \widetilde{P}_c(f)\widetilde{P}_i^*(f)\rangle / \langle |\widetilde{P}_i(f)|^2 \rangle$. Here the angled brackets $\langle ... \rangle$ indicate ensemble averaging, the $*$ denotes the complex conjugate, and capitalised variables with a tilde indicate the Fourier transformed quantity, *e.g.*, $\widetilde{P}_c(f) = \mathscr{F}\left[p_c(t)\right]$. Subsequently, a second-order model was fit to the gain of this transfer kernel and is denoted as $|H_r(f)|$. This procedure enabled the identification of the resonance frequency of the pinhole–sub-surface-cavity at $f_r = 4\,350$ Hz. Implications of the resonance phenomenon on the wall-pressure measurements and coherence analyses are discussed later in § 4.4.

Regarding the pressure sensors themselves, GRAS 46BE 1/4 in. CCP free-field micro-

phones were employed. These have an adequate dynamic range (35 to 160 dB, with a reference pressure of $p_{\text{ref}} = 20\,\mu$Pa) with an accuracy of ± 1 dB within the range of 10 Hz to 40 kHz. Data were acquired with two NI9234 analogue-input boards, comprising a 24-bit A/D conversion resolution. A total of five microphones were employed (labelled $\mathscr{M}1$ to $\mathscr{M}5$ in Fig. 4.1c): four were integrated in the pipe for wall-pressure measurements ($\mathscr{M}1$ to $\mathscr{M}4$), and one was mounted on a streamlined holder along the pipe center-line for monitoring the acoustic noise of the facility ($\mathscr{M}5$). Microphone $\mathscr{M}5$ was equipped with a GRAS RA0020 nose cone to reduce stagnation-driven turbulence pressure fluctuations on the otherwise flow-exposed diaphragm. The wall-mounted microphones were arranged in two streamwise pairs, separated by a distance of 4.22 m ($\Delta x = 9.37R$). Microphones in one pair were located in azimuthally-opposite positions to facilitate the removal of facility (acoustic) noise.

Time series of streamwise velocity at two wall-normal locations in the logarithmic region ($y_A = 0.011$ m $= 0.025R$ and $y_F = 0.061$ m $= 0.135R$), and at five streamwise locations (points A to E in Fig. 4.1d), were acquired using hot-wire anemometry (HWA). Synchronised measurements were performed of all microphones' signal at once, while velocity could only be measured at a single y-location for a given run. Each measurement was performed with an acquisition frequency of $f_s = 51.2$ kHz, for an uninterrupted duration of $T_a = 480$ s (relatively long time series were acquired to ensure sufficient convergence of the spectral statistics at the lowest frequencies of interest). A Dantec Streamline 90C10 CTA module was used, with a Dantec 55P15 single-wire boundary layer probe. Additionally, time series of the wall-normal velocity component were acquired using a Dantec 55P61 miniature x-wire probe at one point in the logarithmic region (point A in Fig. 4.1d). All Pt-plated tungsten wires of the single-wire and x-wire probes comprised sensing lengths of $l_{\text{hw}} = 1.25$ mm and nominal diameters of $d_{\text{hw}} = 5\,\mu$m (thus, $l_{\text{hw}}/d_{\text{hw}} \approx 250$). Hot-wire probes were calibrated *ex-situ* by employing a planar calibration jet. The single-wire probe was calibrated by fitting a 5^{th}-order polynomial function to 11 calibration points of velocity versus measured voltage, $U = f(E)$. For the x-wire instead, seven velocity settings and thirteen angular positions were set to generate a two-dimensional look-up table [Burattini and Antonia, 2004] relating the two velocity components to the measured voltages of each wire: $(U_1, U_2) = f(E_1, E_2)$. During the measurements, the probe was oriented in such a way that it measured the streamwise (u) and wall-normal (v) velocity components simultaneously. More details of similar HWA measurements in the CICLoPE facility can be found in the works by Örlü et al. [2017b] and Zheng et al. [2022].

4.2.3. EXPERIMENTAL CONDITIONS AND MEASUREMENT RESOLUTION

Seven experimental conditions were considered for measurements of the fluctuating wall-pressure and velocity in the CICLoPE long-pipe facility. Flow parameters of all test cases are reported in Table 4.1. With the aid of a heat exchanger, the facility was operated at constant temperature and the angular velocities of the two co-axial fans were set to generate center-line velocities in the range $3.837\,\text{m/s} \leq U_{\text{CL}} \leq 44.60\,\text{m/s}$ (measured with a Pitot-static probe). Corresponding values of the wall-shear stress, τ_w, were inferred from static pressure drop measurements [following Fiorini, 2017]. Values for the air density were indirectly measured with the air flow temperature and barometric pres-

	Case	1	2	3	4	5	6	7
	Label							
Pipe flow parameters	Re_τ	4 794	7 148	14 004	22 877	31 614	38 271	47 015
	U_τ (m/s)	0.162	0.242	0.473	0.773	1.068	1.293	1.588
	τ_w (Pa)	0.032	0.070	0.269	0.718	1.368	2.008	3.001
	l^* (μm)	94.0	63.0	32.2	19.7	14.3	11.8	9.58
	U_{CL} (m/s)	3.837	5.833	12.11	20.71	29.50	34.13	44.60
Instrumentation characteristics	d_p^+	4.257	6.347	12.43	20.31	28.07	33.98	41.75
	l_{hw}^+	13.30	19.84	38.86	63.48	87.72	106.2	130.5
	f_{s}^+	29.71	13.36	3.482	1.305	0.683	0.466	0.301
	$T_a U_{\mathrm{CL}}/R$	4 088	6 214	12 902	22 066	31 431	36 364	47 520
	y_A^+	117.1	174.6	342.0	558.6	771.9	934.5	1 148
	y_F^+	649.2	968.0	1 896	3 097	4 281	5 182	6 366

Table 4.1.: Flow parameters corresponding to the seven test conditions in the CICLoPE long-pipe facility, with alongside nondimensional parameters of the instrumentation's geometry and acquisition details.

sure, so that values for the friction velocity, U_τ, could be computed. For the experiments reported in this work, friction Reynolds numbers were in the range $4\,794 \lesssim Re_\tau \lesssim 47\,015$.

Spatial and temporal resolutions need to be considered for both the fluctuating wall-pressure and velocity measurements. For the measurement of wall-pressure, the pinhole orifice diameter dictates the spatial resolution, while for the measurement of velocity the hot-wire sensing length is determining the spatial resolution. The temporal resolution was limited by the acquisition frequency. All three parameters relevant for the measurement resolutions (d_p, l_{hw} and f_s) are listed in Table 4.1 after normalization with the viscous scales.

For fully-resolved wall-pressure measurements the pinhole orifice diameter must be $d_p^+ < 20$ [Gravante et al., 1998b]. Hence, the pinhole diameter is not sufficiently small to claim fully-resolved wall-pressure measurements for test cases 4 to 7 (the relatively large values of d_p^+ result in an attenuation of small-scale energy). However, this work does not revolve around conducting fully-resolved measurements, but rather focuses on the correlation between velocity fluctuations in the logarithmic region and wall-pressure. As reviewed in §4.1, the scales of interest for the correlation analyses reside at streamwise wavelengths of $\lambda_x/y \gtrsim 3$ (when considering u fluctuations) and $\lambda_x/y \gtrsim 1$ (when considering v fluctuations). Smaller streamwise scales in both the pressure and pressure-squared time series are not relevant, as they do not correlate with the ones in the turbulent velocity signals. Consequently, for all Re_τ test cases, a minimum streamwise wavelength that needs to be resolved for the coherence analyses is given by $\lambda_{x,\mathrm{res}}/y_A = 1$ (recall that y_A is the lowest wall-normal position being considered), resulting in a streamwise wavelength of $\lambda_{x,\mathrm{res}} = y_A = 11$ mm. The pinhole orifice diameter of $d_p = 0.3$ mm

is a factor 36.6 smaller and, thus, sufficient for capturing the streamwise wavelengths of interest.

When considering the spatial resolution of the HWA measurements, a similar reasoning can be applied. Statistically, the velocity structures of relevance to the wall-pressure–velocity correlations adhere to a self-similar scaling in all three dimensions. Baidya et al. [2019] showed that the aspect ratio of coherent velocity structures is 7:1, in terms of their characteristic streamwise-to-spanwise length scales. Hence, the smallest structures of relevance have spanwise wavelengths of $\lambda_{z,\mathrm{res}} = \lambda_{x,\mathrm{res}}/7 \approx 1.6\,\mathrm{mm}$. For the HWA measurements with the x-wire probe, the spanwise separation between both sensing wires is $\approx 1.0\,\mathrm{mm}$, which is sufficient to resolve the scales of interest. In the y-direction the sensing length of the x-wire probe is also adequate, given the strong wall-normal coherence of the velocity structures. For the single-wire probe, its spanwise sensing length of $l_{\mathrm{HW}} = 1.25\,\mathrm{mm}$ is more than sufficient given that the u fluctuations of interest are three times larger than the v fluctuations of interest.

Regarding the temporal measurement resolution, this is set by the data acquisition rate. For the highest Re_τ test case (number 7), the acquisition time step is largest in terms of viscous time scales and equals $\Delta T^+ = 1/f_s^+ \approx 3.3$. Even though Hutchins et al. [2009] indicates a required time step ΔT^+ of unity or less for fully-resolved measurements, the current acquisition rate is more than sufficient given the interest in much lower frequencies (larger spatial scales) than the ones corresponding to the dissipative regime.

4.3. POST-PROCESSING OF WALL-PRESSURE SIGNALS

Even though the CICLoPE laboratory has been designed to minimize noise in the test section, the facility is non-anechoic and acoustic pressure fluctuations do contaminate the measured wall-pressure signals. A superposition of facility noise onto the time series of the hydrodynamic wall-pressure affects the wall-pressure statistics. Furthermore, the correlation analyses are affected since, by construction, facility noise and velocity fluctuations are uncorrelated. Therefore, a normalized correlation (with the additive facility noise present) is lower than the true value [Saccenti et al., 2020].

Wall-pressure measurements by means of microphones, mounted within sub-surface-cavities communicating with the flow through a pinhole orifice, result in signal contamination from two main sources: (1) acoustic noise from the flow facility, and (2) acoustic resonance as a consequence of the pinhole–sub-surface-cavity geometry (see Ch. 2). While a correction for the latter can directly be implemented in the frequency domain and takes the form of a division of the spectrum by the gain-squared of a correction kernel (as done in §4.4), the former requires a more elaborate procedure. In particular, when considering a raw pressure time series of one of the microphones in Fig. 4.1c, it is necessary to disambiguate hydrodynamic wall-pressure signatures from the one induced by acoustic phenomena. In the case of turbulence-induced fluctuations, especially wall-pressure, they possess negligible streamwise and spanwise (azimuthal) coherence when considering relatively large sensor separations. Acoustic pressure fluctuations, however, convect from sensor to sensor retaining high correlation between detection stations, both in the streamwise and spanwise directions directions of the flow.

With the experimental setup illustrated in § 4.2, the acoustic waves produced by the operation of the CICLoPE facility will be detected by all microphones embedded with the aid of the pinhole–sub-surface-cavity, $\mathscr{M}1$ to $\mathscr{M}4$, and the microphone mounted along the center-line of the pipe, $\mathscr{M}5$. However, the pressure time series measured by $\mathscr{M}5$ will not contain hydrodynamic wall-pressure fluctuations. Removing facility noise requires the identification of spatial modes that are correlated among the spatially-separated sensors and whose signatures are also detected by the center-line microphone. Harmonic proper orthogonal decomposition (hPOD) is suitable to identity these modes as, compared to conventional POD, the spatial decomposition is performed in the spectral domain, which accounts for phase-shifts of pressure signatures between sensors [see Tinney et al., 2020]. During hPOD, a signal is decomposed into complex-valued and frequency-dependent eigenvalues and eigenmodes. These eigenvalues and eigenmodes follow from solving an eigenvalue problem with the harmonic complex-valued kernel (see § 3.4).

For one of the current datasets (test case 3, $Re_\tau \approx 14\,004$), the five frequency-dependent eigenvalues are shown in Fig. 4.2a. The first two eigenvalues contain clear signatures of facility noise, especially at the low frequencies. The spectra of the first four eigenvalues show a broadband distribution in the mid-to-high frequency band, whereas the fifth eigenvalue only has significant energy in the low-frequency band at $f \lesssim 60\,\mathrm{Hz}$. To determine which mode set to retain for filtering the wall-pressure time series, the spatial distribution of eigenmodes is also examined. In particular, by construction of the experiment, the ideal set of modes to retain consists of the ones that exhibit no activity at the center-line microphone, $\mathscr{M}5$. To aid in the selection of modes, only frequencies in the range $0 < f < f_c$, with $f_c = 70\,\mathrm{Hz}$ are considered, as the facility noise is concentrated in this band. The magnitude of the eigenmodes, integrated over the aforementioned frequency range, is displayed in Fig. 4.2b. Upon inspection of the five curves, it is clear that modes 3 and 4 are the ones encompassing negligible activity at the position of the center-line microphone, $\mathbf{x}_{\mathscr{M}5}$. Based on this, it was decided to reconstruct the wall-pressure time series with modes 3 and 4 only. And so, the filtered wall-pressure time series can be computed as the inverse Fourier transform of the frequency-dependent lower-order (following Eq. 3.4):

$$\widetilde{P}_{w,f}\left(\mathbf{x};f\right) = \sum_{n=\{3,4\}} \check{A}^{(n)}\left(f\right)\check{\phi}^{(n)}\left(\mathbf{x};f\right) \quad \rightarrow \quad p_{w,f}\left(x,t\right) = \mathscr{F}^{-1}\left[\widetilde{P}_{w,f}(\mathbf{x};f)\right]. \tag{4.1}$$

For the other friction Reynolds numbers considered in this study (see Table 4.1), a similar procedure was applied. Similar conclusions could be drawn in regards to the selection of modes to retain for filtering, with the only minor difference lying in the selection of the upper frequency bound for acoustic contamination, f_c. For increasing Reynolds numbers, f_c increases; physically this is caused by a larger blade passing frequency of the axial fans operating the pipe flow facility.

For reference, when considering the other two filtering technique mentioned in Ch. 3, Fig. 4.3 reports the effect of the three filtering procedures for one Reynolds number, namely $Re_\tau = 14\,004$. As per the figure, all proposed techniques successfully attenuate facility noise. Only a negligible amount of acoustic energy survives at low frequencies in the case of the spectral subtraction method at low Reynolds number.

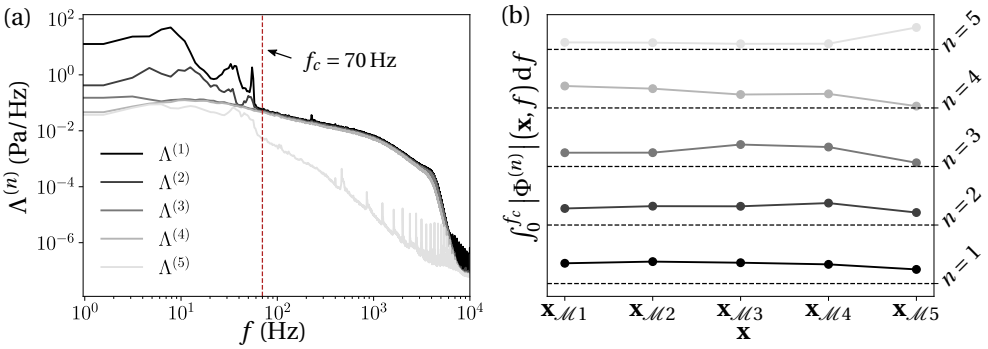

Figure 4.2.: (a) Spectra of the eigenvalue obtained from the complex-valued $\check{R}$ kernel, for test case 3 ($Re_\tau \approx 14004$). (b) Normalised magnitude of the complex modes $\Phi^{(n)}$, for $n = 1\ldots5$, integrated over the range $0 < f \lesssim 70$ Hz. Each curve is offset by one unit vertically for graphical readability.

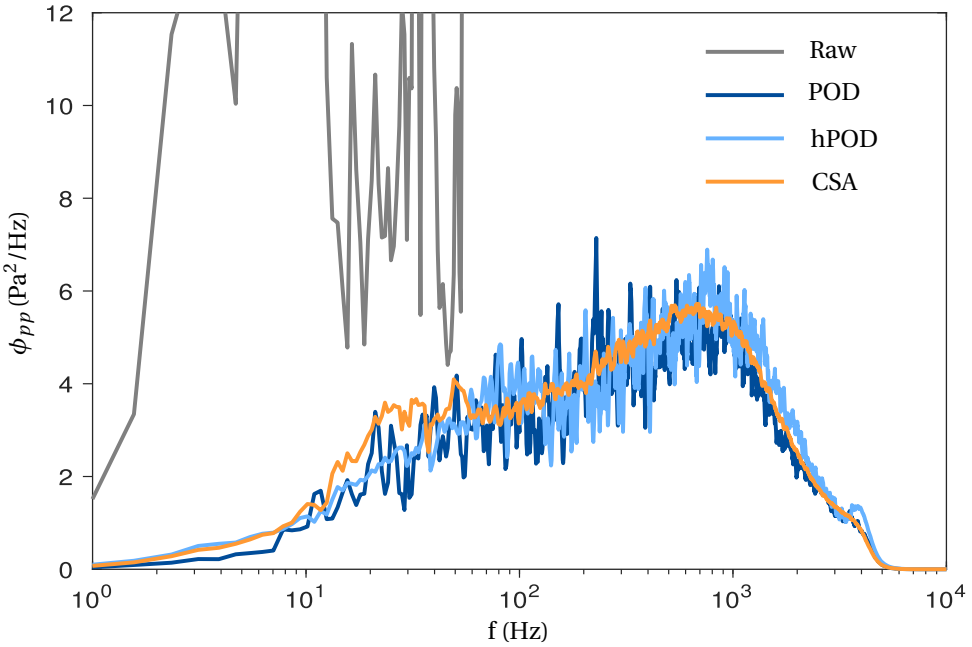

Figure 4.3.: Power spectral densities of the hydrodynamic pressure fluctuation from microphone $\mathscr{M}1$ at $Re_\tau = 14004$: raw signal (grey) and signals filtered using POD (blue), filtered with hPOD (light blue) and filtered using CSA (orange).

4.4. WALL-PRESSURE STATISTICS IN THE CICLOPE FACILITY

Statistics of the wall-pressure fluctuations are presented to demonstrate the validity of the data for the correlation analyses presented in § 4.5-4.6.

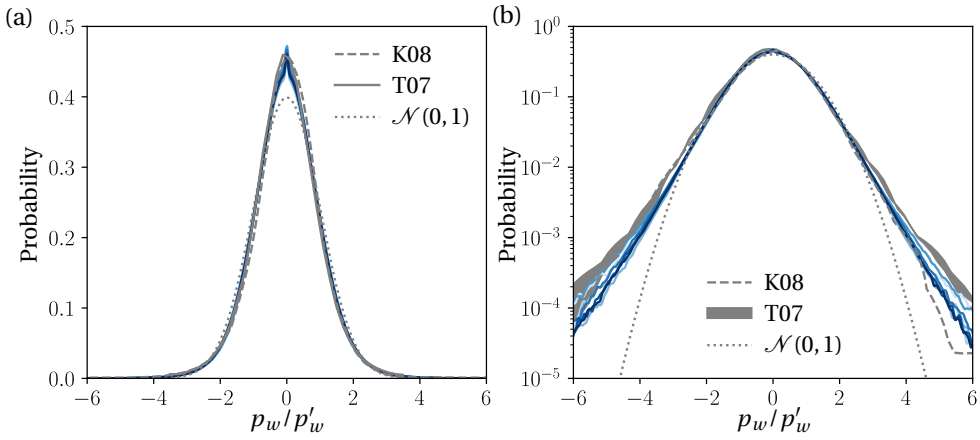

Figure 4.4.: Probability density functions of the wall-pressure fluctuations in the CICLoPE facility, for all Re_τ test cases considered (see Table 4.1). Current data are compared to a pdf obtained from atmospheric boundary layer data at $Re_\tau \approx 10^6$ [Klewicki et al., 2008, label K08], and a band representing the spread of pdf's obtained from zero-pressure-gradient TBL data at $1313 \lesssim Re_\tau \lesssim 3826$ [Tsuji et al., 2007, label T07]. A standard $\mathcal{N}(0,1)$ Gaussian distribution is added for reference. Probability density functions are plotted with (a) a linear scale and (b) a logarithmic scale on the ordinate axes.

Probability density functions (pdf's) of the wall-pressure time series are shown in Fig. 4.4a and Fig. 4.4b, with a linear and logarithmic scale on the ordinate axes, respectively. For both figures the amplitude-axes are scaled with the wall-pressure intensity (root-mean-square), denoted as p'_w. Superimposed are several pdf's from the literature: a pdf corresponding to an atmospheric boundary layer flow at $Re_\tau \approx 1\times10^6 \pm 2\times10^5$ [Klewicki et al., 2008], and a band representing the spread of pdf's corresponding to zero-pressure-gradient TBL flow at $1313 \lesssim Re_\tau \lesssim 3826$ [Tsuji et al., 2007]. All pdf's of the current datasets show negligible disparity between the test cases, and are consistent with the distributions from the literature. Minor deviations appear in the tails of the pdf's (Fig. 4.4b), yet comparable with the degree of deviation in the work by Tsuji et al. [2007] and without a noticeable monotonic trend with an increase in Re_τ.

Pre-multiplied energy spectra of wall-pressure fluctuations are shown in Fig. 4.5a and Fig. 4.5b for all values of Re_τ, with an inner-scaled and outer-scaled streamwise wavelength on the abscissa, respectively. Here, the streamwise wavelength is obtained by applying Taylor's hypothesis: $\lambda_x \equiv U_c/f$, where f is the frequency, and U_c is the convection velocity taken as $U_c^+ = 10$. Despite the convection velocity of the wall-pressure field being scale-dependent [*e.g.*, Luhar et al., 2014], and the temporal-to-spatial conversion of near-wall fluctuations in velocity/pressure not abiding by Taylor's hypothesis [Dennis and Nickels, 2008, del Álamo and Jiménez, 2009], the conversion is kept equal across all test cases. In essence, temporal spectra are compared (since $\lambda_x^+ = 10U_\tau^2/\nu/f = 10/f^+$). Still the temporal-to-spatial conversion was applied because § 4.5–4.6 consider all coherence spectra as a function of wavelength for ease of comparison to the only data

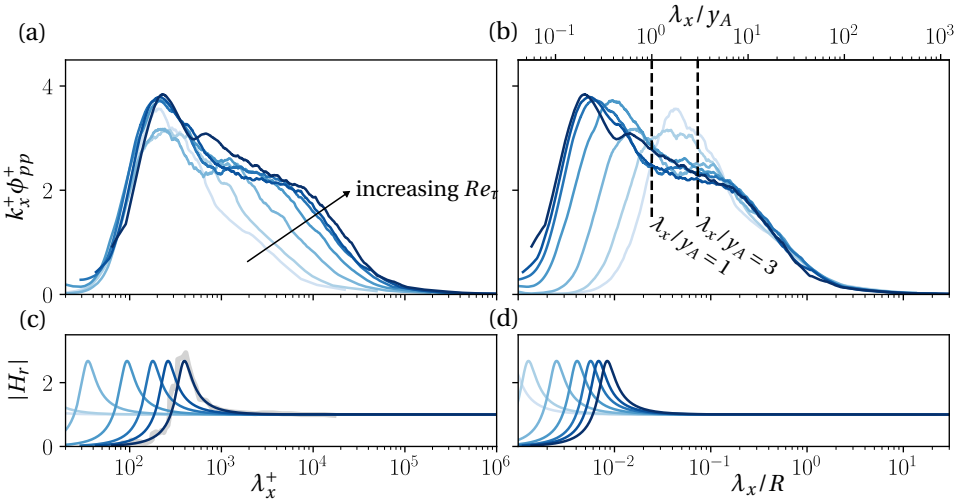

Figure 4.5.: (a,b) Pre-multiplied energy spectra of wall-pressure fluctuations, for all Re_τ test cases considered (an increase in colour intensity of corresponds to an increase in Re_τ following test cases $1 \rightarrow 7$, listed in Table 4.1), as a function of (a) the viscous scaled wavelength and (b) the outer-scaled wavelength. Note that the temporal spectra are plotted as spatial spectra by converting frequency into wavelength, using $\lambda_x \equiv U_c/f$ with $U_c^+ = 10$. Vertical dashed lines in sub-figure (b) indicate the minimum wavelength in the dataset for which wall-pressure–velocity correlations become appreciable when considering u fluctuations ($\lambda_x/y_A = 3$) and v fluctuations ($\lambda_x/y_A = 1$). (c,d) Gain of transfer kernel H_r that characterizes the pinhole–sub-surface-cavity as described in § 4.2.2, including in (c) the gain of the raw kernel, H_r^{exp} (light grey line).

available (those from *spatial* DNS of turbulent channel flow).

Before commenting on the wall-pressure spectra, note that Fig. 4.5c and Fig. 4.5d present the gain of the transfer kernel that characterizes the pinhole–sub-surface-cavity (described in § 4.2.2). Because the transfer kernel is a function of frequency, and the frequency-to-wavelength conversion includes the friction velocity of each test case, seven identical kernels are shown (but shifted along λ_x). For reference, the raw experimental kernel, H_r^{exp}, is shown in Fig. 4.5c for the highest Re_τ test case with a thick grey line, while the other kernels correspond to the fitted kernel of the second-order model, H_r. Noticeably, resonance occurs at scales where the wall-pressure spectra are energetic. It is thus necessary to correct the spectra for the amplification/attenuation effect. Current wall-pressure spectra *were corrected* before plotting, by dividing the spectra with the frequency-dependent model kernel [$\phi_{pp}(f) = \phi_{pp,f}(f)/|H_r(f)|^2$, with $\phi_{pp,f}$ being the spectrum after removing facility noise from the raw measurements of wall-pressure following § 4.3]. The resonance-correction works theoretically, but practically the kernel (which was found with the aid of a flow-off experiment) changes when wall-bounded turbulence grazes the pinhole orifice [see Dacome et al., 2024], making the correction imperfect. In practice, this results in an erroneous 'wiggle' in various spectra, and is

most noticeable in the spectrum of test case 7.

Close inspection of the wall-pressure spectra reveals expected Reynolds-number trends. The location of the inner-spectral peak at $\lambda_{x,p}^{+} \approx 250$ (Fig. 4.5a) agrees with previous work [Farabee and Casarella, 1991, Tsuji et al., 2007, Klewicki et al., 2008, Panton et al., 2017]. A slight increase in the inner-spectral peak magnitude, with an increase in Re_τ, is also noticeable for test cases 4 to 7 [expected per the trends in Tsuji et al., 2007, Panton et al., 2017, Yu et al., 2022]. The large-scale energy content also progressively increases with Re_τ and exhibits a collapse in outer-scaling, for the range $\lambda_x/R \gtrsim 0.2$ (Fig. 4.5b). This trend is in line with the findings reported in DNS studies at lower Re_τ [Panton et al., 2017, Yu et al., 2022]. It also conforms to the work by Deshpande et al. [2024], who reason that the intermediate and large scales of the wall-pressure spectra grow with Re_τ due to the contributions of both the active and inactive motions in the grazing flow. Spectra corresponding to test cases 1 and 2 are outliers in that their broadband peak-magnitudes are relatively high. It is postulated that this is due to an incomplete removal of facility noise, as any remaining signature of facility noise is more pronounced in the spectra of lower Re_τ test cases. That is, the degree of facility noise was quantified with a signal-to-noise ratio (SNR), defined as the intensity-ratio of turbulence-induced wall-pressure fluctuations, relative to those induced by facility noise: $\text{SNR} = p'_w/(p'_{w,r} - p'_w)$. Here, $p'_{w,r}$ is the pressure intensity (root-mean-square) of the raw, measured wall-pressure. SNRs in the dataset increase monotonically with Re_τ, in the interval $0.08 \leq \text{SNR} \leq 0.25$. Additive facility noise is thus more noticeable in the spectra at lower Re_τ. For the remainder of the paper, it is important to recall from §4.2.3 that for the correlation analysis the scales of interest reside at streamwise wavelengths beyond $\lambda_x/y \approx 3$ (when considering u fluctuations) and $\lambda_x/y \approx 1$ (when considering v fluctuations). Both of these limits are indicated in Fig. 4.5b; within the scale-range of interest the spectra are not affected by the kernel-correction and only the two lowest test cases seem affected by additive (acoustics-driven) noise.

As a final wall-pressure statistic, wall-pressure intensities are considered, resulting from the integration of the energy spectra. Here, the root-mean-square intensity is considered and inner-normalized following $p'^{+}_w = p'_w/\tau_w$. Wall-pressure intensities are plotted in Fig. 4.6 and compared to a variety of datasets from the literature. Data from channel flow DNS are added Panton et al. [2017], together with the various datasets assembled by Klewicki et al. [2008] (and named in the caption), that include both numerical and experimental studies, comprising zero-pressure-gradient turbulent boundary layer (ZPG-TBL), turbulent channel (TCF) and pipe flows. The current data confirms the trend of increasing pressure intensity with Re_τ, and closely follows the empirical relation of Klewicki et al. [2008]. Only the data point of test case 1 (at $Re_\tau \approx 4794$) is an outlier, which is ascribed to the imperfect facility noise-filtering causing an overestimation of the wall-pressure intensity.

4.5. COHERENCE BETWEEN STREAMWISE VELOCITY AND WALL-PRESSURE

To analyse the scale-dependent coupling between the fluctuations in streamwise velocity (u) and wall-pressure (p_w), the linear coherence spectrum (LCS) is employed.

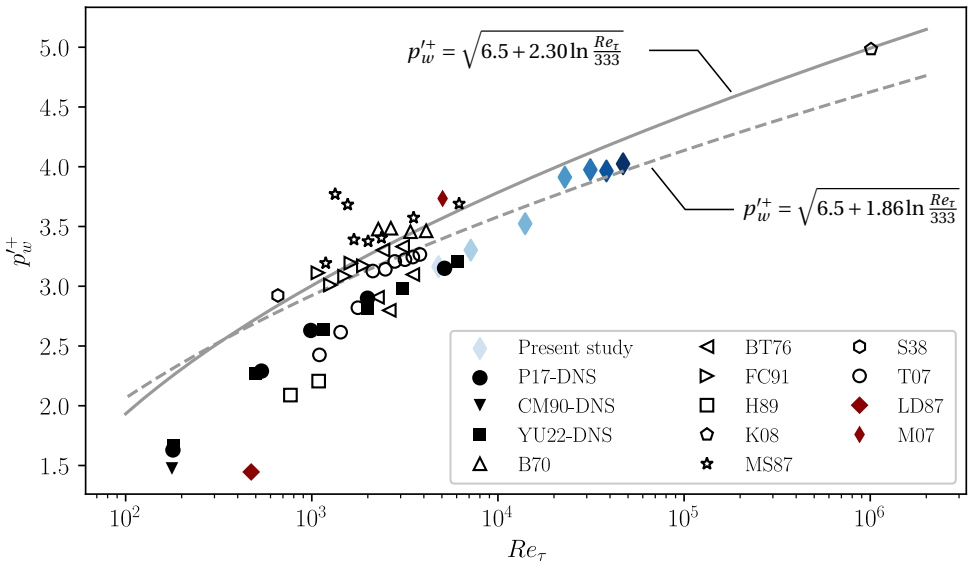

Figure 4.6.: Wall-pressure intensity inferred from integrating the wall-pressure spectra. Current results are compared to several datasets available from the literature. Data are taken from the DNS studies of Panton et al. [2017] (P17-DNS, •, ZPG-TBL), Choi and Moin [1990] (CM90-DNS, ▼, TCF) and Yu et al. [2022] (YU-DNS, ■, pipe flow). Furthermore, data are collected from experimental studies of ZPG-TBL flows: Blake [1970] (B70, △), Bull and Thomas [1976] (BT76, ◁), Farabee and Casarella [1991] (FC91, ▷), Horne [1989] (H89, □), Klewicki et al. [2008] (K08, ⬠), McGrath and Simpson [1987] (MS87, ☆), Schewe [1983] (S83, ⬡) and Tsuji et al. [2007] (T07, ○), and of experimental studies of pipe flows: Lauchle and Daniels [1987] (LD87, ★) and Morrison [2007] (M07, ⧫). Solid and dashed lines are the formulations presented by Klewicki et al. [2008], in which the pressure variance increases logarithmically with increasing Re_τ.

The LCS describes the stochastic coupling, on a per-scale basis, as the degree of *phase-consistency*. The LCS is defined as the magnitude-squared of the cross-spectrum between u and p_w, normalized with the two auto-spectra of u and p_w:

$$\gamma^2_{up_w}(y,\lambda_x) \equiv \frac{|\langle \widetilde{U}(y,\lambda_x)\,\widetilde{P}^*_w(\lambda_x)\rangle|^2}{\langle|\widetilde{U}(y,\lambda_x)|^2\rangle\langle|\widetilde{P}_w(\lambda_x)|^2\rangle}, \tag{4.2}$$

where the angled brackets $\langle ... \rangle$ indicate ensemble averaging, the $*$ denotes the complex conjugate, and capitalised variables with a tilde indicate the Fourier transformed quantity, *e.g.*, $\widetilde{P}_w(f) = \mathscr{F}[p_w(t)]$. Because in the remainder of the manuscript scale-dependent data as a function of streamwise wavelength are presented, the argument in (4.2) is taken as λ_x and is, as for the energy spectra in § 4.4, obtained by applying Taylor's hypothesis: $\lambda_x \equiv U_c/f$, with $U_c^+ = 10$.

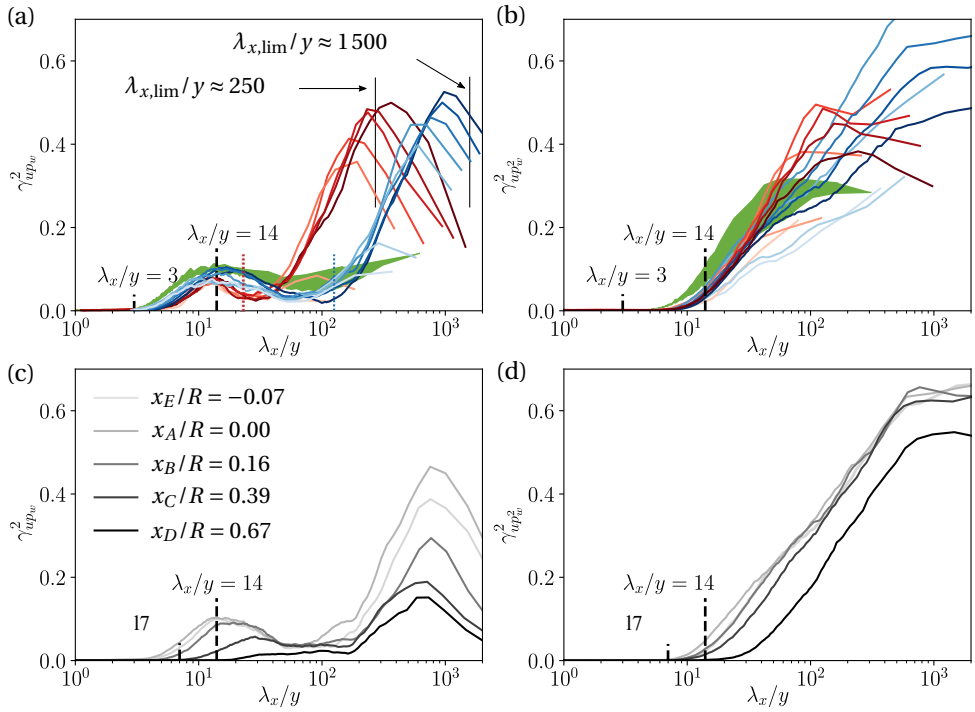

Figure 4.7.: (a) Coherence spectra for the fluctuations in streamwise velocity and wall-pressure, and (b) the streamwise velocity and wall-pressure–squared. Two sets of coherence spectra are shown, corresponding to velocity fluctuations measured at point A (blue colour scale) and point F (red colour scale); an increase in colour intensity corresponds to an increase in Re_τ following test cases $1 \rightarrow 7$, listed in Table 4.1. Reference data are shown with a light grey shaded area, associated with the spread of coherence spectra from spatial DNS data at $Re_\tau = 5200$ [Baars et al., 2024]. (c) Coherence spectra for the fluctuations in streamwise velocity and wall-pressure, and (d) the streamwise velocity and wall-pressure–squared, for test case 3 ($Re_\tau \approx 14004$), and for velocity fluctuations measured at points E, A-D spanning a range of streamwise locations, $-0.07 \leq x/R \leq 0.67$. Note that all current coherence spectra are generated from temporal data, and plotted as spatial spectra by converting frequency into wavelength using $\lambda_x \equiv U_c/f$ with $U_c^+ = 10$.

Figures 4.7a,b present the LCS for u and p_w, for two positions of the velocity measurement (points A and F in Fig. 4.1d) and for all values of Re_τ. In presenting the scale-dependent spectra, the choice is made to scale λ_x with the distance-from-the-wall, so that the abscissae are in terms of λ_x/y with $y = \{y_A, y_F\}$ for these graphs. With negligible coherence reported at small wavelengths, a steady rise in the LCS can be observed in Fig. 4.7a for increasing λ_x/y until a local maximum is reached at $(\lambda_x/y, \gamma^2_{up_w}) \approx (14, 0.1)$. Given that the current data span nearly a decade in Re_τ, it can be concluded that the

region of coherence centered at $\lambda_x/y \approx 14$ is Reynolds-number invariant.

Only the two LCS corresponding to test cases 1 and 2 have a slightly lower value near $\lambda_x/y = 14$. This is ascribed to the incomplete removal of facility noise in the wall-pressure spectra of these two test cases (recall the discussion in §4.4), and the fact that additive noise in the spectra causes an attenuation of the LCS. A second region of significant coherence appears at large wavelengths where the velocity fluctuations continue to be energetically relevant. To illustrate this, an amplitude threshold of the pre-multiplied streamwise energy spectra is taken as $k_x^+\phi_{uu}^+ = 0.2$ at the large-scale end. Energy levels only drop below this threshold for outer-scaled wavelengths of $\lambda_{x,\mathrm{lim}}/R \gtrsim 35$. This limit is included in Fig. 4.7a for reference, and corresponds to $\lambda_{x,\mathrm{lim}}/y \approx \{250, 1\,500\}$ for $y = \{y_A, y_F\}$, respectively. Moreover, this region of high coherence (in excess of $\gamma^2_{up_w} = 0.5$) becomes relevant at a scale of $\lambda_{x,\mathrm{lim}}/R \approx 3.5$ (or $\lambda_{x,\mathrm{lim}}/y \approx \{25, 150\}$ for $y = \{y_A, y_F\}$ as indicated with thin solid lines in Fig. 4.7a), and thus adheres to a Reynolds-number invariant scaling when λ_x is scaled with the outer-scale, R. This large-scale region of strong coherence between u fluctuations in the logarithmic region and the wall-pressure field is presumably related to global velocity modes [Bullock et al., 1978, del Álamo and Jiménez, 2003]. These global modes are 'inactive' in the view of Townsend's attached-eddy hypothesis [Townsend, 1976] (thus large-scale eddies that do not contribute to the Reynolds shear stress uv). Inactive motions are coupled to the very large scales in the pressure spectrum [as shown explicitly by Deshpande et al., 2024], while the active motions contribute directly to the intermediate scales.

Before further discussing the trends of the coherence spectra, the coherence involving the quadratic term of the wall-pressure is inspected. The inclusion of this term was deemed important for stochastically estimating off-the-wall velocities from wall-pressure data. The quadratic term of the wall-pressure is taken as $p_w^2 = \left[p_w^2\right]_\mathrm{r} - \overline{\left[p_w^2\right]_\mathrm{r}}$ with $\left[p_w^2\right]_\mathrm{r}$ denoting the time series of the wall-pressure–squared prior to the subtraction of its mean. Differently to the behaviour displayed by the linear term of wall-pressure, the LCS for u and p_w^2 rises starting from $\lambda_x/y \approx 7$ (see Fig. 4.7b). Again a Reynolds-number invariant trend appears in the rise of coherence around scales of $\lambda_x/y = 14$ and beyond, with once more the LCS of test cases 1 and 2 comprising a lower magnitude due to the incomplete removal of facility noise from the wall-pressure spectra. To further conclude the Reynolds-number invariant trends observed in Figs. 4.7a,b, the current experimental coherence spectra generated from temporal data are compared to the coherence spectra presented by Baars et al. [2024], generated from spatial DNS data of turbulent channel flow. These reference data are shown with the light grey shaded area, indicating the spread of coherence spectra at $Re_\tau = 5\,200$ when considering a range of wall-normal positions across the logarithmic region [$80 \lesssim y^+ \lesssim 0.15Re_\tau$, see Fig. 6 of Baars et al., 2024]. Moreover, Baars et al. [2024] also revealed a Reynolds-number invariant trend for these DNS data, spanning $550 \lesssim Re_\tau \lesssim \approx 5\,200$. It must be noted that even though these DNS data are associated with turbulent channel flow, it was shown that coherence spectra from a relatively low Reynolds number TBL flow ($Re_\tau \approx 2\,280$) were also in agreement with these channel flow data. And so, with the current LCS for pipe flow collapsing for the full range of Re_τ, for both wall-normal positions, $y = \{y_A, y_F\}$ (while agreeing with the reference data), it can be concluded that the coherence is statistically similar across several canonical flow geometries.

Universal trends in the coherence spectra are reflective of how coherent velocity fluctuations are interlinked to the wall-pressure. The scales around which $\gamma^2_{up_w}$ and $\gamma^2_{up^2_w}$ become non-zero ($\lambda_x/y \approx 3$ and $\lambda_x/y \approx 7$, respectively), as well as the logarithmic growth of coherence [most noticeable in Fig. 4.7b, where $\gamma^2_{up^2_w} \propto \ln(\lambda_x/y)$] follow a pattern presented in the work by Baars et al. [2017]. They considered the coherence between the near-wall velocity fluctuations and the ones in the logarithmic region. The logarithmic growth of coherence, which occurs over the inertial-range of wavelengths, was interpreted as the range of scales that contains turbulence energy that is statistically self-similar (following a hierarchical structure of wall-attached eddies).

An increase in large-scale coherence for the wall-pressure–squared term suggests that large-scale u fluctuations modify (modulate) the wall-pressure field following nonlinear dynamics. To analyse this phenomenon, a Hilbert transform is used to retrieve an "envelope" of the wall-pressure time series. Figure 4.8a presents the normalised wall-pressure time series ($\widetilde{p}_w = p_w/p'_w$) at $Re_\tau \approx 14004$ for microphone $\mathscr{M}1$, over a short time interval, together with the magnitude of its Hilbert transform, $|H(\widetilde{p}_w)|$, and the de-meaned wall-pressure–squared time series. By visual inspection, these last two time series have similar large-scale energy content. Figure 4.8b quantifies this further by overlaying the LCS for u and $|H(\widetilde{p}_w)|$ and the LCS for u and p^2_w (those are identical to the ones shown in Fig. 4.7b). A remarkable collapse is observed for the two sets of LCS spectra, for all Re_τ cases considered. Hence, the large-scale variations in the wall-pressure intensity are directly linked to the passage of streamwise velocity fluctuations modulating the near-wall intensity [Tsuji et al., 2015].

Gaining knowledge on how the coherence decays as a function of the streamwise separation between the velocity measurement and the wall-pressure sensor is highly relevant for real-time flow control (*e.g.,* when sensors and actuators are separated to allow for control actions while the flow convects downstream). For the current data, the $\gamma^2_{up_w}$ and $\gamma^2_{up^2_w}$ coherence spectra are considered as a function of the streamwise distance of the velocity measurement (relative to the wall-pressure sensor at $x = 0$), for test case 3 corresponding to $Re_\tau \approx 14004$. Coherence spectra are shown in Figs. 4.7c,d, for $\gamma^2_{up_w}$ and $\gamma^2_{up^2_w}$, respectively. When increasing the streamwise distance, $\gamma^2_{up_w}$ decays with the coherence decreasing faster at smaller scales, as is expected. Similar conclusions were drawn for all other Re_τ test cases. When inspecting the decay in $\gamma^2_{up^2_w}$ (Fig. 4.7d), it becomes clear that the coherence with the quadratic wall-pressure term remains considerably larger than the one with the linear term. This means that the mechanism of large-scale modulation of the smaller-scale wall-pressure fluctuations (by the large-scale u fluctuations) is dominant over the direct (linear) imprint of u fluctuations on the wall-pressure.

4.6. COHERENCE BETWEEN WALL-NORMAL VELOCITY AND WALL-PRESSURE

To further characterise the dynamics between fluctuations in velocity and wall-pressure, the foregoing presents a similar analysis as the one described in § 4.5, but now considering v fluctuations. Coherence spectra for v and p_w (Fig. 4.9a) exhibit local maxima

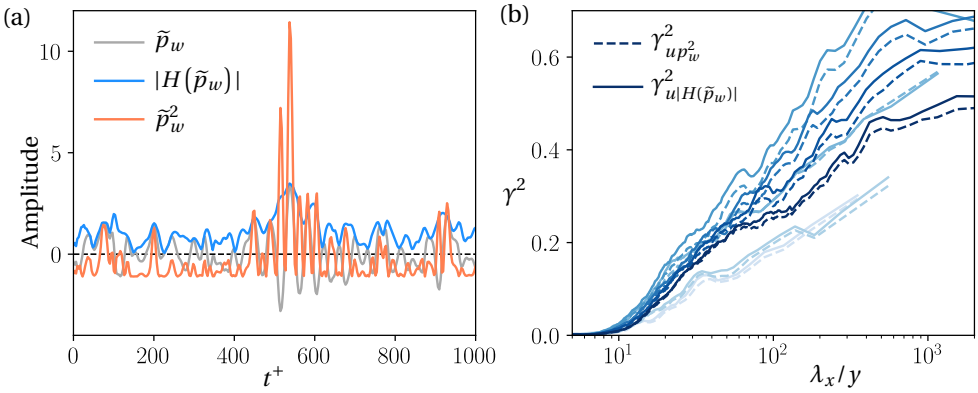

Figure 4.8.: (a) Normalised wall-pressure time series of microphone $\mathcal{M}1$, for test case 3 ($Re_\tau \approx 14\,004$), its Hilbert transform, and the corresponding de-meaned wall-pressure–squared. (b) Coherence spectra for the fluctuations in streamwise velocity and wall-pressure–squared (dashed lines, identical to the coherence spectra in Fig. 4.7b), compared to the coherence spectra for fluctuations in the streamwise velocity at point y_A and the Hilbert transform of the wall-pressure (solid lines).

around $\lambda_x/y \approx 10$ [instead of $\lambda_x/y \approx 8$, as indicated by Baars et al., 2024] and $\gamma^2_{vp_w} \approx 0.15$, a magnitude which is roughly 50% higher than local maxima in the LCS for u and p_w. Squaring the wall-pressure fluctuations brings higher levels of $\gamma^2_{vp_w^2}$ (see Fig. 4.9b), starting to rise at $\lambda_x/y \approx 3$. A similar Reynolds-number-independence is observed as was seen in the coherence analyses with the u fluctuations.

Higher coherence between wall-normal velocity and wall-pressure fluctuations complies with earlier findings [*e.g.*, Gibeau and Ghaemi, 2021]. In fact, given the non-permeability boundary condition, fluid motions directed towards the wall (with a negative v-component) will stagnate and thus give rise to a positive fluctuation in wall-pressure. Conversely, $v > 0$ fluctuations will tend to lower the unsteady wall-pressure. In general, the higher correlation between v and p_w can be ascribed to the Orr-mechanism [see Jiménez, 2013, Luhar et al., 2014, among others]. Therefore, there exists a rather strong coupling between v and p_w. Note, however, that the current work is motivated by using wall-pressure information to, eventually, predict the off-the-wall velocity fluctuations. Using pressure information to predict wall-normal velocity fluctuations for real-time control is not as effective as when considering streamwise velocity fluctuations, because the streamwise ones provide a stronger contribution to wall-shear stress generating mechanisms [*e.g.*, Deck et al., 2014, among others]. Furthermore, v fluctuations have a considerably shorter characteristic wavelength than u fluctuations ($\lambda_x^+ \approx 250$ for the former, and $\lambda_x^+ \approx 1\,000$ for the latter). This not only requires faster processing for real-time operations, but would also constrain the sensor-actuator spacing due to the faster de-correlation of the v fluctuations in the streamwise direction.

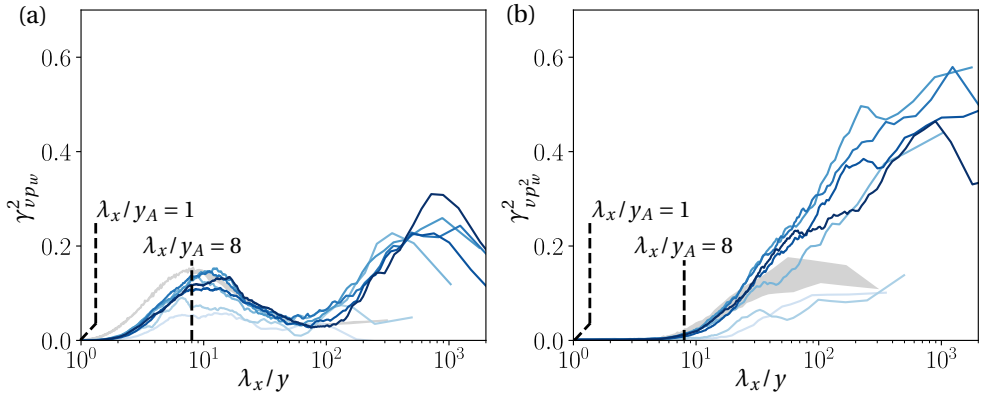

Figure 4.9.: (a) Coherence spectra for the fluctuations in wall-normal velocity and wall-pressure, and (b) the wall-normal velocity and wall-pressure–squared. Two sets of coherence spectra are shown, corresponding to velocity fluctuations measured at point A; an increase in colour intensity corresponds to an increase in Re_τ following test cases $1 \rightarrow 7$, listed in Table 4.1. The light grey shaded area is associated with the spread of coherence spectra from DNS data, as reported by Baars et al. [2024]. Note that all current coherence spectra are generated from temporal data, and plotted as spatial spectra by converting frequency into wavelength using $\lambda_x \equiv U_c/f$ with $U_c^+ = 10$.

4.7. STOCHASTIC ESTIMATION OF STREAMWISE VELOCITY FLUCTUATIONS

For real-time control purposes, wall-pressure sensing can be employed to generate an estimate of the fluctuating velocities in the logarithmic region of a wall-bounded turbulent flow. To this end, the foregoing will examine the accuracy of the prediction of u fluctuations, performed with Linear and Quadratic Stochastic Estimation methods (LSE and QSE, respectively). These methods solely employ the time series of wall-pressure, and wall-pressure–squared, as the input quantities.

Estimates of the u fluctuations in the logarithmic region at position y_e can be formed through a convolution of time-domain kernels. Estimates of unconditional time series of off-the-wall velocity fluctuations, with the LSE and QSE procedures, follow from the formulations:

$$\widehat{u}_{\mathrm{LSE}}\left(y_e,t\right) = \left(h_l \circledast p_w\right)(t) \tag{4.3}$$

$$\widehat{u}_{\mathrm{QSE}}\left(y_e,t\right) = \left(h_l \circledast p_w\right)(t) + \left(h_q \circledast p_w^2\right)(t), \tag{4.4}$$

where the (stochastic) temporal kernels of the linear term (h_l) and quadratic term (h_q) are the inverse Fourier transforms of the complex, frequency-domain kernels, *e.g.*, $h_l\left(y_e,t\right) = \mathscr{F}^{-1}\left[H_L\left(y_e,f\right)\right]$ and similar for h_q. The linear kernel equals the cross-spectrum between u and p_w, divided by the auto-spectra of p_w (the input quantity during the estimation

method),

$$H_L(y_e, f) = \frac{\langle \widetilde{U}(y_e, f)\, \widetilde{P}_w^*(f) \rangle}{\langle |\widetilde{P}_w(f)|^2 \rangle}, \tag{4.5}$$

whereas the quadratic kernel includes the wall-pressure–squared term, p_w^2, instead of the linear one,

$$H_Q(y_e, f) = \frac{\langle \widetilde{U}(y_e, f)\, \widetilde{P}_{w,sq}^*(f) \rangle}{\langle |\widetilde{P}_{w,sq}(f)|^2 \rangle}, \tag{4.6}$$

with $\widetilde{P}_{w,sq}(f) = \mathscr{F}[p_w^2(t)]$. Given the current dataset, two estimation locations are considered ($y_e = y_A$ and $y_e = y_F$). Further details of the stochastic estimation procedures can be found elsewhere [Naguib et al., 2001, Baars et al., 2024].

4

To evaluate the accuracy of the estimation with respect to the reference time series, $u(y_0, t)$, the Pearson correlation coefficient is employed. It is defined as the ratio of the covariance of two input signals to the product of the standard deviation of the two. Figure 4.10b presents values of $\rho[u_W(y,t), \widehat{u}_{\mathrm{QSE}}(y,t)] = \mathrm{cov}[u_W(y,t), \widehat{u}_{\mathrm{QSE}}(y,t)] / (u'_W \widehat{u}'_{\mathrm{QSE}})$: the correlation coefficient between the reference time series $u_W(y,t)$ at points A and F (see Fig. 4.1b) to the QSE-based time series, $\widehat{u}_{\mathrm{QSE}}(y,t)$. Here time series $u_W(y,t)$ is not equal to $u(y,t)$, because u_W only retains wall-attached eddies. Effectively, u_W is a large-scale pass-filtered signal of u, with its Reynolds number-invariant kernel characterized by a definitive cut-off at $\lambda_x/y = 14$ [Baars et al., 2017].

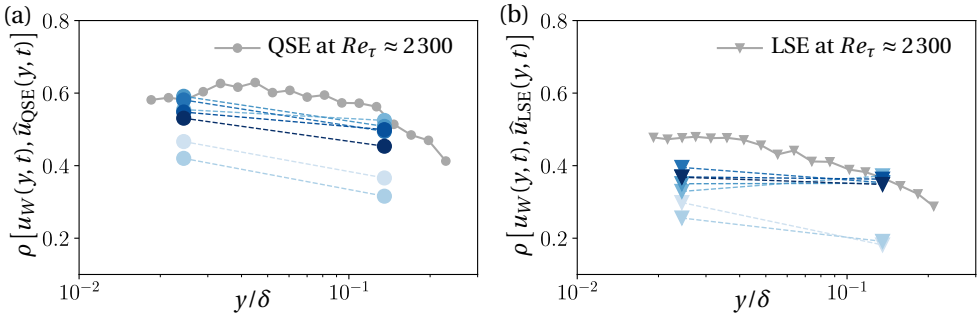

Figure 4.10.: (a) Correlation coefficient computed with the QSE-based streamwise velocity fluctuations in the logarithmic region, $\widehat{u}_{\mathrm{QSE}}$, and the reference time series, u_W. (b) Correlation coefficient computed with the LSE-based streamwise velocity fluctuations in the logarithmic region, $\widehat{u}_{\mathrm{LSE}}$, and the reference time series, u_W. Reference data are taken from Baars et al. [2024] at $Re_\tau \approx 2300$.

With the exception of the data at the two lowest Re_τ test cases 1 and 2—whose time series are still affected by imperfect noise filtering (see § 4.3)—collapse for all Re_τ test cases considered. A slight attenuation of ρ is observed with respect to the reference data, which is attributed to a systematic error [Saccenti et al., 2020] caused by additive facility noise. Furthermore, the data are in good agreement with the reference data from Baars et al. [2024] at $Re_\tau \approx 2300$. This result solidifies the conclusion of Reynolds-number independent estimation accuracy of wall-attached velocity fluctuations, based

on wall-pressure sensing alone. As expected, a lower correlation coefficient appears in Fig. 4.10b, where the estimation is performed with only the linear term of wall-pressure (thus using the LSE method). The performance of the statistical estimator now decays by about 20% with respect to QSE-based estimation, across the given range of wall-normal distances.

4.8. CONCLUSIONS

This chapter illustrates a unique correlation analysis that was performed to understand the relation between velocity fluctuations in the logarithmic region of a turbulent wall-bounded flow and the wall-pressure fluctuations. With a unique experimental dataset spanning a decade in Reynolds number, it was possible to prove Reynolds-number independence of the spectral coherence between wall-pressure and velocity fluctuations, both for the streamwise and wall-normal components. Additionally, the quadratic term of wall-pressure fluctuations is extremely beneficial for employing wall-pressure fluctuations as an input to a real-time control system. In particular, not only its spatial coherence decreases less rapidly than the linear term in the streamwise direction, but also its inclusion in a stochastic estimation procedure greatly improves the accuracy of this technique. This is highly relevant when needing to identify a real-time transfer kernel to map the instantaneous input signal to a physical control output. To conclude, wall-pressure fluctuations represent a viable input quantity for a real-time control system for the manipulation of a wall-bounded turbulent flow not only for experimental activity at relatively low Reynolds numbers, but also for high-Re_τ applications.

III

FEEDFORWARD CONTROL OF TURBULENT BOUNDARY LAYERS

5

FEEDFORWARD CONTROL WITH WALL-SHEAR STRESS INPUT

Mystery creates wonder and wonder is the basis of man's desire to understand.

Neil Armstrong (Apollo 11)

This chapter explores the dynamic response of a turbulent boundary layer to large-scale reactive opposition control, at a friction Reynolds number of $Re_\tau \approx 2240$. *A surface-mounted hot-film is employed as the input sensor, capturing large-scale fluctuations in the wall-shear stress, and actuation is performed with a single on/off wall-normal blowing jet positioned* 2.4δ *downstream of the input sensor, operating with an exit velocity of* $v_j = 0.4U_\infty$. *With the control-off calibration-experiment conducted* a-priori, *a transfer kernel is identified so that the velocity fluctuations that are to-be-controlled can be estimated. Direct measures of the skin friction-drag are inferred from PTV data. Results indicate that the opposing control logic yields the lowest wall-shear stress (3% lower than the desynchronized control, and 10% lower than the uncontrolled flow). Finally, a FIK-decomposition of the skin-friction coefficient revealed that the off-the-wall turbulence follows a consistent trend with the PTV-based wall-shear stress measurements, although biased by an increased shear in the wake of the boundary layer given the formation of a plume due to the jet-in-crossflow actuation.*

Parts of this chapter are published in:

- G. Dacome, R. Mörsch, M. Kotsonis, W. J. Baars (2024) Opposition flow control for reducing skin-friction drag of a turbulent boundary layer. Phys. Rev. Fluids **9**, 064602.

5.1. INTRODUCTION

Before delving into the development of a real-time control system utilizing wall-pressure fluctuations as the principal input quantity, it is important to generate a proof-of-concept for a real-time controller interacting with a TBL flow. For this matter, since the intricacies of the employment of wall-pressure are not yet known to the community, it was decided to first tackle the definition of a controller considering instantaneous wall-shear stress fluctuations instead. Wall-shear is a quantity that displays high levels of statistical coherence with off-the-wall streamwise velocity fluctuations and, therefore, renders it an ideal candidate to evince physical phenomena from a wall-based location. This is in reason of the superposition of a large-scale footprint onto the near-wall flow (see Ch. 1). Abbassi et al. [2017] documents the implementation and the TBL response to such a real-time controller, with encouraging findings.

The principal goal of this part of the work, in further contrast to the work of Abbassi et al. [2017], is to relate changes in the mean skin-friction drag to changes in the turbulence statistical integral measures of the TBL flow as a result of control in an attempt to unravel the physical mechanisms underlying changes in skin-friction as a result of control. For Zero-Pressure-Gradient (ZPG) uncontrolled TBL flows this has been detailed by Renard and Deck [2016] and Deck et al. [2014]; they relate integral measures of the TKE production (and a FIK decomposition [Fukagata et al., 2002] of the turbulent flow field) to the mean wall-shear stress. While it is known from aforementioned studies that the chosen actuator (a wall-normal blowing jet) can potentially reduce skin-friction drag, the goal of this work is to analyze the variation of wall-shear stress as a function of the chosen control mode (*i.e.* of reactive, real-time actuation targeting drag-producing large-scale structures). With a unique experimental dataset the relation of such integral measures of the flow to the mean wall-shear stress downstream of the control-action will be examined.

5.2. EXPERIMENTAL SETUP AND METHODOLOGY

5.2.1. TURBULENT BOUNDARY LAYER SETUP

Experiments were carried out in an open-return wind tunnel facility (W-Tunnel) at the Delft University of Technology. This facility has a contraction ratio of 4:1, with a square cross-sectional area of $0.6 \times 0.6\,\mathrm{m}^2$ at the inlet of the test section. Driven by a centrifugal fan, the flow at the test section's inlet can reach a velocity of up to $\sim 16.5\,\mathrm{m/s}$. A schematic of the facility is presented in Fig. 5.1a. More details regarding the design of the facility can be found in § 2.1.

5.2.2. MEASUREMENT TECHNIQUES

Time-series of the streamwise velocity component were acquired using Hot-Wire Anemometry (HWA). A TSI IFA-300 Constant Temperature Anemometer (CTA) was used, with a standard Dantec 55P15 boundary layer probe. Data were sampled at a rate of $f^+_{HW} = 3.16$ ($f_{HW} = 51.2\,\mathrm{kHz}$) with a 24-bit A/D conversion for an uninterrupted duration of $T_a = 150\,\mathrm{s}$ at each measurement point. This acquisition duration equates to $T_a U_\infty/\delta \approx 32\,000$ boundary layer turnover times; this was checked to be sufficient for converged spec-

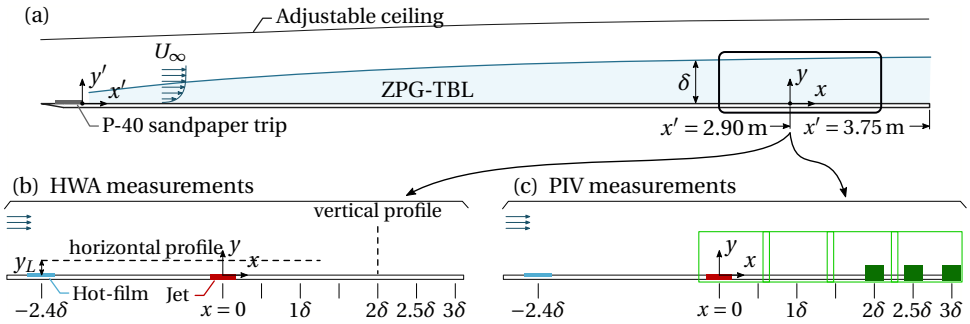

Figure 5.1.: (a) Schematic of the turbulent boundary layer test section at the Delft University of Technology. (b) Schematic indicating the locations of hot-wire measurements, with a streamwise profile taken at $y_L^+ = 3.9\sqrt{Re_\tau}$ and a wall-normal profile taken at $x = 2\delta$. (c) Positions of the fields of view for PTV (filled dark green) and PIV (open light green) measurements.

5

tral statistics at the lowest frequencies of interest. The hot-wire was calibrated in-situ by fitting King's Law to 17 points of increasing velocity. Measurement time-series were corrected for temperature drift following the procedure outlined by Hultmark and Smits [2010]. By mounting the probe to a dual-axis traversing system, with a step accuracy of 10 µm (smaller than 0.3 viscous units), a wall-normal profile consisting of 40 logarithmically-spaced points was acquired at $x = 2\delta$. A streamwise profile was also measured within the geometric center of the logarithmic region, at a location of $y_L^+ = 3.9\sqrt{Re_\tau} \approx 190$ ($y_L = 6.3$ mm), see Fig. 5.1b. The uncertainty in the hot-wire measurements was computed following the procedure of Smith et al. [2018], and resulted in uncertainties in the estimation of the average velocity and standard deviation (at $y^+ \approx 15$) of 0.26 % and 1.02 %, respectively.

Planar Particle Tracking Velocimetry (PTV) data were acquired with a Field Of View (FOV) of approximately $0.33\delta \times 0.28\delta$. A relatively small FOV was chosen to maximise the resolution in the viscous sub-layer, such that the wall-shear stress could be inferred directly from the velocity gradient at the wall, $\tau_w = \mu \partial\overline{u}/\partial y|_{y=0}$ (see § 5.7.1). Particle Image Velocimetry (PIV) was also employed in a planar Two-Dimensional Two-Component (2D2C) configuration, with a larger FOV spanning approximately $3.6\delta \times 0.8\delta$ (divided over two cameras). This PIV campaign was tailored to studying the flow well into the wake of the boundary layer. For both the PTV and PIV measurements, data were acquired at several streamwise locations, indicated in Fig. 5.1c with the blue filled rectangles (for PTV) and the green open rectangles (for PIV). Table 5.1 lists the acquisition parameters for both the PTV and PIV campaigns. LaVision Imager sCMOS cameras with a sensor size of 2650×2160 pix^2 were used in both types of acquisitions. All measurement sets comprised a total of 2000 statistically independent image pairs that were recorded at a frequency of 15 Hz. Illumination was provided by a Quantel Evergreen 200 Nd:YAG laser, operating in double-pulse mode with a maximum energy per pulse of 125 mJ. Finally, seeding was generated by an atomized glycol-water mixture, yielding an average particle size of ~ 1 µm.

Campaign	FOV size	# cam.	dt (µs)	l_f (mm)	$f_\#$	Res. (pix/mm)
PTV	$0.33\delta \times 0.28\delta$	1	15	200	11	114
PIV	$3.6\delta \times 0.8\delta$	2	35	105	8	18

Table 5.1.: Image acquisition parameters for the PTV and PIV campaigns, with dt being the time separation between images in one pair, and l_f and $f_\#$ the focal length and f-stop of the camera lens.

5.3. DESIGN AND CHARACTERIZATION OF ACTUATORS

Control experiments were only performed in the W-tunnel facility at Delft University of Technology. Control experiments required several pieces of hardware: input sensors, actuators and real-time controllers. Different input sensors and controllers were used across this work, and an introduction to each input sensor type will be provided in the relevant section of this dissertation. The actuators, however, were common to all control experiments. Thus, a review of the design choices and parameters is included hereby.

During this study, control is performed in real-time of the large-scale structures in a TBL flow. The requirement to develop an effective actuator is thus central for the successful implementation of such a control strategy. Given the challenge to impart a significant control action on large-scale structures in the logarithmic region, it is necessary to design an actuator device that is able to effectively target those, without generating unwanted additional drag. For this reason, the most effective configuration for such an actuator is one whereby the device is embedded in the wall of the wind tunnel facility. For effective real-time active control for skin-friction control, selectivity is key. In particular, skin-friction is a mean quantity; nevertheless, instantaneous, as well as spatial, fluctuations occur. For this reason, the work is based on a control strategy which is able to influence skin-friction in a time-varying sense and is spatially selective (from Ch. 5 onwards). Spatial selectivity derives from the natural behavior of LSMs, which show alternating high and low-momentum zones (causing an increase and decrease in instantaneous skin-friction, respectively) both in the streamwise and spanwise directions (see Fig. 5.2). A controller that aims at the opposition of turbulence drag-inducing motions, will therefore target the high-speed zones.

In summary, the principal requirement is to design an actuator that is effective enough to interact with structures in the logarithmic region while, at the same time, minimize the interference with the natural development of the wall-bounded flow.

For this reason, a non-zero net mass flux blowing jet is chosen as the actuator. Since its exit velocity and frequency response can be tuned with relatively simple adjustments to the hardware, this actuator is ideal for tuning the region of interaction between the jet flow and the grazing crossflow. The development of a jet in crossflow in a TBL flow is such that an upwash is created downstream of the injection point as a result of wall-normal momentum injection. Additionally, the steady jet in crossflow creates a counter-rotating vortex pair (CVP), originating from the roll-up of the jet plume as the mean shear of the turbulent crossflow transfers streamwise momentum to it. Off the center-line, this CVP generates a downwash [New et al., 2003, Sau and Mahesh, 2008, Mahesh, 2013]. For a thorough overview of the actuators that have been studied and developed in the litera-

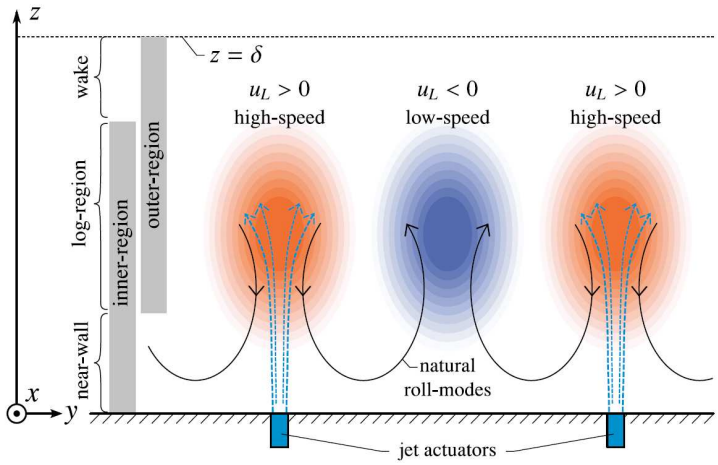

Figure 5.2.: Schematic of coherent large-scale structures controlled by wall-normal blowing jets on a spanwise wall-normal plane. Taken from Abbassi et al. [2017].

ture for active flow control, the work of Cattafesta and Sheplak [2011] is a recommended read.

5.3.1. ACTUATOR ARCHITECTURE

The principal target of the jet actuator is to interact with large-scale motions convecting within the logarithmic region (*i.e.* point $\mathscr{T}$ in Fig. 5.4) of the TBL flow based on an input signal measured a distance s_1 upstream of the control location (*i.e.* point $\mathscr{I}$ at $y = y_L$ in Fig. 5.4). Furthermore, the actuator is required to produce streamwise-persistent features upon exhausting into the turbulent crossflow for prolonged control authority downstream of the control point. Thus, the jet flow exhausts in the grazing TBL flow through a rectangular exit slit. The slit was strongly elongated in the streamwise direction and comprised dimensions of 15 mm × 1.5 mm (in the x and z directions, respectively), or approximately $0.2\delta \times 0.02\delta$ (see Fig. 5.3). The streamwise elongation of the exit slit ensures the formation of a more persistent vortical structure in the streamwise direction, compared to the case when the jet exit is circular in shape [Gutmark et al., 2008, Pokharel and Acharya, 2021].

At the same time, given the highly three-dimensional nature of the TBL flow, it is essential to consider that actuation will need to tackle instantaneously spanwise-varying conditions and increase the region of influence of the control system. Thus, an architecture consisting of an array of jet actuators (instead of a single actuator) is necessary for successful implementation of a control framework with sufficient control authority to quench drag-producing large-scale turbulent structures. The spanwise separation between adjacent jets was established following the study of Hutchins et al. [2011], whereby point-to-point two-dimensional correlation maps were presented of the streamwise velocity coherence in the logarithmic region of a TBL. In particular, the peak-to-

peak distance between the large-scale high-correlation zones was reported to be 0.3δ. This distance is also chosen as the spanwise separation between consecutive jet actuators in this work.

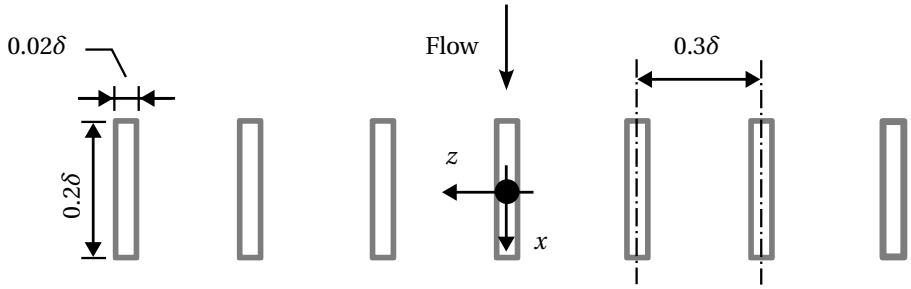

Figure 5.3.: Schematic displaying the layout of the actuator array designed for the real-time control experiments described in this dissertation and employed for all flow control experiments.

Compressed dry air is drawn from the laboratory pneumatic system and feeds into the actuator, which is operated in an on/off state using an electrically actuated, nominally closed, binary solenoid valve (FESTO MHJ-10-S-2). This valve has a maximum switching frequency, according to the manufacturer, of 1 kHz. Figure 5.4 illustrates a schematic of the installation and working principle of the jet actuator in the TBL crossflow, as integrated in the control system (with $\mathscr{H}$ being an arbitrary control law). By way of characterization experiments, described in the following section, the frequency response was quantified as well as the jet trajectory into the TBL crossflow as a function of the jet exit velocity.

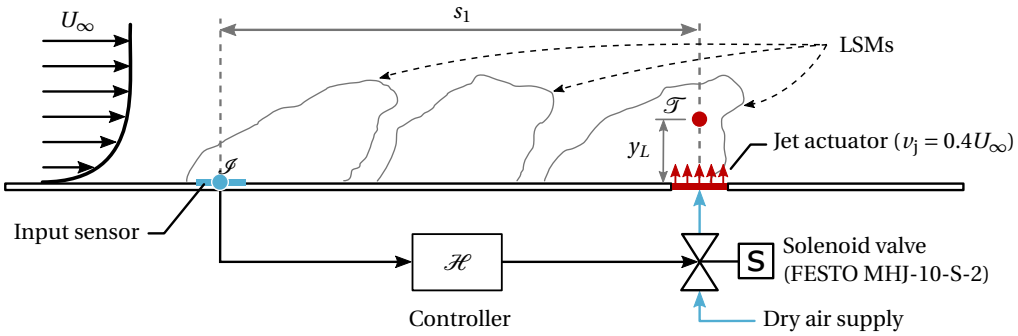

Figure 5.4.: Two-dimensional schematic of the control system for real-time boundary layer manipulation, integrated in the W-Tunnel facility.

5.3.2. CHARACTERIZATION OF THE JET ACTUATORS

Since the aim of control is to manipulate large-scale structures in the logarithmic region, the actuator should have enough control authority to reach such wall-normal locations where LSMs are most energetic. Thus, the actuator's (jet in crossflow) wake needs to trail within this region to achieve a proper interaction. The jet flow may not reach a sufficient height when the jet exit velocity, v_j, is too low. Conversely, if v_j is too high, the jet's trajectory may penetrate the edge of the boundary layer, thereby altering the free-stream flow and generating unwanted additional drag. To study how the jet trajectory depends on its exit velocity, a characterization experiment was conducted. The wall-normal jet flow was operated in a continuous on-state at several velocity ratios, $r = v_j/U_\infty$. The mean velocity field was inferred from two-dimensional two-component particle image velocimetry (2D2C-PIV) performed with 2000 image pairs, and over a FOV spanning roughly 1.8δ in x and 0.35δ in y. The trajectory of the jet is taken as the streamline emanating from the center of the jet exit plane, as shown in Fig. 5.5a for several velocity ratios. It is evident that the two highest velocity ratios of $r = 0.5$ and 0.6 result in trajectories with a high likelihood of penetrating the upper edge of the logarithmic region (here indicated with the dashed line at $y/\delta = 0.2$) within $x/\delta < 0.5$. As expected, with a lower velocity ratio of $r = 0.4$, the jet trajectory remains within the logarithmic region for a prolonged distance ($\sim 1\delta$) and is therefore adopted in the current study. The momentum coefficient for $r = 0.4$ is $C_\mu = (\rho_j v_j^2 l_j)/(\rho_\infty U_\infty^2 \delta) = 0.75$, with $l_j = 0.15$ mm being the length of the jet exit-slit. Velocity ratios lower than $r \leq 0.3$ cause the plume to remain within the logarithmic region for a longer streamwise extent. However, the feed system, including a pressure regulator, was not able to produce a stationary flow across the slit, as relatively large velocity fluctuations were observed over time.

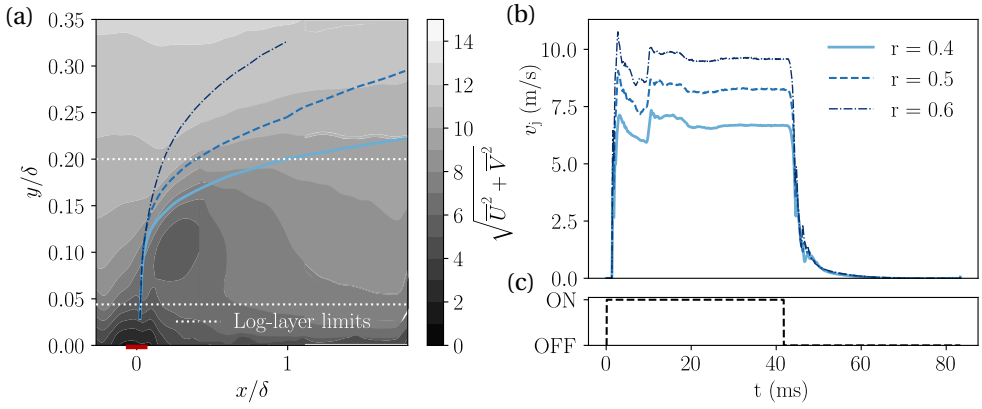

Figure 5.5.: (a) Trajectories of the wall-normal jet actuator flow within the grazing TBL flow, for three different velocity ratios. Lower and upper bounds of the logarithmic region are also indicated. A filled contour in the background shows the magnitude of in-plane velocity for the $r = 0.4$ case; the jet exit slit is indicated with a red line. (b) Phase-averaged jet exit velocity over 2048 on/off cycles. (c) Periodic valve command over one period of $T_j = 1/f_j \approx 83$ ms.

Latency is essential to consider in designing an opposition control system, for timing purposes as well as the frequency response of the jet actuator. The hardware latency associated with the time it takes for the compressed air to accelerate through the valve, pneumatic tubing and flow conditioners, was quantified with an experiment: the valve was operated at a constant frequency f_j, with a 50 % duty cycle (for a total duration of 2048 periods). This frequency was based on a statistical time-scale of the LSMs, following $f_j = U_c/(2l_{LSM}) \approx 12$ Hz, where U_c is the convection velocity taken at the geometric center of the logarithmic region, $y_L^+ = 3.9\sqrt{Re_\tau}$, and $l_{LSM} = 6\delta$ is the statistical length of a high- or low-speed region [Hutchins and Marusic, 2007, Baars and Marusic, 2019]. A time-series of the jet exit velocity was measured with HWA as described in § 2.3.2, but with the difference being the use of a Dantec 55P11 probe. This probe was placed at $y = 3$ mm above the center of the jet exit slit. Phase-averaged responses of the jet exit velocity (with $t = 0$ being the instant of the valve on-command) over all periods are presented in Fig. 5.5b. The velocity sharply rises approximately 1 ms after the on-command, and overshoots its steady-state value after roughly 3 ms. Subsequently, steady-state is reached at roughly 6 ms. When the valve receives the off-command, the shut down phase lasts for approximately 10 ms before the exit velocity returns to zero. It was confirmed that shortening the period of actuation did not alter the start- and shut-down transients. Hence, the maximum frequency for which an on- and off-state is reached is constrained by a 6 ms start-up time and a 10 ms shut-down time; this yields a frequency response of $f_{act} \approx 63$ Hz. Table 5.2 reports the main values associated with the latency of the actuator hardware.

Variable	Description	Value
$\tau_{a,1}$	Start-up time of the valve	3 ms
$\tau_{a,2}$	Time required for jet plume to reach the logarithmic region	3 ms
$\tau_{a,3}$	Shut-down time	10 ms

Table 5.2.: Table reporting the latency values of the actuator hardware

5.4. CONTROL SYSTEM ARCHITECTURE

From a high-level perspective, the control system consists of a wall-embedded sensor and actuator, and a real-time target machine. Downstream flow measurements are performed to assess the controller's performance. For the controller to be effective, it is critical for the input sensor to provide sufficient information to estimate the state of the to-be-controlled plant (*i.e.*, the TBL flow). Similarly, the actuator is required to have enough control authority to generate a significant effect in the logarithmic region, where the large-scale structures are most energetic.

The control logic aims at actuating upon structures that convect in the logarithmic region and that leave a footprint at the wall [Marusic et al., 2010, Baars et al., 2016]. Similar to Abbassi et al. [2017], a Dantec 55R47 glue-on hot-film was selected as the surface-mounted input sensor. Its sensing element measures 0.1 mm in the streamwise direction ($\delta x_{HF}^+ = 3.2$) and 0.9 mm ($\delta z_{HF}^+ = 28.8$) in the spanwise one. The sensor is deposited on

a ~ 50µm thick ($1.6l^*$) KaptonT foil. This thickness makes the hot-film a non-intrusive sensor, since it can be considered hydrodynamically smooth. The sensor was glued in the spanwise center at $x = -2.4\delta$ ($x = -0.17$ m), to a polycarbonate insert within floor panel $\mathscr{C}$ (see Fig. 5.1). Its lead-wires were routed downstream and out of the tunnel through 0.4 mm diameter holes.

The hot-film was operated using a second CTA channel in the TSI IFA-300 anemometer, also used for operating the hot-wire (§ 2.3.2). The sensor operating temperature was set at 90 °C, yielding an overheat ratio of 1.18. No sensor calibration was performed or applied, and so the raw voltage-output of the CTA bridge was fed directly into the controller. Working with the raw voltage as proxy for the wall-shear stress is justified, given that the control action is binary (controlling an on/off jet) and only involves thresholding around the mean value of the input signal. Moreover, the system identification procedure described in § 5.5 is performed with the raw voltage signal, and it was verified that coherence characteristics are retained even without calibrating the sensor.

For actuation, a non-zero net mass flux blowing jet is used. Since its exit velocity and frequency response can be tuned with relatively simple adjustments to the hardware, this actuator is ideal for tuning the region of interaction between the jet flow and the grazing crossflow. The development of a jet in crossflow is such that an upwash is created downstream of the injection point as a result of wall-normal momentum injection. Additionally, the steady jet in crossflow creates a Counter-rotating Vortex Pair (CVP), originating from the roll-up of the jet plume as the mean shear of the crossflow transfers streamwise momentum to it. Off-centerline, this CVP generates a downwash [New et al., 2003, Sau and Mahesh, 2008, Mahesh, 2013]. Note that an investigation of the off-centerline behaviour of the boundary layer is not part of the current study; the sole focus is on the impact of control directly downstream of the injection point ($z = 0$). The jet flow exhausts in the grazing TBL flow through a rectangular exit slit. Given the requirement of the control system to be persistent downstream, the slit was strongly elongated in the streamwise direction and comprised dimensions of 15 mm × 1.5 mm (in the x and z directions, respectively), or approximately $0.2\delta \times 0.02\delta$. The streamwise elongation of the jet exit slit ensures the formation of a more persistent vortical structure in the streamwise direction, compared to the case when the jet exit is circular in shape [Gutmark et al., 2008, Pokharel and Acharya, 2021].

Compressed dry air feeds into the actuator, which is operated in an on/off state using an electrically actuated, nominally closed, binary solenoid valve (FESTO MHJ-10-S-2). By way of PIV characterization experiments, described in § 5.3, the frequency response was quantified as well as the jet trajectory into the TBL crossflow as a function of the jet exit velocity. For the frequency response, latencies were inferred from the characterization experiments, and are associated with the time it takes for fluid to accelerate through the pneumatic components ($\tau_{a,1} \approx 3$ ms), for the jet plume to reach the logarithmic region ($\tau_{a,2} \approx 3$ ms), and for the jet to shut-down ($\tau_{a,3} \approx 10$ ms). Even though the solenoid valve has a maximum switching frequency of 1 kHz, the maximum operating frequency for which on- and off-states are reached is lower due to the latencies and equals $f_{act} \approx 63$ Hz, given the 6 ms start-up time and 10 ms shut-down time. Concerning the exit velocity, in the final control configuration it was set at $v_j = 0.4U_\infty$ ($v_j = 6$ m/s). This ensured that the jet plume remained within the bounds of the logarithmic region for

a downstream distance of approximately 1δ. As mentioned in § 5.3, a lower exit velocity can be beneficial to ensure a lower disturbance on the TBL flow; however, technical limitations of the compressed air supply did not allow operation at lower r.

5.5. SYSTEM IDENTIFICATION PROCEDURE

The Linear Coherence Spectrum (LCS) evaluates the stochastic degree of coupling between the voltage fluctuations of the wall-mounted hot film, $e(t)$ [the input] and the streamwise velocity fluctuations within the logarithmic region, $u(t)$ [the output], as a function of the streamwise separation distance s. The LCS is defined as [Bendat and Piersol, 2000],

$$\gamma_L^2(f,s) = \frac{|\langle E(f)U^*(f,s)\rangle|^2}{|\langle E(f)\rangle|^2|\langle U(f,s)\rangle|^2}, \tag{5.1}$$

where $|\cdot|$ denotes the modulus. Here $E(f)$ and $U(f,s)$ are the temporal FFT's of the input and output signals, respectively. The coherence is bounded by 0 (no coherence) and 1 (perfectly coherent) and is presented in Fig. 5.6a as a function of $f\delta/U_\infty$ and separation distance, s/δ. With an increase in s, the coherence decays only marginally and its maximum value at low frequencies still remains at a level beyond 0.35 at the most downstream position. Figure 5.6b shows the LCS for $s = 2.4\delta$ in specific, which corresponds to the sensor-actuator spacing that was implemented (the reasoning for this is provided in § 5.5.1). Fig. 5.6b shows an initial trend of coherence that is nearly constant for low frequencies up to $f\delta/U_\infty \approx 0.1$ with $\gamma_L^2 \approx 0.3$, which is proven to be a sufficient coherence-magnitude for an opposition control scheme on the large-scale energy (in terms of its binary accuracy, see § 5.5.2). Coherence drops sharply for smaller scales beyond $f\delta/U_\infty \gtrsim 0.1$, which renders it impossible to actuate upon those turbulence scales.

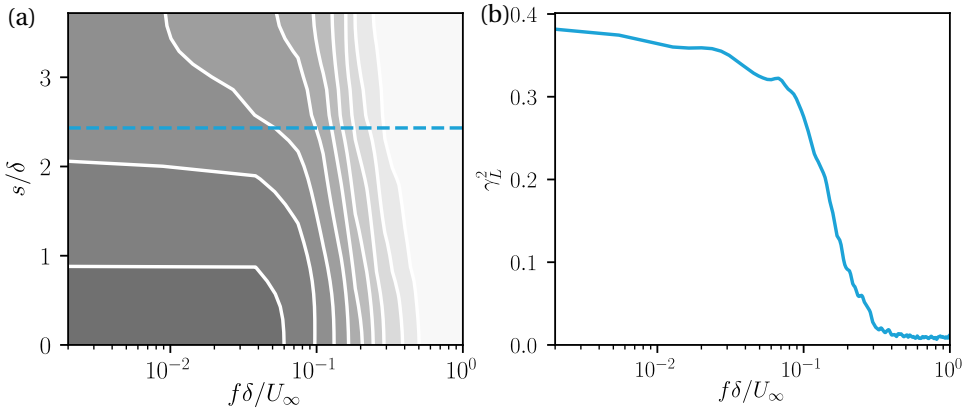

Figure 5.6.: (a) Spectrogram of $\gamma_L^2(f,s)$, as a function of frequency and the separation distance s between the wall-mounted hot film and velocity fluctuations in the logarithmic region. Filled iso-contours correspond to magnitudes of 0.05:0.05:0.5. (b) One coherence spectrum for $s = 2.4\delta$.

An input-output relation can be inferred from a calibration experiment in order to relate the input's voltage fluctuations to the velocity fluctuations at the downstream target-point (see Fig. 5.7); allowing for an LSE of the latter during real-time control. Given the presence of significant coherence, the linear transfer kernel, $H_L(f)$, will relate an estimate of the output (denoted with a hat) and the input signal in the frequency domain, following

$$\widehat{U}(f,s) = H_L(f,s)E(f). \tag{5.2}$$

The complex-valued kernel has a frequency-dependent gain and phase, given by

$$|H_L(f,s)| = \frac{|\langle E(f)U^*(f,s)\rangle|}{\langle |E(f)|^2\rangle}, \text{ and} \tag{5.3}$$

$$\phi_H(f,s) = \arctan\left\{\frac{\mathscr{I}\left[\langle E(f)U^*(f,s)\rangle\right]}{\mathscr{R}\left[\langle E(f)U^*(f,s)\rangle\right]}\right\}, \tag{5.4}$$

where $\langle E(f)U^*(f,s)\rangle$ is the input-output cross-spectrum.

Both the input sensor and actuator of the control system interact with the grazing flow (see Fig. 5.7 for a schematic representation of the control system). The streamwise sensor-actuator spacing, s, has important implications given that an increase in s will result in a progressive loss-of-coherence between the turbulence velocities at both stations. Practically, there is a minimum (non-zero) spacing that is realizable for two primary reasons: (1) coherent structures in TBL flow possess an average streamwise inclination angle of 14° to 16° due to the mean shear [Hutchins et al., 2012, Baars et al., 2017]; their footprints are only visible to the wall-based sensor after their signature has passed in the logarithmic region, and (2) input processing introduces latencies in addition to the one of the actuator described earlier. Hence, only with a non-zero distance s it can be guaranteed that there is enough time to act upon LSMs in real-time. In order to inspect whether a sufficient correlation remains present between sensor and actuator for a non-zero spacing s, a Single-Input/Single-Output (SISO) linear time-invariant system analysis was applied as reported in Appendix 5.5. A sufficient level of linear coherence was observed between the input and target locations (points $\mathscr{I}$ and $\mathscr{T}$ in Fig. 5.7), particularly for a sensor-actuator spacing of $s = 2.4\delta$ that is used in the current study. A motivation for this spacing is presented later on. Given the significant coherence, a linear transfer kernel, H_L, relating the streamwise velocity $u(t)$ in the logarithmic region (the target point) to the voltage signal $e(t)$ of the hot-film (the input point) was determined through an LSE procedure based on data of a control-off experiment (Appendix 5.5). A bode plot of the frequency-dependent kernel $H_L(f)$ is shown in Figs. 5.8a,b. A maximum gain of $|H_L| \approx 2.6\,\mathrm{ms}^{-1}/\mathrm{V}$ occurs at $f\delta/U_\infty \approx 0.06$. The gain decays at higher frequency and is retained up to a cut-off frequency of $f\delta/U_\infty \approx 0.7$, at which the coherence drops below a threshold of $\gamma_L^2 = 0.05$. Beyond this frequency, the scales are incoherent and the kernel's phase becomes random.

Instead of performing an estimation in spectral space following Eq. (5.2), the time-domain convolution equivalent is embedded on a real-time controller. The convolutional estimate is $\widehat{u}(t) = (h \circledast e)(t)$, with h being the inverse FFT of the frequency-domain kernel, $h(\tau) = \mathscr{F}^{-1}\left[H_L(f)\right]$ (and h thus resembles a Finite Impulse Response (FIR) filter for the input data). The inverse FFT over the full range of frequencies for generating

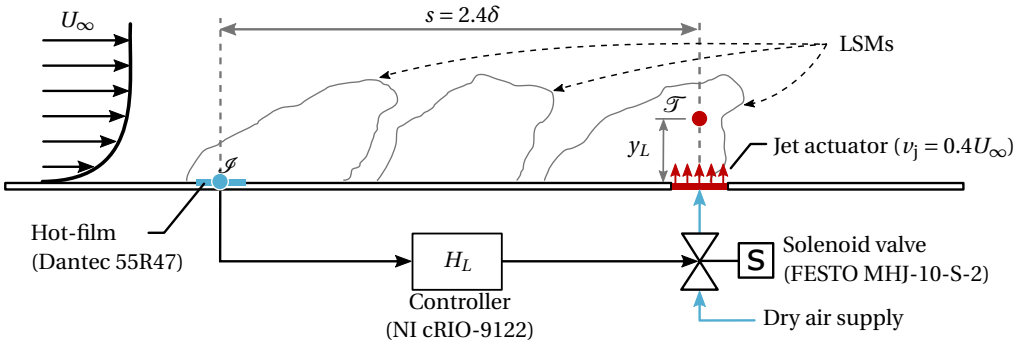

Figure 5.7.: Schematic of the control system for real-time boundary layer manipulation, integrated in the W-Tunnel facility.

$h(\tau)$ from $H_L(f)$ yields a kernel in the physical domain with the length of one ensemble size ($N = 2^{17}$, thus $\Delta t_N = 2.56$ s). However, given that an FIR convolution in real-time introduces an inherent delay of half the filter-width, the kernel $h(\tau)$ is only retained over a temporal horizon of $\tau_H/2 = 7.5$ ms (centered at the peak-instance of the FIR filter, see the temporal extent of the dotted kernel in Fig. 5.8c). The shortened kernel length ensures that the sensor-actuator spacing of $s = 2.4\delta$ is attainable in real-time. Note that omitting the tails of the kernel is justified given the negligible contribution to the estimate. Future improvements of a short kernel can be based on the Wiener-Hopf framework so that causality of the kernel is taken into account [Martini et al., 2022].

Finally, the control loop was implemented on a National Instruments Compact Reconfigurable Input-Output (NI-cRIO-9122) machine with an embedded Field Programmable Gate Array (FPGA) chassis (cRIO-9022). The control logic was implemented in LabVIEW on the FPGA chip with a loop frequency of $f_{FPGA} = 2$ kHz, and FPGA processing was conducted with a 16-bit fixed-point precision. The kernel $h(\tau)$ was down-sampled to the loop frequency of the FPGA controller ($f_{HW} \rightarrow f_{FPGA}$). When operating in real-time, the input signal was also sampled at the loop frequency with the aid of an analog-to-digital NI-9234 input module. Trigger commands were provided to the solenoid valve with the aid of a 5V analog signal that was relayed through a NI-9472 digital output module.

5.5.1. CONTROL LOGIC DEFINITION

For the control problem the actuator interacts with the high- and low-speed LSMs. Based on the input sensor and the pre-identified transfer kernel, the controller is able to estimate the flow state $\hat{u}$ at the target-point through the convolution mentioned before: $\hat{u}(t) = (h \circledast e)(t)$. Note that input signal $e(t)$ is a zero-mean signal since the controller only acts upon the fluctuations. The zero-mean signal was obtained in real-time by the subtraction of a converged running mean over a 2 s interval duration [this accounts for a potential drift in the hot-film reading, Jimenez et al., 1981]. Based on the real-time estimate $\hat{u}(t)$, high- and low-speed zones are then targeted following a nominal control

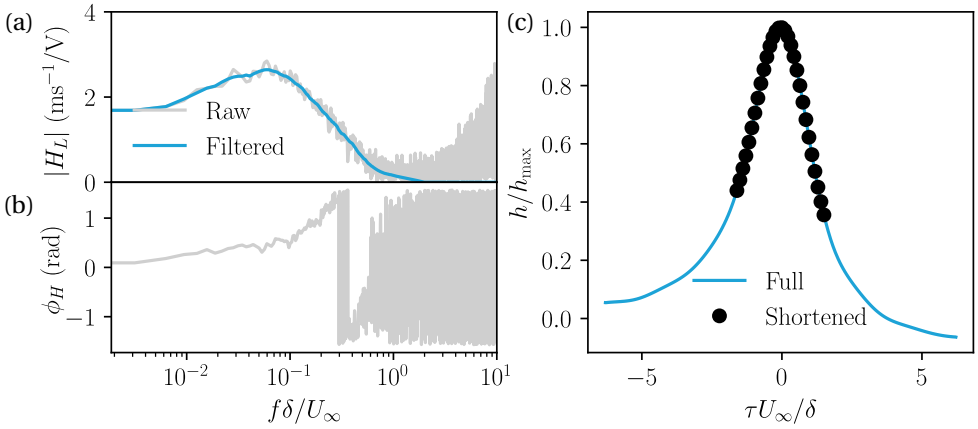

Figure 5.8.: (a,b) Bode plot of kernel $H_L(f)$ with the frequency-dependent gain and phase. The gain is shown with both the raw data and a bandwidth-moving filtered version (25% bandwidth). (c) Kernel in physical time, both at the sampling frequency of the calibration experiment (solid line; $f_{HW} = 51.2\,\text{kHz}$) and at the controller frequency (round markers; $f_{FPGA} = 2\,\text{kHz}$).

law:

$$v_j(t) = \begin{cases} 0.4U_\infty, & \text{if } \hat{u}(t) \geq 0 \\ 0, & \text{if } \hat{u}(t) < 0 \end{cases} \tag{5.5}$$

with v_j being the binary velocity state of the jet actuator. This *opposition* controller will thus only actuate on those large-scale events which are estimated to be more drag-producing than the mean flow. A *reinforcing* controller was also implemented, where the control law is inverted and the actuator targets a low-speed region instead. In order to also isolate the effect of operating the jet in a synchronized manner with respect to the incoming LSM structures, versus a desynchronized manner (in essence no real-time control), a *desynchronized* control law was also implemented following Abbassi et al. [2017]. For the desynchonized control, an on/off signal from the opposition control case was used for actuation, irrespective of the input signal. Given the sensor-actuator spacing s, the control system needs to digitize the analog voltage-input signal, convolve it with the transfer kernel and generate the control-output within the time it takes for the LSM structures to convect to the target point. With $s = 2.4\delta$ ($s = 0.17\,\text{m}$) and $U_c = 9.9\,\text{m/s}$, this duration is $\tau_{conv} = s/U_c \approx 17.2\,\text{ms}$. The sensor-actuator spacing was chosen based on an analysis of the delays inherent to a real-time controller. First, as mentioned in § 5.5, the real-time convolution of the input signal with the FIR-like kernel requires half the temporal horizon, thus $\tau_H/2 = 7.5\,\text{ms}$. Additionally, a delay of $\tau_{FPGA} = 0.5\,\text{ms}$ is added due to the controller looping at $f_{FPGA} = 2\,\text{kHz}$. As explained in §5.4, the actuator itself also introduces two sources of lag: $\tau_{a,1} \approx 3\,\text{ms}$ and $\tau_{a,2} \approx 3\,\text{ms}$. In total, the controller requires the following time for providing an output:

$$\tau_C = \tau_H/2 + \tau_{FPGA} + \tau_{a,1} + \tau_{a,2} \approx 14\,\text{ms}. \tag{5.6}$$

Since $\tau_{conv} > \tau_C$ the sensor-actuator spacing of $s = 2.4\delta$ yields a slightly conservative setup. However, this was deliberately done so that control that would be 'too early' could also be investigated. But, for the nominal opposition control mode presented in this paper an extra delay of 7 control loops (*i.e.,* 3.5 ms) was implemented for correct timing of the opposition and reinforcing control modes.

5.5.2. PERFORMANCE EVALUATION OF THE STATE ESTIMATION

The state of the boundary layer that the controller actuates upon, $\widehat{u}(t)$, is an estimate. To gauge the performance of the controller, the *binary accuracy* of the estimated state will be considered, $\widehat{u}(t)$, that the control actuates upon. Fig. 5.9a displays the measured streamwise velocity $u(t)$, as well as the LSE-based estimate simulating real-time conditions. Note that the estimate $\widehat{u}(t)$ would be shifted by half the kernel's horizon length as a result of the real-time convolution, but this shift is omitted for evaluating the binary accuracy. Since the controller only actuates based upon the estimated signal's sign, it is possible to binarize $u(t)$ and $\widehat{u}(t)$ and compare them directly. At every instant, a true positive (TP) prediction is made when both signals are positive, whereas both signals being negative will yield a true negative (TN) prediction. Additionally, false positive (FP) and false negative (FN) outputs will occur if $u(t) < 0$ and $\widehat{u}(t) \geq 0$, or vice versa, respectively. The binary accuracy (BACC) is then defined as,

$$\mathrm{B}ACC = \frac{T_{TP} + T_{TN}}{T_a}, \tag{5.7}$$

with the numerator representing the cumulative time that the estimate is true positive (T_{TP}) and true negative (T_{TN}). Note that a BACC of unity does not mean that the $\widehat{u}(t) = u(t)$, but only that $sgn[\widehat{u}(t)] = sgn[u(t)]\ \forall\ t$. Fig. 5.9b reports the binary performance with BACC equal to 72.1%. This value is significantly larger than 50 % (which would indicate a random process) and justifies the wall-based sensing approach for reactive real-time control. In fact, albeit the imperfect binary accuracy, results in later sections corroborate a statistically correct implementation and targeting of the large-scale structures.

5.6. RESPONSE OF THE TURBULENT BOUNDARY LAYER FLOW

5.6.1. MEAN FLOW AND TURBULENCE KINETIC ENERGY

Wall-normal profiles of the mean velocity and streamwise TKE (based on the hot-wire profile taken at $x = 2\delta$) aid in explaining the effect of control on the TBL, and allow for a direct comparison to the work of Abbassi et al. [2017]. Fig. 5.10a presents the profiles for both the uncontrolled flow and the opposing, reinforcing and desynchronized control cases. It is evident that only in the logarithmic region a velocity deficit manifests itself for the control cases, in comparison to the uncontrolled flow. This is consistent with the jet injecting momentum in the wall-normal direction, thereby reducing streamwise momentum from the grazing TBL flow [Smith, 2002, Mahesh, 2013]. At $x = 2\delta$, the jet plume penetrates primarily within the logarithmic region (recall Fig. 5.5a and its discussion), while the mean velocity in the inner region already recovered to the uncontrolled flow

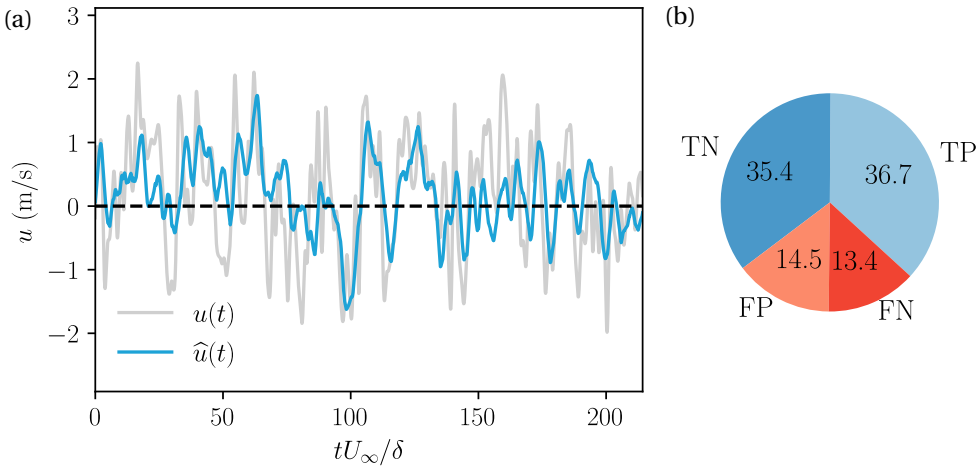

Figure 5.9.: (a) Sample portion of the measured streamwise velocity $u(t)$, at $x = 0$ and $y = y_L$, compared to the estimated velocity $\widehat{u}(t)$. (b) Pie chart of the binary performance of the estimation, with in blue the true positive (TP) and true negative (TN) predictions; in red the false positive (FP) and false negative (FN) ones (values are in percentage).

condition. Since the jet is activated for the same fraction of time amongst all three control modes (50 %), the wall-normal momentum being injected into the boundary layer is equal and thus explains the collapse of the profiles in Fig. 5.10a.

Distinctions between the control modes become apparent from the streamwise TKE, $\overline{u^2}$, presented in Fig. 5.10b. All profiles collapse in the wake and show that the control influence is confined to the inner region. Near the upper edge of the logarithmic region, a hump of $\overline{u^2}$ occurs for all control modes and increases when moving from the opposing, to the desynchronised, and finally to the reinforcing control case. This trend is reflective of the presence of an internal shear layer between the upper side of the jet plume and the grazing TBL flow [Sau and Mahesh, 2008]. The opposing control case lowered the u-variance the most, below $y/\delta \approx 0.1$. This reduction is not only apparent in the logarithmic region, but persists down to the wall.

To analyse how the energy across all turbulent scales is changed as a result of control, premultiplied energy spectra are considered in a similar manner as in Fig. 2.3b. Fig. 5.11a displays the spectrogram $f^+\phi^+_{uu,\mathrm{des}}(f,y)$ for the desynchornized case with the black isocontours, overlayed on a filled contour that represents the percentage difference in spectrograms between said case ($\phi_{uu,\mathrm{des}}$) and the uncontrolled flow ($\phi_{uu,\mathrm{unc}}$), following

$$\Delta\phi_{uu} = \frac{\phi_{uu,\mathrm{des}} - \phi_{uu,\mathrm{unc}}}{\phi_{uu,\mathrm{unc}}} \times 100. \tag{5.8}$$

A region of remarkably higher energy is observed above $y/\delta \approx 0.1$ for all frequencies. This relates to the location where an increase in streamwise TKE was also observed in Fig. 5.10b (note that $\overline{u^2} = \int \phi_{uu}\mathrm{d}f$). Given the nature of the jet actuator, not only wall-

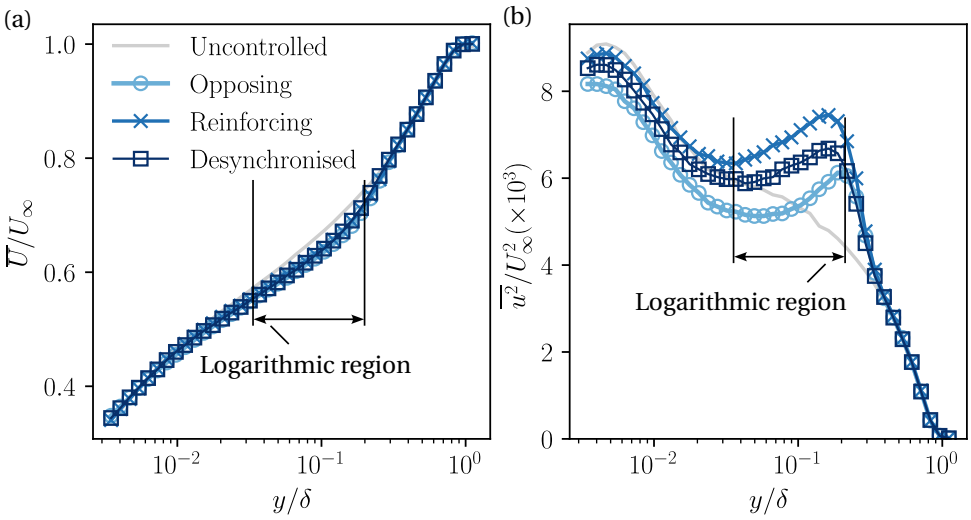

Figure 5.10.: (a) Wall-normal profiles of mean streamwise velocity, $\overline{U}/U_\infty$, and (b) streamwise TKE, $\overline{u^2}/U_\infty^2$, for the uncontrolled case, as well as for the three control modes, at $x = 2\delta$.

normal momentum is imparted to the flow, but the shear layer developing between the jet plume and the TBL flow enhances turbulent fluctuations. This increase in TKE is thus broadband in nature and is unavoidable with the current type of actuator flow. In fact, actuation by means of unsteady wall-normal momentum injection biases the effect of control towards an increase in energy in the logarithmic region and wake of the TBL, irrespective of the control law. However, this was measured not to have an effect on the absolute skin-friction, as will be presented in § 5.7. Below $y/\delta \approx 0.1$, a slight decrease in energy is observed. The superposition effect that the jet actuator was suggested to have in §5.6.1 also appears to be present over a vast frequency band in proximity to the wall ($0.1 < f\delta/U_\infty < 10$). To highlight the changes in spectral energy that the turbulence in the boundary layer undergoes as a result of purely the control logic, and not the actuator-induced flow, reactive control cases are compared to the desynchronised one.

Figs. 5.11b and 5.11c present the percentage difference in the spectrograms with respect to the desynchronised control mode for the TBL targeted by opposing and reinforcing control, respectively. An almost perfect symmetry is visible: a region of reduced energy for opposing control is juxtaposed to one of increased energy for the reinforcing control mode, with a maximum effect residing around the geometric center of the logarithmic region at $y_L^+ = 3.9\sqrt{Re_\tau}$ (indicated by the dashed line). A reduction of ~ 40 % in ϕ_{uu} in the opposing mode is accompanied by a ~ 45 % increase in spectral energy for the reinforcing case. For both modes, the largest change in energy is concentrated at $f\delta/U_\infty < 0.1$, which indicates a successful targeting of the low-frequency (*i.e.,* large wavelength) structures in the logarithmic region. Recall from § 5.5 that the higher-frequency (smaller-scales) cannot be targeted with the real-time controller due

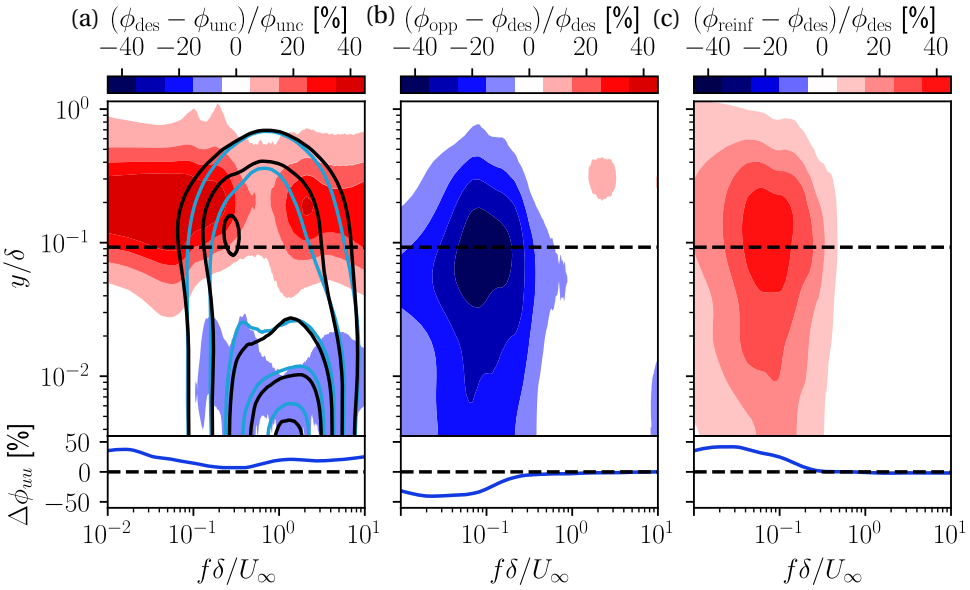

Figure 5.11.: (a) Filled contours: percentage difference in the premultiplied energy spectrograms of the streamwise velocity, between the TBL affected by desynchronised control and the uncontrolled case. Black contours: spectrogram of the TBL flow subject to desynchronised control (contour levels at 0.4:0.4:2.0). Light blue contours: spectrogram of the uncontrolled TBL flow (contour levels at 0.4:0.4:2.0). (b) Percentage difference spectrograms between the flow subject to opposing control and the desynchronised case. (c) Percentage difference spectrograms between the flow subject to reinforcing control and the desynchronised case. Difference in the energy spectrum at y_L shown below the contour plots in (a,b,c) for the corresponding case. All spectrograms were acquired at $x = 2\delta$ and filtered with a bandwidth-moving filter of 25% in width.

to the absence of input/output coherence at these scales. Energy spectra in the geometric center of the logarithmic region (displayed explicitly in the insets below the contour plots in Fig. 5.11) furthermore reveal how the percentage difference collapses to zero for $f \gtrsim 0.3U_\infty/\delta$.

5.6.2. CONDITIONALLY AVERAGED VELOCITY FLUCTUATIONS

Conditional averages of the streamwise velocity were constructed for examining the local response of the TBL flow. Time-series of the streamwise velocity acquired using HWA at all 40 wall-normal locations in the boundary layer were conditioned on the positive-gradient zero-crossings of the estimated velocity signal, $\widehat{u}(t)$, following

$$\widetilde{u}(y,\tau) = \langle u(y,t) \mid \left(\widehat{u}(y,t) = 0 \ \wedge \ \partial\widehat{u}/\partial t(y,t) > 0\right)\rangle, \tag{5.9}$$

with τ being the time coordinate of the conditional average and $\tau = 0$ corresponding to the positive-time-gradient zero-crossing. The present work considers the conditional average in a variable time interval (VTI) formulation [Erengil and Dolling, 1991]. Given a signal $\alpha(t)$, it can be binarized to obtain $\overline{\alpha}(t) = 1$ where $\alpha(t) \geq 0$ and $\overline{\alpha}(t) = 0$ otherwise. In the context of the work, this signal corresponds to the estimated velocity signal $\widehat{u}(t)$, which is thresholded to create the on/off signal that drives the actuator in real-time. For the VTI analysis, following Eq. (5.9), the signal is conditioned $\alpha(t)$ on the rising edges of the binarized signal $\overline{\alpha}(t)$ between the previous and the consecutive falling edges:

$$\widetilde{\alpha}(\tau) = \sum_{i=1}^{N_c} \frac{\left[\alpha(t) \mid (t_{f,i-1} < \tau < t_{f,i})\right]}{N_c}, \tag{5.10}$$

with N_c being the total number of conditioning points (i.e. the total number of averaged signal samples), $t_{f,i}$ is the time instant corresponding to the falling edge in $\overline{\alpha}(t)$ following the conditioning rising edge and $t_{f,i-1}$ the instant corresponding to the preceding falling edge.

The conditionally averaged velocity contour, $\widetilde{u}(y,\tau)/U_\infty$, is shown in Fig. 5.12 for the uncontrolled, opposing and reinforcing control cases. The time coordinate τ is non-dimensionalized using the factor U_∞/δ, making it representative of the non-dimensional distance from the streamwise position of the actuator to the downstream position of the hot-wire probe ($x = 2\delta$). Thus, the zero-crossing occurs at $\tau U_\infty/\delta = (2\delta/U_c)U_\infty/\delta \approx 3$ (remember $U_c = \overline{u}(y_L^+ \approx 190)$ is the convection velocity in the logarithmic region). In the contour representation a total time-interval of $\Delta\tau U_\infty/\delta \approx 11.2$ is presevered around the conditioning point. When the convection velocity reduces, such as at locations close to the wall, the time needed for the response to be measured is longer. Hence, the time-instant of the zero-crossing in $\widetilde{u}(y,\tau)$ gradually shifts towards increasing values of τ when approaching the wall.

The uncontrolled case in Fig. 5.12a reports the baseline velocity fluctuations the controller will actuate upon. The effect of control becomes apparent in the conditional averages for the opposing and reinforcing cases. The former causes an overall reduction of more than 60 % in the amplitude of the oscillation observed in the uncontrolled case, while the latter clearly amplifies it by approximately 60 %. This effect is particularly visible in the bottom insets, showing the conditionally-averaged time-series at y_L. Residing back to the wall-normal TKE profiles presented in Fig. 5.10b, an increase in TKE in the logarithmic region and in the wake of the TBL was noticeable when control is active. However, this is accompanied in the conditional average with still a reduction in the amplitude of $\widetilde{u}$ as seen in Fig. 5.12. This can be explained as follows: the spectrograms in Fig. 5.11 revealed a *broadband* increase in energy in the wake of the TBL. Since the controller only detects and acts upon large-scale velocity structures, with frequencies lower than $f\delta/U_\infty \lesssim 0.3$, conditionally-averaging on the velocity fluctuations targeted by control inherently averages-out the small-scale fluctuations.

Conditional average velocity fluctuations as shown in Fig. 5.12 only report the fluctuations in streamwise velocity as a result of control, but fail to capture the global interaction of the actuator flow with the grazing TBL flow. This void can be filled by utilizing PIV velocity fields, which are here presented for a domain with dimensions of roughly $1.8\delta \times 0.8\delta$ (half of the FOV listed in the bottom line of Table 5.1). Processing was per-

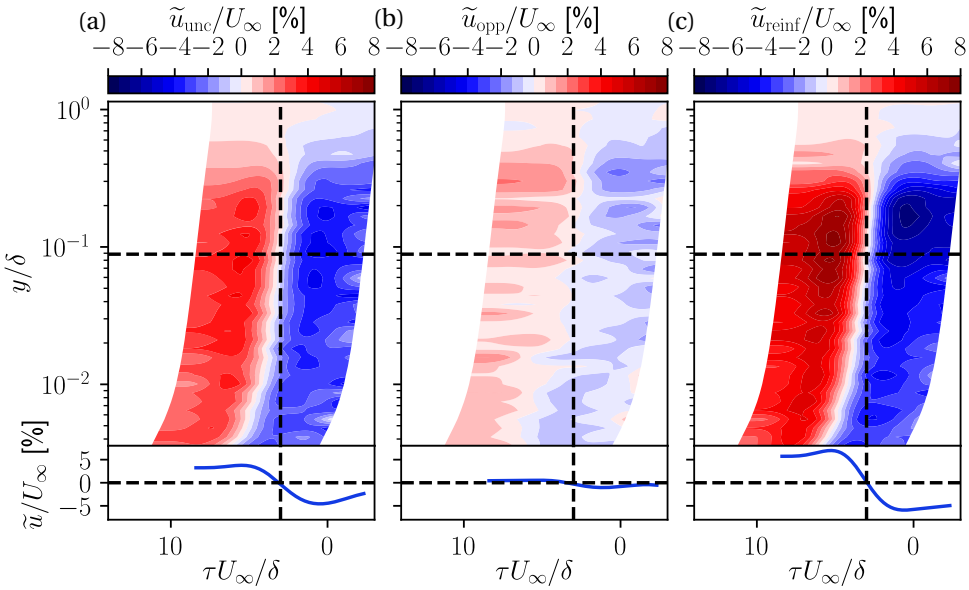

Figure 5.12.: Conditionally averaged response, $\widetilde{u}/U_\infty(y,\tau)$, of the streamwise velocity, conditioned on the zero-crossing positive-time-gradient of the estimated signal $\widehat{u}(t)$. Detail of response at y_L shown below the filled contour plot. (a) Uncontrolled flow, (b) opposing and (c) reinforcing control modes.

formed with the aid of LaVision DaVis 10.2 utilizing a multi-pass approach, leading to a final vector resolution of 2.25 vectors/mm. The acquisition was synchronized to the controller and was triggered with a specified delay, relative to the instance of an actuator on-command. This was repeated for a sequence of delays, allowing a visualization of the jet plume entering into the grazing TBL flow. The fields shown in Fig. 5.13 display the percentage variation of the streamwise velocity component, $\Delta\overline{u}_{control} = \left(\overline{u}_{control}/\overline{u}_{\mathrm{unc}} - 1\right)\times 100$ (%), with respect to the uncontrolled flow for three temporal delays, $\widetilde{\tau}$. Results for the opposing control mode are shown in the top row, whereas the results corresponding to the reinforcing strategy are shown in the bottom one. The low-velocity (blue) region on the bottom of each contour plot corresponds to the jet plume entering the domain. At an early stage ($\widetilde{\tau}U_\infty/\delta = 1.1$, or $\widetilde{\tau} = 5$ ms), a higher-than-average velocity is observed for the opposing case, which also persists at $\widetilde{\tau}U_\infty/\delta = 2.1$ ($\widetilde{\tau} = 10$ ms), suggesting that the controller successfully targets high-speed events. The opposite condition is, instead, measured in the reinforcing control scenario, where the controller is observed to intervene on low-speed events rather than high-speed ones. When time elapses to $\widetilde{\tau}U_\infty/\delta = 4.3$ ($\widetilde{\tau} = 20$ ms), the conditional flow field evolves to a condition where lower and higher streamwise velocity above the actuator are observed for the opposing and reinforcing cases, respectively.

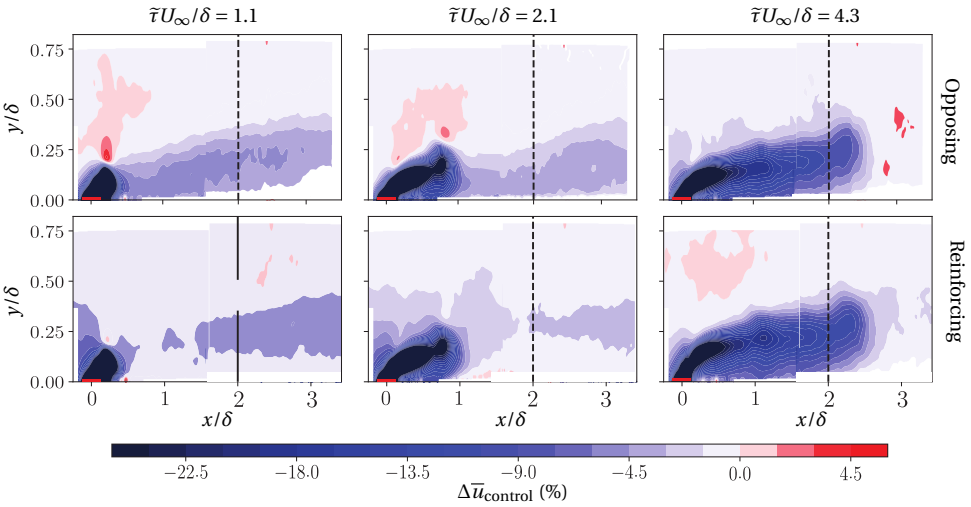

Figure 5.13.: Phase-averaged field of the percentage variation of mean streamwise velocity component $\overline{u}$ for opposing (top row) and reinforcing (bottom row) control modes with respect to the uncontrolled flow. Phase-averaged acquisition acquired at $\tilde{\tau}U_\infty/\delta = 1.1$, $\tilde{\tau}U_\infty/\delta = 2.1$, and $\tilde{\tau}U_\infty/\delta = 4.3$. All fields were filtered with a Gaussian filter having a kernel width of $0.25\delta \times 0.25\delta$ and $\sigma = 0.1\delta$. Dashed lines indicate the position of the hot-wire profile. Shown in red is the position of the jet exit slit.

5.7. EFFECT OF CONTROL ON TURBULENT SKIN-FRICTION DRAG

The principal goal is to investigate the change in turbulent skin-friction drag in relation to a control logic that specifically targets drag-producing large-scale structures. While any wall-normal jet actuator causes reductions in wall-shear stress, which can even lead to flow separation in the near-field of the actuator for elevated momentum coefficients, the goal of this section is to illustrate the benefits of performing *timely* actuation to attenuate high-momentum large-scale events.

The dimensional form of the wall-shear stress, $\tau_w = \mu \partial\overline{u}/\partial y|_{y=0}$, is analysed in terms of the skin-friction coefficient,

$$C_f = \frac{\tau_w}{q_\infty} = 2\frac{U_\tau^2}{U_\infty^2}. \tag{5.11}$$

Here, $q_\infty = \rho_\infty U_\infty^2/2$ is the freestream dynamic pressure. However, due to heat transfer effects from a hot-wire to the tunnel's surface, the HWA technique cannot reliably capture the velocity in the linear region [Shi et al., 2003, Zanoun et al., 2009]. As such, traditional estimates of C_f from hot-wire measurements typically rely on boundary layer scaling laws and mathematical fits to the streamwise velocity profile (*e.g.,* the composite fit [Chauhan et al., 2009] or the well-known Clauser fit procedures). With a boundary layer strongly affected by control and additional momentum injection from the jet actuator,

the assumptions behind these methods are violated. Therefore, a direct measurement of the velocity gradient at the wall, based on PTV, is pursued in the current work.

5.7.1. SKIN FRICTION DETERMINATION FROM PTV

The PTV technique was applied to a relatively small FOV of size $0.33\delta \times 0.28\delta$ (recall Table 5.1). The acquisition was not time-resolved, thus all PTV tracks consist of only two points. A PTV-based approach was implemented with an unparalleled resolution of velocity vectors over a PIV-based technique. With the given pixel resolution and typical interrogation window sizes, only very few valid vectors would be obtained from PIV in the linear region ($y^+ < 5$) for the Reynolds number of $Re_\tau \approx 2240$. Given the linear dependence $\overline{u}^+ = y^+$ for the velocity profile in this region, only two measurement points would theoretically be required to compute the gradient, $\partial\overline{u}/\partial y$. However, more information is required to increase the robustness of the measurement-based due to stochastic noise and uncertainty. The following six post-processing steps were implemented to infer the skin-friction data from the raw images.

1. **Particle track computation.** 2D Lagrangian particle tracks are computed with the aid of LaVision DaVis, version 10.2. Only a small subset of the original FOV is retained, that encompasses the wall and a small region above and below it ($\Delta y = 0.05\delta$ and the full streamwise extent).
2. **Wall identification.** Reflections of the particles in the flow result in mirrored particle tracks "below" the wall. This reflection allows for a precise identification of the wall. The ensemble-averaged mean velocity field is computed through traditional PIV processing on a subset of image pairs (500 out of the 2 000 in total), after which the wall position is found by utilizing the wall-mirrored field [Kempaiah et al., 2020, Sun et al., 2021]. That is, a parabola fitted to points in the linear region (both above and below the reflection line) yields $\overline{u} = f(y)$. Its minimum velocity point is taken to be the y-position of the wall, denoted as y_w. This procedure is performed over 330 streamwise positions spanning the entire FOV (corresponding to the vector spacing of the coarse PIV processing), resulting in a functional form for the wall position, $y_w(x)$.
3. **Particle track correction.** Each y-coordinate from the particle tracks found in step 1 is corrected to account for the true wall-position. This correction is based on each x position of the particle track, for which the wall position $y_w(x)$ is known. After this correction, the wall-normal profiles of $\overline{u}$ are symmetric around $y = 0$, as seen in Fig. 5.14.
4. **Binning definition.** All corrected tracks are binned spatially. Streamwise-elongated bins of size 128×1 pix^2 are initialized. Given the pixel resolution of the images, this equates to a size of 1.08×0.008 mm^2 ($34.7l^* \times 0.27l^*$). Note that the FOV spans 20 bins in x (given the 2 650 pixels in the streamwise direction, and the 128 pixel bin size). The degree of elongation is only feasible if the wall is parallel to the major axis of the bin, which was ensured through steps 2 and 3.
5. **Binning procedure.** Each individual particle track is collected in the bins defined in step 4 according to the coordinates of their mid-points.

6. **Velocity profile generation.** Particle tracks in each bin are averaged to compute the mean streamwise velocity per bin. Knowing the vertical bin spacing, the gradient $\partial\overline{u}/\partial y$ can be determined to infer C_f.

The higher the number of particle tracks, the more statistically reliable the estimation of the mean C_f becomes. A convergence analysis was performed by considering one single bin at $y^+ \approx 15$, where the highest fluctuations in streamwise velocity fluctuations occur. For convergence of the mean streamwise velocity $\overline{u}$, it was found that at least 1 500 image pairs are required for an estimate within 0.8 % of its final value (determined from all 2 000 image pairs).

For each of the vertical profiles (each corresponding to one column of bins), 18 velocity vectors reside within the range $y^+ < 5$. Fig. 5.14 displays 9 wall-normal profiles of $\overline{u}$. The (corrected) wall is positioned at $y = 0$ and is shown with the blue dashed line. Due to some noise in the particle images in proximity to the wall, the points that were selected for determining the gradient $\partial\overline{u}/\partial y$ were within the range $2 < y^+ < 4.5$ (a buffer of $0.5l^*$ is taken between the linear and the buffer regions). This results in 11 points (black markers in Fig. 5.14) being available for fitting the linear relation, shown in light blue. To enforce the no-slip condition at the wall, the fitting procedure also includes the constraint $(\overline{u}, y) = (0, 0)$. The final value of the wall-shear stress is taken as the average of the individual gradients computed from each of the 20 wall-normal profiles in one FOV, thus assuming streamwise-invariance.

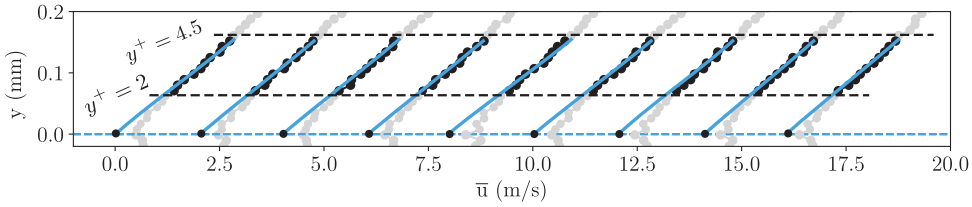

Figure 5.14.: PTV-based profiles of the streamwise velocity $\overline{u}$ with increasing wall-normal distance y for the uncontrolled flow at the FOV centered at $x/\delta = 2.0$. Profiles are sequentially separated in the horizontal direction by $\Delta\overline{u} = 2$ m/s for ease of inspection.

The procedure thus far allows for an estimation of C_f for each FOV of the PTV campaign and thus for the three FOV's centered at $x/\delta = \{2, 2.5, 3\}$ (recall Fig. 5.1c). At the same time, four control modes are considered (uncontrolled flow, and desynchronized, opposing and reinforcing control). Fig. 5.15a displays the percentage difference between the C_f of the desynchronized case and the one of the other three cases (thus $\Delta C_f = 100(C_{f,i} - C_{f,des})/C_{f,des}$, with i being the control mode in consideration and $C_{f,des}$ corresponds to the desynchronized case). The choice of the desynchronized control as the reference case follows the same reasoning as was followed in presenting the spectrograms in § 5.6.1. Opposing control shows a reduction of 7-11 % in C_f, whereas the reinforcing case reduces friction by 3-7 %, depending on the streamwise location. All control modes appear to reduce friction drag with respect to the uncontrolled flow, which is mainly the consequence of the jet injecting wall-normal momentum, which reduces the

streamwise momentum of the grazing TBL flow. Reinforcing control has a comparable effect on the TBL to the desynchronised mode in this regard, but it is evident that the opposing mode reduces C_f by 2-3 % for all streamwise locations.

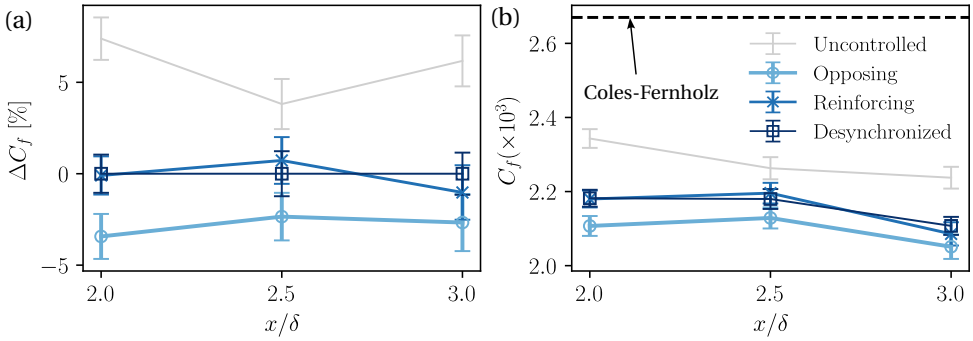

Figure 5.15.: (a) Percentage difference between the skin-friction coefficients of uncontrolled, opposing and reinforcing cases with respect to the desynchronized one with error bars showing the uncertainty. (b) Absolute skin-friction coefficient for the four control modes with error bars showing the uncertainty. Dashed line plotted for the value of C_f estimated from the Coles-Fernholz relation.

Fig. 5.15b displays the absolute skin friction coefficient. The displayed error bars were computed by assuming that each vertical profile of the streamwise velocity from binned PTV tracks generates a statistically independent result, and thus indicate the estimation uncertainty. This uncertainty can be attributed to two main factors: (1) the uncertainty in the convergence of the average streamwise velocity from the PTV measurements, and (2) the uncertainty in the linear fitting procedure described earlier. The former can be computed by considering the number of tracks in each bin and can be defined as $\varepsilon = \sigma_u/\sqrt{N_t}$, where σ_u is the standard deviation of the streamwise velocity samples in the considered bin and N_t the number of tracks. The latter source of error stems from the linear fitting procedure at each streamwise location and is defined as the average RMS residual across all fitted curves.

The skin friction from the empirical Coles-Fernholz relation ($C_f = 2\left[\frac{1}{\kappa}\ln Re_\theta + C\right]^{-2}$, with $\kappa = 0.38$, $C = 3.7$ and $Re_\theta = 6830$) is also plotted in Fig. 5.15b. The uncontrolled flow experiment yields a C_f that is roughly 15 % lower than the one found with the skin-friction determination. This discrepancy is minor, given that the empirical Coles-Fernholz relation is valid for equilibrium (ZPG) and smooth-wall TBL flow. The experiment may include a residual signature from the upstream trip [Marusic et al., 2015] and the jet exit slit embedded within the wall. As such, the uncontrolled and desynchronized cases serve as baseline scenarios.

5.7.2. TURBULENT SKIN FRICTION INTEGRALS

Direct assessments of skin friction do not capture the mechanisms behind skin-friction generation. Analysis of PIV data on a larger field of view allows for the computation

of TBL integral measures, and to relate them to the changes in skin friction for different control modes. The work of Abbassi et al. [2017] is thus extended, in an attempt to shed more light on the effect of the different control modes on the main skin-friction-generating mechanisms. At first, the TKE production term is informative for investigating the relation between the mean C_f and fluctuations of velocity. TKE production is defined as the product of the Reynolds stress component $R_{xy} = \overline{u'v'}$ and the wall-normal gradient of $\overline{u}$ [Pope, 2000], for a "two-dimensional" turbulent boundary layer:

$$P(y) = -\overline{u'v'}\frac{\partial \overline{u}}{\partial y}. \tag{5.12}$$

A bulk TKE production following $\widetilde{P} = \int P(y)\mathrm{d}y$ is an indicator of the total turbulent shear stress within the TBL flow [Deck et al., 2014, Harsha and Lee, 1970]. Essential to the computation of P is the Reynolds shear stress R_{xy}, of which a comparison is shown in Fig. 5.16, for the uncontrolled and the desynchronised control cases. While for the uncontrolled case the Reynolds stress monotonically decreases with increasing y (and resembles a streamwise invariant behaviour), the desynchronised case is associated with a band of high-magnitude R_{xy} around $y/\delta \approx 0.35$ at $x/\delta = 2$. A large increase in the magnitude of R_{xy} occurs where the jet enters the domain. As the plume develops into the mid-to-far field of the jet actuator, given the relatively low velocity ratio, the plume resembles a concatenation of hairpin vortices, which eventually rise and break up Sau and Mahesh [2008], creating an internal shear layer and, thus, an increase in turbulent fluctuations. The signature of high R_{xy} magnitude persists to the downstream end of the FOV in Fig. 5.16b.

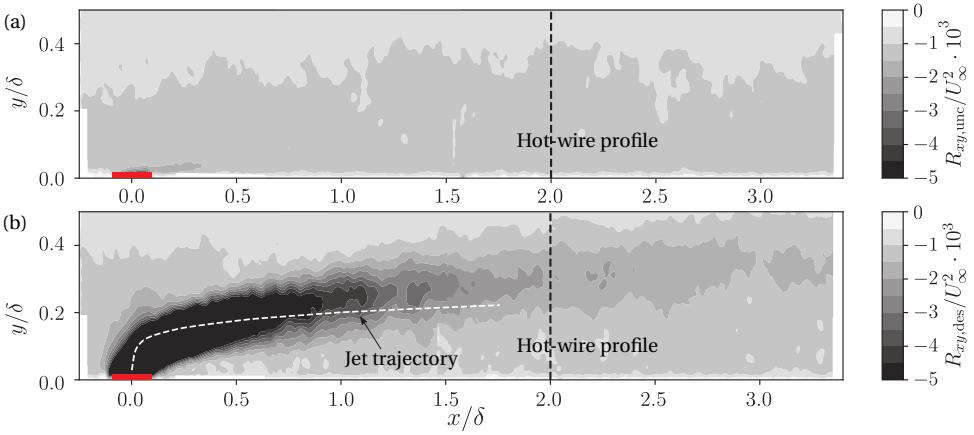

Figure 5.16.: Contours of the Reynolds stress R_{xy} obtained from PIV data for (a) the uncontrolled flow, and (b) the desynchronised control case; the jet trajectory is duplicated from Fig. 5.5a. Shown in red is the position of the jet exit slit.

To continue a more quantitative assessment, the TKE production term at a single streamwise location ($x = 2\delta$) is considered first. Further on, this is extended to all streamwise locations captured by the PIV data in Fig. 5.16. So for $x = 2\delta$, Fig. 5.17a displays the

premultiplied TKE production term as a function of wall-normal distance, for the four control modes. Streamwise averaging over a width of 0.2δ in the interval $1.9 < x/\delta < 2.1$ was performed to attenuate measurement noise. The production curve for the uncontrolled case rises to a maximum around $y/\delta \approx 0.01$, before plateauing in the logarithmic region and further decreasing into the wake; this is consistent with the literature [Harsha and Lee, 1970, Pope, 2000]. The TKE production curves for all other cases show a lower magnitude, up to $y/\delta \approx 0.2$. The region of strong R_{xy} on the upper side of the jet flow-trajectory (seen in Fig. 5.16b) is responsible for the drastic increase in P. In order to assess changes in the bulk TKE production, integrals of the curves shown in Fig. 5.17a are considered. Here, the integration is split into two different domains. A first contribution comes from integrating the profiles from the lowest y-location up to $y/\delta = 0.2$, where the control cases show a decrease in TKE production. A second contribution comes from the part of the curve at $y/\delta > 0.2$, up to the upper edge of the FOV near $y/\delta \approx 0.8$. Fig. 5.17b displays the two portions of the bulk TKE production as a percentage change with respect to the uncontrolled flow. The first integral shows a trend that resembles the behaviour observed in Fig. 5.15. Namely, the uncontrolled case shows the highest value, followed by reinforcing, desynchronized and opposing control modes. The integral in the outer region of the boundary layer contributes up to ~ 30% to the total integral value, $\widetilde{P}$, in the uncontrolled case. For the flow subject to control, this shows a drastic increase of the control modes' production term with respect to the uncontrolled flow, which is again ascribed to the region of strong R_{xy} in Fig. 5.16b. This drastic increase in off-diagonal Reynolds stresses is purely related to the development of a shear layer between the main jet plume and TBL crossflow and does not alter the principal working mechanism of the opposition control logic, as can also be observed from direct skin-friction measurements (see Fig. 5.15).

Fukagata et al. [2002] derived the so-called *FIK identity* to decompose the flow contributions to turbulent skin friction coefficient into three components, each of which is responsible for a different mechanism of skin-friction generation [Fukagata et al., 2002, Kasagi and Fukagata, 2006]. The first component ($C_{f,1}$, Eq. 5.13a) is dependent on the displacement thickness of the boundary layer and is known as the "laminar component". For a TBL flow, $C_{f,1}$ only accounts for a marginal fraction of the total friction coefficient (about 1.4% in the present study). The second component ($C_{f,2}$, Eq. 5.13b) is related to turbulence fluctuations generating wall-shear and is dependent on the off-diagonal Reynolds stress. Finally, the last component accounts for the spatial and temporal development of the flow ($C_{f,3}$, Eq. 5.13c) and is relatively small for a ZPG-TBL [Deck et al., 2014]. For the current analysis, given long-time average statistics, the temporal term $\partial\overline{u}/\partial t$ can be neglected.

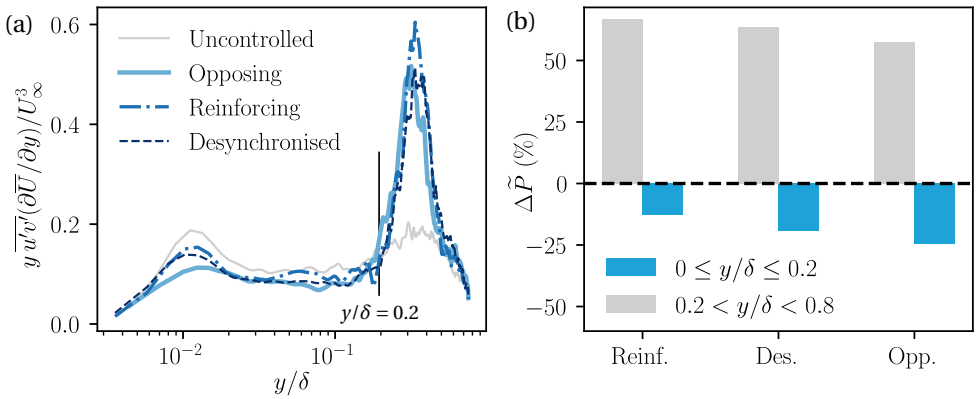

Figure 5.17.: (a) Plot of normalized, premultiplied TKE production $yP = y\,\overline{u'v'}(\partial\overline{U}/\partial y)/U_\infty^3$, as a function of wall-normal distance at $x = 2\delta$ and the four control modes. Wall-normal profiles of P were computed by averaging PIV data in the streamwise direction in the interval $1.9 < x/\delta < 2.1$. (b) Bar chart displaying the percentage difference of the integrated TKE production term with respect to the uncontrolled flow, for $0 \le y/\delta \le 0.2$ (blue) and for $0.2 < y/\delta \le 0.8$ (grey bars).

$$C_{f,1} = \frac{4(1-\delta^*/\delta)}{Re_\delta} \tag{5.13a}$$

$$C_{f,2} = \int_0^1 \underbrace{-\frac{4}{U_\infty^2}\left[\overline{u'v'}\left(1-\frac{y}{\delta}\right)\right]}_{=f_2(y)} \mathrm{d}\left(\frac{y}{\delta}\right) \tag{5.13b}$$

$$C_{f,3} = \int_0^1 \underbrace{-2\left(1-y/\delta\right)^2 \left[\cancelto{\approx 0}{\frac{\partial\overline{u}}{\partial t}} + \frac{\partial\overline{u}^2}{\partial x} + \frac{\partial(\overline{u}\,\overline{v})}{\partial y}\right]}_{=f_3(y)} \mathrm{d}\left(\frac{y}{\delta}\right) \tag{5.13c}$$

In must be stressed here that a few assumptions underlying the formulation of the FIK identity are not met in the present work. Namely, the controlled TBL is not in a canonical state (especially in the region close to the actuator) and the flow is spanwise inhomogeneous. However, given the complexity in performing direct skin-friction measurements and the strong relation that exists between the principal term of the FIK identity, $C_{f,2}$, and drag-producing mechanisms, it is still explored as a metric in evaluating the change in flow physics as a result of control on the TBL and validating the drag-reducing trend inferred with direct C_f measurements.

The integrand of $C_{f,2}$ ($f_2(y)$ in Eq. 5.13b) vaguely resembles the premultiplied TKE production term, where R_{xy} is scaled with the wall-normal coordinate. However, the former

scales directly with y, while the latter scales with $1 - y/\delta$, thus being multiplied by a factor that decreases with wall-normal distance. Fig. 5.18a displays the integrand of $C_{f,2}$ as a function of y/δ and the four control modes. A steady rise is observed up to $y/\delta \approx 0.01$, followed by a plateauing region. In the wake of the boundary layer, again a sharp peak is reminiscent of the enhanced Reynolds shear stress caused by the jet plume. Fig. 5.18b shows Eq. (5.13b) split up in two contributions: again, up to $y/\delta = 0.2$ (blue) and from 0.2 to the edge of the FOV (grey). Also for this metric, the observation can be made that the opposing control law is the most effective in lessening shear stress (at least when integrated up to the $y/\delta = 0.2$).

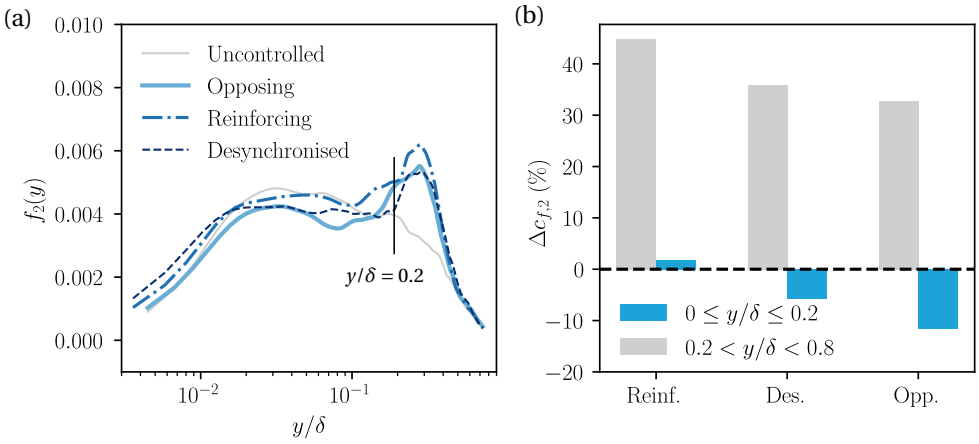

Figure 5.18.: (a) Integrand of the $C_{f,2}$ expression of Eq. (5.13b) as a function of wall-normal distance, for $x = 2\delta$ and the four control modes. (b) Bar chart displaying the percentage difference of the integrated $\partial C_{f,2}/\partial y$ term with respect to the uncontrolled flow, for $0 \leq y/\delta \leq 0.2$ (blue bars) and for $0.2 < y/\delta \leq 0.8$ (grey bars).

The analysis of turbulent skin-friction drag integrals assists in identifying where important mechanisms occur within the TBL that contribute to the generation of skin-friction drag. Both the integrated TKE production (Fig. 5.17) and $C_{f,2}$ (Fig. 5.18) reveal how the spatio-temporal dynamics of the TBL are altered as a function of y. The full integrals over the available wall-normal range suggest an increase in skin-friction drag, but this contradicts the measured skin-friction coefficients presented in § 5.7.1. This discrepancy can be explained by analysing the trends of the curves in the wake of the TBL flow. By inspection of the TKE profiles in Fig. 5.10b, as a well of the distribution of R_{xy} in Fig. 5.16b, it is evident how the jet plume created by the actuator is responsible for this sudden rise. Instabilities induced by the break-up of the shear layer of the jet in the TBL are superimposed on top of the naturally-occurring Reynolds stresses, thus biasing the integral values of $\widetilde{P}$ and $C_{f,2}$. Still, the reduction in the integrand curves observed in the logarithmic region and below show that the main wall-shear producing dynamics are, in fact, suppressed below the wall-normal coordinate where R_{xy} suddenly rises.

The integrand of $C_{f,3}$ ($f_2(y)$ in Eq. 5.13c) is presented in Fig. 5.19a at $x = 2\delta$ and shows

a rather low and constant value, especially when compared to the dominant (second) component, as illustrated in the bar chart in Fig. 5.19b. Here, the relative contributions of the three components of skin-friction are presented for the uncontrolled case as well as the three control modes, in comparison to the friction coefficient components obtained for the uncontrolled flow. For the latter, the magnitude of the relative contributions of the three components of skin-friction to the total wall-shear is in accordance with the results of Deck *et al.* Deck et al. [2014] at $Re_\theta = 7{,}000$. For the three active control modes, it is evident that the dominant contributing component is $C_{f,2}$ at $y/\delta > 0.2$, which is greatly increased by the actuator-induced internal shear layer.

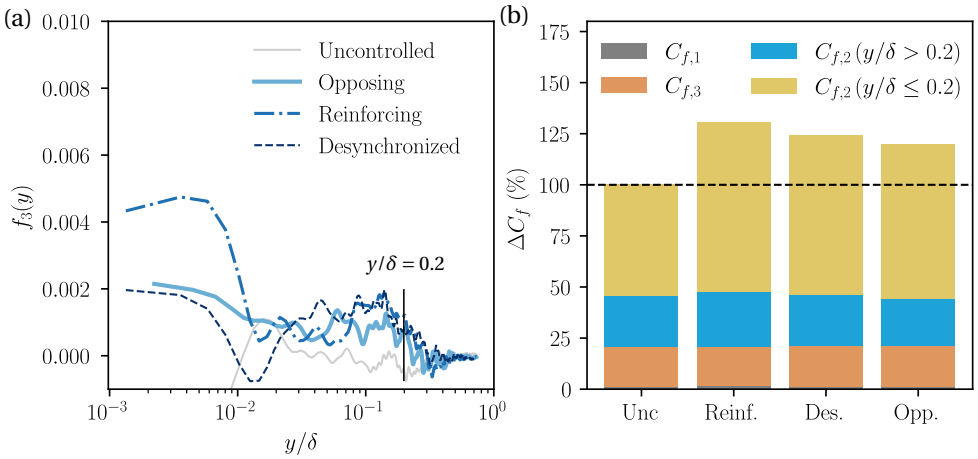

Figure 5.19.: (a) Integrand of the $C_{f,3}$ expression of Eq. (5.13c) as a function of wall-normal distance, for $x = 2\delta$ and the four control modes. (b) Bar chart displaying the relative contribution to the total skin-friction coefficient of each of the three FIK-components for the four control modes. A further subdivision of $C_{f,2}$ is made to report contributions from different regions in wall-normal direction.

While Figs. 5.17, 5.18 and 5.19 present an analysis of the turbulence integral quantity at one streamwise location of $x/\delta = 2$, Fig. 5.20 illustrates the streamwise variation of the same integral quantities over the whole domain captured by the PIV acquisitions. As it was the case for the above-mentioned figure, integration was performed on streamwise-averaged wall-normal profiles having a width of 0.2δ. Figs. 5.20a and 5.20c display the streamwise variation of the integral quantities in the vicinity of the jet actuator ($-0.1 \leq x/\delta \leq 1$). Given the dominant presence of the jet exit plume developing through the inner region of the TBL in the considered part of the domain, strong spatial gradients are hereby induced, which result in the local integral attaining extreme values. Figs. 5.20b and 5.20d, however, report the same variation in a region of the fluid domain where the streamwise development of the jet plume has tapered off. Here, the trend that was already discussed in Figs. 5.17 and 5.18 is evident for a much larger streamwise extent. The opposing control scheme causes the most reduction in both $\widetilde{P}$ and $C_{f,2}$,

with reinforcing control instead causing either an increase or no change in either metric. Given that direct skin-friction measurements are characterized by a relatively high uncertainty, this trend consistency also serves as validation to the direct inference procedure.

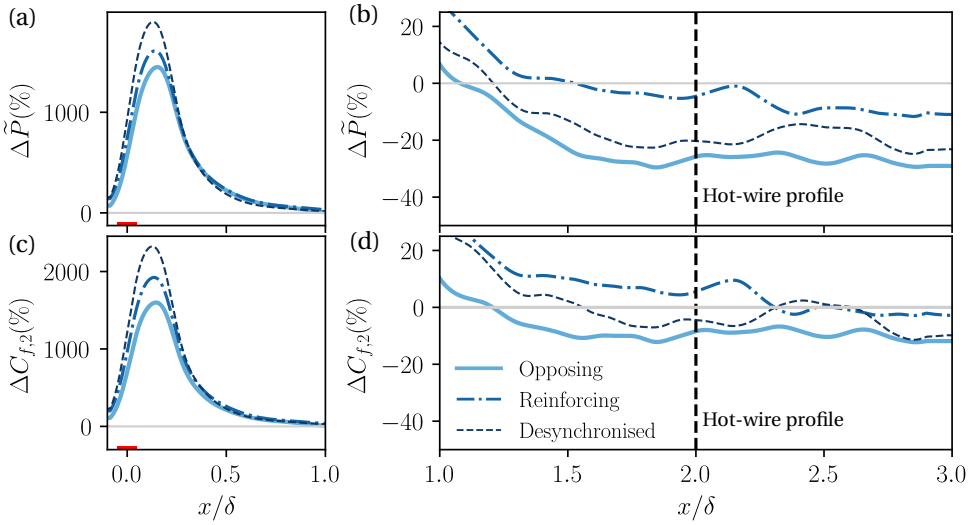

Figure 5.20.: (a,b) Streamwise percentage variation in turbulence kinetic energy integrated in the region $0 < y/\delta \leq 0.2$ for the three cases influenced by control with respect to the uncontrolled flow. Shown for (a) $-0.1 \leq x/\delta \leq 1$ and (b) for $1 < x/\delta \leq 3$. (c,d) Streamwise percentage variation in $C_{f,2}$ integrated in the region $0 < y/\delta \leq 0.2$ for the three cases influenced by control with respect to the uncontrolled flow. Shown for (c) $-0.1 \leq x/\delta \leq 1$ and (d) for $1 < x/\delta \leq 3$.

5.8. CONCLUSIONS

This chapter reports an experimental implementation of a real-time control system based on instantaneous wall-shear stress fluctuations. The results confirm the successful implementation of a drag-reducing real-time control strategy, with drag reduction of about 3% for the opposing control scenario. However, the core of the work lies in the understanding of the alteration of the skin-friction drag production mechanisms by means of the investigation of the integral drag measures. Although an increase in the drag integral statistics is observed above the logarithmic region, which is induced by the increase in fluctuations caused by the breakup of the actuator-induced flow, drag production metrics are considerably attenuated in the logarithmic region and below. In general, this works proves the effectiveness of targeting LSMs, pointing at a considerable streamwise persistence of this control method.

6

FEEDFORWARD CONTROL WITH WALL-PRESSURE INPUT

Your vision is not limited by what your eye can see, but by what your mind can imagine.

Ellison Onizuka (STS-51-L)

A multiple-input multiple-output control logic is experimentally implemented for real-time control of large-scale velocity fluctuations in a turbulent boundary layer. Spatially sparse wall-pressure data are employed as the input quantity to the controller, measured by a spanwise array of microphones. Downstream of these, a spanwise array of on/off wall-normal jet actuators oppose large-scale positive streamwise velocity fluctuations in real-time. System identification is performed by applying an adaptive Wiener filtering procedure to relate the system state (streamwise velocity fluctuations) to the system input (signals of wall-pressure and wall-pressure–squared). In particular, the wall-pressure–squared term exhibits a higher coherence with large-scale structures compared to the linear term, and aids in increasing the accuracy of control. It is revealed that the controller is successful in selectively reducing the streamwise kinetic energy contained in large-scale structures by $\approx 25\%$*. This work provides evidence that wall-pressure can be employed reliably to detect large-scale velocity structures for real-time control, even with limited observability, a sparse sensing layout, and low signal-to-noise ratios of input sensing caused by acoustic facility noise in experimental applications.*

Parts of this chapter are published in:

- G. Dacome, M. Kotsonis, W. J. Baars (2025) Experimental study of real-time control of a turbulent boundary layer using wall-pressure sensing. Exp. Therm. Fluid Sci. **In review.**

6.1. INTRODUCTION

Wall-pressure fluctuations have been found to display non-negligible coherence with streamwise velocity fluctuations in the logarithmic region of a turbulent wall-bounded flow. This highlights the potential of employing wall-pressure fluctuations for the estimation of the passage of LSMs for control purposes. In particular, the findings of Ch. 4 reveal Reynolds-number-invariant distance-from-the-wall scaling of wall-pressure–velocity and wall-pressure–squared–velocity coherence. This suggests ease of scalability of an input strategy utilizing wall-pressure fluctuations as the input quantity, from a laboratory to an engineering setting. In light of the findings of Ch. 4 and the exploration of a feedforward control system configuration, illustrated in Ch. 5, the present chapter delves into the definition of a multi-channel feedforward multiple-input single-output control system targeting LSMs in the logarithmic region for skin-friction drag reduction. The novel, and pioneering, element of this part of the work is the utilization of wall-pressure, instead of wall-shear, as the input quantity to the real-time control system.

6.2. CONTROL SYSTEM DESIGN AND EXPERIMENTAL SETUP

A schematic of the real-time control system for the TBL in consideration (described in § 6.2.1) is presented in Fig. 6.1. An upstream sensing zone and a downstream actuation zone (described in § 6.2.2) are separated by a streamwise distance, s. The state of the TBL flow to control corresponds to the instantaneous velocity fluctuations in the logarithmic region, at the streamwise location of the actuators (point $\mathscr{P}$ in Fig. 6.1 when considering the sensor/actuator in the spanwise center). An estimate for the streamwise velocity fluctuations, $\widehat{u}(t)$, is to be obtained from the wall-based pressure. The quantity $\widehat{u}(t)$ is what determines the controller's output, following an opposition control logic (see § 6.2.3). Transfer functions (denoted by h in Fig. 6.1) relate wall-pressure input data to velocity states, and its system identification procedure will detailed in § 6.3.

6.2.1. TURBULENT BOUNDARY LAYER FACILITY

Experiments were carried out in an open-return wind tunnel facility (W-Tunnel) at the Delft University of Technology. The facility has a cross-sectional area of $0.6 \times 0.6\,\mathrm{m}^2$ at the inlet of a dedicated test section for studying TBL flows. This section has a total length of 3.75 m, and includes a flexible ceiling configured for a zero-pressure-gradient streamwise development of the flow. A Cartesian right-handed coordinate system (x, y, z) is employed for presenting results throughout the paper; this coordinate system is centered at $x' = 2.90$ m downstream of a boundary layer trip (P40-grit sandpaper) and at the spanwise centerline of the test section. Hence, $x = 0$ aligns with the actuation zone. One operating condition is considered, with a freestream velocity of $U_\infty = 15\,\mathrm{m/s}$. Without control and at $x = 0$, the TBL attains a thickness of $\delta = 0.07$ m and a friction velocity of $U_\tau = 0.49\,\mathrm{m/s}$, resulting in $Re_\tau \approx 2240$. Parameters of the canonical TBL flow (including the momentum thickness, θ, and the wake parameter, Π) are reported in Tab. 6.1. Additional details of the facility can be found in Ch. 2.

U_∞ (m/s)	δ (mm)	θ (mm)	Re_θ	U_τ (m/s)	Re_τ	Π	l^* (μm)
15	69.9	6.83	6 830	0.49	2 240	0.61	31.25

Table 6.1.: Experimental parameters of the uncontrolled TBL flow in the W-Tunnel facility at $x' = 2.90$ m downstream of the sandpaper trip ($x' = 0$).

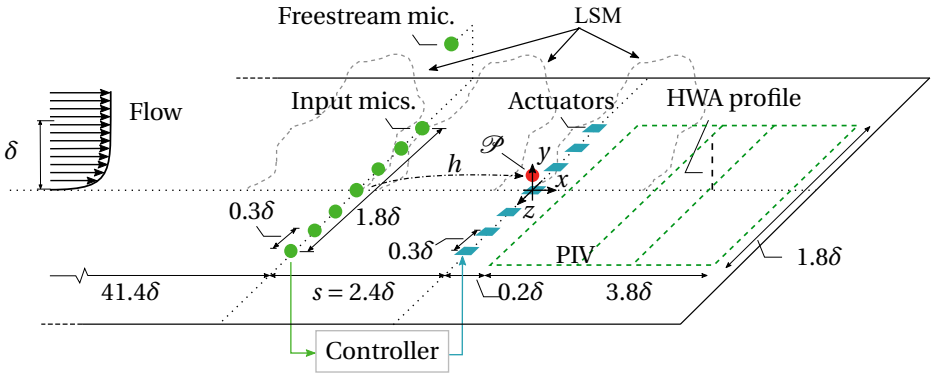

Figure 6.1.: Schematic representation of the control hardware (*i.e.*, sensors and actuators) employed for control embedded in the TBL facility as well as the location of the main flow measurements. More details regarding the specifics of flow measurement techniques will be elaborated on in § 6.5.

6

6.2.2. CONTROL HARDWARE

To allow for sensing based on wall-pressure (usually found in the literature as p_w, it is going to be referred to in the foregoing as p), a spanwise array of seven microphones was employed (Fig. 6.1). The array was positioned at $x = -2.4\delta$ and comprised a total width of $b = 1.8\delta$ (spanwise spacings between adjacent sensors of $\Delta z_m = 0.3\delta = 0.17b$). Spacing Δz_m was chosen so that the mean spanwise separation of (V)LSMs in a TBL could be resolved [Hutchins et al., 2011]. Sensors consisted of GRAS 46BE 1/4-in. free-field CCP microphones with a nominal sensitivity of 3.6 mV/Pa. These have an adequate dynamic range to capture the pressure fluctuations of interest (35 to 160 dB, with a reference pressure of $p_{\text{ref}} = 20\,\mu$Pa) with an accuracy of ± 1 dB within the range of 10 Hz to 40 kHz. Each microphone was integrated within a circular sub-surface-cavity, communicating with the boundary layer flow by means of a circular neck-orifice (or pinhole), having a diameter of $d_p^+ = 12.8$ ($d_p = 0.4$ mm). Cavity resonance poses no concern to the utilization of this sensor configuration, as the resonance frequency of $f_r = 2\,725$ Hz [Baars et al., 2024] lies well beyond the frequency band of interest for real-time flow control. An additional microphone of the same make and model was mounted at $x = -2.4\delta$ on a streamlined holder in the freestream flow; this microphone was fitted with a GRAS RA0020 nosecone to reduce stagnation-driven turbulence pressure fluctuations. This monitors the acoustic noise emitted by the wind tunnel and facilitates the implementation of acoustic noise removal in real-time.

Seven non-zero-net-mass-flux unsteady blowing jets were employed as actuators. These were arranged in a spanwise array and located at $x = 0$, at a distance of $s = 2.4\delta$ downstream of the wall-embedded microphones (Fig. 6.1). The spanwise positioning and separation between actuators was chosen to be the same as for the input sensors. Compressed, dry air exhausts into the TBL flow through streamwise-elongated rectangular slits having dimensions of $0.2\delta \times 0.02\delta$. This type of actuator is intended to oppose downward-directed large-scale events originating in the logarithmic region, by inducing an upwash at (and downstream of) the injection location. All jets were operated in an on/off fashion, and their exit velocities were either 0 (off) or $v_{\text{jet}} = 0.4U_\infty$ (on). This exit velocity ensured that the jet plume trails within the logarithmic region, without penetrating beyond $y = \delta$ [see § 5.3 for additional details].

Finally, the controller itself was implemented using MathWorks Simulink, and deployed on a Speedgoat Performance (P3) real-time target machine. A control loop frequency of $f_{\text{loop}} = 10\,\text{kHz}$ was adopted to ensure adequate timing. Wall-pressure signals were acquired with a Speedgoat IO109 24-bit analog input module, while binary output signals for on/off actuation of the valves are sent through a Speedgoat IO205 digital output module.

6.2.3. INPUT SIGNAL CONDITIONING

A challenge when employing wall-pressure sensing is that the signals acquired by the microphones not only contain hydrodynamic wall-pressure fluctuations, but also additive acoustic noise. A sample spectrum of one of the acquired microphone signals is shown in Fig. 6.2a, and is duplicated in Fig. 6.2b (curve $p_{4,r}$). Although Ch. 3 and § 4.3 treat some techniques to remove facility acoustic noise in post-processing to obtain the hydrodynamic wall-pressure signal, those techniques are not applicable in real-time. Filtering in real-time can be accomplished following a simple subtraction, at each time-step, of the spatial mean of the eight input microphones [*including* the raw pressure fluctuations in the freestream, $p_{8,r}(t)$]:

$$p_{k,f}(t_m) = p_{k,r}(t_m) - \frac{1}{8}\sum_{k=1}^{8} p_k(t_m), \tag{6.1}$$

with $p_{k,r}$ being the raw signal, $p_{k,f}$ the resulting filtered pressure signal and k a subscript indicating a discrete spanwise location [*i.e.* $p_k(t) = p(z_k, t)$]. The outcome of the noise-filtering procedure results in the curve $p_{4,f}$ in Fig. 6.2b.

This technique was proven effective in the work of Baars et al. [2024] as a low-overhead technique for noise-filtering. Once this is complete, the freestream pressure signal is terminated, as it carries no wall-pressure information that can be used for the estimation of the off-the-wall velocity state, $\widehat{u}(t)$. The remaining seven wall-pressure fluctuation signals are further filtered with a Butterworth low-pass filter (the output of which is presented as curve p_4 in Fig. 6.2b) having a cut-off frequency of $f_c\delta/U_\infty = 0.84$ ($f_c = 180\,\text{Hz}$). This frequency is chosen such that all high-energy wall-pressure fluctuations are retained, while removing any remaining signature of facility noise (as well as cavity resonance), which anyhow resides beyond the frequency range of interest.

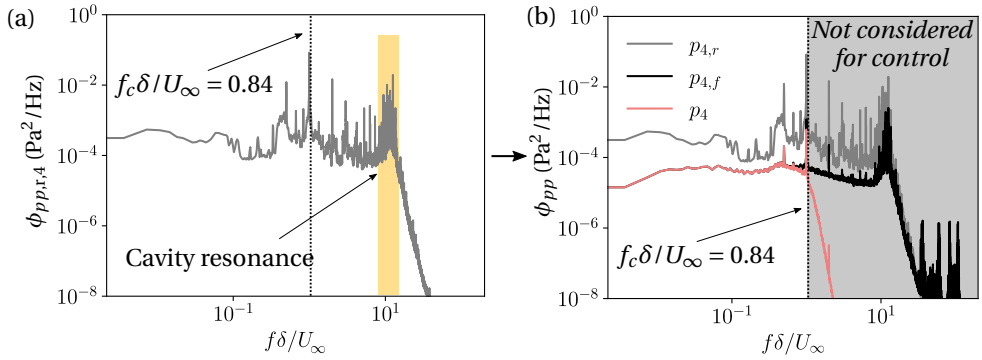

Figure 6.2.: (a) Spectrum of the raw signal from the central input sensor $[p_{4,r}(t)]$. (b) Spectrum obtained after the application of the noise-filtering procedure and the conditioning low-pass filter on $p_{4,r}(t)$.

6.3. ADAPTIVE FILTERING PROCEDURE FOR SYSTEM IDENTIFICATION

For system identification, a transfer function needs to be found that relates the instantaneous wall-pressure measurements to velocity fluctuations in the logarithmic region at the streamwise location of the actuator array. Instead of a single multiple-input multiple-output (MIMO) kernel, seven MISO spatio-temporal kernels were found, each relating the instantaneous wall-pressure measurements to the velocity fluctuations measured at the spanwise locations of each of the seven actuators.

Each one of the MISO kernels was obtained as an adaptive Wiener filter kernel. This filter consists of an array of taps (or coefficients), obtained by solving the linear system of equations $\Phi\mathbf{h} = \Psi$:

$$\begin{bmatrix} \Phi_{11} & \Phi_{12} & \dots & \Phi_{1N} \\ \Phi_{21} & \Phi_{22} & & \vdots \\ \vdots & & \ddots & \\ \Phi_{N1} & & & \Phi_{NN} \end{bmatrix} \begin{bmatrix} h_{1k} \\ h_{2k} \\ \vdots \\ h_{Nk} \end{bmatrix} = \begin{bmatrix} \Psi_{11} \\ \Psi_{21} \\ \vdots \\ \Psi_{Nk} \end{bmatrix}. \tag{6.2}$$

Here, $\Phi_{ij} = \langle p_i p_j \rangle$ is the cross-correlation between the input signals (*i.e.* between the wall-pressure time-series measured at different spanwise locations) and $\Psi_{ik} = \langle p_i u_k \rangle$ is the cross-correlation between the reference velocity signal at one spanwise location, $u_k(t)$, and the input signals, $p_i(t)$. For the problem considered in this work, $N = 7$. The identified vector of filter taps, $\mathbf{h}_{L,k}$, is one that, when convolved with the spatial array of instantaneous wall-pressure measurements at time-step t_m, produces an estimate of the velocity fluctuations in the logarithmic region at time-step t_{m+1}.

To adequately model the convective footprint of large-scale motions, it is essential to include temporal dynamics. For this, Eq. 6.2 can be solved at multiple time-steps contained within an arbitrary *temporal horizon* $t_{m-H} < t < t_m$, with t_m being the present time step and $\Delta t_h = t_m - t_{m-H}$ is the total horizon length. The filter is convolved in real-

time with the input wall-pressure signals as a finite impulse response (FIR) filter on the horizon to generate seven velocity estimates, $\widehat{u}_{k,L}(t_m)$, at one time-step and one spanwise location:

$$\begin{aligned}\widehat{u}_{L,k}(t_m) = {} & h_{1k}(t_m)\cdot p_1(t_m) + h_{2k}(t_m)\cdot p_2(t_m) + \cdots + h_{Nk}(t_m)\cdot p_N(t_m) \\ & + h_{1k}(t_{m-1})\cdot p_1(t_{m-1}) + h_{2k}(t_{m-1})\cdot p_2(t_{m-1}) + \cdots + h_{Nk}(t_{m-1})\cdot p_N(t_{m-1}) \\ & + h_{1k}(t_{m-2})\cdot p_1(t_{m-2}) + h_{2k}(t_{m-2})\cdot p_2(t_{m-2}) + \cdots + h_{Nk}(t_{m-2})\cdot p_N(t_{m-2}) \\ & + \quad \ldots \\ & + h_{1k}(t_{m-H})\cdot p_1(t_{m-H}) + h_{2k}(t_{m-H})\cdot p_2(t_{m-H}) + \cdots + h_{Nk}(t_{m-H})\cdot p_N(t_{m-H}) \\ = {} & \mathbf{h}_{L,k}(t) \circledast \mathbf{p}(t).\end{aligned} \tag{6.3}$$

The same procedure can be applied independently for the wall-pressure–squared term, whereby seven additional kernels ($\mathbf{h}_{Q,k}$) are identified that relate instantaneous wall-pressure–squared to velocity fluctuations. The estimated velocity signal, $\widehat{u}(z_k,t)$ at a single spanwise location, therefore, is obtained from a quadratic stochastic estimation (QSE) procedure through the inclusion of both kernels:

$$\widehat{u}_k(t) = \underbrace{\underbrace{\mathbf{h}_{L,k}(t) \circledast \mathbf{p}(t)}_{\text{LSE}} + \mathbf{h}_{Q,k}(t) \circledast \mathbf{p^2}(t)}_{\text{QSE}}. \tag{6.4}$$

6.3.1. QUADRATIC STOCHASTIC ESTIMATION FOR SYSTEM IDENTIFICATION

A relation must be established between the input quantity [wall pressure and wall pressure square fluctuations, $p(z,t)$ and $p^2(z,t)$] and the state of the dynamic plant to control [streamwise velocity fluctuations in the logarithmic region, $u(z,t)$]. For the system identification procedure, data were acquired by the seven wall-embedded microphones, the microphone situated in the freestream, and a hot-wire probe located above each of the seven downstream actuator jets during a control-off scenario. Seven multiple-input single-output (MISO) kernels were generated, using an adaptive Wiener filtering procedure (see 6.3 for technical details) relating a spatio-temporal wall-pressure matrix to a single hot-wire time series in the logarithmic region above each actuator: $u_k(t)$. Seven additional MISO kernels were obtained independently by applying the same Wiener filtering procedure to a spatio-temporal matrix of wall-pressure–squared fluctuations (instead of the linear ones). The identification of seven different kernels is, statistically, not necessary. In fact, a canonical TBL flow is homogeneous in the spanwise direction, meaning that a kernel identified for any given spanwise position should be deployable (given the appropriate spanwise shift) for the estimation of any of the seven output signals. In this work, however, all seven kernels are identified to remove uncertainties related to the specific TBL flow in the facility at Delft University of Technology. The estimated signal, at spanwise location z_k, is then generated by the convolution of the input signals with the transfer kernels:

$$\widehat{u}_k(t) = \mathbf{h}_{L,k}(t) \circledast \mathbf{p}(t) + \mathbf{h}_{Q,k}(t) \circledast \mathbf{p^2}(t). \tag{6.5}$$

Here, $\mathbf{h}_{L,k}$ and $\mathbf{h}_{Q,k}$ are the spatio-temporal kernels relating the linear and quadratic terms of wall-pressure, respectively, to the velocity fluctuations in the logarithmic region at location z_k; the terms $\mathbf{p}$ and $\mathbf{p^2}$ refer to arrays containing the spatial distribution of the wall-pressure and wall-pressure–squared signals at one time-step (*i.e.*, $\mathbf{p}(t_i) = [p_1(t_i)\ p_2(t_i) \ldots\ p_7(t_i)]$ and $\mathbf{p^2}(t_i) = [p_1^2(t_i)\ p_2^2(t_i) \ldots\ p_7^2(t_i)]$). The term $p_k^2 = p_{k,r}^2 - \overline{p_k^2}$ is the (temporally) de-meaned wall-pressure–squared signal, with p_r^2 being the wall-pressure–squared signal prior to the subtraction of its mean.

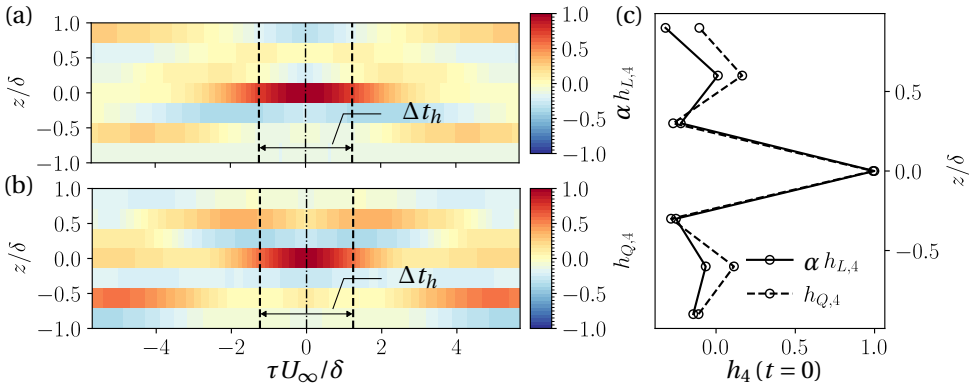

Figure 6.3.: Spatio-temporal kernels relating streamwise velocity fluctuations above the central actuator jet to the instantaneous (a) wall-pressure and (b) wall-pressure–squared fluctuations. Each row of the matrix displayed in the contour plot represents the temporal variation of the transfer kernel. The extent of the temporal horizon, Δt_h, is the temporal extent over which the kernel is convolved with the input signals in real-time. (c) Spanwise profile of both $h_{L,4}$ and $h_{Q,4}$ at $t = 0$.

Figure 6.3a displays one of the seven linear kernels (kernel $\mathbf{h}_{L,4}$, see 6.3 for the notation). The central row of the contour has the largest amplitude among rows, since the correlation is maximum for spanwise co-located wall-pressure and streamwise velocity fluctuations. Symmetric bands of positive and negative correlation appear on either side of $z = 0$ (see Fig. 6.3c), which are consistent with the two-point correlation pattern of large-scale structures in the logarithmic region of a TBL [Hutchins et al., 2011]. Similar observations can be asserted for the kernel relating velocity to wall-pressure–squared fluctuations: $\mathbf{h}_{Q,4}$ (see Fig. 6.3b). Note that for ease of comparison, both kernels presented in Figs. 6.3a and 6.3b are normalized, such that their maximum intensity is equal to unity. In reality, the ratio of the peak-intensities $\alpha = h_{Q,k,\text{peak}}/h_{L,k,\text{peak}} = 1.8$, meaning the quadratic component has greater influence than the linear one (see Fig. 6.5b). The truncation of the kernel at the edges of the temporal horizon introduces an error in the estimation when convolution is performed with an input signal. Future improvements for optimizing a time-constrained (short) kernel can be implemented through a Wiener-Hopf framework in future developments of this flow control strategy, so that the adverse effect of kernel truncation is minimized [Martini et al., 2022].

To understand the importance of the quadratic wall-pressure term, one needs to con-

sider that the large-scale structures that are to be targeted by the controller carry most of their energy at scales where the coherence between wall-pressure and velocity fluctuations is relatively low. Therefore, a controller purely based on the linear term of hydrodynamic wall-pressure fluctuations is defective in accuracy, as it does not encompass any large-scale statistical coupling. However, Naguib et al. [2001] illustrated that the *turbulent-turbulent* source term of the Poisson equation for pressure is proportional to the square of the wall-pressure. Therefore, the inclusion of the wall-pressure–squared term to the estimation problem is essential for bringing the accuracy of the controller to a level comparable (and higher, depending on the specific wavelength considered) to the accuracy of an equivalent wall-shear–based estimation [Baars et al., 2024].

Finally, the accuracy of the control logic can be inferred from the system identification procedure. In particular, given the binary nature of the control output (with the actuator either being 'on' or 'off' according to the sign of the velocity estimate, as discussed next in § 6.3.2), an appropriate metric to assess the accuracy of the controller is the *binary accuracy*. This metric is a statistical measure of the probability that the sign of the estimated signal is equal to the sign of a "true" reference signal. In the present work, the binary accuracy is computed by comparing the estimated signal, $\widehat{u}_k(t)$, to a large-scale filtered time-series of the raw streamwise velocity fluctuations signal in the logarithmic region, measured with a hot-wire probe [see Baars et al., 2024, for details]. The so-computed accuracy amounts to 72.1%, which is considerably higher than the binary accuracy corresponding to a completely random estimation (*i.e.*, 50%).

6.3.2. CONTROL LOGIC

To generate the control output, the velocity state estimates [$\widehat{u}_k(t)$] are binarized to produce digital on/off sequences that drive the solenoid valves. Nominally the controller operates with an *opposition control* law, which counteracts large-scale streamwise velocity regions with a positive estimated velocity fluctuation (Eq. 6.6). Similarly to Ch. 5, *reinforcing* and *desynchronized* control modes were also implemented.

$$v_{\mathrm{jet,k}}(t) = \begin{cases} 0.4U_\infty, & \text{if } \widehat{u}_k(t) \geq 0 \\ 0, & \text{if } \widehat{u}_k(t) < 0 \end{cases}. \tag{6.6}$$

Note that the output signal needs to be accurately timed with the passage of large-scale structures in the logarithmic region, to account for their convection time between the sensing and actuation stations. For this reason, an accurate bookkeeping of the controller latency, delays introduced by hardware components, and flow convection times is necessary in order to ensure a properly timed output, a description of which can be found in 6.4.

6.4. OUTPUT TIMING

For accurate timing of the control output, it is essential to consider the physical separation between the input and output control hardware, as well as their inherent latency. In fact, given convection between upstream (sensor array) and downstream (actuator array) stations, there is a limited time interval available for the generation of the

estimated signal, before structures convect past the actuators' location. With $s = 2.4\delta$ ($s = 0.17$ m) and $U_c = 9.9$ m/s (the measured mean streamwise velocity in the logarithmic region, at $y^+ = 190$), this duration is $\tau_{\text{conv}} = s/U_c \approx 17.2$ ms. First, the real-time convolution of the input signal with the FIR filter requires half the temporal horizon, thus $\tau_h/2 = 7.5$ ms. Additionally, a delay of $\tau_{\text{loop}} = 0.1$ ms is added due to the controller looping at $f_{\text{loop}} = 10$ kHz. As explained in § 5.3, the actuator itself also introduces a mechanical lag of $\tau_a \approx 6$ ms. Thus, the controller requires the following time for providing an output:

$$\tau_C = \tau_h/2 + \tau_{\text{loop}} + \tau_a \approx 13.6\,\text{ms}. \tag{6.7}$$

Since $\tau_{\text{conv}} > \tau_C$, the sensor-actuator spacing of $s = 2.4\delta$ yields a slightly conservative setup (*i.e.*, the control output is "early"). Hence, to accurately time the actuation, an internal delay of 3.6 ms was added within the controller.

6.5. FLOW ASSESSMENT METHODOLOGY

Several measurement techniques were employed to assess the response of the TBL flow to control. These include HWA for time-resolved statistics of the streamwise velocity fluctuations and PIV for an analysis of the turbulent flow within a wall-parallel plane located in the logarithmic region.

For HWA measurements, a TSI IFA-300 constant temperature anemometer was employed, with a standard Dantec 55P15 boundary layer probe. The acquisition configuration for HWA data in this work is identical to the one presented in Ch. 5 and, thus, the interested reader is referred to that part of the work for further details.

Spatial data were also acquired on a wall-parallel (x,z)-plane in the logarithmic region at $y^+_{\text{PIV}} \approx 190$ ($y_{\text{PIV}} = 5.9$ mm) by means of low-speed planar two-dimensional two-component (2D2C) PIV. The field of view (FoV) spanned $3.5\delta \times 1.8\delta$, encompassing the full spanwise extent of the actuator array. The upstream edge of the FoV is located at $x = 0.2\delta$ (see Fig. 6.1). For imaging on this plane, two LaVision sCMOS cameras were used. These are low-speed, 16-bit, double-shutter cameras, with a sensor size of $2\,560 \times 2\,160\,\text{px}^2$ and pixel pitch of 6.5 μm. A Nikkor 60 mm lens was fitted to both cameras, with their f-stops set at $f_\# = 11$. The two imagers were positioned above the test section such that their respective FoVs overlap over a streamwise extent of 0.15δ. Seeding consisted of 1 μm tracer particles from an atomized glycol-water mixture, injected into the wind tunnel flow by a SAFEX 2010+ fog machine. Tracer particles had a diameter of 2-3 px on the image plane. Illumination was provided by a Quantel Evegreen 200 Nd:YAG laser, operating in double-pulse mode with a maximum energy per pulse of 125 mJ. The acquisition frequency was set to 15 Hz, and the time separation between frames in one image pair was $\mathrm{d}t = 75\,\mu$s, ensuring an average pixel displacement of $\approx$ 10 px. A total of 3 000 images were acquired per case, yielding a statistical uncertainty of 0.95% for the mean flow and 2.3% on second-order statistics. Processing was performed with the aid of LaVision DaVis 10.2 by employing a multi-pass algorithm, whereby an initial window of size $48 \times 48\,\text{px}^2$ was first convolved with the particle images, followed by one having size of $24 \times 24\,\text{px}^2$. The overlap length was set to 50% of the interrogation window size. The final vector resolution was 60.68 vectors/δ (0.87 vectors/mm).

6.6. FLOW RESPONSE TO CONTROL

6.6.1. WALL-NORMAL STATISTICS

Response of the TBL flow to control is here considered in terms of the mean and the variance of the streamwise velocity, along a wall-normal profile at $(x,z) = (2\delta,0)$ (see Fig. 6.1).

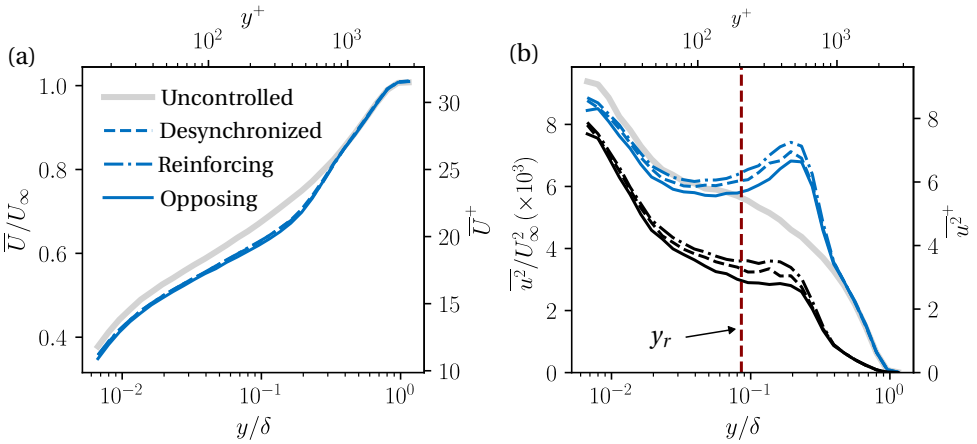

Figure 6.4.: Wall-normal profile of (a) the mean and (b) the turbulence kinetic energy of the streamwise velocity at $(x,z) = (2\delta,0)$, obtained from hot-wire data. Subfigure (b) also illustrating variance of the velocity signal filtered in the spectral range $20 < \lambda_x/y_r < 500$ ($\overline{u_f^2}$), where the largest effect of control is observed (see § 6.6.2).

The mean velocity profile is presented in Fig. 6.4a for the uncontrolled flow as well as for the opposing, reinforcing and desynchronized control modes. A reduction in the mean streamwise velocity for all three control modes is observed, compared to the baseline flow. This observation is consistent with the wall-normal momentum injection imparted by the actuators (see § 5.3). No conclusive difference can be noticed between these curves, and this is ascribed to the actuators being 'on' for the same fraction of time ($\approx 50\%$) among all three control modes. Further inspection of this plot reveals how the effect of control diminishes in the wake of the TBL, where all mean velocity profiles collapse for $y/\delta \gtrsim 0.4$.

Inspection of the streamwise TKE in Fig. 6.4b reveals pronounced differences between control modes. With the flow exposed to opposing control clearly portraying a lower energy content, with respect to the flow undergoing control by the other two control laws, a reduction in the streamwise TKE of $\approx 10\%$ is first evidence of the effectiveness of this controller in quenching energetic structures in the TBL. Furthermore, this trend matches the findings of Ch. 5, albeit this study utilized a different architecture and used wall-shear stress as input quantity instead of wall-pressure. As will emerge in the foregoing, the controller is mostly effective in a specific (low-frequency, *i.e.* large-scale) spectral band, whereby $20 < \lambda_x/y < 500$ (see § 6.6.2 for technicalities regarding the scaling of the

streamwise wavelength). Thus, Fig. 6.4b also display curves corresponding to the wall-normal profile of streamwise large-scale–filtered velocity variance ($\overline{u_f^2}$, in black). These profiles are better suited in displaying the effect of the controller on the TBL flow. In fact, the increase in unfiltered variance around $y/\delta \approx 0.2$ is known to be caused (see § 6.6.2) by the actuator-induced flow, and not by the targeting of LSMs implemented by design.

6.6.2. SPECTRAL ANALYSIS IN THE LOGARITHMIC REGION

Given the goal of the work to prove the effectiveness of a wall-pressure–based real-time controller, it is necessary to understand how the control output modifies the turbulence spectrum. In particular, Fig. 6.5a presents the pre-multiplied inner-scaled spectra of the streamwise velocity fluctuations at $y^+ = 190$. Here, the choice is made to normalize the abscissa as λ_x/y_r according to *wall-scaling*, with $y_r = 5.9\,\text{mm}$ being the wall-normal coordinate of the velocity probe. Wall-scaling was proven to be effective in collapsing the coherence spectra between wall-pressure and streamwise velocity [Baars et al., 2024], which is reported in Fig. 6.5b. Here, the coherence between streamwise velocity and wall-pressure (and wall-pressure–squared) is reported between $p_4(t)$ and velocity fluctuations above the central wall-pressure sensor at $y^+ \approx 190$. Comparing Fig. 6.5a to Fig. 6.5b, it is evident how the most notable effect of control does not appear in proximity of the shallow peak of γ^2_{up} at $\lambda_x/y_r \approx 14$, but is rather more relevant towards larger wavelengths, where the squared wall-pressure term displays the most coherence with $u(t)$. In fact, as the coherence between velocity and the linear term of wall-pressure rapidly decays with downstream distance, the squared term remains more coherent (see Ch. 4).

A direct comparison of the uncontrolled case to the cases under active control highlights an energy increase towards to the low-wavelength (or high-frequency) end of the spectrum, irrespective of control mode. The reason for this energy increase towards to the small-scale end of the spectrum is twofold: (1) the topology of the wake of the actuator-induced flow and (2) the spectral energy content of the velocity estimate, $\widehat{u}(t)$. On the one hand, the actuator jet-in-crossflow system, in fact, generates an internal shear layer within the TBL. As the jet plume convects downstream of the injection point, the shear layer becomes unstable, causing small-scale eddies to break-up and, therefore, cause small-scale energy to increase. On the other hand, the estimated velocity signal is characterized by non-negligible energy content in the small scales. In fact, the pre-multiplied energy spectra of the estimated (output) signal for the central spanwise location [$\widehat{u}_4(t)$] is presented in Fig. 6.5c. Here, a considerable energy content is visible towards the low-wavelength end of the spectrum ($\lambda_x/y_r \lesssim 20$), which corresponds to the sharp energy increase measured in the flow subject to active control, particularly when considering the binarized output that is actually driving the actuators.

6.6.3. RESPONSE OF THE TBL IN THE LOGARITHMIC REGION

Results in the previous section have shown the response of the TBL along either a wall-normal profile or at a single point in the logarithmic region. In the foregoing, results obtained over a two-dimensional plane, resulting from the processing of PIV data, will be introduced. The plane of interest encompasses a FoV that captures the downstream development of the jet actuators' wake, up to a distance of 4δ from the injection loca-

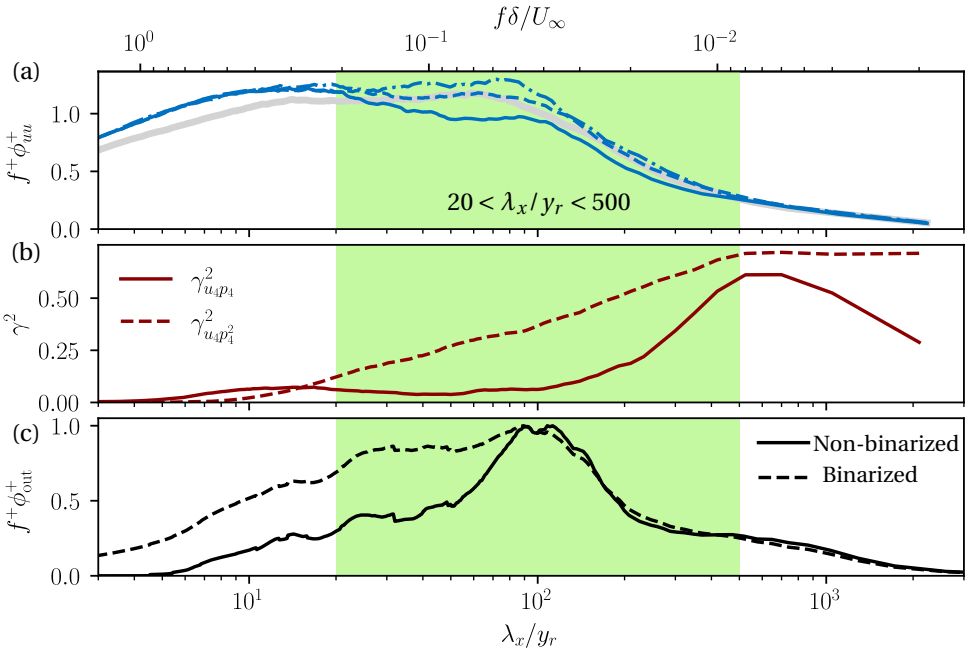

Figure 6.5.: (a) Inner-scaled pre-multiplied energy spectrum of streamwise velocity fluctuations at $y^+ = 190$ for the uncontrolled flow as well as for the three active control modes. (b) Linear coherence spectrum between the streamwise velocity fluctuations and the fluctuations of wall-pressure and wall-pressure–squared at $z = 0$. (c) Pre-multiplied energy spectrum of the estimated signal $\widehat{u}_4(t)$. Also indicating the spectral range where the control effect is mostly noticeable with a pale band. Note that the temporal spectra are plotted as spatial spectra by converting frequency into wavelength, using $\lambda_x \equiv U_c/f$ with $U_c^+ = \overline{U}(y = y_r)$.

tion (see Fig. 6.1a). This allows to thoroughly analyse the spatial response of the TBL to control both at spanwise locations directly downstream and in-between actuators.

Figure 6.6a displays contours of the large-scale–filtered variance of the streamwise velocity fluctuations in the opposing case. Filtering was performed on each instantaneous vector field to only retain the scales affected by control: $\lambda_x/y \gtrsim 20$ (see Fig. 6.5a). For this, an anisotropic streamwise-aligned Butterworth 3$^{\text{rd}}$-order low-pass filter kernel was convolved with the instantaneous spatial data with a cutoff wavelength of $\lambda_x = 20y$. Smaller scales are omitted to allow for the visualization of the flow response induced by the controller, and not by small-scale energy-increasing mechanisms discussed above. Seven low-intensity streaks are visible at the upstream edge of the FoV, which extend all the way to the downstream edge of the domain. These correspond to each of the seven jet actuator wakes, which persist almost up to the downstream edge of the FoV, where the jet plume rises above the laser sheet. Between the wakes of the seven actuators, the velocity

variance is higher than the variance of the uncontrolled flow at the same location. As the jet flow is injected into the TBL crossflow, in fact, a counter-rotating vortex pair is generated, whereby streamwise vorticity carries low-momentum fluid from the downstream near-wall region towards the freestream flow. Conversely, higher-momentum fluid is brought towards the wall by the lateral downward-directed segment of the rotating vortex.

A more direct comparison between the three flow cases in consideration is provided in Fig. 6.6b, whereby the opposing and random cases are compared, in terms of the difference in the large-scale–filtered variance $[\Delta\overline{u_f^2} = \left(\overline{u_f^2}_{\text{opp}} - \overline{u_f^2}_{\text{rnd}}\right) / \overline{u_f^2}_{\text{opp}} \times 100]$. This visualization clearly displays an overall reduction in streamwise large-scale–filtered variance when the control law is set to selectively oppose high-intensity LSMs. Some small-sized regions of the PIV domain do display a relative energy increase, in-between core of the developing jet plumes. The beneficial energy-attenuating effect becomes more homogeneous for $x/\delta \gtrsim 2.5$, with maximum local attenuation reaching 25-30%.

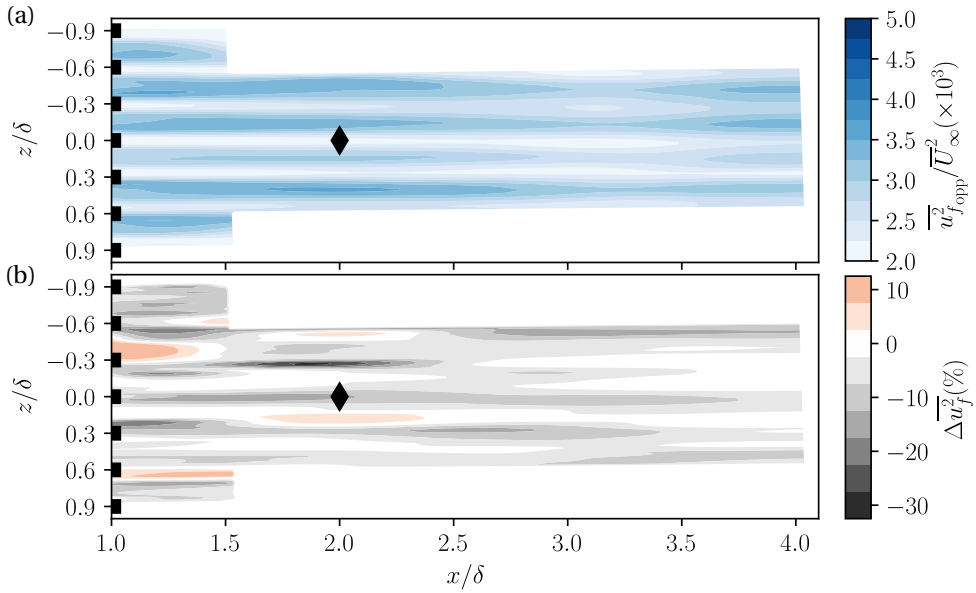

Figure 6.6.: (a) Contour plots of large-scale–filtered variance on a wall-parallel plane of the streamwise velocity for the flow subject to opposing control. (b) Contour displaying the percentage difference in large-scale–filtered variance between the flow subject to opposing and random control strategies. Showing the location of the hot-wire probe at $(x, y, z) = (2\delta, y_r, 0)$ as a black diamond (♦). Displaying the spanwise position of the actuators with black squares (■, note that they were positioned at $x = 0$).

6.6.4. DIRECT SKIN-FRICTION QUANTIFICATION

The principal objective of the real-time controller is to act upon large-scale velocity fluctuations in the logarithmic region as, upon superimposition onto smaller scales in the inner region, a drag reduction can be obtained. Quenching turbulent velocity fluctuations, in fact, can have a profound impact on the principal skin-friction–generating mechanisms [Deck et al., 2014, Renard and Deck, 2016]. Figure 6.7 presents the obtained skin-friction values for both the uncontrolled flow and the flow subject to opposing control. In particular, Figs. 6.7a,b present absolute wall-shear stress for the two cases, while Fig. 6.7c reports the relative change between the two, $\Delta\tau_w = 100\times(\tau_{w,\mathrm{opp}}-\tau_{w,\mathrm{unc}})/\tau_{w,\mathrm{unc}}$. The relative difference reports a positive friction drag reduction across most points, apart from a few outliers, especially at $x = 2\delta$ and $x = 3\delta$. The deviation in these measurement points is attributed to post-processing or measurement error, and not to physical discrepancies in wall-shear. Uncertainty analysis was, however, not performed for these measurements. Still, some points appear as outliers, which results from some user-introduced error or low robustness of the technique. However, when considering the overall trend in skin-friction drag for both flow cases a global spanwise uniformity can be deducted both for the controlled and uncontrolled flows. At this downstream positions, in fact, the wake of the jet-induced actuator flow, in the proximity of the wall, is not affected by spanwise variations in the flow in the logarithmic region and above.

6.7. CONCLUSIONS

To the author's knowledge, this chapter marks the first time that real-time control of wall-bounded flow has been attempted by utilizing wall-pressure fluctuations as the input quantity. The results detailing the response of the TBL flow to control confirm a successful implementation of this pioneering control strategy, both in terms of velocity statistics and of direct skin-friction measurements. Although small-scale energy was introduced in the flow as a result of the actuator-induced flow, this chapter validates the finding of the previous Ch. 4 in the context of being able to use wall-pressure (and wall-pressure–squared) fluctuations as a reliable input quantity.

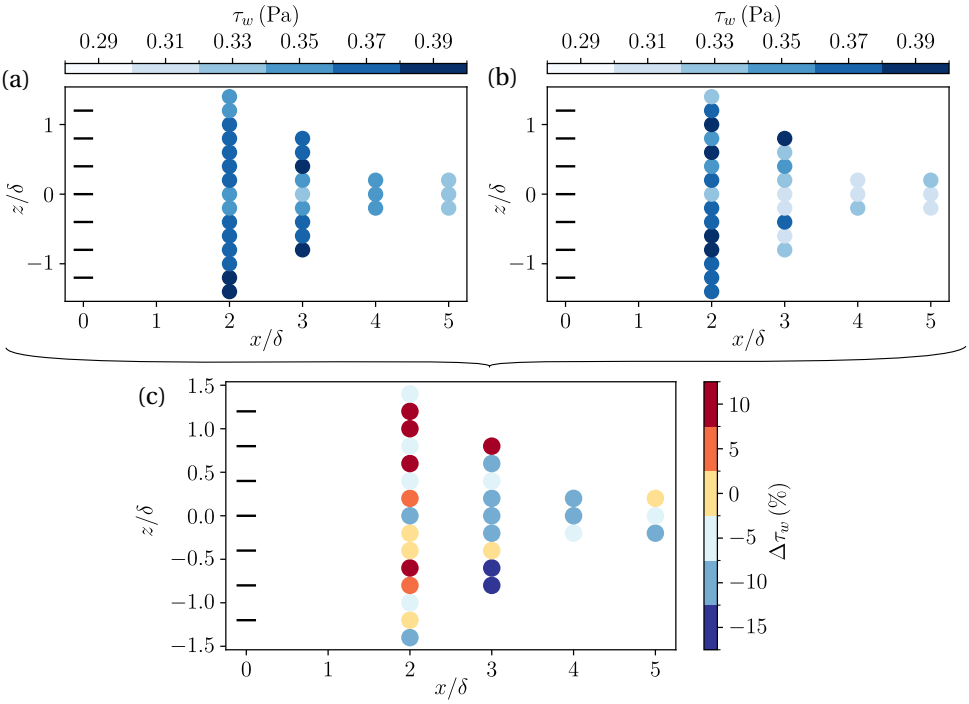

Figure 6.7.: Absolute wall-shear stress at several locations on the wall downstream of the jet actuators obtained from OFI data for (a) the uncontrolled flow and (b) the flow subject to opposing control. (c) Relative difference between the wall-shear stress of the opposing and uncontrolled cases.

IV

TOWARDS ADAPTIVE CONTROL

7

ADAPTIVE CONTROL OF WALL-BOUNDED TURBULENCE

Reach for the stars.

Christa McAuliffe (STS-51-L)

This final chapter of the dissertation comprises a study and a series of experiments conducted on the development and deployment of a more advanced control logic compared to the feedforward opposition control logic illustrated in previous chapters. In particular, an adaptive Filtered-X Least Means Squares (Fx-LMS) algorithm was deployed for the control of a wall-bounded turbulent flow. Given the increased complexity behind the design of this control law, initial experiments were not conducted on the control of a fully broadband turbulent flow, as was the case in previous parts of this work. Instead, a flow case characterized by strong harmonic content and periodic behavior was considered: a TBL modulated by vortex shedding in the wake of a two-dimensional spanwise-aligned cylinder. Building on top of the results obtained from this preliminary set of experiments, this chapter will be concluded by presenting results obtained from the deployment of the same control algorithm to the fully broadband case.

7.1. INTRODUCTION

In earlier chapters of this dissertation, an opposition control law was defined and a static transfer function was identified based on input-output data acquired *a priori*. In particular, simultaneous data were usually acquired from the input sensor(s) and the flow state in the logarithmic region at the streamwise position of the actuator (usually, streamwise velocity fluctuations). For engineering applications, the ability to acquire such data prior to the deployment of the controller is not fully representative of the input-output system dynamics that characterize the flow. For instance, cruise airspeed or altitude for an airliner might change, thus changing the local Reynolds number and, thus, also changing the transfer function that estimates the flow state, given a certain input signal. A controller can automatically adapt to slowly-varying conditions is beneficial in terms of operational flexibility.

Literature on the implementation of such control strategies for turbulent flow control applications is limited. Few studies are available that either tackle the problem from an analytical [Breuer and Wu, 2006] or a numerical point of view [Farazmand and Sapsis, 2019], considering very-low-Reynolds number flows. Further work that illustrates the application of adaptive control strategies to flow control problems can be found in the publication by Kotsonis et al. [2013], who deploy an adaptive controller for the attenuation of harmonic flow disturbances in a transitional boundary layer flow.

To the author's knowledge, there exists no work in the open literature that deals with the implementation of an adaptive controller to (1) a turbulent wall-bounded flow and (2) in an experimental setting. The complexity to deal with the former issue lies in the fact that a turbulent wall-bounded flow, such as a TBL, is inherently characterized by fluctuations with an extremely broadband spectrum. Thus, a controller faces the challenge of needing to identify spectral components that can attenuate a certain (arbitrary) "error" signal. The latter issue, instead, stems from the fact that, as was mentioned in previous chapters, access to the fluid domain is limited in a laboratory setting. This renders the identification of the required transfer kernels more intricate, as only spatially sparse information are available to the controller.

In this chapter, the development of a control strategy based on the adaptive feedforward Filtered-X Least Mean Squares (Fx-LMS) algorithm is going to be illustrated. First, the working principle of the Fx-LMS algorithm will be presented in § 7.2, together with initial testing performed on acoustic wave control in § 7.3. Consequently, the algorithm is going to be first deployed for the control of a turbulent flow with a strong harmonic content: a TBL flow modulated by the vortex shedding in the wake of a spanwise-aligned two-dimensional cylinder (§ 7.4). The response of the flow is going to be analyzed by means of both HWA and PIV measurements, with an attenuation of the vortex shedding intensity expected as a result of control. Finally, the Fx-LMS algorithm is going to be employed for the control of the fully broadband TBL flow (§ 7.5)

7.2. THE FX-LMS ALGORITHM

The Fx-LMS algorithm is an adaptive control strategy that was initially developed for active noise control (*e.g.* noise-cancelling devices) [Hansen, 2001]. This algorithm (whose block diagram is presented in Fig. 7.1) essentially operates as a gradient-descent–based optimizer that works towards the minimization of an error signal. Whereas in the case of acoustic noise attenuation the goal would be to minimize the noise at a certain "error" location, in this work it coincides with the attenuation (or *opposition*) of the turbulence-induced fluctuations at the location of the downstream array of error sensors. This is accomplished with the aid of the real-time identification of two finite impulse response (FIR) kernels: the cancellation path [FIR 2, with coefficients $\mathbf{w}^{(2)}$] and the control [FIR 1, with coefficients $\mathbf{w}^{(1)}$] kernels.

The former is identified in an initial phase of the deployment of the Fx-LMS (prior to the identification of the control kernel) and models the conditional response of the error signal as a function of the actuator output. In order to model the response of the error signal to an arbitrary action of the actuator, a control output needs to be generated whose statistics differ from the ones of the dynamic plant to control. This difference is required not to "bias" the controller towards the unique signature of the dynamic system to-be-controlled and avoid overfitting to it, thus leading to loss of generality. For this reason, Hansen [2001] suggests an approach whereby a completely random signal is fed to the actuator in this phase of system identification. When dealing with highly non-linear complex dynamic systems, one can resort to an approach that is designated as *overall modelling* in the work of Hansen [2001]. Here, the random signal ($\mathbf{r}$) driving the actuator is linearly combined with the physical input signal ($\mathbf{x}$), with a certain input-to-random intensity ratio (regulated by the gain G in the block diagram in Fig. 7.1). The random signal consisted of white noise, bandpassed in the frequency range of interest. The resulting signal is denoted as $\mathbf{f}^{(2)}(k) = \mathbf{x}(k) + G\mathbf{r}(k)$. [Note that the quantities denoted by a bold symbol are taken as arrays over a certain temporal horizon.] Then, at time-step k, the FIR 2 filter coefficients $\mathbf{w}^{(2)}$ at the following time-step, $k+1$, are given by the update law:

$$\mathbf{w}^{(2)}(k+1) = \mathbf{w}^{(2)}(k) - 2\mu_2 e(k)\mathbf{f}^{(2)}(k)\,, \tag{7.1}$$

with $\mu_2 = 10^{-5}$ being the convergence (or *learning*) rate. During the identification of the cancellation path kernel, the goal is to minimize the difference the error signal and the difference $\Delta^{(2)} = \mathbf{x}^{(2)}(k) \circledast \mathbf{f}^{(2)}(k) - e(k)$. Once FIR 2 is identified, a copy of said kernel is deployed to the bottom-left block in Fig. 7.1, and is used to produce the filtered input signal that feeds into the LMS update law for the identification of FIR 1, which is rather similar to the one for FIR 2:

$$\mathbf{w}^{(1)}(k+1) = \mathbf{w}^{(1)}(k) - 2\mu e(k)\mathbf{f}^{(1)}(k)\,. \tag{7.2}$$

Now, $\mu_1 = 10^{-3}$ is the learning rate and $\mathbf{f}^{(1)}(k) = \mathbf{w}^{(2)}(k) \circledast \mathbf{x}$ is the result of the convolution with the cancellation path transfer function with the input signal, over a designated temporal horizon. Here, the goal is to minimize the error signal. A small note on the convergence rates μ_1 and μ_2 is in order. In fact, the value of both constants is highly dependent on the dynamic plant to be controlled. Too large of a value leads to divergence in the identification of the corresponding kernel (either FIR1 or FIR2). Instead, too low of

a value leads to extremely slow convergence, leading to impractical identification delays. In this work, both constant were chosen following a sensitivity analysis of the identified kernel coefficients and convergence behaviour.

In essence, the goal of the Fx-LMS procedure is to perform a gradient-descent–based optimization of the coefficient of the FIR kernels that need to be identified. The complete derivation for the update law in Eq. 7.1, as well as most technicalities regarding the development of the Fx-LMS algorithms, can be found in the work of Hansen [2001].

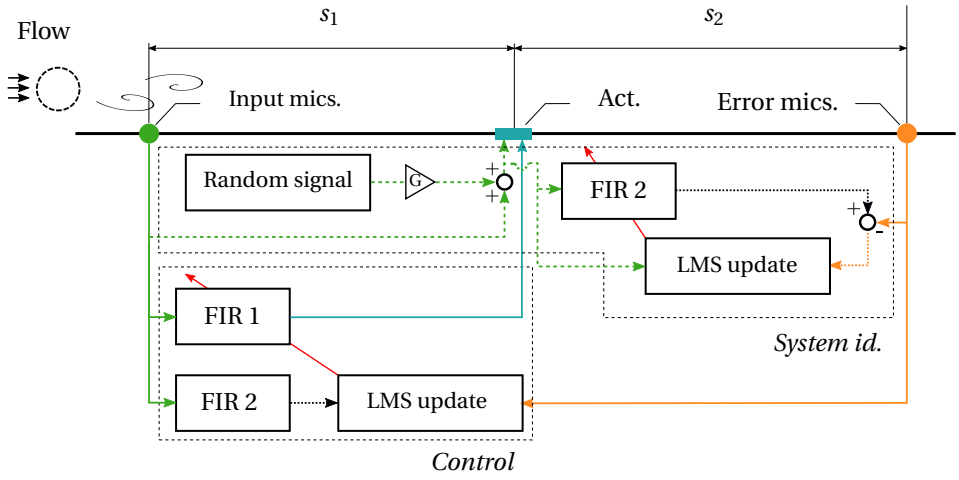

Figure 7.1.: Block diagram of the single-channel feedforward FxLMS algorithm, recreated and adapted from the work of Hansen [2001].

7.3. INITIAL DEVELOPMENT AND TESTING OF THE FX-LMS ALGORITHM

For the initial development and troubleshooting of the adaptive Fx-LMS algorithm, a control experiment was realized with the aim to attenuate (multi-)tonal planar acoustic waves. The choice of this particular configuration is owed to the initial intended target for the deployment of the Fx-LMS algorithm: noise-canceling devices [Hansen, 2001], with an example schematic of which found in Fig. 7.2a. Initial testing of the Fx-LMS algorithm on an acoustic problem had three principal goals.

1. To establish the performance of the Fx-LMS algorithm on a quiescent flow case, where the only control target was the attenuation of harmonic acoustic waves.

2. To understand the principal limitations and pitfalls of the control algorithm in relation to subsequent experiments, where the input signals are going to be broadband in nature.

3. To troubleshoot with real (*i.e.* not simulated) signals.

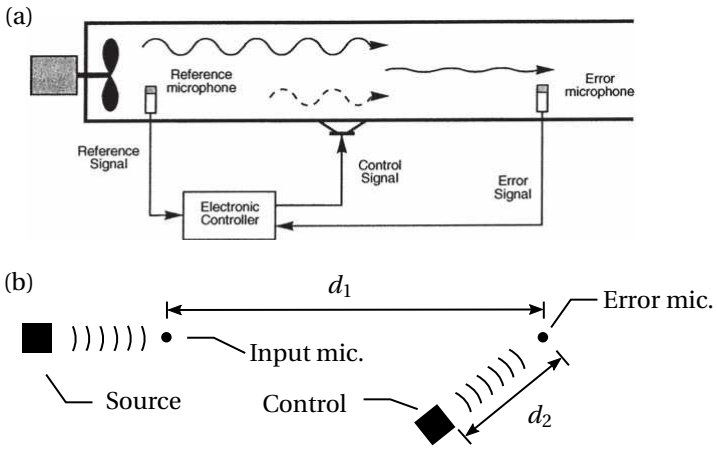

Figure 7.2.: (a) Schematic of control system for the cancellation of acoustic waves. Taken from the work of Hansen [2001].(b) Schematic of the setup for acoustic noise control testing carried out for the current work.

Here, a disturbance source (or a periodic flow excitation, as shown in the left-hand side of the diagram as a propeller) is used to generate the wave fronts that need to be attenuated[1]. Downstream (in the direction sound propagation) a second speaker is located that acts as actuator. Finally, an error microphone is placed in the line of action of both the input and the control speakers. This is where an attenuation of the acoustic waves should be achieved and measured. Note that, in our work, the input consist of acoustic waves with three distinct tonal peaks, namely located at $f_{\text{input}} = \{310\,\text{Hz}, 700\,\text{Hz}, 1\,000\,\text{Hz}\}$ and denoted by dashed gray vertical lines in Fig. 7.3. The simplicity of this sound spectral signature was chosen in such a way that the controller *should* readily identify the three tonal peaks (or at least the most energetic ones) and attenuate their intensity. The corresponding spectrum of the sound emitted by the input speaker is shown as a solid black curve in Fig. 7.3.

The hardware employed for this test comprised comprised a Fun Generation BP115A 140W speaker as the input (sound source) and a Marshall MG51G as the control speaker. The input and error sensors consisted of a single GRAS46BE 1/4-in. free-field CCP microphone, located at a distance of $d_1 = 3.5\,\text{m}$ from the input speaker and $d_2 = 1.2\,\text{m}$ from the control speaker (see Fig. 7.2b). The algorithm was run on a Speedgoat Performance real-time target machine at a loop frequency of $f_{\text{loop}} = 10\,\text{kHz}$ within a Simulink real-time environment. The input and output signals were produced by the same control model and sent to the speakers by means of a 16-bit analog output module (IO235). The signal of the error microphone was measured with the aid of a 24-bit A/D module (IO109).

The spectra presented in Fig. 7.3 already hint at an effective implementation of the Fx-LMS algorithm for acoustic noise cancellation. In particular, the signal driving the control speaker has the same spectral signature as the input. To verify the inner workings of

[1] Please note that the testing environment was not anechoic, meaning that random reflections and reverberations were present at the time of testing.

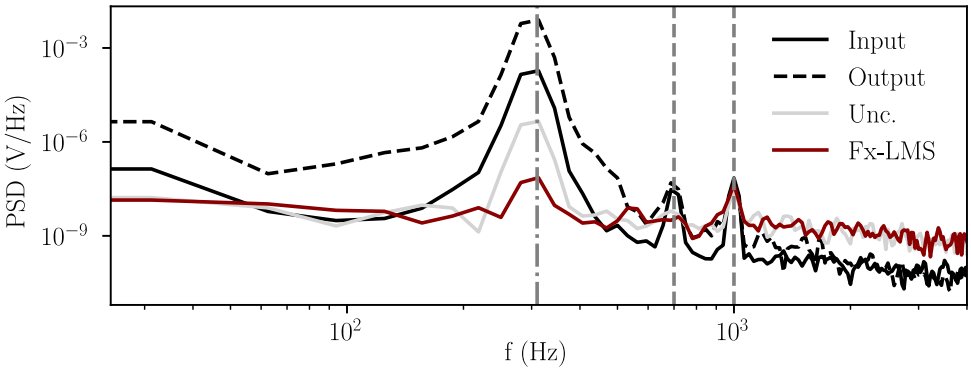

Figure 7.3.: Power spectral density spectra of the input and output waves generated by the input and output speakers shown as solid and dashed black curves, respectively. The spectra of the signals measured by the error microphone for the uncontrolled (unc.) and controlled (Fx-LMS) cases, instead, are shown with as a light gray and dark red curves, respectively.

the controller, the two identified FIR filters (cancellation path and control kernels) can be analyzed. Both of them are plotted in Fig. 7.4 and clearly show a periodicity that is consistent with the lowest-frequency tonal peak that characterizes the spectral signature of the input sound waves (and whose period is indicated by a vertical dash-dotted line). The relative phase-shift between FIR 1 and FIR 2 is to be owed to the different physical locations of the control and input speakers. The temporal extent (or *horizon*) of the identified kernels is such that the lowest dominant frequency can be captured within said horizon. However, too long of an horizon can lead to issues with the statistical convergence of the kernel as the controller needs to run gradient-based optimization for a large number of coefficients [Hansen, 2001].

To analyze the effect of the Fx-LMS–based controller onto the acoustics of this preliminary experiment, one can also directly inspect the time series of the error microphone, to compare uncontrolled and actuated cases. First, the input signal (measured by the input speaker) is plotted in Fig. 7.5a. The error microphone's time series is then plotted over a longer time interval, including the time when the Fx-LMS controller was actually started (dash-dotted vertical line), upon conclusion of the cancellation path identification procedure, in Fig. 7.5b. Here, one can appreciate the reduction of the amplitude of the envelope (*i.e.* the intensity) of the error signal, following the deployment of the controller. Over an interval of ≈ 2 s, in fact, the control kernel is identified by the controller and the intensity of the error signal drops to a steady noise-attenuated level. Finally, Fig. 7.5c shows the time series of the error signal before and after the activation of the controller (in black and red solid curves, respectively). The reduction of the amplitude of the controlled signal is clear when superimposed on top of the uncontrolled one. Finally, the time series of the output signal is also plotted. A time-shift is applied to correct for the non-zero travel time from the output speaker to the error microphone. Once applied, it is clear how the output signal acts in phase opposition to the input signal such

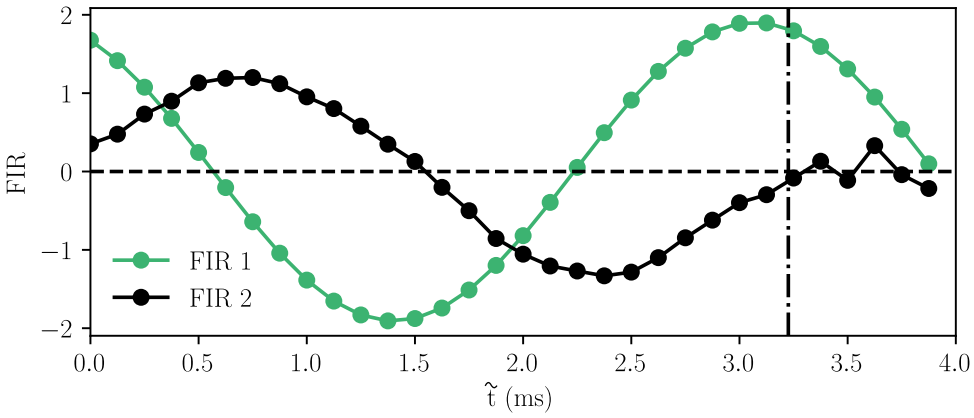

Figure 7.4.: Plot of the FIR coefficients for the cancellation path and control kernels. Displaying the length of the period of the first tonal peak at $f = 310\,\text{Hz}$ as a dash-dotted black vertical line. Here, the x-axis refers to time on the horizon of the controller. $t = 0$ is the present, with increasing t referring to values in the past.

that, when superimposed, the result is an attenuated condition.

7.4. CONTROL OF CYLINDER VORTEX SHEDDING

The step to applying the Fx-LMS algorithm to a fully broadband TBL flow is one that is not easily accomplished. Therefore, an intermediate step is taken, whereby harmonic disturbances are introduced in a broadband turbulent flow. For this purpose, vortex shedding in the wake of a two-dimensional spanwise-aligned cylinder is going to be considered. The high-intensity harmonic passage of vortices in the Kálmán vortex street is superimposed onto the broadband signature of the TBL flow in which the cylinder is immersed. The Fx-LMS controller, therefore, is expected to readily identify the vortex shedding as the principal component to oppose.

7.4.1. EXPERIMENTAL IMPLEMENTATION

Experiments were carried out in an open-return wind tunnel facility (W-Tunnel) at the Delft University of Technology, the detailes of which can be found in §2.1. A coordinate system (x, y, z) is used that has its origin on the wall at the spanwise center of the test section, at a distance of 2.90 m downstream of the trip. To harmonically force the flow, a wall-parallel, spanwise-oriented cylinder was installed, having a diameter of $D = 0.032\,\text{m}$. The diameter of the cylinder such that vortex shedding would occur at frequency that is representative of the passage of LSMs in the logarithmic region of a TBL. The cylinder was positioned with its centerline at $(x, y) = (-7.3, 1.5)D$. A schematic of the experimental setup is presented in Fig. 7.6a.

Input sensors consisted of eight GRAS 46BE quarter-inch free-field CCP microphones,

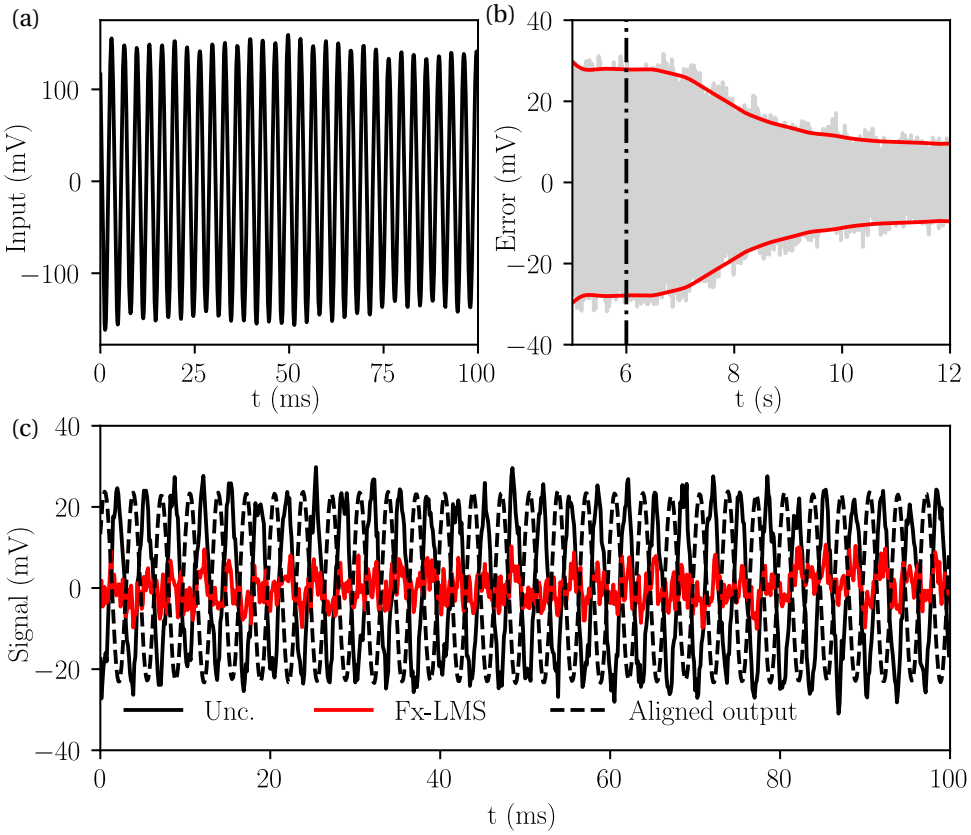

Figure 7.5.: (a) Time series of the input signal over a short time interval. (b) Time series of the error microphone signal over a time interval when the Fx-LMS controller has completed the identification of the cancellation path kernel and the identification of the control kernel is started (at $t = 6\,\mathrm{s}$, as shown by the vertical dash-dotted line). Also displaying the envelope of the error signal to further illustrate the attenuation of its intensity. (c) Time series of the uncontrolled microphone signal (Unc.), the time series of the error microphone subject to control (Fx-LMS) and the output signal (Aligned output).

having a nominal sensitivity of 3.6 mV/Pa. Seven of them were integrated in a spanwise array of pinhole-cavities, flush-mounted to the wind tunnel wall at $x = -5.3D$. Additionally, a single microphone was sting-mounted into the freestream flow to monitor acoustic noise and to facilitate real-time noise-removal. Note that the freestream microphone was not employed in the control loop for other purposes other than for noise-cancelling procedures.This procedure is based on a real-time projection of all eight instantaneous pressure signals onto pre-identified spatial POD modes. Actuators comprise three wall-normal blowing jets triggered simultaneously, activated by fast-acting on/off solenoid valves, with an exit velocity of $v_{\mathrm{jet}} = 0.8U_\infty$. The actuators are situated at $x = 0$. Finally,

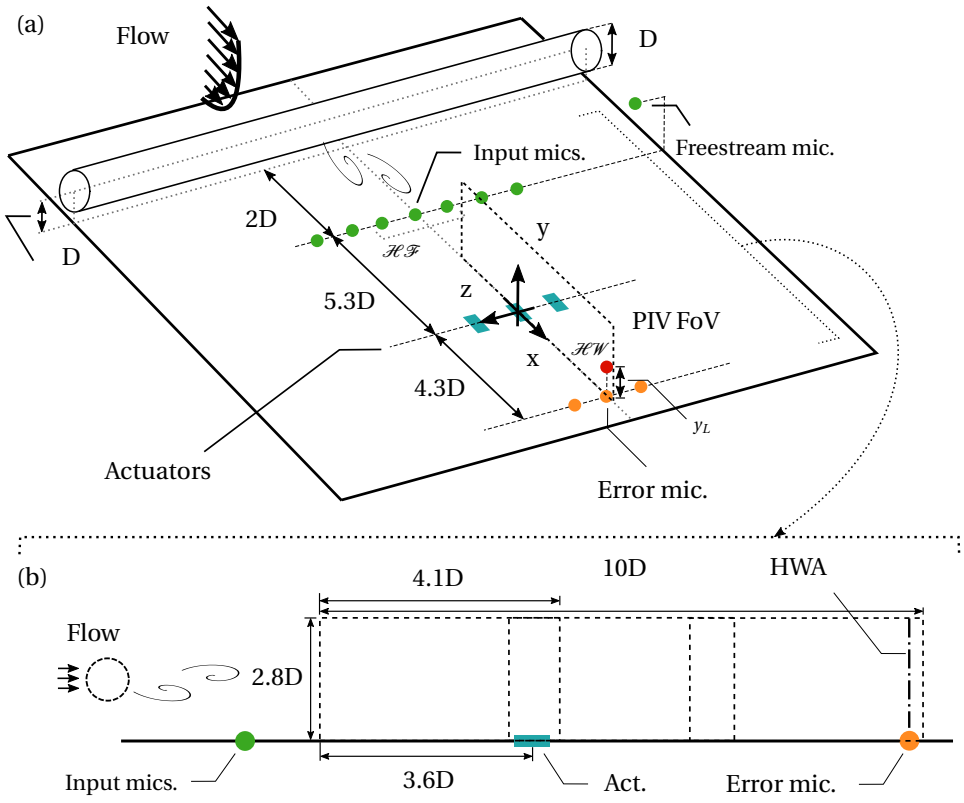

Figure 7.6.: (a) Schematic of the experimental setup in Delft University of Technology for testing the Fx-LMS algorithm for the control of the vortex shedding induced in the wake of a spanwise-aligned two-dimensional cylinder. (b) Illustration showing the extent of the field of view employed for planar PIV acquisitions and the position of the wall-normal profile where hot-wire anemometry measurements were performed.

error sensors are integrated at $x = 4.3D$ and consisted of 7 PUI AOM-5035L-HD3 electret microphones. A noise-correction procedure based on POD was also implemented for this downstream array of sensors. The control loop runs at a frequency of $f_{\text{loop}} = 2.5\,\text{kHz}$ on a Speedgoat Performance real-time target machine.

For assessment of the controlled flow, fields of the streamwise and wall-normal velocity components were acquired using two-dimensional two-component (2D2C) planar PIV. For this, a setup comprising three cameras was employed, resulting in a streamwise-elongated field of view (FoV), having a size of $10D \times 2.4D$ ($4.57\delta \times 1.10\delta$, see Fig. 7.6b). The imagers consisted of LaVision sCMOS cameras, which are double-shutter, low-noise, low-speed cameras, with a sensor size of $2560 \times 2160\,\text{px}^2$ and a pixel pitch of $6.5\,\mu\text{m}$. A total of 4 000 images were acquired per case. Illumination was provided by a Quan-

tel Evergreen 200 Nd:YAG double-pulse laser, with a maximum energy output per pulse of 125 mJ. Finally, seeding particles with a mean diameter of $\approx 1\,\mu$m were used, generated by the atomization of a glycol-mixture by a SAFEX 2010+ fog machine. Processing was performed with the aid of LaVision DaVis 10.2 and a multi-pass routine, with the first window having a size of $48 \times 48\,\text{px}^2$, followed by one having size of $24 \times 24\,\text{px}^2$. With a window overlap of 50% in both passes, the final vector pitch was 19.20 vec/D (42.00 vec/δ). Additionally, hot-wire measurements were performed along a wall-normal profile at the streamwise location of the error microphones (see the dash-dotted line in Fig. 7.6b). Technicalities regarding the hardware for running the HWA measurements can be found in § 2.3.2.

7.4.2. SYSTEM IDENTIFICATION

Following the system identification procedure outlined in § 7.2, the cancellation path and control kernels were identified, and are plotted in Fig. 7.7. Similarly to the control of acoustic waves mentioned in the previous section and the kernels for which were presented in Fig. 7.4, the kernels that were identified for the control of harmonic vortex shedding converge to a sinusoidal wave whose period matches the one that characterizes the period of vortex shedding. This confirms that the Fx-LMS alghorithm correctly identifies the dominant frequency in the flow and, inherently, works towards attenuating it.

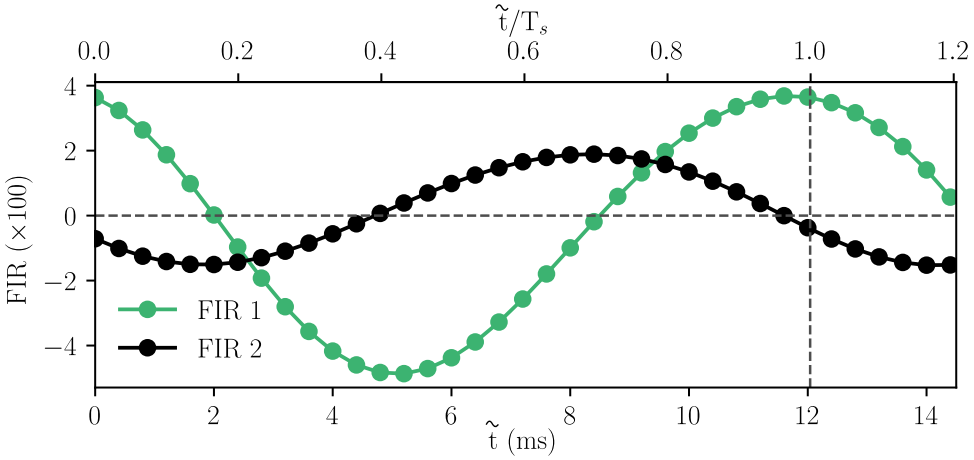

Figure 7.7.: Plot of the FIR coefficients for the cancellation path (FIR 2) and control (FIR 1) kernels for the control problem aiming at the attenuation of vortices in the wake of a spanwise-aligned two-dimensional cylinder. Displaying the length of the period of the characteristic vortex shedding ($f = 88\,\text{Hz}$) as a dashed black vertical line.

7.4.3. FLOW RESPONSE TO ADAPTIVE CONTROL

The response of the flow to control is here presented first in terms of streamwise velocity spectra along a wall-normal profile at $x = 4.3D$. Pre-multiplied energy spectra of the streamwise velocity component are shown in Fig. 7.8a, in terms of a spectrogram for the uncontrolled flow: $\phi_{uu}(St^*, y/D)$. Here, St^* refers to the characteristic Strouhal number $St^* = fD/U^*$, with $U^* = 12.5\,\mathrm{m/s}$ being the average streamwise velocity at the y-location of the cylinder axis ($y = 2D$) in the clean TBL (*i.e.*, when no cylinder is installed in the test section). The spectrogram in Fig. 7.8a shows a sharp energy increase around $St^* = 0.22$ ($f = 85\,\mathrm{Hz}$). The high-intensity energy is concentrated, as expected, around the upper and lower shear layers of the cylinder wake Michelis and Kotsonis [2015]. The percentage difference of the wall-normal spectrogram of the controlled flow, with respect to the uncontrolled case, is presented in Fig. 7.8b. A clear reduction in peak-energy of up to $\approx 39\%$ at $St^* \approx 0.22$ is observed in the region $0.2 \leq y/D \leq 1$. Similar conclusions can be drawn from wall-normal hot-wire velocity profiles acquired at $x = 0$ and $x = 2.15D$, but the results are not presented here for brevity. Stronger attention is given to the spectrum at $y = 1.5D$ (in line with the axis of the cylinder, in Fig. 7.8c), where a comparison is drawn between the uncontrolled and the opposing flow cases and an attenuation is observed of the vortex shedding peak is observed for the flow subject to opposition control by the Fx-LMS algorithm.

Generalizing the findings from hot-wire anemometry measurements, planar PIV data can be processed to show the total energy (*i.e.* the variance) of fluctuations of the wall-normal velocity component, $\overline{v^2}$. Figure 7.9a reports a contour of wall-normal velocity variance in the PIV FoV (see Fig. 7.6b) for the vortex shedding flow in the wake of the cylinder, but without control being applied. Figure 7.9b reports, instead, the same contour, but now for the random and opposing control modes. By close inspection, one can notice that, in the upstream portion of the contour plot, the random control variance is, on average, higher than for the opposing mode. This points at a successful targeting of the most energetic v-fluctuations by the controller and, in fact, an overall reduction in wall-normal variance can be formally evinced from the relative difference in variance, reported in Figure 7.9c.

Consequently, the response of the flow to control is now presented in terms of the wall-normal velocity spatial spectra, extracted from PIV data throughout the complete FoV. We hereby compare the spectral response of the flow under opposing control to the one where random control was deployed. Energy spectra of the wall-normal velocity component are shown in Fig. 7.10a, as a spectrogram for the flow under the influence of random control: $\phi_{vv}(St^*, y/D)$. To be noted that, since the original dataset is distributed spatially (PIV-based vector fields), a transformation needs to be applied to convert spatial information to temporal data. Two assumptions are hereby made: (1) we apply Taylor's frozen turbulence hypothesis, as $f = U^*/\lambda \implies St^* = D/\lambda$, with λ being the spatial wavelength of v-velocity fluctuations, and (2) that the flow is homogeneous in the streamwise direction (x). However, the flow is slowly developing along x, thus introducing a slight distortion in the spectra presented in the foregoing. The spectrograms in Fig. 7.10a and Fig. 7.10b show a sharp energy increase around $St^* = 0.22$ ($f = 85\,\mathrm{Hz}$). The percentage difference of the wall-normal spectrogram of the controlled flow, with respect to the uncontrolled case, is presented in Fig. 7.10c. A clear reduction in peak-

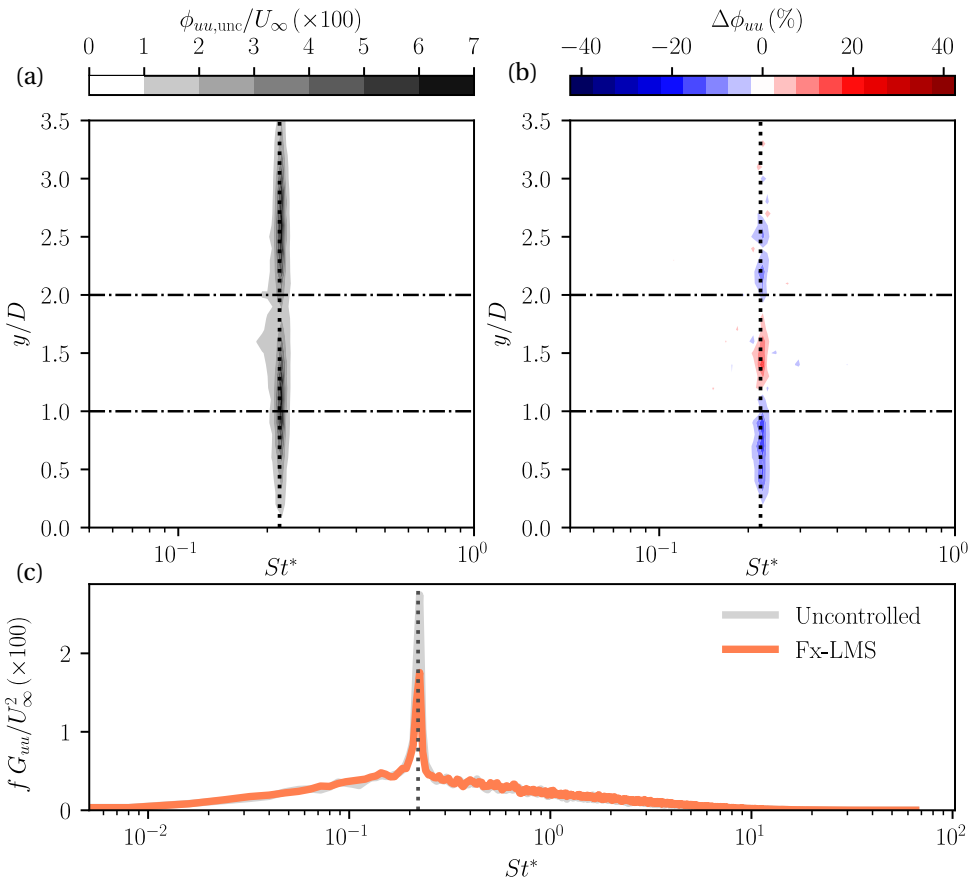

Figure 7.8.: (a) Spectrogram $\phi_{uu}(y;f)$ of the fluctuations of streamwise velocity, measured along a wall-normal profile with hot-wire anemometry for the uncontrolled case. (b) Same as (a), but now considering the difference-spectrogram between the case where the flow was subject to opposing control and the case where random control was performed. (c) Spectrum of the streamwise velocity fluctuations at $y/D = 1.5$, directly comparing the uncontrolled case to the one where Fx-LMS control was applied. Displaying the location of the characteristic vortex shedding frequency at $St^* = 0.22$ with a vertical dotted line.

energy of up to ≈ 15% at $St^* \approx 0.22$ is observed in the region $0.7 \leq y/D \leq 2.2$. Similar conclusions can be drawn from wall-normal hot-wire velocity profiles acquired at $x = 0$ and $x = 4.3D$, but the results are not presented here for brevity.

Thus far, results confirm that, spectrally, the controller is able to successfully counteract and attenuate the highly-energetic wall-normal velocity fluctuations that occur in the wake of the spanwise-aligned cylinder. In the foregoing, it will be shown how the

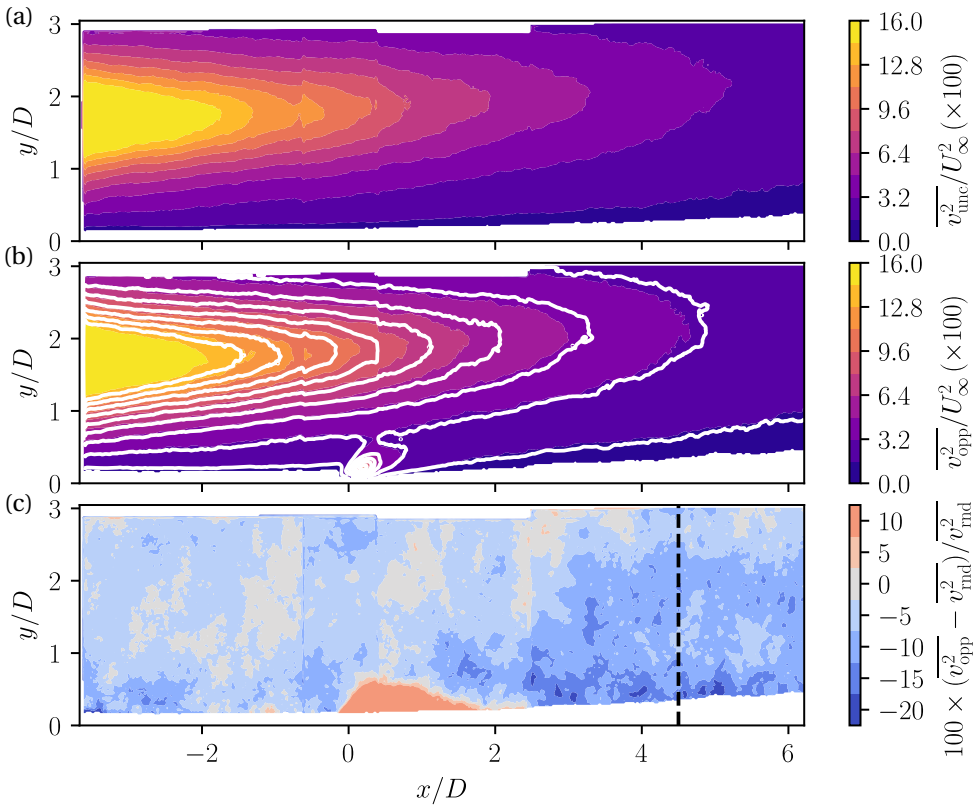

Figure 7.9.: (a) Contour of the variance of wall-normal velocity fluctuations in the wake of the spanwise-aligned cylinder for the uncontrolled case, captured with planar PIV. (b) Same as (a), but now considering the case where control was opposing the vortex shedding (filled contours) and where random control was applied instead (white contours, levels at 0:1.6:16). (c) Filled contour of the difference between the variance of wall-normal velocity fluctuations in the opposing and random control scenarios. Dashed black line referring to the nominal hot-wire streamwise position.

controller interacts with the incoming flow and, specifically, which structures are identified by the Fx-LMS algorithm as the ones to be targeted. This is accomplished via the presentation of phase-averaged velocity fields:

$$\langle \mathbf{u}_k \rangle = \frac{1}{n_k} \sum_{i \in \mathrm{bin}\ k} \mathbf{u}_i, \tag{7.3}$$

where n_k is the number of frames in each bin, with the number of bins depending on the chosen discretization of the phase ($\phi_i = 2\pi \cdot t_i \bmod T/T$, with t_i being the time instant the frame was taken and T the characteristic period of the conditioning signal) of the conditioning signal. In fact, phase-averaging requires the selection of a condi-

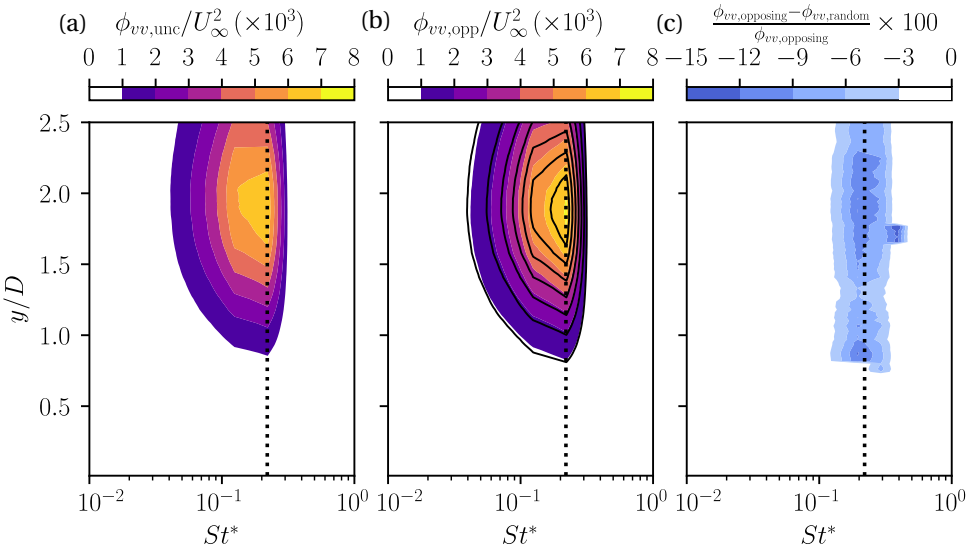

Figure 7.10.: Spectrogram $\phi_{vv}(y;f)$ of wall-normal velocity fluctuations (acquired with planar PIV) of the (a) opposing and (b) random cases. (c) Difference spectrogram between the opposing and random control cases. Displaying the location of the characteristic vortex shedding frequency at $St^* = 0.22$ with a vertical dotted line.

7

tioning signal and conditioning events. For this work, the former is chosen to be the control signal (*i.e.* the signal that is sent to the actuator before binarization), whereas the latter consist of its positive-gradient zero-crossings. Figure 7.11 presents the phase-averaged v-fields for the uncontrolled case, where the signature of the vortex shedding in the Kármán vortex street can clearly be noticed [please note that, when considering phases "away" from the condition point (*i.e.*, $\phi = 0$), the amplitude of the averaged oscillation decreases, given the limited length of the integral time scale]. For comparison, Fig. 7.12 presents the phase-averaged contours for the case subject to opposition control with the aid of the Fx-LMS algorithm. Whereas the shedding was extremely clear in Fig. 7.11, here one can notice a disruption of the naturally-occurring vortex shedding, to give way to a more smeared sequence of spanwise-aligned vortices. In particular, the downward-directed motions appear of lower intensity, given the upward-directed actuator flow. This is clear evidence of the correct implementation of considerable control effect that was obtained with this adaptive control law. A word of caution needs to be mentioned. In fact, for the last three phases in consideration (*i.e.* $\varphi = \{3\pi/3, 4\pi/3, 5\pi/3\}$), the jet should nominally be off. However, a clearly non-zero vertical velocity component is appreciably visible in the vicinity of $x = 0$, where the actuator was placed. Although the reason for this is still unclear to the author, two factors can potentially be the cause of this observation:

1. **A leak in the feed system.** Improper closing of the solenoid on the plane of acqui-

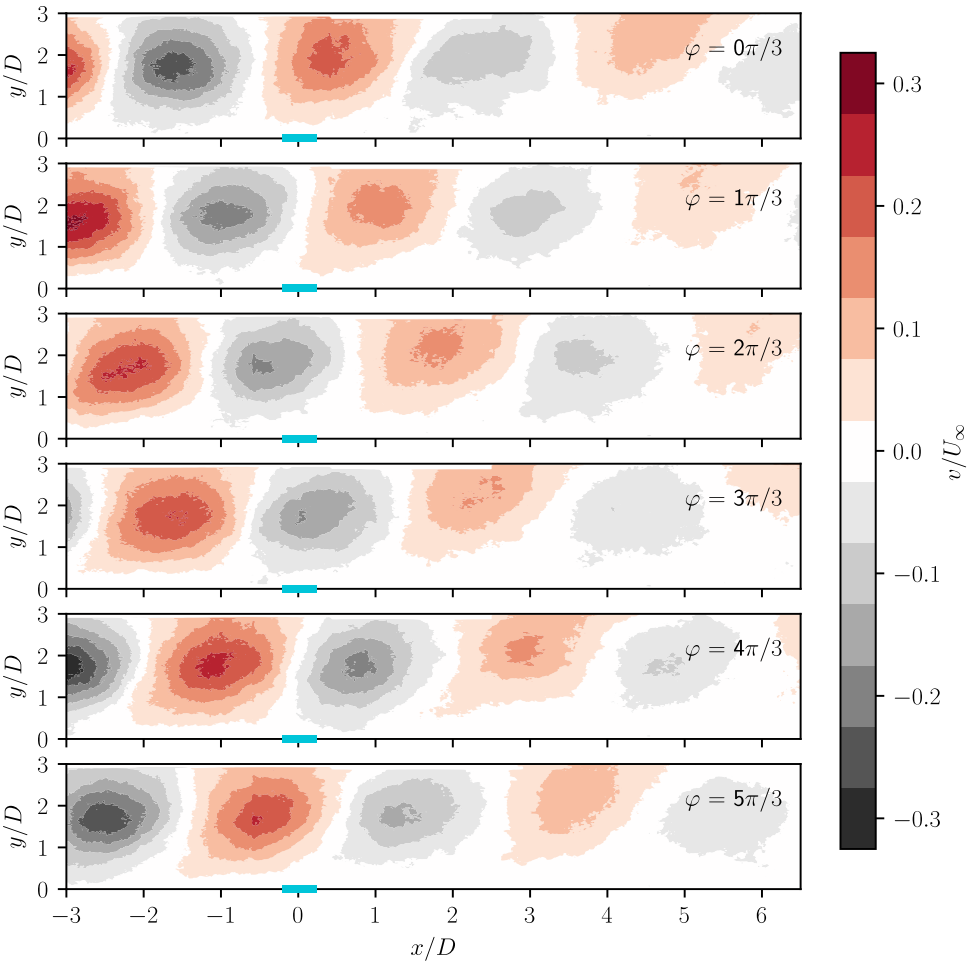

Figure 7.11.: Phase-averaged wall-normal velocity fields for the uncontrolled flow modulated by periodic vortex shedding, conditioned on the positive-gradient zero-crossings of the control signal before binarization for actuation. The phase-average consists of 6 evenly-spaced bins: from $\varphi = 0$ to $\varphi = 5\pi/3$. The streamwise location of the jet actuators is indicated with the aid of a blue rectangle.

sition (*i.e.* the central valve) could explain a mild outflow of fluid from the jet exit slit.

2. **The relatively high frequency of actuation.** As mentioned in § 5.3, the frequency response of the actuator and the pneumatic feed system is such that, when approaching a frequency of ≈ 100 Hz, the flow measured at the jet exit slit does not fully shut down. In fact, a frequency-response analysis of the jet outflow revealed

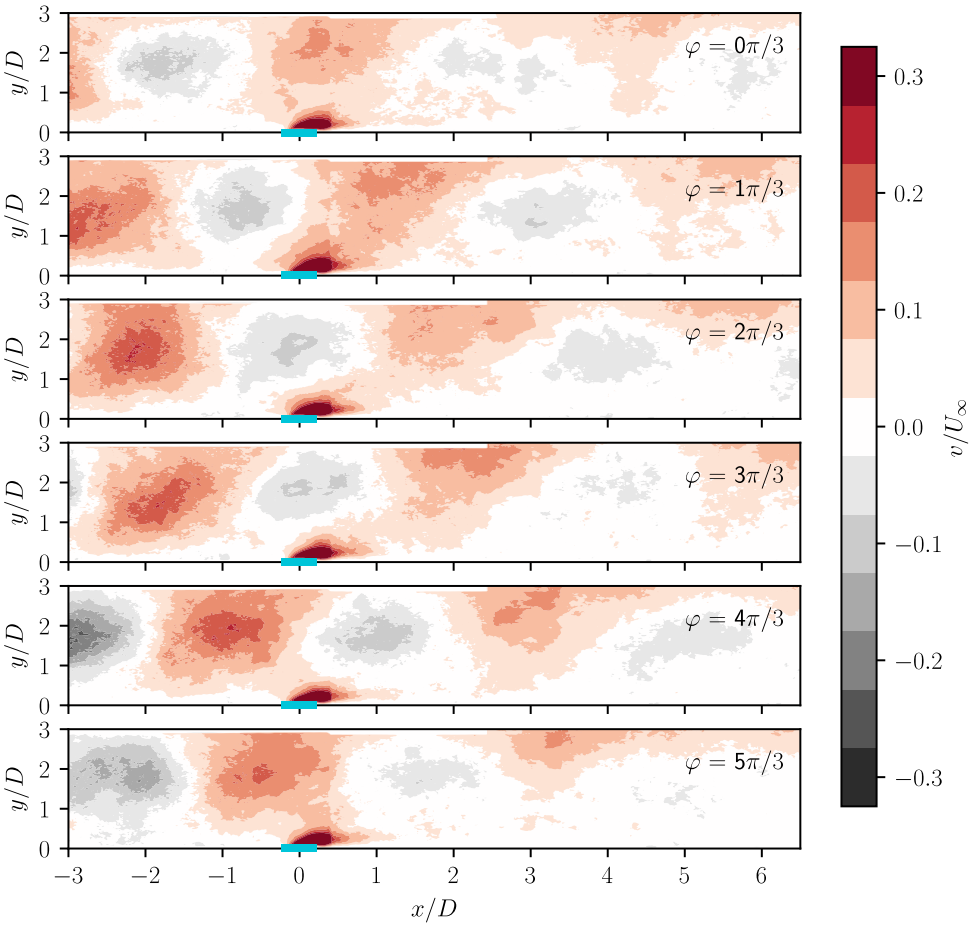

Figure 7.12.: Phase-averaged wall-normal velocity fields for the flow modulated by periodic vortex shedding and controlled by means of the Fx-LMS algorithm, conditioned on the positive-gradient zero-crossings of the control signal before binarization for actuation. The phase-average consists of 6 evenly-spaced bins: from $\varphi = 0$ to $\varphi = 5\pi/3$. The streamwise location of the jet actuators is indicated with the aid of a blue rectangle.

characteristic start-up and shut-down times, as given in § 5.3. Given that the spectrum of the control signal, although broadband, peaks at $f \approx 88$ Hz, it is plausible that the limit frequency of the actuator is reached.

Albeit the uncertainty in the full functionality and reliability of the actuator, our results confirm the effective deployment of the Fx-LMS to the cylinder-induced vortex shedding control, as a clear reduction in shedding intensity was measured. Now the questions arises as to the Fx-LMS controller will perform in a flow characterized by a more broad-

band spectral signature, such as an equilibrium TBL flow.

7.5. APPLICATION TO FULLY BROADBAND TBL

One of the principal goals of this dissertation is to develop real-time flow control techniques for a TBL flow. The analysis of a control problem involving the attenuation of harmonic wake vortex shedding downstream of a spanwise-aligned cylinder was just a preliminary experiment to verify the working principle of the Fx-LMS algorithm. Having successfully tested the controller in harmonic conditions, one can now analyze its performance when applied to the fully broadband TBL flow scenario (*i.e.* with no cylinder).

7.5.1. EXPERIMENTAL IMPLEMENTATION

The experimental setup employed for the real-time control of the TBL flow using an adaptive control law is the same as described in § 7.4.1. Clearly, the cylinder was removed such that the dynamic plant in consideration for control was the "clean" TBL flow without the superposition of a harmonic forcing. The major difference with respect to the experimental setup for the control of wake vortices was in the input and error sensors. Instead of wall-pressure sensing, an architecture now based on wall-shear and velocity fluctuations is adopted. This was for two principal reasons.

- **Loss of coherence.** As highlighted in Ch. 4, the decay of coherence between wall-pressure and streamwise velocity fluctuations is rather sharp as a function of streamwise separation of the two sensors. The streamwise separation is acceptable up to a distance of roughly 2δ, when factoring in the quadratic term of wall-pressure, and this was the main factor underlying the success of the opposition control strategy based on wall-pressure input of Ch. 6. However, the separation between streamwise input and downstream error sensors is, in the context of this part of the dissertation, of 4.4δ. The considerably larger separation between the two sensors leads to extremely low coherence between the corresponding signals and, thus, an ineffective control system.

- **Stronger signal-to-noise ratio.** Given the broadband nature of the TBL dynamics not modulated by wake vortex shedding, a quantity that is relatively immune to contamination by external noise sources will certainly aid the controller in identifying the principal statistical events that need to be attenuated.

The input and error sensors that were employed in this phase of the dissertation, therefore, consist of three flush-mounted hot-films as the input sensors. These are Dantec 55R47 glue-on hot-film probes. Being these the same sensors that were used in Ch. 5, the interested reader can refer to that part of the work for further specifications and technicalities regarding the characteristics and integration of these in the experimental facility. The location of the three input sensors is designated with the symbol $\mathscr{HF}$ in Fig. 7.6a. The error sensor, instead, consisted of a single hot-wire probe located at the streamwise position of the error microphones, used in the vortex shedding experiment, but at $y^+ = 190$ (in the logarithmic region, see Fig. 7.6a). Three jet actuator only were employed

in this control loop: the ones located directly downstream of the three hot-film probes used as input sensors.

The controller was run in single-input single-output mode. Thus, the identification of both FIR kernels needed for the Fx-LMS algorithm was run by only considering the central hot-film's and the hot-wire's signal. The identified kernels, once converged, were then deployed to the three spanwise stations: *i.e.* the three hot-film–actuator pairs. This is justified following spanwise homogeneity of the flow in the spanwise direction.

7.5.2. SYSTEM IDENTIFICATION

Identification of the FIR kernels underlying the deployment of the Fx-LMS algorithm for the broadband case follows the same procedure outline in the above for both the acoustic wave control and the control of vortex shedding in the wake of a cylinder. Both kernels are plotted in Fig. 7.13a. Note that the length of the temporal horizons of both kernels are different. The longer streamwise separation between the hot-film probe and error sensor, compared to the separation between the input sensor and the jet actuator, requires a longer temporal horizon for the identification of the cancellation path kernel. Although the same physical separation between sensors was employed for the experiments aimed at the attenuation of cylinder wake vortices, that was a periodic system. Vortex shedding was strongly concentrated around a tonal peak, which inherently results in both the control and cancellation path kernels being characterized by the same wavelength. However, being the TBL a dynamic system characterized by broadband fluctuations, no such tonal properties exist. Thus, one needs to account for the high energy contained in the low-frequency components (contained over the longer streamwise extent), to allow for proper system identification.

To understand the structures identified by the controller as the most energetic one, a spectrum is plotted of both kernels, together with the spectrum of the hot-film input signal (see Fig. 7.13b). For ease of comparison, the magnitude of the FIR kernels is normalized in such a way that the maximum amplitude is equal to the maximum amplitude of the spectrum of the input signal. By inspection of said figure, one can immediately see how the dominant feature being targeted by the Fx-LMS controller corresponds to $f\delta/U_\infty \approx 0.7$, which lies in the spectral range displaying the most energy in the input signal, hinting at a correct identification of the most energetic frequency components in the dynamic plant.

7.5.3. TBL RESPONSE TO ADAPTIVE CONTROL

The results of the Fx-LMS control applied to TBL fluctuations in terms of the spectrum of streamwise velocity fluctuations (see Fig. 7.14) provide important insights into the system's behavior under different control strategies. In the opposing case, where the control system generates an anti-phase signal to counteract the turbulence, a clear and statistically-significant reduction in the fluctuation levels is observed at large wavelengths. This reduction is in line with the theoretical expectation that an anti-phase signal would suppress disturbances in the turbulent flow by introducing "destructive" control inputs. The spectral analysis of the opposing case shows a significant decrease in the energy at the frequencies corresponding to the turbulence, reinforcing the idea that Fx-LMS con-

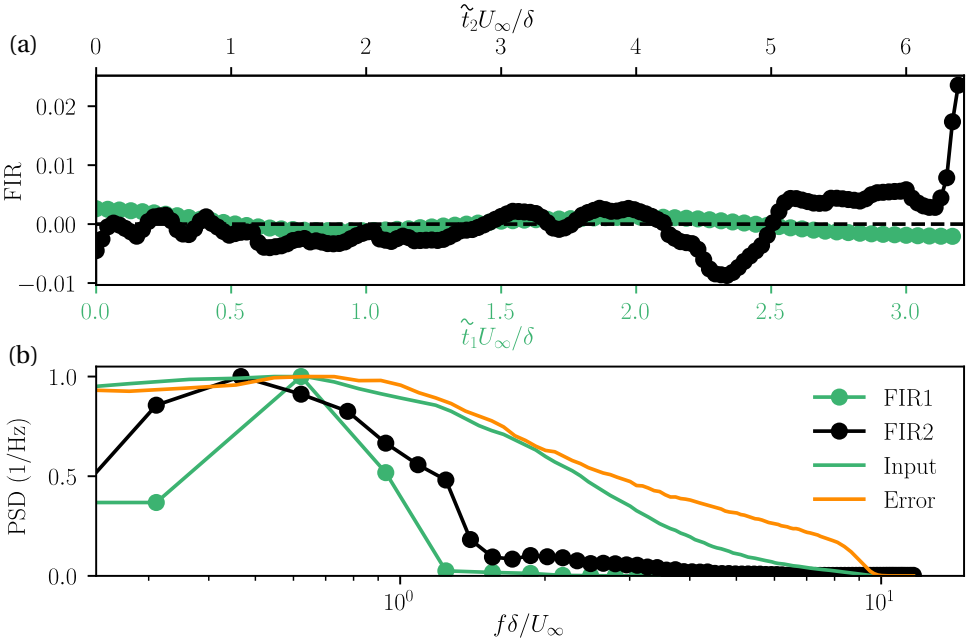

Figure 7.13.: (a) Plot of the control and cancellation path kernels identified for the control of the fully broadband TBL flow. The length of the temporal horizons of either kernels are different. Note the different time axis for each of the curves. (b) Spectra of the hot-film input and error hot-wire signals, as well as the normalized magnitude of the cancellation path and control kernels.

trol is effective in actively attenuating targeted disturbances when the control signal is appropriately aligned with the turbulence.

Overall, the spectral response of the flow to control aligns with the expected theoretical outcome: the opposing control reduces spectral energy. These findings underscore the effectiveness of Fx-LMS control in targeted suppression of turbulence, as well as its limitations in dealing with broadband disturbances. While the system demonstrates clear potential for active control in turbulent flows, further refinement and potentially alternative adaptive techniques may be necessary to handle the more unpredictable, chaotic nature of turbulence. However, this work demonstrates the effectiveness of this control algorithm, without resorting to complex high-dimensional non-linear control laws.

7.6. CONCLUSIONS

This chapter proves the potential of the adaptive Fx-LMS algorithm to be suitable for its application in real-time turbulence control. Not only it displays significant performance for a flow case subjected to strong harmonic forcing, but it also demonstrates its applicability to a broadband flow case. In essence, from a physical perspective, the Fx-LMS algorithm is able to accurately retain the information that remains correlated over

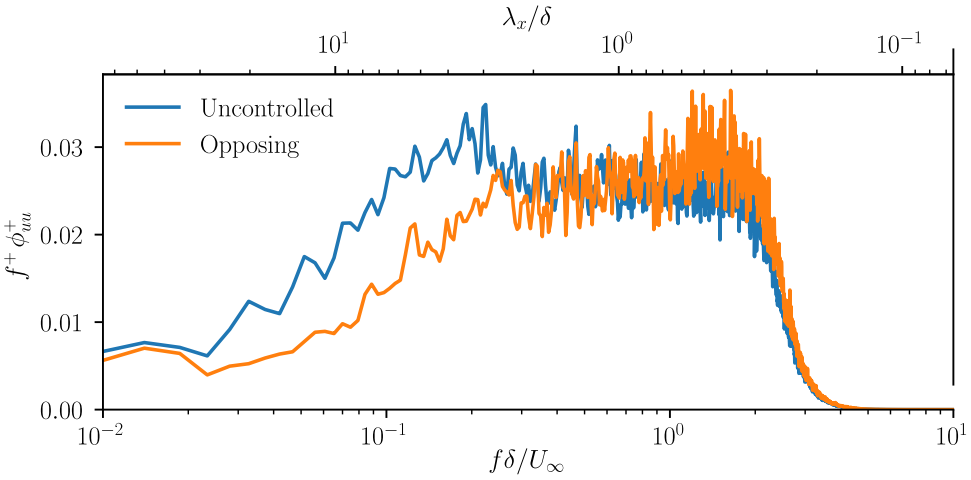

Figure 7.14.: Pre-multiplied spectra of the streamwise velocity fluctuations, measured with the aid of a hot-wire probe located at $(x, y, z) = (2\delta, y_L, 0)$. Comparing the uncontrolled case (blue) to the case where opposing control was performed using the Fx-LMS algorithm.

the large streamwise extent separating input and error sensors. In a turbulent boundary layer case, this only coincides with structures having typical length scales of several boundary layer thicknesses: the LSMs.

V

Conclusion and epilogue

8

CONCLUSIONS AND OUTLOOK

Do good work.

Gus Grissom (Apollo 1)

This chapter summarizes the main findings and conclusions based on the research work that has been presented in previous chapters. Furthermore, it reflects on the societal relevance of the work contained in this booklet and provides recommendations for future developments.

8.1. CONCLUSIONS

The work contained in this dissertation examines the development and deployment of real-time control strategies for skin-friction drag reduction in a turbulent boundary layer flow by means of manipulation of large-scale velocity fluctuations. A pioneering use of wall-pressure as the input quantity for real-time control has also been explored an implemented experimentally, with successful attenuation of targeted velocity fluctuations.

WALL-PRESSURE SENSING, FILTERING AND SCALING

A preliminary part of the work (Ch. 3) has demonstrated the effectiveness of applying reduced-order models, such as classical proper orthogonal decomposition (POD), harmonic POD (hPOD), and conditional spectral analysis (CSA), to extract meaningful physical insights from wall-pressure measurements taken in a high-Reynolds-number turbulent pipe flow facility: the Centre for International Cooperation on Long-Pipe Experiments (CICLoPE). Specifically, the challenge has been addressed of filtering unwanted noise originating from facility-related sources and preserving the key hydrodynamic wall-pressure information. The filtered energy spectra confirmed the alignment of the small-scale energy peak at $\lambda_x^+ \approx 250$, which is consistent with the expected near-wall flow dynamics. Moreover, a progressive increase in large-scale energy content with increasing Re_τ was observed, as predicted by the literature.

In general, Ch. 3 proves the potential of these reduced-order models not only in denoising complex turbulent datasets but also in reliably retrieving hydrodynamic pressure information. This is critical for further applications in flow control and drag reduction strategies, where robust wall-pressure measurements are crucial. These methods provide a solid foundation for further developments in turbulence studies, ensuring that essential flow features are captured even in the presence of facility noise.

Once filtering techniques have been established to reliably retain hydrodynamic wall-pressure fluctuations, statistical correlations of hydrodynamic wall-pressure and velocity fluctuations in the logarithmic region of a turbulent pipe flow were experimentally investigated (Ch. 4). With a unique dataset acquired in the CICLoPE long-pipe facility, spanning a large range of friction Reynolds numbers ($4\,794 \lesssim Re_\tau \lesssim 47\,015$), this study reveals definitive Reynolds number trends of the scale-dependent wall-pressure–velocity coherence. For the linear coherence between the u velocity (and v velocity) and wall-pressure, a Reynolds-number-independent scaling of the coherence spectra appears at the intermediate scale range when scaled with distance-from-the-wall. This trend is also statistically similar across several wall-bounded flows when compared to the data available from the open literature. When the squared wall-pressure fluctuations are considered instead of the linear wall-pressure, the coherence spectra for the wall-pressure and velocity fluctuations are higher in amplitude at the (very) large-scale end of the spectra. Physically, this link between wall-pressure–squared and velocity typifies a modulation effect. Squaring the wall-pressure introduces low-frequency content that is reflective of how the higher-frequency wall-pressure intensity varies. Current findings of the coherence spectra bear relevance to stochastic estimation schemes, in which wall-pressure can be considered as an input to estimate off-the-wall velocity fluctuations. With the aid of a quadratic stochastic estimation method, it was shown that, for each Re_τ investigated, the estimated time series and a true temporal measurement of velocity inside the

turbulent pipe flow yielded a normalized correlation coefficient of up to $\rho \approx 0.6$ (while this was below 0.4 for a linear stochastic estimation method excluding the wall-pressure–squared term). This demonstrates that (sparse) wall-pressure sensing can be employed for meaningful estimation of off-the-wall velocity fluctuations. Also, it is shown that wall-pressure as an input for estimation schemes is scalable to application-level conditions.

FEEDFORWARD REAL-TIME CONTROL OF TBL FLOW

In Ch. 5, successful experimental real-time targeting of large-scale motions has been accomplished by means of a control system comprising a surface-mounted hot-film as the input sensor and a wall-embedded blowing jet actuator, located downstream of the sensing element. An opposition control logic was implemented for which the controller activated the actuator at regions of streamwise momentum surplus. The inverse control law, reinforcing control, was also implemented, where the jet fired into regions of momentum deficit with the goal of enhancing turbulence instead of suppressing it.

The principal objective of this part of the dissertation was to analyze skin-friction drag-generating mechanisms by considering statistical integral measures. The bulk turbulence kinetic energy production term decreases up to a wall-normal location where the actuator-induced fluctuations are strong. The sharp increase in the Reynolds shear stresses R_{xy} induces a bias in this integral measure as well as the second component of skin-friction following FIK-decomposition: $C_{f,2}$. The applicability of the FIK decomposition relies on the assumption of zero-pressure-gradient turbulence, which might be violated in proximity to sites where flow control is performed by means of fluidic actuators. However, when focusing on the region downstream of the actuator ($x/\delta > 1$), the Reynolds shear-stresses show streamwise-invariant behavior in the logarithmic region, where the LSMs were targeted. When evaluating $C_{f,2}$ in this region, an identical trend in the change of the skin-friction was found as compared to the direct PTV-based measurements. This opens up an avenue for using off-the-wall flow field information downstream of control for the purpose of optimizing a drag-reducing control scheme. Still, the observation that statistical integrands directly reflect changes in PTV-inferred skin-friction coefficient supports the conclusion that the controller presented in Ch. 5 is able to alter skin-friction generating mechanisms not only in the logarithmic region, but also in the near-wall region, where small viscous scales are energetically dominant.

A feedforward real-time control logic had already proven effective in the literature in the work of Abbassi et al. [2017], and in this work further working mechanisms of this strategies have been elucidated and clarified. With the experimental real-time control configuration presented in Ch. 5 and the treatment and scaling of wall-pressure measurements illustrated in Chs. 3 and 4, the groundwork is laid for tackling a change in the input quantity of the controller: from wall-shear stress to wall-pressure fluctuations.

Evidence of the efficacy of a control strategy utilizing wall-pressure fluctuations as the input quanity can be found in an attenuation of the variance of large-scale velocity fluctuations in the logarithmic region (Ch. 6). Despite an increase in small-scale energy, which is attributed to shear layer instability in the wake of the jet actuator, this control method proves to be effective in a spectral band where the most coherence can be found not between wall-pressure, but rather wall-pressure–squared, and velocity fluc-

tuations. Consistently with results from the literature, in fact, the squared term retains more coherence than the linear term when considering streamwise separation between upstream and downstream stations. For the first time, the efficacy of an opposition control strategy targeting large-scale structures based on sparse wall-pressure measurements is proven. This was shown to be effective even in the presence of strong contamination by facility noise in the input signal. Future work in our group is currently being conducted on the implementation of more advanced control algorithms, such as adaptive control strategies, in an attempt to further increase the accuracy of the controller and mitigate the adverse effects of the actuator-induced flow on the spectral response of the TBL.

ADAPTIVE CONTROL OF WALL-BOUNDED TURBULENCE

The final chapter of this dissertation (Ch. 7) reports on the development and implementation of an adaptive control strategy for the control of large-scale velocity fluctuations in a turbulent wall-bounded flow. Based on Fx-LMS control algorithm, an initial investigation was carried out to analyze the response of a TBL flow, strongly modulated by vortex shedding. This was induced by a two-dimensional spanwise-aligned cylinder, whose shedding frequency closely matched the one of the most energetic large-scale modes of an uncontrolled TBL. In this preliminary phase of deployment of the Fx-LMS, an attenuation of the intensity related to the cylinder vortex shedding was observed, in compliance with the objective of the study. In a secondary phase of this chapter, the Fx-LMS algorithm was deployed to the fully broadband TBL case, without modulation by a two-dimensional cylinder. Although with limited flow diagnostics available, it was possible to confirm a successful deployment of the control law for the control and attenuation of large-scale–induced velocity fluctuation in the logarithmic region.

8.2. RECOMMENDATIONS AND OUTLOOK

This booklet has touched upon several aspects of the development and experimental implementation of real-time flow control strategies for the control of velocity fluctuations in turbulent wall-bounded flows. However, this dissertation does not tackle many more issue that afflict full-scale deployment of real-time flow control technology for turbulence, nor it claims that real-time control systems, such as the ones described in previous chapters, can be directly integrated in engineering systems. With the technology readiness of a “lab-proven" technique, the maturity of turbulence real-time control is not high-enough for industrialization. Still, this work serves as proof of concept and for unraveling large-scale flow mechanisms that contribute to the production of friction drag and develop low-complexity real-time control systems for its control.

Regarding the work conducted as part of this dissertation, the main line of work that certainly requires more thorough investigation is the analysis of the response of the TBL flow to the adaptive Fx-LMS control law. While at the moment only limited hot-wire diagnostics have been presented, a more complete PIV campaign would be required to fully characterize the two- (and three-)dimensional flow field. From the algorithmic point of view, the author strongly suggests moving from a single-channel feedfoward

single-input single-output Fx-LMS algorithm to a formulation whereby a multiple-input multiple-output configuration is considered.

This step would ensure an improvement in the reliability and the precision of the controller, and aid in the development of an adaptive control strategy that is in-line with the requirements of an industrially-viable control system. Furthermore, with industrialization and up-scaling in mind, one needs to thoroughly tackle the issue of net power savings of the control system. Skin-friction force reduction occurs on order of magnitude that are way lower than the current state-of-the-art actuators power requirements, especially when considering the power required to drive real-time processing hardware and input sensors.

Addressing the above challenges would represent a step forward in the direction of understanding the requirements, design issues and constraints of a real-time control system for skin-friction drag reduction and, eventually, deployment to engineering systems of practical relevance.

BIBLIOGRAPHY

M. R. Abbassi, W. J. Baars, N. Hutchins, and I. Marusic. Skin-friction drag reduction in a high-Reynolds-number turbulent boundary layer via real-time control of large-scale structures. *Intl. J. Heat Fluid Flow*, 67:30–41, 2017.

N. Aubry, P. Holmes, J. L. Lumley, and E. Stone. The dynamics of coherent structures in the wall region of a turbulent boundary layer. *J. Fluid Mech.*, 192:115–173, 1988.

W. J. Baars and I. Marusic. Data-driven decomposition of the streamwise turbulence kinetic energy in boundary layers. Part 1. Energy spectra. *J. Fluid Mech.*, 882, 2019.

W. J. Baars and C. E. Tinney. Proper orthogonal decomposition-based spectral higher-order stochastic estimation. *Phys. Fluids*, 26(5), 2014.

W. J. Baars, N. Hutchins, and I. Marusic. Spectral stochastic estimation of high-Reynolds-number wall-bounded turbulence for a refined inner-outer interaction model. *Phys. Rev. Fluids*, 1(5):054406, 2016. ISSN 2469-990X.

W. J. Baars, N. Hutchins, and I. Marusic. Self-similarity of wall-attached turbulence in boundary layers. *J. Fluid Mech.*, 823:R2, 2017.

W. J. Baars, G. Dacome, and M. Lee. Reynolds-number scaling of wall-pressure–velocity correlations in wall-bounded turbulence. *J. Fluid Mech.*, 981:A15, 2024.

H. L Bai, Y. Zhou, W. G Zhang, S. J Xu, Y. Wang, and R. A Antonia. Active control of a turbulent boundary layer based on local surface perturbation. *Journal Fluid Mech.*, 750:316–354, 2014.

R. Baidya, W. J. Baars, S. Zimmerman, M. Samie, R. J. Hearst, E. Dogan, L. Mascotelli, X. Zheng, G. Bellani, A. Talamelli, B. Ganapathisubramani, N. Hutchins, I. Marusic, J. Klewicki, and J. P. Monty. Simultaneous skin friction and velocity measurements in high Reynolds number pipe and boundary layer flows. *J. Fluid Mech.*, 871:377–400, 2019.

G. Bellani and A. Talamelli. The final design of the long pipe in CICLoPE. *Prog. in Turb. VI*, pages 205–209, 2016.

J. S. Bendat and A. G. Piersol. *Random Data: Analysis and Measurement Procedures*. John Wiley & Sons, Inc., USA, 3rd edition, 2000. ISBN 0471317330.

W. K. Blake. Turbulent boundary-layer wall-pressure fluctuations on smooth and rough walls. *J. Fluid Mech.*, 44(04), 1970.

W. K. Bonness and D. M. Jenkins Jr. Coherent noise removal from dynamic wall pressure and vibration signals. In *41st International Congress and Exposition on Noise Control Engineering 2012, INTER-NOISE 2012*, pages 118–127, 2012.

K. Breuer and K. Wu. Models for adaptive feedforward control of turbulence. In *IUTAM Symposium on Flow Control and MEMS*, 2006.

S. L. Brunton and B. R. Noack. Closed-loop turbulence control: Progress and challenges. *App. Mech. Rev.*, 67(5), 2015.

M. K. Bull and A. S. W. Thomas. High frequency wall-pressure fluctuations in turbulent boundary layers. *Phys. Fluids*, 19(4):597–599, 1976.

K. J. Bullock, R. E. Cooper, and F. H. Abernathy. Structural similarity in radial correlations and spectra of longitudinal velocity fluctuations in pipe flow. *J. Fluid Mech.*, 88:585–608, 1978.

P. Burattini and R. A. Antonia. The effect of different X-wire calibration schemes on some turbulence statistics. *Exp. in Fluids*, 38(1):80–89, 2004.

J. Canton, R. Örlü, C. Chin, N. Hutchins, J. Monty, and P. Schlatter. On large-scale friction control in turbulent wall flow in low Reynolds number channels. *Flow Turb. Comb.*, 97 (3):811–827, 2016a.

J. Canton, R. Örlü, C. Chin, and P. Schlatter. Reynolds number dependence of large-scale friction control in turbulent channel flow. *Phys. Rev. Fluids*, 1(8):9, 2016b.

L. N. Cattafesta and M. Sheplak. Actuators for active flow control. *Ann. Rev. Fluid Mech.*, 43(1):247–272, 2011.

R.C. Chanaud. Effects of geometry on the resonance frequency of helmoltz resonators. *J. Sound Vibr.*, 178:337–348, 1994.

K. A. Chauhan, P. A. Monkewitz, and H. M. Nagib. Criteria for assessing experiments in zero pressure gradient boundary layers. *Fluid Dyn. Res.*, 41(2), 2009.

X. Q. Cheng, Z. X. Qiao, X. Zhang, M. Quadrio, and Y. Zhou. Skin-friction reduction using periodic blowing through streamwise slits. *J. Fluid Mech.*, 920, 2021a.

X. Q. Cheng, C. W. Wong, F. Hussain, W. Schröder, and Y. Zhou. Flat plate drag reduction using plasma-generated streamwise vortices. *J. Fluid Mech.*, 918, 2021b.

H. Choi and P. Moin. On the space-time characteristics of wall-pressure fluctuations. *Phys. Fluids*, 2(8):1450–1460, 1990.

H. Choi, P. Moin, and J. Kim. Active turbulence control for drag reduction in wall-bounded flows. *J. Fluid Mech.*, 262:75–110, 1994.

G. Dacome, R. Siebols, and W. J. Baars. Small-scale Helmholtz resonators with grazing turbulent boundary layer flow. *J. Turbul.*, 25(12):461–481, 2024.

S. Deck, N. Renard, R. Laraufie, and P.E. Weiss. Large-scale contribution to mean wall shear stress in high-Reynolds-number flat-plate boundary layers up to $Re_\theta = 13650$. *J. Fluid Mech.*, 743:202–248, 2014.

J. C. del Álamo and J. Jiménez. Spectra of the very large anisotropic scales in turbulent channels. *Phys. Fluids*, 15(6):L41–L44, 2003.

J. C. del Álamo and J. Jiménez. Estimation of turbulent convection velocities and corrections to Taylor's approximation. *J. Fluid Mech.*, 640:5–26, 2009.

D. J. C. Dennis and T. B. Nickels. On the limitations of Taylor's hypothesis in constructing long structures in a turbulent boundary layer. *J. Fluid Mech.*, 614:197–206, 2008.

R. Deshpande, D. Chandran, A. J. Smits, and I. Marusic. The relationship between manipulated inter-scale phase and energy-efficient turbulent drag reduction. *J. Fluid Mech.*, 972:A12, 2022.

R. Deshpande, R. Vinuesa, J. Klewicki, and I. Marusic. Active and inactive contributions to the wall pressure and wall-shear stress in turbulent boundary layers. *arXiv:2406.15733,*, 2024. Accepted in *J. Fluid Mech.* (in press).

M. E. Erengil and D. S. Dolling. Unsteady wave structure near separation in a Mach 5 compression ramp interaction. *AIAA J.*, 29(5):728–735, 1991.

R. E. Falco. Coherent motions in the outer region of turbulent boundary layers. *Phys. Fluids*, 20(10), 1977.

T. M. Farabee and M. J. Casarella. Spectral features of wall pressure fluctuations beneath turbulent boundary layers. *Phys. Fluids A*, 3(10):2410–2420, 1991.

M. Farazmand and T. P. Sapsis. Closed-loop adaptive control of extreme events in a turbulent flow. *Phys. Rev. E*, 100(3-1):033110, 2019.

T. Fiorini. Turbulent pipe flow - high resolution measurements in CICLoPE. *Ph.D. thesis. Scuola di Ingegneria e Architettura University of Bologna, Forli, Italy*, 2017.

K. Fukagata, K. Iwamoto, and N. Kasagi. Contribution of Reynolds stress distribution to the skin friction in wall-bounded flows. *Phys. Fluids*, 14(11):L73–L76, 2002.

D. Gatti and M/ Quadrio. Reynolds-number dependence of turbulent skin-friction drag reduction induced by spanwise forcing. *J. Fluid Mech.*, 802:553–582, 2016.

D. Gatti, M. Quadrio, A. Chiarini, F. Gattere, and S. Pirozzoli. Turbulent skin-friction drag reduction via spanwise forcing at high reynolds number. *arXiv*, 2409.07230, 2024.

B. Gibeau and S. Ghaemi. Low- and mid-frequency wall-pressure sources in a turbulent boundary layer. *J. Fluid Mech.*, 918:A18, 2021.

I. Gluzman, P. Gray, K. Mejia, T. C. Corke, and F. O. Thomas. A simplified photogrammetry procedure in oil-film interferometry for accurate skin-friction measurement over arbitrary geometries. *Exp. in Fluids*, 63(7):118, 2022.

S. P. Gravante, A. M. Naguib, C. E. Wark, and H. M. Nagib. Characterization of the pressure fluctuations under a fully developed turbulent boundary layer. *AIAA J.*, 36(10):1808–1816, 1998a.

S. P. Gravante, A. M. Naguib, C. E. Wark, and H. M. Nagib. Characterization of the pressure fluctuations under a fully developed turbulent boundary layer. *AIAA J.*, 36(10):1808–1816, 1998b.

Anna Guseva and Javier Jiménez. Linear instability and resonance effects in large-scale opposition flow control. *J. Fluid Mech.*, 935:A35, 2022.

E. J. Gutmark, I. M. Ibrahim, and S. Murugappan. Circular and noncircular subsonic jets in cross flow. *Phys. Fluids*, 20(7):075110, 2008.

J. M. Hamilton, J. Kim, and F. Waleffe. Regeneration mechanisms of near-wall turbulence structures. *J. Fluid Mech.*, 287:317–348, 1995.

C. H. Hansen. *Understanding active noise cancellation.* Taylor & Francis, London, UK, 1st edition, 2001. ISBN 0415231922.

P. T. Harsha and S. C. Lee. Correlation between turbulent shear stress and turbulent kinetic energy. *AIAA J.*, 8(8):1508–1510, 1970.

M. P. Horne. *Physical and computational investigation of the wall pressure fluctuations in a channel flow.* Ph.D. thesis, The Catholic University of America, 1989.

M. Hultmark and A. J. Smits. Temperature corrections for constant temperature and constant current hot-wire anemometers. *Meas. Sci. Tech.*, 21(10), 2010.

N. Hutchins and I. Marusic. Evidence of very long meandering features in the logarithmic region of turbulent boundary layers. *J. Fluid Mech.*, 579:1–28, 2007.

N. Hutchins, T. B. Nickels, I. Marusic, and M. S. Chong. Hot-wire spatial resolution issues in wall-bounded turbulence. *J. Fluid Mech.*, 635:103–136, 2009.

N. Hutchins, J. P. Monty, B. Ganapathisubramani, H. C. H. Ng, and I. Marusic. Three-dimensional conditional structure of a high-Reynolds-number turbulent boundary layer. *J. Fluid Mech.*, 673:255–285, 2011.

N. Hutchins, K. Chauhan, I. Marusic, J. Monty, and J. Klewicki. Towards reconciling the large-scale structure of turbulent boundary layers in the atmosphere and laboratory. *Boundary-Layer Met.*, 145(2):273–306, 2012.

D. Hwang. Review of research into the concept of the microblowing technique for turbulent skin friction reduction. *Prog. Aerosp Sci.*, 40(8):559–575, 2004.

IATA. Global outlook for air transport: Deep change. Report, International Air Transport Authority, 2024.

J. Jiménez. How linear is wall-bounded turbulence? *Phys. Fluids*, 25(11):110814, 2013.

J. Jiménez and S. Hoyas. Turbulent fluctuations above the buffer layer of wall-bounded flows. *J. Fluid Mech.*, 611:215–236, 2008.

J. Jimenez and A. Pinelli. The autonomous cycle of near-wall turbulence. *J. Fluid Mech,*, 389:335–359, 1999.

J. Jimenez, R. Martinez-Val, and M. Rebollot. Hot-film sensors calibration drift in water. *J. Phys. E: Sci. Inst.*, 14:569–572, 1981.

Javier Jiménez. Coherent structures in wall-bounded turbulence. *J. Fluid Mech.*, 842, 2018.

R. E. Kalman. Mathematical description of linear dynamical systems. *Journal of the Society for Industrial and Applied Mathematics Series A Control*, 1(2):152–192, 1963.

N. Kasagi and K. Fukagata. *The FIK identity and its implication for turbulent skin friction control*, volume 8 of *Lecture Notes Series Institute for Mathematical Sciences National University of Singapore*. World Scientific Publ Co Pte Ltd, Singapore, 2006. ISBN 981-256-594-9.

N. Kasagi, Y. Suzuki, and K. Fukagata. Microelectromechanical systems–based feedback control of turbulence for skin friction reduction. *Ann. Rev. Fluid Mech.*, 41(1):231–251, 2009.

K. U. Kempaiah, F. Scarano, G. E. Elsinga, B. W. van Oudheusden, and L. Bermel. 3-dimensional particle image velocimetry based evaluation of turbulent skin-friction reduction by spanwise wall oscillation. *Phys. Fluids*, 32(8), 2020.

K. C. Kim and R. J. Adrian. Very large-scale motion in the outer layer. *Phys. Fluids*, 11(2): 417–422, 1999.

J. C. Klewicki, P. J. A. Priyadarshana, and M. M. Metzger. Statistical structure of the fluctuating wall pressure and its in-plane gradients at high Reynolds number. *J. Fluid Mech.*, 609:195–220, 2008.

S. J. Kline, W. C. Reynolds, F. A. Schraub, and P. W. Runstadler. The structure of turbulent boundary layers. *J. Fluid Mech.*, 30(4):741–773, 1967.

V.I. Kornilov. Current state and prospects of researches on the control of turbulent boundary layer by air blowing. *Prog. Aero. Sci.*, 76:1–23, 2015.

V.I. Kornilov and A.V. Boiko. Efficiency of air microblowing through microperforated wall for flat plate drag reduction. *AIAA J.*, 50:724–732, 2012.

V.I. Kornilov and A.V. Boiko. Flat-plate drag reduction with streamwise noncontinuous microblowing. *AIAA J.*, 52:93–103, 2014.

M. Kotsonis, R. Giepman, S. Hulshoff, and L. Veldhuis. Numerical study of the control of Tollmien–Schlichting waves using plasma actuators. *AIAA J.*, 51(10):2353–2364, 2013.

G. C. Lauchle and M. A. Daniels. Wall-pressure fluctuations in turbulent pipe flow. *Phys. Fluids*, 30(10):3019–3024, 1987.

J. H. Lee and Hyung J. Sung. Very-large-scale motions in a turbulent boundary layer. *J. Fluid Mech.*, 673:80–120, 2011.

M. Lee and R. D. Moser. Direct numerical simulation of turbulent channel flow up to $Re_\tau = 5200$. *J. Fluid Mech.*, 774:395–415, 2015.

S. J. Leib, M. N. Glauser, and W. K. George. Application of Lumley's orthogonal decomposition to the axisymmetric turbulent jet mixing layer. *Adv. in Turb.*, 1984.

C. G. Lomas. *Fundamentals of Hot Wire Anemometry*. Cambridge University Press, UK, 1st edition, 1985. ISBN 9780521283182.

M. Luhar, A. S. Sharma, and B. J. McKeon. On the structure and origin of pressure fluctuations in wall turbulence: predictions based on the resolvent analysis. *J.Fluid Mech.*, 751:38–70, 2014.

J. L. Lumley. The structure of inhomogeneous turbulent flows. *Atm. Turb. Radio Wave Prop.*, pages 166–178, 1967.

K. Mahesh. The interaction of jets with crossflow. *Ann. Rev. Fluid Mech.*, 45(1):379–407, 2013.

E. Martini, J. Jung, A. V. G. Cavalieri, P. Jordan, and A. Towne. Resolvent-based tools for optimal estimation and control via the Wiener–Hopf formalism. *J. Fluid Mech.*, 937: A19, 2022.

I. Marusic and Jason P. Monty. Attached eddy model of wall turbulence. *Ann. Rev. Fl. Mech.*, 51(1):49–74, 2019.

I. Marusic, R. Mathis, and N. Hutchins. Predictive model for wall-bounded turbulent flow. *Science Mag.*, 329:193–196, 2010.

I. Marusic, K. Chauhan, V. Kulandaivelu, and N. Hutchins. Evolution of zero-pressure-gradient boundary layers from different tripping conditions. *J. Fluid Mech.*, 783:379–411, 2015.

I. Marusic, D. Chandran, A. Rouhi, M. K. Fu, D. Wine, B. Holloway, D. Chung, and A. J. Smits. An energy-efficient pathway to turbulent drag reduction. *Nat. Commun.*, 12(1): 5805, 2021.

R. Mathis, N. Hutchins, and I. Marusic. Large-scale amplitude modulation of the small-scale structures in turbulent boundary layers. *J. Fluid Mech.*, 628:311–337, 2009.

B. E. McGrath and R. L. Simpson. Some features of surface pressure fluctuations in turbulent boundary layers with zero and favorable pressure gradients. *NASA Contractor Rep.*, 4051, 1987.

R. Merino-Martínez, A. Rubio Carpio, L. Lima Pereira, S. van Herk, F. Avallone, D. Ragni, and M. Kotsonis. Aeroacoustic design and characterization of the 3D-printed, open-jet, anechoic wind tunnel of Delft University of Technology. *Appl. Acoust.*, 170:107504, 2020.

T. Michelis and M. Kotsonis. Interaction of an off-surface cylinder with separated flow from a bluff body leading edge. *Exp. Therm. Fl. Sc.*, 63:91–105, 2015.

J. F. Morrison. The interaction between inner and outer regions of turbulent wall-bounded flow. *Phil. Trans. Royal Soc.*, 365(1852):683–98, 2007.

A. M. Naguib, C. E. Wark, and O. Juckenhöfel. Stochastic estimation and flow sources associated with surface pressure events in a turbulent boundary layer. *Phys. Fluids*, 13 (9):2611–2628, 2001.

R. Narasimha and S. N. Prasad. Leading edge shape for flat plate boundary layer studies. *Exp. in Fluids*, 17, 1994.

T. H. New, T. T. Lim, and S. C. Luo. Elliptic jets in cross-flow. *J. Fluid Mech.*, 494:119–140, 2003.

P. Orlandi and J. Jiménez. On the generation of turbulent wall friction. *Phys. Fluids*, 6(2): 634–641, 1994.

R. Örlü, T. Fiorini, A. Segalini, G. Bellani, A. Talamelli, and P. H. Alfredsson. Reynolds stress scaling in pipe flow turbulence—first results from CICLoPE. *Philosophical Transactions of the Royal Society A: Mathematical, Physical and Engineering Sciences*, 375(2089), 2017a. ISSN 1364-503X 1471-2962. doi: 10.1098/rsta.2016.0187.

R. Örlü, T. Fiorini, A. Segalini, G. Bellani, A. Talamelli, and P. H. Alfredsson. Reynolds stress scaling in pipe flow turbulence—first results from CICLoPE. *Phil. Trans. R. Soc. A.*, 375:20160187, 2017b.

R. L. Panton, M. Lee, and R. D. Moser. Correlation of pressure fluctuations in turbulent wall layers. *Phys. Rev. Fluids*, 2(9):094604, 2017.

F. R. Payne and J. L. Lumley. Large eddy structure of the turbulent wake behind a circular cylinder. *Phys. Fluids*, 10(9):S194–S196, 1967.

B. Podvin and Y. Fraigneau. A few thoughts on proper orthogonal decomposition in turbulence. *Phys. Fluids*, 29(2), 2017.

P. Pokharel and S. Acharya. Dynamics of circular and rectangular jets in crossflow. *Comp. & Fluids*, 230, 2021.

S. B. Pope. *Turbulent Flows.* Cambridge University Press, 2000.

Z. X. Qiao, Y. Zhou, and Z. Wu. Turbulent boundary layer under the control of different schemes. *Proc. Math. Phys. Eng. Sci.*, 473(2202):20170038, 2017.

M. Raffel, C. E. Willert, F. Scarano, C. J. Kähler, S. T. Wereley, and J. Kompenhans. *Particle image velocimetry: a practical guide*. Springer, 2018.

R. Rathnasingham and K. S. Breuer. System identification and control of a turbulent boundary layer. *Phys. Fluids*, 9(7):1867–1869, 1997.

R. Rathnasingham and K. S. Breuer. Active control of turbulent boundary layers. *J. Fluid Mech.*, 495:209–233, 2003.

H. Rebbeck and K. Choi. Opposition control of near-wall turbulence with a piston-type actuator. *Phys. Fluids*, 13(8):2142–2145, 2001.

H. Rebbeck and K. Choi. A wind-tunnel experiment on real-time opposition control of turbulence. *Phys. Fluids*, 18(3), 2006.

N. Renard and S. Deck. A theoretical decomposition of mean skin friction generation into physical phenomena across the boundary layer. *J. Fluid Mech.*, 790:339–367, 2016.

S. Rezaeiravesh, R. Vinuesa, M. Liefvendahl, and P. Schlatter. Assessment of uncertainties in hot-wire anemometry and oil-film interferometry measurements for wall-bounded turbulent flows. *Euro. J. Mech. - B/Fluids*, 72:57–73, 2018.

P. Ricco, M. Skote, and M. A. Leschziner. A review of turbulent skin-friction drag reduction by near-wall transverse forcing. *Prog. Aero. Sci.*, 123, 2021.

R. Richardson, Y. Zhang, and L. N. Cattafesta. Sensor decontamination via conditional spectral analysis. *Exp. Fluids*, 64(10):163, 2023.

H. Ritchie. What share of global CO_2 emissions come from aviation? *Our World in Data*, 2024.

E. Saccenti, M. H. W. B. Hendriks, and A. K. Smilde. Corruption of the Pearson correlation coefficient by measurement error and its estimation, bias, and correction under different error models. *Sci. Rep.*, 10(438), 2020.

M. Samie, W. J. Baars, A. Rouhi, P. Schlatter, R. Örlu, I. Marusic, and N. Hutchins. Near wall coherence in wall-bounded flows and implications for flow control. *Int. J. Heat Fluid Flow*, 86, 2020. 108683.

K. Sasaki, R. Vinuesa, A. V. G. Cavalieri, P. Schlatter, and D. S. Henningson. Transfer functions for flow predictions in wall-bounded turbulence. *J. Fluid Mech.*, 864:708–745, 2019.

R. Sau and K. Mahesh. Dynamics and mixing of vortex rings in crossflow. *J. Fluid Mech.*, 604:389–409, 2008.

G. Schewe. On the structure and resolution of wall-pressure fluctuations associated with turbulent boundary-layer flow. *J. Fluid Mech.*, 134:311–328, 1983.

W. Schoppa and F. Hussain. A large-scale control strategy for drag reduction in turbulent boundary layers. *Phys. Fluids*, 10(5):1049–1051, 1998.

M. P. Schultz and K. A. Flack. The rough-wall turbulent boundary layer from the hydraulically smooth to the fully rough regime. *J. Fluid Mech.*, 580:381–405, 2007.

A. Sciacchitano. Uncertainty quantification in particle image velocimetry. *Meas. Sci. Tech.*, 30(9), 2019.

M. Sheplak, L. Cattafesta, T. Nishida, and C. McGinley. MEMS Shear Stress Sensors: Promise and Progress. *24th AIAA Aerodynamic Measurement Technology and Ground Testing Conference*, 2004.

J.-M. Shi, D. Gerlach, M. Breuer, and F. Durstb. Analysis of heat transfer from single wires close to walls. *Phys. Fluids*, 15:908–921, 2003.

B. L. Smith, D. R. Neal, M. A. Feero, and G. Richards. Assessing the limitations of effective number of samples for finding the uncertainty of the mean of correlated data. *Meas. Sci. Tech.*, 29(12), 2018.

Douglas R. Smith. Interaction of a synthetic jet with a crossflow boundary layer. *AIAA J.*, 40(11):2277–2288, 2002.

A. J. Smits, B. J. McKeon, and I. Marusic. High–Reynolds number wall turbulence. *Annu. Rev. Fluid Mech.*, 43:353–375, 2011a.

A. J. Smits, J. Monty, M. Hultmark, S. C. C. Bailey, N. Hutchins, and I. Marusic. Spatial resolution correction for wall-bounded turbulence measurements. *J. Fluid Mech.*, 676: 41–53, 2011b.

L. C. Squire. The motion of a thin oil sheet under the steady boundary layer on a body. *J. Fluid Mech.*, 11(2):161–179, 1961.

B. Sun, M. Shehzad, D. Jovic, C. Cuvier, C. Willert, Y. Ostovan, J. Foucaut, C. Atkinson, and J. Soria. Distortion correction of two-component two-dimensional PIV using a large imaging sensor with application to measurements of a turbulent boundary layer flow at $\mathrm{Re}_\tau = 2386$. *Exp. Fluids*, 62(9), 2021.

A. Talamelli, F. Persiani, J. H. M. Fransson, P. H. Alfredsson, A. V. Johansson, H. M. Nagib, J.-D. Rüedi, K. R. Sreenivasan, and P. A. Monkewitz. CICLoPE—a response to the need for high Reynolds number experiments. *Fluid Dyn. Res.*, 41:021407, 2009.

L. H. Tanner and L. G. Blows. A study of the motion of oil films on surfaces in air flow, with application to the measurement of skin friction. *J. Phys. E: Sci. Inst.*, 9:194–202, 1976.

S. F. Tardu. Near wall turbulence control by local time periodical blowing. *Exp. Therm. Fluid Sci.*, 16:41–53, 1998.

A. S. W. Thomas and M. K. Bull. On the role of wall-pressure fluctuations in deterministic motions in the turbulent boundary layer. *J. Fluid Mech.*, 128:283–322, 1983.

T.G. Tillman and D.P. Hwang. Drag reduction on a large-scale nacelle using a microblowing technique. *37th Aero. Scie. Meeting and Exh.*, 1999.

C. E. Tinney, F. Coiffet, J. Delville, A. M. Hall, P. Jordan, and M. N. Glauser. On spectral linear stochastic estimation. *Exp. Fluids*, 41(5):763–775, 2006.

C. E. Tinney, J. Shipman, and P. Panickar. Proper-Orthogonal-Decomposition-Based Reduced-Order Models for Characterizing Ship Airwake Interactions. *AIAA Journal*, 58(2):633–646, 2019.

C. E. Tinney, J. Shipman, and P. Panickar. Proper-orthogonal-decomposition-based reduced-order models for characterizing ship airwake interactions. *AIAA J.*, 58(2):633–646, 2020.

A. Towne, O. T. Schmidt, and T. Colonius. Spectral proper orthogonal decomposition and its relationship to dynamic mode decomposition and resolvent analysis. *J. Fluid Mech.*, 847:821–867, 2018.

A. A. Townsend. *The structure of turbulent shear flow*. Cambridge University Press, 1976.

Y. Tsuji, J. H. M. Fransson, P. H. Alfredsson, and A. V. Johansson. Pressure statistics and their scaling in high-Reynolds-number turbulent boundary layers. *J. Fluid Mech.*, 585: 1–40, 2007.

Y. Tsuji, I. Marusic, and A. V. Johansson. Amplitude modulation of pressure in turbulent boundary layer. *Intl. J. Heat Fluid Flow*, 61:2–11, 2015.

M. Tutkun and W. K. George. Lumley decomposition of turbulent boundary layer at high reynolds numbers. *Phys. Fluids*, 29(2):020707, 2017.

J. Yu, D. Fan, B. R. Noack, and Y. Zhou. Genetic-algorithm-based artificial intelligence control of a turbulent boundary layer. *Acta Mech. Sin.*, 2021.

M. Yu, A. Ceci, and S. Pirozzoli. Reynolds number effects and outer similarity of pressure fluctuations in turbulent pipe flow. *Intl. J. Heat Fluid Fl.*, 96:108998, 2022.

E. S. Zanoun, F. Durst, and J. M. Shi. The physics of heat transfer from hot wires in the proximity of walls of different materials. *Int. J. Heat Mass Trans.*, 52(15-16):3693–3705, 2009.

X. Zheng, G. Bellani, L. Mascotelli, R. Örlü, A. Ianiro, C. Sanmiquel Vila, S. Discetti, J. Serpieri, M. Raiola, A. Talamelli, and N. Jiang. Inter-scale interaction in pipe flows at high Reynolds numbers. *Exp. Therm. Fluid Sci.*, 131:110529, 2022.

BIOGRAPHICAL NOTE

Figure 1.: The author of this dissertation heroically engaging in the act of surfing a 0.2 m-high swell.

It was a bright sunny day[1] on July 8th 1996, and the clocks were striking 5 AM[2]. Giulio came into this world the same way he will approach most of his life: following his guts, at a time and in a place he was not supposed to be born in: the former (albeit temporary) capital of the Roman Empire: Ravenna (Italy). World domination wishes (and utter panic from his parents' side) aside, Giulio grew up in the place he was actually supposed to be born in: Milan (Italy). Once he realized that he could not make his birth town the capital of the world again, he spent most of his childhood playing with Legos and, once completed, disassembling them and turning them into, of course, cutting-edge aircraft. This is when he realized that he had a strong interest and passion for anything that flew, which turned his head up in search for a path to the sky.

His interest in Lego aircraft matured into a genuine passion for aeronautics, which led him to pursue scientific secondary studies in Italy, and then venture into the world below sea level: The Netherlands. Here, he undertook studies in Aerospace Engineering both for his B.Sc. and M.Sc., making him unravel a particular interest towards fluid mechanics. After his masters, instead, he rose to new heights by diving deep into the (still-below-sea-level) field of Aerodynamics for his Ph.D. Here, Giulio's interests for aerodynamic experimental activities grew so much that he now monitors outside air temperature at all times to the tenth of a degree.

Actually, him being keen on fluid mechanics was a constant throughout his whole life; his university years have only acted as an emotional trigger. In fact, he has always been very fond of sailing, swimming and, more recently, surfing (the interested reader is referred to Fig. 1 of this chapter).

[1] The author is not 100% certain of weather conditions on that day.
[2] ± 2 hr

SUMMARIZED CURRICULUM VITÆ

Giulio DACOME

08-07-1996	Born in Ravenna, Italy.

EDUCATION

2015-2018	B.Sc. in Aerospace Engineering Delft University of Technology, Delft The Netherlands
2018-2021	M.Sc. in Aerospace Engineering - Aerodynamics Delft University of Technology, Delft The Netherlands
2021-2025	Ph.D. in Aerodynamics Delft University of Technology, Delft The Netherlands

OTHER EXPERIENCE

2020-2021	Technical Consultant INCYDE Foundation, Spain
2019-2020	Researcher San Diego State University, U.S.A.
2018-2019	Founding board member 180 Degrees Consulting, The Netherlands
2016-2018	Honours Programme Delft Delft University of Technology, The Netherlands

List of Publications

Journal publications

5. DACOME, G., KOTSONIS, M., BAARS, W.J. 2025. Experimental study of real-time control of a turbulent boundary layer using wall-pressure sensing. *Experimental Thermal and Fluid Science* (in review).

4. DACOME, G., LAZZARINI, L., TALAMELLI, A., BELLANI, G., BAARS, W.J. 2025. Wall-pressure–velocity correlations in high Reynolds number pipe flow. *Journal of Fluid Mechanics* (1013, A48).

3. DACOME, G., MÖRSCH, R., KOTSONIS, M., BAARS, W.J. 2024. Opposition flow control for reducing skin-friction drag of a turbulent boundary layer. *Physical Review Fluids* (9, 064602).

2. BAARS, W.J., DACOME, G., LEE, M.K. 2024. Reynolds-number scaling of wall-pressure–velocity correlations in wall-bounded turbulence. *Journal of Fluid Mechanics* (981, A15).

1. RUSSO, L., SAETTA, E., TOGNACCINI, R., DACOME, G., DEMASI, L. 2022. Aerodynamic analysis of a box winglet: viscous and compressible flow predictions. *Aerotecnica Missili e Spazio* (101).

Conference contributions

6. DACOME, G., KOTSONIS, M., BAARS, W.J. 2025. Adaptive control of turbulent wall-bounded flows. *International Conference on Experimental Fluid Mechanics 2025 (ICEFM25)*.

5. DACOME, G., KOTSONIS, M., BAARS, W.J. 2024. Towards adaptive control of wall-bounded turbulence. *Europeanm Drag Reduction and Flow Control Meeting 2024 (EDRFCM24)*.

4. DACOME, G., LAZZARINI, L., KOTSONIS, M., G., BAARS, W.J. 2024. Closed-loop control of large-scale coherent structures in wall-bounded turbulence for skin-friction drag reduction. *Euromech Colloquim 631*.

3. DACOME, G., LAZZARINI, L., KOTSONIS, M., G., BAARS, W.J. 2023. Real-time flow control of drag-producing structures in wall-bounded turbulence. *Engineering Turbulence Modelling and Measurements Symposium (ETMM14)*.

2. DACOME, G., LAZZARINI, L., TALAMELLI, A., BELLANI, G., BAARS, W.J. 2023. Turbulent wall-pressure fluctuations in the CICLoPE facility. *Interdisciplinary Turbulence Initiative X (iTi X)*.

1. DACOME, G., SCHRIJER, F.F.J., VAN OUDHEUSDEN, B.W. 2022. The interaction between a sonic jet and an oblique shock wave in a supersonic crossflow. *AIAA SciTech Forum*.

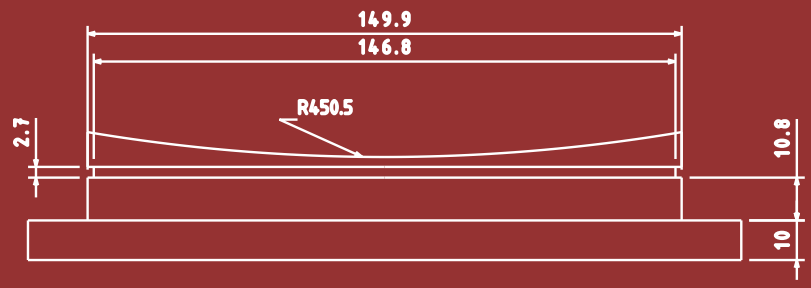

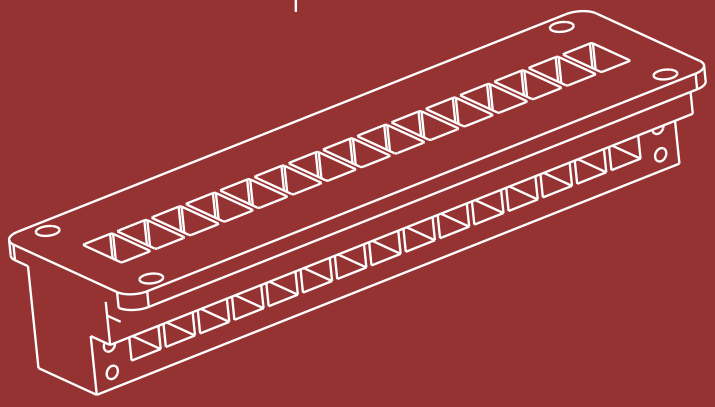

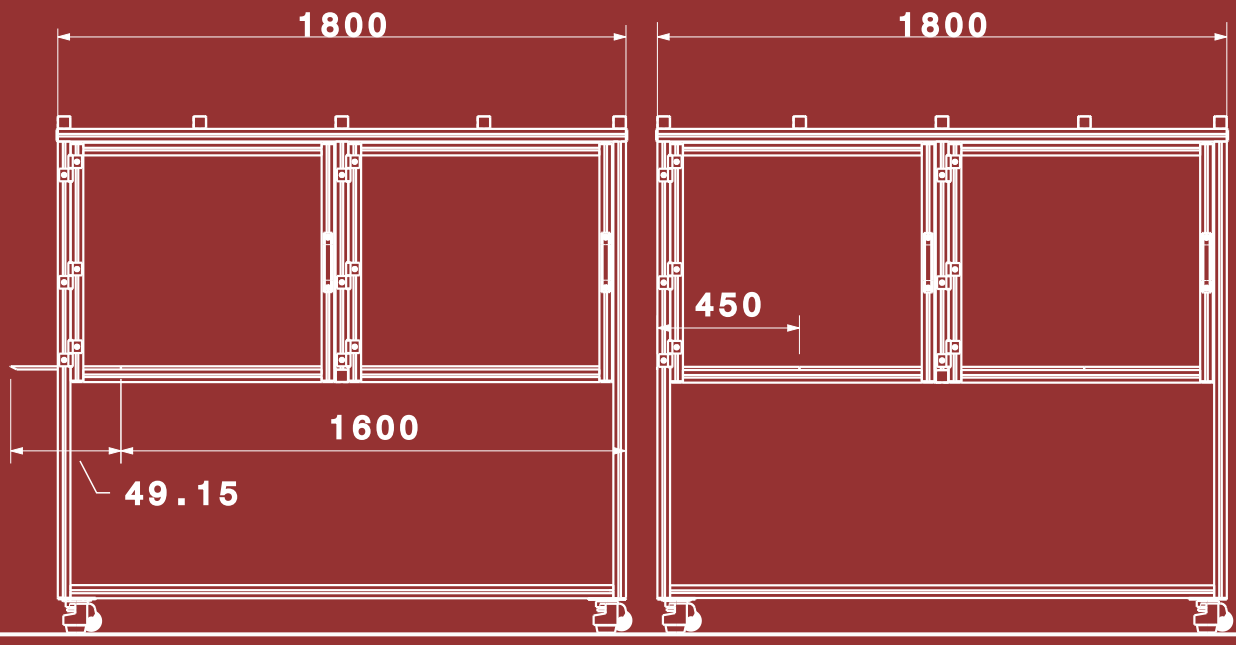

TU Delft Delft University of Technology

ISBN 978-94-6384-859-6